

University of Bath



PHD

Ray tracing coverage and capacity studies for SISO and MIMO communication systems

Tila, Fai

Award date:
2003

Awarding institution:
University of Bath

[Link to publication](#)

General rights

Copyright and moral rights for the publications made accessible in the public portal are retained by the authors and/or other copyright owners and it is a condition of accessing publications that users recognise and abide by the legal requirements associated with these rights.

- Users may download and print one copy of any publication from the public portal for the purpose of private study or research.
- You may not further distribute the material or use it for any profit-making activity or commercial gain
- You may freely distribute the URL identifying the publication in the public portal ?

Take down policy

If you believe that this document breaches copyright please contact us providing details, and we will remove access to the work immediately and investigate your claim.

Ray Tracing Coverage and Capacity Studies for SISO and MIMO Communication Systems

Submitted by Fai Tila

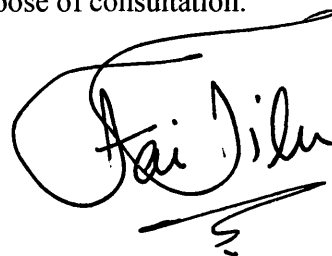
**for the degree of PhD
of the University of Bath**

2003

Copyright

Attention is drawn to the fact that copyright of this thesis rests with its author. This copy of the thesis has been supplied on condition that anyone who consults it is understood to recognise that its copyright rests with its author and that no quotation from the thesis and no information derived from it may be published without the prior written consent of the author.

This thesis may be made available for consultation within the University Library and may be photocopied or lent to other libraries for the purpose of consultation.

A handwritten signature in black ink, reading "Fai Tila", with a large, sweeping flourish above the name and a horizontal line underneath.

UMI Number: U602096

All rights reserved

INFORMATION TO ALL USERS

The quality of this reproduction is dependent upon the quality of the copy submitted.

In the unlikely event that the author did not send a complete manuscript and there are missing pages, these will be noted. Also, if material had to be removed, a note will indicate the deletion.



UMI U602096

Published by ProQuest LLC 2014. Copyright in the Dissertation held by the Author.
Microform Edition © ProQuest LLC.

All rights reserved. This work is protected against
unauthorized copying under Title 17, United States Code.



ProQuest LLC
789 East Eisenhower Parkway
P.O. Box 1346
Ann Arbor, MI 48106-1346

UNIVERSITY OF BATH
LIBRARY
70 - 7 JUL 2003
PHD

Abstract

Over the last decade the use of wireless devices has increased significantly and demand for ever higher bit rates has emerged. The design of efficient radio networks requires a clear knowledge of the underlying channel characteristics. In this thesis a thorough examination of indoor radiowave propagation at 2, 5, 11 and 17 GHz is performed. Propagation data is extracted from a newly developed ray-tracing propagation model. Ray tracing was chosen to enable site specific analysis over a range of radio architectures and configurations. The model supports advanced features such as multiple antennas and transmission from High Altitude Platforms (HAPs).

All radio systems are known to suffer from multipath fading. To overcome this problem, a number of enhancements are developed in this thesis. The work initially focuses on the use of space, frequency and polarisation diversity. Beam switched and sectorised antennas are also explored at the access point. More significantly, recent solutions suggest the use of Multiple Input Multiple Output (MIMO) communications. Theoretically, this technology achieves a revolutionary increase in channel capacity. In this thesis, the practical implementation of MIMO is quantitatively explored under realistic (rather than mathematically abstract) radio channel conditions. A detailed analysis of indoor coverage from a distant HAP in the 2GHz UMTS band is presented with and without the use of space diversity at the terminal.

Theoretical capacity analysis is performed for MIMO communications assuming perfectly uncorrelated or perfectly correlated Rayleigh and Rician fading channels. The results confirmed that MIMO communications improves the theoretical capacity in a rich scattering environment, providing the fading over the array is uncorrelated. For correlated MIMO channels, the capacity was seen to drop with increasing scatter. Using a modified version of the ray tracing model, the channel matrix was predicted for 4x4 micro and macro MIMO configurations.

Finally, the structure of the MIMO link matrix was analysed over an entire indoor environments. The effective rank and Eigenvalue spread were analysed together with micro and macro-MIMO coverage and capacity for a site specific indoor environment. Results are compared with mathematical models assuming Rayleigh fading.

Acknowledgements

I would like to thank my project advisers, Drs Peter Shepherd and Steve Pennock, whose help and advice throughout the project was invaluable. Their patience, support and guidance are gratefully acknowledged.

I would like to acknowledge the Department of Electrical and Electronic Engineering for the part-funding of my final year of study.

Finally, I would like to thank my family and friends for their financial and emotional support.

This work is dedicated to the beautiful memory of my dad, to my mum and to my special friend BoB. Thank you for your love, your kindness and your support. Dad's wonderful memory lives on within my heart and keeps me going through the hard times.

God bless you all.

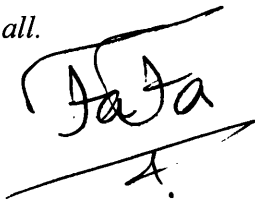
A handwritten signature in black ink that reads "Jaja". The signature is written in a cursive, slightly stylized font. Below the name, there is a horizontal line that starts under the 'J' and ends with a small upward-pointing flourish under the 'a'.

Table of Contents

ABSTRACT	II
ACKNOWLEDGEMENTS	III
TABLE OF CONTENTS	V
LIST OF SYMBOLS	X
LIST OF ABBREVIATIONS	XI
Chapter 1: Introduction	1
1.1 INTRODUCTION	1
1.2 GROWTH AND FUTURE OF WIRELESS COMMUNICATIONS	2
1.3 INDOOR NETWORKS AND COMMUNICATIONS.....	3
1.4 AIMS AND MOTIVATION.....	4
1.5 ACHIEVEMENTS AND KEY CONTRIBUTIONS	4
1.6 STRUCTURE OF THESIS.....	5
1.7 REFERENCES	7
Chapter 2: Propagation and Capacity Theory.....	8
2.1 INTRODUCTION	8
2.2 MULTIPATH AND SHADOWING	9
2.2.1 RECEIVED POWER DENSITY AND ELECTRIC FIELD STRENGTH	10
2.2.2 RECEIVED POWER AND ELECTRIC FIELD	11
2.2.3 PRACTICAL ANTENNA GAIN, EFFECTIVE AREA AND BEAMWIDTH	12
2.2.4 RECEIVED POWER AND FIELD STRENGTH USING PRACTICAL ANTENNAS	13
2.2.5 PROPAGATION PATH LOSS AND NORMALISED RECEIVED POWER	14
2.2.6 SIGNAL TO NOISE RATIO	16
2.3 MULTIPATH PROPAGATION.....	17
2.3.1 FAST AND SLOW FADING.....	18
2.3.2 LINE OF SIGHT (RICIAN) AND NON-LINE-OF-SIGHT (RAYLEIGH) FADING	18
2.3.3 CONSTRUCTIVE AND DESTRUCTIVE INTERFERENCE	19
2.3.4 K-FACTOR	21
2.4 WIDEBAND CHANNELS.....	21
2.4.1 RMS DELAY SPREAD	22
2.4.2 COHERENCE BANDWIDTH.....	23
2.5 INDOOR/OUTDOOR HAP.....	24
2.6 SHANNON CAPACITY EQUATION.....	25
2.7 MIMO SYSTEMS AND THE FOSCHINI EQUATION	27
2.8 SUMMARY.....	30
2.9 REFERENCES	31
Chapter 3: Ray Tracing Principles and Techniques	35
3.1 INTRODUCTION.....	35
3.2 LITERATURE REVIEW IN RAY TRACING	36
3.2.1 DETERMINISTIC PROPAGATION MODELS	36
3.2.1.1 <i>Image-based Technique</i>	37

3.2.1.2	Ray Launching Technique	38
3.3	BASIC ELEMENTS OF RAY TRACING	39
3.3.1	SINGLE REFLECTION AND TRANSMISSION	39
3.3.2	MULTI-REFLECTION USING IMAGE THEORY.....	41
3.3.3	POLARISATION	43
3.3.4	DIFFRACTION	45
3.4	LIMITATIONS OF RAY-TRACING MODEL	45
3.5	PROPAGATION MODEL: PROGRAM STRUCTURE AND I/O	46
3.5.1	DEFINITION OF INPUT DATABASE.....	47
3.5.2	ENVIRONMENT GRID SOFTWARE.....	49
3.5.3	PROGRAM INPUT/OUTPUT	50
3.5.4	INPUT FILE FORMAT AND DESCRIPTION	51
3.5.5	OUTPUT FILE FORMATS AND DESCRIPTION.....	51
3.5.6	MATERIAL CHARACTERISTICS AND ATTENUATION PER METRE	53
3.6	RAY-TRACING PROGRAM CODE.....	54
3.7	FIELD-RECONSTRUCTION PROGRAM CODE	55
3.8	POST-PROCESSING SOFTWARE.....	56
3.9	TRACING OF RAYS.....	58
3.10	AVERAGE POWER AND SIGNAL TO NOISE CALCULATIONS	60
3.11	SUMMARY.....	64
3.12	REFERENCE	65
Chapter 4:	Indoor Systems and Diversity	68
4.1	INTRODUCTION TO DIVERSITY	68
4.2	GENERATION TECHNIQUES	68
4.2.1	SPACE DIVERSITY.....	68
4.2.1.1	Receiver Space Diversity.....	69
4.2.1.2	Transmitter Space Diversity	70
4.2.2	POLARISATION DIVERSITY	71
4.2.3	FREQUENCY DIVERSITY	71
4.3	DIVERSITY COMBINING METHODS	73
4.3.1	SELECTION COMBINING.....	73
4.3.2	EQUAL GAIN COMBINING.....	74
4.3.2.1	Amplitude Summation.....	74
4.3.2.2	Vector Summation.....	75
4.4	INTRODUCTION TO FREQUENCY DIVERSITY	76
4.4.1	SINGLE BRANCH NORMALISED FIELD STRENGTH RESULTS	76
4.4.2	FREQUENCY DIVERSITY COMBINING	80
4.4.2.1	Comparison of EG-AC, EG-VC and SC results	83
4.4.2.2	Detailed Combining Analysis: Branches 1 and 5	83
4.4.3	DIVERSITY GAIN VERSUS FREQUENCY SEPARATION	84
4.4.4	FREQUENCY DIVERSITY CDF RESULTS.....	86
4.4.4.1	Comparison of Combining Strategies.....	86
4.5	INTRODUCTION TO POLARIZATION DIVERSITY	89
4.5.1	POLARISATION SETUP AND SIMULATION STRATEGY	90
4.5.2	POLARISATION RESULTS: GROUP 1	91
4.5.2.1	Diversity Combining: Group 1 (Polarisation Signals)	92
4.5.2.2	Diversity Combining: Group 2 (higher centre frequency).....	93
4.5.2.3	Diversity Combining: Group 3 (lower cut off level)	94
4.5.3	POLARISATION DIVERSITY CDF ANALYSIS.....	95

4.6	INTRODUCTION TO SPACE DIVERSITY	97
4.6.1	RECEIVER SPACE DIVERSITY	97
4.6.1.1	Receiver Spacing Setup and Simulation Strategy	97
4.6.1.2	Receiver Space Diversity Results: Group 1	99
4.6.1.3	Branch input statistics	102
4.6.1.4	Diversity Combining: Group 2	103
4.6.1.5	Receiver Space Diversity Gain versus Receiver Spacing	103
4.6.1.6	Receiver Space Diversity CDF Analysis	105
4.6.2	TRANSMITTER SPACE DIVERSITY	107
4.6.2.1	Transmitter Space Diversity Setup and Simulation Strategy	108
4.6.2.2	Transmitter Space Diversity Results: Group 1	108
4.6.2.3	Branch input statistics	111
4.6.2.4	Diversity Combining: Group 2	112
4.6.2.5	Transmitter Space Diversity Gain versus Antenna Spacing	112
4.6.2.6	Transmitter Space Diversity CDF Analysis	114
4.7	SUMMARY	117
4.8	REFERENCES	118
 Chapter 5: Sectorised Antenna Beam Patterns		121
5.1	INTRODUCTION	121
5.2	RAY MODEL & ENVIRONMENT	122
5.3	DIVERSITY GENERATION AND COMBINING	123
5.3.1	BEAM PATTERN DIVERSITY	124
5.4	SYSTEM ANALYSIS	125
5.5	SUMMARY	131
5.6	REFERENCES	132
 Chapter 6: High Altitude Platform (HAP)		134
6.1	INTRODUCTION	134
6.2	MODELLING OF SATELLITE/HAP TO INDOOR PROPAGATION	135
6.2.1	APPROXIMATING THE RECEIVED IN-BUILDING SIGNAL FROM A DISTANT SATELLITE	135
6.2.2	REAL SCENARIO	136
6.2.3	DESCRIPTION OF APPROXIMATION USED	138
6.3	ACCURATE MODEL FOR HAP-INDOOR PROPAGATION	139
6.3.1	USE OF VIRTUAL TRANSMITTERS	140
6.4	HAP ENVIRONMENT DESCRIPTION AND MODEL MODIFICATIONS	142
6.4.1	ENVIRONMENT DESCRIPTION	142
6.4.2	MODIFICATION OF THE FIELD RECONSTRUCTION SOFTWARE	143
6.5	HAP-INDOOR FIELD STRENGTH PREDICTIONS	144
6.5.1	RECONSTRUCTED FIELD STRENGTH: SIMPLIFIED METHOD	144
6.5.2	RECONSTRUCTED FIELD STRENGTH: ACCURATE METHOD	145
6.5.3	POWER CDF AND PDF FOR THE SIMPLIFIED METHOD	146
6.5.4	POWER CDF AND PDF FOR THE ACCURATE METHOD	147
6.5.5	FIELD STRENGTH CDF COMPARISON FOR SIMPLIFIED AND ACCURATE METHODS	148
6.6	INDOOR PROPAGATION AND DIVERSITY EVALUATION USING HAPS	149
6.6.1	HAP PATH LOSS CALCULATION	149
6.6.2	HAP RAY MODELLING	151
6.6.3	TEST ENVIRONMENT	152
6.6.4	PROPAGATION RESULTS	153
6.6.5	HAP SYSTEM PERFORMANCE	156
6.6.6	CONCLUSIONS	159

6.7	SUMMARY OF HAP MODELS.....	159
6.8	REFERENCES	161
Chapter 7: Indoor MIMO Communications.....		165
7.1	INTRODUCTION	165
7.2	THEORETICAL MIMO CAPACITY	166
7.2.1	RAY MODELLING AND CALCULATION OF THE H-MATRIX.....	166
7.2.2	GENERATING THE NORMALISED H-MATRICES (STEP 1)	166
7.2.3	CALCULATING AVERAGE CAPACITY (STEP 2)	168
7.2.4	DISPLAYING THE RESULTS (STEP 3)	168
7.3	THEORETICAL MIMO RESULTS AND DISCUSSION	169
7.3.1	SINGLE ANTENNA CONFIGURATION	169
7.3.2	MIMO CONFIGURATION (2 TRANSMIT, 2 RECEIVE ANTENNAS).....	171
7.3.3	MIMO CONFIGURATION (4 TRANSMIT, 4 RECEIVE ANTENNAS).....	174
7.4	MIMO DETERMINISTIC MODELLING	177
7.4.1	MICRO AND MACRO MIMO	179
7.4.2	AVERAGE RECEIVED POWER, NORMALISATION AND CHANNEL CAPACITY.....	180
7.4.3	REFERENCE GRAPHS	181
7.5	ROUTE BASED MIMO CAPACITY RESULTS USING ULAS	182
7.5.1	MICRO-MIMO	183
7.5.2	MACRO-MIMO	190
7.5.3	SUMMARY OF MICRO/MACRO MIMO CAPACITIES FOR ROUTES 1 & 2.....	195
7.6	GRID BASED MIMO CAPACITY RESULTS USING ULAS	196
7.6.1	MICRO-MIMO STUDY.....	197
7.6.2	MACRO-MIMO STUDY	201
7.7	SUMMARY	205
7.8	REFERENCES	207
Chapter 8: Conclusions and Further Work.....		209
8.1	INTRODUCTION.....	209
8.2	PROPAGATION THEORY AND CHANNEL CAPACITY.....	210
8.3	RAY TRACING PRINCIPLES AND TECHNIQUES.....	211
8.4	DIVERSITY COMBINING AND GENERATION	211
8.5	SECTORISED AND BEAM SWITCHED ANTENNAS	213
8.6	HIGH ALTITUDE PLATFORMS.....	214
8.7	MIMO COMMUNICATIONS.....	215
8.8	FUTURE WORK.....	217
Appendix A: Boundary Analysis		219
A.1	VERTICAL AND HORIZONTAL BOUNDARIES.....	219
A.1.1	RELATIONSHIP BETWEEN ANG, AL AND ALFA	219
A.1.1.1	Ang in Quadrant 1	219
A.1.1.2	Ang in Quadrant 2	220
A.1.1.3	Ang in Quadrant 3	220
A.1.1.4	Ang in Quadrant 4	221
A.1.2	SIMULATION OF TRANSMISSION OR REFLECTION	222
A.2	BOUNDARY ANALYSIS.....	222
A.2.1	VERTICAL BOUNDARY, THE CASE OF $E_2 < E_1$	222

A.2.1.1	<i>Geometry Case 1</i>	222
A.2.1.2	<i>Geometry Case 2</i>	223
A.2.1.3	<i>Geometry Case 3</i>	224
A.2.1.4	<i>Geometry Case 4</i>	226
A.2.2	HORIZONTAL BOUNDARY, THE CASE OF $E_2 > E_1$	227
Appendix B: Diversity Methods and Techniques		228
B.1	DETAILED COMBINING ANALYSIS.....	228
B.1.1	BRANCHES 1 AND 2	228
B.1.2	BRANCHES 1 AND 3	229
B.1.3	BRANCHES 1 AND 4	229
B.2	RECEIVER SPACE DIVERSITY GAIN VERSUS ANTENNA SPACING	230
B.2.1	GROUP 8 RELATIVE TO BRANCH 2	230
B.3	RECEIVER SPACE DIVERSITY COMBINING.....	232
B.3.1	GROUP 1: 0.25 λ SPACING.....	232
B.3.2	GROUP 3: λ SPACING.....	233
B.3.3	GROUP 4: 1.5 λ SPACING.....	234
B.3.4	GROUP 5: 2 λ SPACING.....	235
B.3.5	GROUP 6: 2.5 λ SPACING.....	236
B.3.6	GROUP 7: 3 λ SPACING.....	237
B.3.7	GROUP 8: 3.5 λ SPACING.....	238
B.4	TRANSMITTER SPACE DIVERSITY COMBINING	239
B.4.1	GROUP 1: 0.25 λ SPACING.....	239
B.4.2	GROUP 3: λ SPACING.....	240
B.4.3	GROUP 4: 1.5 λ SPACING.....	241
B.4.4	GROUP 5: 2 λ SPACING.....	242
B.4.5	GROUP 6: 2.5 λ SPACING.....	243
B.4.6	GROUP 7: 3 λ SPACING.....	244
B.4.7	GROUP 8: 3.5 λ SPACING.....	245
Appendix C: HAP Ray Tracing Symmetry Tests		246
C.1	INTRODUCTION	246
C.1.1	CASE 1: DOWNWARD VERTICAL RAY TEST.....	246
C.1.2	CASE 2: UPWARD VERTICAL RAY TEST.....	247
C.1.3	CASE 3: RIGHT HORIZONTAL RAY TEST.....	248
C.1.4	CASE 4: LEFT HORIZONTAL RAY TEST.....	248
C.2	TESTING AND VERIFICATION OF SATELLITE MODEL.....	248
C.2.1	SYMMETRY VERIFICATION	248
C.2.1.1	<i>Case 1: Downward Vertical Ray Test</i>	249
C.2.1.2	<i>Case 2: Upward Vertical Ray Test</i>	251
C.2.1.3	<i>Case 3: Right Horizontal Ray Test</i>	252
C.2.1.4	<i>Case 4: Left Horizontal Ray Test</i>	253
Appendix D: MIMO Micro versus Macro for Route 2.....		254
D.1	MICRO RESULTS.....	254
D.2	MACRO RESULTS	257
Appendix E: List of Publications.....		261

List of Symbols

σ	Conductivity
λ	Wavelength
μ	Permeability
μ_0	Free Space Permeability $\approx 4\pi \cdot 10^{-7} \text{ H m}^{-1}$
μ_r	Relative Permeability = μ / μ_0
π	Pi = 3.14 radians /180 degrees
ε	Permittivity
ε_0	Free Space Permittivity $\approx 8.85 \cdot 10^{-12} \text{ Fm}^{-1}$
ε_r	Relative Permittivity = $\varepsilon / \varepsilon_0$
α	Attenuation factor
δ	Delta
ω	$2\pi f$
f	Frequency
τ	RMS delay
ρ	Signal to Noise ratio
B_c	Coherence Bandwidth $\approx 1/6\tau$

List of Abbreviations

2D	2 Dimensional
3D	3 Dimensional
AP	Access Point
AWGN	Additive White Gaussian Noise
B1	Branch1
B2	Branch2
BER	Bit Error Rate
CDF	Cumulative Distribution Function
CDMA	Code Division Multiple Access
Codec	Coder/Decoder
EG-AC	Equal Gain Amplitude Combining
EG-VC	Equal gain Vector Combining
EGC	Equal Gain Combining
ETSI	European Telecommunications Standard Institute
HAP	High Altitude Platform
HIPERLAN	High Performance Radio Local Area Network
IEE	Institute of Electrical Engineers
IEEE	Institute of Electrical and Electronics Engineers
i.i.d	Independent Identically Distributed
ISI	Intersymbol Interference
ISM	Industrial, Scientific and Medical
LAN	Local Area Network
LOS	Line Of Sight
MEA	Multi Element Array
Met	Method
MIMO	Multiple Inputs Multiple Outputs
MMSE	Minimum Mean Square Error
MT	Mobile Terminal
PAN	Personal Area Network
PDA	Personal Digital Assistant
PDF	Probability Distribution Function
PHY	Physical

RMS	Root Mean Square
RSSI	Received Signal Strength Indication
SC	Selective Combining
SISO	Single Input Single Output
SNR	Signal-to-Noise Ratio
ULA	Uniform Linear Array
UMTS	Universal Mobile Telecommunication Systems
Ver	Version
WLAN	Wireless Local Area Network

Chapter 1: Introduction

1.1 Introduction

Over the last decade there has been a dramatic increase in the penetration and use of digital communication devices. It is now an everyday requirement to support wireless connectivity in the home and office. Demand for higher bit rates is increasing due to the proliferation of the internet and the push to transmit image and video over wireless bearers [1]. The growth of low cost colour displays and the introduction of new radio standards such as Bluetooth [2] will continue to fuel the demand for ever faster wireless links. Radio spectrum is a scarce resource and current cellular and wireless local area network (WLAN) bands are already highly congested [3]. The next generation of wireless LANs, for example 802.11a [4], are migrating to the 5GHz band and it is inevitable that future services will occupy even higher frequencies in the search for available bandwidth.

The design of efficient radio networks requires a clear knowledge of the underlying channel characteristics. In this thesis a thorough examination of indoor radiowave propagation at 2, 5, 11 and 17 GHz is performed. The propagation data for each significant multipath is extracted from a developed ray-tracing propagation model. The model has been extended to support certain advanced and novel features such as the use of multiple antennas at both the terminal and access point [5] and the broadcast of signals from distant High Altitude Platforms (HAP) [6].

All radio systems are known to suffer from multipath fading. This requires a significant increase in transmit power to ensure reliable transmission is achieved. However, as the numbers of users increases, higher transmit powers generate a significant interference problem. To overcome this problem, a number of enhancements are developed and quantified in this thesis. These techniques improve the reliability of the transmission and/or enhance the overall capacity of the communications system. The more obvious solutions make use of space, frequency and polarisation diversity [7] either at the mobile terminal or access point. The use of beam switched and sectorised antennas are also explored at the access point. More significantly, recent solutions suggest the use of Multiple Input Multiple Output (MIMO) communications. Theoretically, this technology achieves a revolutionary

increase in channel capacity. In this thesis, the practical implementation of MIMO is quantitatively explored under realistic (rather than mathematically abstract) radio channel conditions.

As mentioned earlier, in addition to standard indoor coverage solutions, the use of HAPs to achieve indoor communication is explored. The underlying ray model was significantly extended using a unique virtual antenna array concept to enable the propagation channel to be evaluated [8]. The use of HAPs is currently being considered by a number of standards bodies as an alternative to more traditional terrestrial networks.

1.2 Growth and Future of Wireless Communications

From a computing, communication and information technology point of view, the last ten years have witnessed considerable change on a number of fronts. Over the same time period there has been a massive increase in the processing power of personal computers and their penetration into the workplace and home. There has been an explosion in the use of mobile telephony, a substantial spread in the use of the internet, an increase in the number of digital entertainment services and a growing reliance of businesses on real time information being available to an increasingly mobile workforce.

Current trends point towards the convergence of computing, communications, information technology and entertainment applications. Standing at the centre of this convergence is the emergence of new forms of wireless communication networks. The challenge for future wireless communication systems is to meet the ever-increasing demand for high information transfer rates in a reliable, cost effective and flexible manner while efficiently using the available frequency spectrum.

Radio wave propagation plays a key role in determining the performance limits for a wireless communications device. This means that a thorough understanding of its nature and an ability to model its behaviour is considered vital as a foundation for the design of wireless communication systems [9]. The above issues are considered core to the work performed in this thesis.

1.3 Indoor Networks and Communications

The increasing reliance on networking in business and domestic environments and the explosion in the use of the internet and online services are providing a substantial market for the growth of indoor communications. A large segment of this market is occupied by Wireless Local Area Networks (WLANs) [5]. The concept of using radio waves as an alternative to physical connections to transfer information around the office and home is becoming increasingly popular. Each user makes use of a radio card in their terminal (laptop or desktop PC, PDA or Mobile phone) to access other devices or core networks. Normally the radio modem communicates with a basestation or access point, which is also fitted with similar radio equipment. The access point is normally connected to the wired network, giving the user access to data and shared network resources. The key challenge is to provide a service that is as fast and reliable as that of a cable. The use of wireless connectivity offers a number of advantages over traditional wired networks. These include:

- Increased productivity: the ability of users to access real-time information anywhere within their organisation;
- Flexibility and speed of installation: as no physical connection is required between the user terminals in a wireless network, its installation can be faster and easier;
- Reduced cost of ownership: In the ever-changing world of today's corporate environments, the long-term cost benefits offered by wireless networks could be of significant importance.

The main disadvantages of a wireless communications link are:

- Reduced data throughputs (compared to emerging fixed technologies such as Gigabit Ethernet [10]);
- Limited user capacities (which prevents a high density of broadband data centric applications);
- Poor security;
- Unreliable communications.

1.4 Aims and motivation

This research programme aims to develop a set of tools to analyse and study the wireless propagation channel. The use of ray tracing as a method of channel modelling [11] was chosen to enable site specific analysis to be performed for a range of radio architectures and configurations. Using the resulting ray models, a range of system enhancements are analysed in an attempt to address the limitations highlighted in section 1.3. Particular highlights include the use of HAPs to provide an alternative to the terrestrial wireless delivery of indoor broadband coverage and the use of a macro-MIMO configuration to significantly enhance the available capacity in future indoor wireless networks.

1.5 Achievements and Key Contributions

The following list of novel achievements and key contributions to the existing body of knowledge were made as a result of the work described in this thesis:

- The development of a novel deterministic propagation model for analysing field strength and multipath statistics in an indoor environment;
- A detailed analysis of diversity and diversity combining strategies for indoor communications at 11 GHz and 17 GHz;
- A comparison of sectorised and beam-switched solutions for indoor communications at 11 GHz and 17 GHz;
- The use of an array of virtual transmitter antennas to simulate propagation from a distant HAP at any elevation angle;
- A detailed analysis of W-CDMA coverage at 2GHz (with and without space diversity at the terminal) given transmission from a distant HAP;
- A theoretical (including ideally correlated and uncorrelated scatter components) and ray-model based analysis and comparison of capacity for MIMO communications;
- A comparison of micro and macro MIMO capacity (for various antenna spacing) over practical indoor communication channels at 5 GHz;

- A site specific grid based analysis of the effective rank and Eigen-structure of the **H**-matrix for micro and macro-MIMO configurations.

1.6 Structure of Thesis

Chapter 2 provides an introduction to the area of wireless propagation. Field strength and coverage factors such as free space path loss, antenna gain, shadowing, link budgets and signal to noise ratios are considered. Multipath effects such as Rayleigh and Rician fading and K-factor are discussed together with wideband parameters such as RMS delay spread, coherence bandwidth and the power delay profile. More advanced concepts such as the use of MIMO and High Altitude Platforms (HAPs) are also introduced.

Chapter 3 introduces the main principles of ray tracing and launching. Fundamental primitives such as line of sight modelling, reflection and transmission are described. The limitations inherent in the ray modelling process are explained in this chapter. The input and output file formats are described and the structure of the ray launching software is defined, including interactions between the ray tracing and field reconstruction software.

Chapter 4 looks at the subject of diversity generation and combining. This section describes the basics of space, polarisation and frequency diversity. Factors such as receiver and transmitter space diversity are explained and the three main methods of combining are described. Field strength results are given for a single antenna and extended to a range of diversity solutions. Analysis includes the calculation of the field strength mean, variance and standard deviation with and without diversity combining. The statistical cumulative distribution function of field strength across the indoor environment is also given.

Chapter 5 describes the use of antenna beam pattern diversity and switched sectorised antennas. The chapter analyses field strength coverage predictions for high frequency indoor communications using these techniques at 17 GHz. Performance is further enhanced by the use of two branch spaced antenna diversity at the mobile terminal.

Chapter 6 describes two new modelling techniques for simulating indoor coverage from a distant HAP. The first method uses a simple mathematical modification

whereas the second technique makes use of a novel virtual transmitter arrangement to simulate accurately near parallel rays entering the indoor environment from a distant HAP. Validation results are used to confirm the correct operation of the modified software. Field strength grids are produced using the accurate HAP extension and compared with the simplified approximation. The chapter ends with a statistical analysis of indoor coverage at 2GHz for a broadband communication network based on HAPs.

Chapter 7 looks at the application of MIMO in an indoor environment. The chapter begins with a mathematical analysis of the MIMO channel capacity. Here the well known Foschini equation is applied to Rayleigh and Rician fading channels. The study is performed for ideally uncorrelated and perfectly correlated fading channels. A MIMO extension is applied to the ray model and indoor coverage and capacity is then studied for micro and macro-MIMO deployment. Here the impact of more realistic multipath fading and practical Access Point (AP) and Mobile Terminal (MT) configurations are studied and results for routes and grids are compared with earlier mathematical bounds.

The thesis ends with a summary and set of conclusions for each work area and by identifying new areas for further work.

1.7 References

- [1] D. Bull, N. Canagarajah, and A. Nix, "Insights into mobile multimedia communications", *Academic Press*, London, 1999.
- [2] The Bluetooth Standard Version 1.0b (<http://www.bluetooth.com>).
- [3] A. Soltanian and R. E. Van Dyck, "Physical Layer Performance for Coexistence of Bluetooth and IEEE 802.11b", *2001 Virginia Tech Symposium on Wireless Personal Communications, Blacksburg, VA*, June 2001.
- [4] IEEE Std 802.11a-1999, Part 11: Wireless LAN Medium Access Control (MAC) and Physical Layer (PHY) specifications: High Speed Physical Layer in the 5GHz Band.
- [5] G. J. Foschini, "Layered Space-Time Architecture for Wireless Communication in a Fading Environment When Using Multi-Element Antennas", *Bell Labs Technical Journal (BLTJ)*, pp. 41-59, Nov. 1996.
- [6] T.C. Tozer, D. Grace, "High Altitude Platforms - The future for Broadband Communications", *Communicate 2000 Online Conf. (Invited Paper)*, Oct. 2000.
- [7] W.C. Jakes, "Microwave Mobile Communication", *John Wiley Inc.*, 1st Edition, ISBN 0-471-43720-4, 1974.
- [8] F. Tila, P.R. Shepherd and S.R. Pennock, "Analysis of Indoor-Indoor and Satellite/Hap-Indoor Propagation Effects", *11th International Antennas and Propagation Professional Network ICAP*, pp. 203-207, Manchester, April 2001.
- [9] B. Sklar, "Rayleigh Fading Channels in Mobile Digital Communication Systems Part I: Characterization", *Communications Engineering Services, IEE Communication Magazine*, July 1997.
- [10] J. Skorupa, G. Prodan, "Battle of the Backbones: ATM vs. Gigabit Ethernet", <http://www.data.com/tutorials/backbones.html>, *Data Communications*, April 1997.
- [11] R.A. Valenzuela, "A Ray Tracing Approach to Predicting Indoor Wireless Transmission", *IEEE Vehicular Technology Conference, Secaucus NJ*, pp. 214-218, May 1993.

Chapter 2: Propagation and Capacity Theory

2.1 Introduction

The propagation environment plays an important role in the performance of any radio communication system. Due to the spreading of the radio signal, path loss occurs in the radio channel and the mean received signal is far weaker than the transmitted signal. This path loss is dependent on the communication range and the carrier wavelength. To improve the received signal level, high gain antennas can be used at the transmitter and/or receiver. Obstacles between the transmitter and receiver, such as walls, floors and furniture, can result in additional losses, often referred to as slow fading, or shadowing. In addition, reflection, transmission and diffraction in the local environment result in the received signal arriving via a number of multiple paths, known as multipaths [1]. These multipaths result in additional effects such as fast fading and time delay spread. Fast fading creates large and rapid fluctuations in the received signal envelope and phase. Time delay spread can result in frequency selective fading, which adds additional distortion when the transmission bandwidth is greater than a critical value, known as the coherence bandwidth. Many channels have a dominant multipath signal or a direct Line-of-Sight (LoS) component. For these types of channel, a parameter known as the K-factor can be defined to quantify numerically the deterministic nature of the channel. In this chapter, the above effects will be discussed in some detail and accurate mathematical expressions introduced where appropriate.

Numerous researchers have applied theoretical methods for simulating and predicting multipath propagation in an indoor or urban environment. In an indoor channel, the received signal is composed of energy that has been reflected, transmitted, or scattered by the local environment. While physical features such as walls, floors and ceilings are key factors in the characterisation of the radio channel; additional scatterers exist in the form of building clutter and furniture. These additional scatterers mostly produce secondary effects and are often neglected in the modelling process [2-3]. Hence, the data required for a deterministic propagation model would normally consist of the geometric and electrical characteristics of the main building structure.

The chapter ends with a study of the theoretical capacity for single antenna and multiple antenna systems. The analysis is based on the well known Shannon [4] and Foschini [5] capacity bounds. For a single transmit and receive antenna configuration, the capacity is a simple function of the signal to noise ratio. However, in the case of multiple antenna systems, the capacity is shown to be a function of the signal to noise ratio, the degree of scattering in the communication channel and the number of antenna elements at both ends of the link. Multiple Input Multiple Output (MIMO) systems represents a revolution in the field of communications and will be shown to offer otherwise unobtainable levels of theoretical capacity.

This chapter begins by explaining the fundamentals of radiowave propagation. Narrowband parameters such as spreading loss, fast fading, K-factor and shadowing are introduced. Wideband parameters are then introduced in the form of RMS delay spread and coherence bandwidth. The chapter ends by describing the use of multiple antenna element systems to enhance the capacity in a rich scatter environment.

2.2 Multipath and shadowing

In this section, an overview of the key radio wave propagation effects is given. For indoor systems, in addition to direct and reflected paths, additional components resulting from transmission through walls, floors and ceilings also need to be taken into account. The following three propagation terms need to be carefully considered when designing a mobile radio communications system [6]:

- Free Space Attenuation
- Multipath & Shadowing
- Time Delay Spread

Radiowave can be characterised into the following six categories depending on their frequency range [7]:

- Very Low Frequency (3 - 30 kHz)
- Low Frequency (30-300 kHz)
- Medium wave or Broadcast frequencies (300 kHz to 3 MHz)
- Short Waves or High Frequency (3 MHz to 30 MHz)

- Very High Frequency (30MHz to 300MHz)
- Ultra High Frequency and Microwave (above 300 MHz)

2.2.1 Received Power Density and Electric Field Strength

To simplify the calculation of power density the use of an isotropic source is assumed. This type of source radiates power uniformly in all azimuth and elevation directions. Although this type of source is not practical, it provides a useful mathematical reference when comparing the performance of real antenna systems.

In free space, an isotropic source transmits power in perfect spheres. Assuming 100% efficient radiation, the transmit power P_t must be evenly distributed over the surface area of this imaginary sphere. The radius of the sphere is given by the separation distance r between the transmitter and receiver. Given that the surface area of a sphere is $4\pi r^2$, the resulting power per unit area is given by [6-7]:

$$P_D = \frac{P_t}{4\pi r^2} \quad (\text{watts/m}^2) \quad (2.1)$$

Equation 2.1 implies that the received power density is inversely proportional to the square of the distance r from the receiver. A graphical depiction of the transmission of a plane wave in three dimensional spaces is given in figure 2.1.

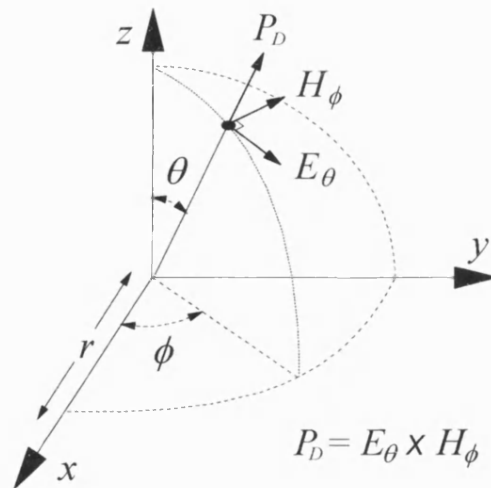


Figure 2.1: 3-D Representation of Plane Wave

Assuming a simple plane wave, the Poynting or power vector is defined such that $P_D = E_\theta \times H_\phi$, where E and H represent the RMS electric and magnetic field strengths respectively. An alternative expression for the magnitude of the power density as a function of the electric field strength in volts per metre can now be written:

$$|P_D| = |E_\theta \times H_\phi| = \frac{|E_\theta|^2}{z_0} \quad (\text{watts/m}^2) \quad \text{since} \quad \frac{E_\theta}{H_\phi} = z_0 \quad (\text{ohms}) \quad (2.2)$$

Combining equations 2.1 and 2.2 and noting that $z_0 = 120\pi$, z_0 represents impedance of free space, the following relationship between the magnitude of the electric field strength and the transmit power can be written:

$$\left| \frac{P_t}{4\pi r^2} \right| = \frac{|E_\theta|^2}{z_0} = \frac{|E_\theta|^2}{120\pi} \quad \text{hence} \quad |E_\theta| = \frac{\sqrt{30P_t}}{r} \quad (\text{volts/m}) \quad (2.3)$$

From equation 2.3 it can be seen that a doubling of the separation distance r halves the magnitude of the electric field and produces a four-fold reduction in the received power density. In dB terms, the doubling of distance represents a 6dB reduction in power density [8].

2.2.2 Received Power and Electric Field

In section 2.2.1 the power density and electric field strength were derived for an isotropic source in free space. In this section the power and electric field will be calculated for a 100% efficient isotropic receiver. This conversion can be performed since an isotropic antenna has an effective area A_e given by [9-10]:

$$A_e = \frac{\lambda^2}{4\pi} \quad (\text{m}^2) \quad (2.4)$$

To calculate the received power in watts we simply multiply the received power density by the effective area of the isotropic receiver.

$$P_r = P_D A_e = \frac{P_t}{4\pi r^2} \frac{\lambda^2}{4\pi} = P_t \left[\frac{\lambda}{4\pi r} \right]^2 \quad (\text{watts}) \quad (2.5)$$

The magnitude of the electric field in volts can now be calculated as shown in equation 2.6.

$$|E_r| = \sqrt{|P_r|z_0} = \sqrt{P_t z_0} \left[\frac{\lambda}{4\pi r} \right] \quad (2.6)$$

2.2.3 Practical Antenna Gain, Effective Area and Beamwidth

In sections 2.2.1 and 2.2.2 the mathematical analysis assumed the use of isotropic antennas. However, all practical antennas exhibit some degree of directivity. In many cases this directivity is a key element of the antenna design. In order to reuse the previous isotropic mathematics, the gain of practical antenna is defined with respect to an ideal isotropic radiator, fed with the same power. Assuming a transmit power of P_t watts, the gain of a transmitting antenna is defined as the ratio of the power density observed from a given direction to the theoretical value for an ideal isotropic antenna. This ratio is expressed logarithmically by equation 2.7.

$$G(\theta, \varphi) = 10 \log \left[\frac{(\text{power density observed at distance } r \text{ from tx})}{P_t / 4\pi r^2} \right] \quad (2.7)$$

By measuring the power density in an anechoic chamber for all azimuth and elevation angles a three dimensional antenna pattern can be generated. In many cases, the two dimensional azimuth or elevation pattern is sufficient. It is important to note that antenna gain should be defined relative to an ideal isotropic source. It is normally quoted in units of dBi (dB relative to an isotropic source); however this can be converted to linear gain if required.

The linear (rather than logarithmic) radiation pattern for one of the simplest antenna structures, a vertical dipole, is shown in figure 2.2. In the vertical directions (directly upwards and downwards) the antenna emits zero radiation. In the horizontal plane (known as the azimuth plane), the dipole emits radiation equally in all directions.

The beamwidth of an antenna is a measure of its directivity and is normally defined as the angle between the half power radiation points (relative to the maximum radiated field E_{max}) in the polar diagram [11-13]. For the dipole pattern shown below, the vertical beamwidth is 90 degrees. The figure was generated for an ideal Hertzian dipole of length δl and current I .

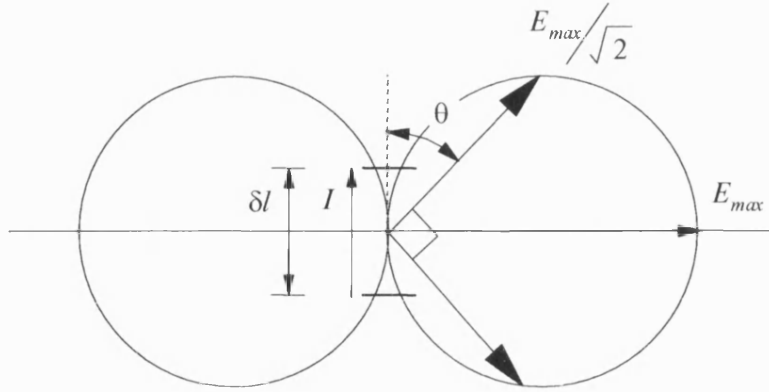


Figure 2.2: Vertical Antenna Pattern for a Dipole

The gain of an antenna is also related to its effective area, with larger effective areas resulting in higher gains [14]. This relationship is defined by equation 2.8.

$$\frac{G_r}{G_i} = \frac{A_r}{A_e} \quad \text{Since } G_i = 1, \quad G_r = A_r \cdot \frac{4\pi}{\lambda^2} \quad (2.8)$$

2.2.4 Received Power and Field Strength using Practical Antennas

Section 2.2.3 defined the antenna gain and effective area for a practical antenna. Assuming G_t and A_r represents the antenna gain and effective area of the transmitter and receiver respectively (relative to an isotropic antenna) then equation 2.1 can be modified to compute the received power density for a practical transmitter.

$$P_D = \frac{P_T G_T}{4\pi r^2} \quad (\text{watts/m}^2) \quad (2.9)$$

The received power can now be computed by multiplying the power density from equation 2.9 by the effective area of the receiving antenna (as defined in equation 2.8). Equation 2.10 is now a function of the two antenna gains and the carrier wavelength λ .

$$P_r = \frac{P_t G_t}{4\pi r^2} [A_r] = \frac{P_t G_t}{4\pi r^2} \left[\frac{G_r \lambda^2}{4\pi} \right] = P_t G_t G_r \left[\frac{\lambda}{4\pi r} \right]^2 \quad (\text{watts}) \quad (2.10)$$

Extending the method given in equation 2.10, the received electric field strength for practical antenna gains is given by:

$$|E_r| = \sqrt{P_D z_0} = \sqrt{\frac{P_t G_t z_0}{4\pi}} \left(\frac{1}{r}\right) \quad (\text{volts/m}) \quad (2.11a)$$

Equation 2.11a can now be further extended to compute the magnitude of the received voltage V_r using knowledge of the radiation resistance R_{rad} (for a 100% efficient antenna).

$$|V_r| = \sqrt{P_t G_t G_r R_{rad}} \left[\frac{\lambda}{4\pi r}\right] \quad (\text{volts}) \quad (2.11b)$$

2.2.5 Propagation Path Loss and Normalised Received Power

Propagation path loss to a given point is defined as the ratio of the transmit power to the received power P_t/P_r . The transmission loss is evaluated in dB using equation 2.12.

$$\frac{P_t}{P_r} = 20 \log\left(\frac{4\pi}{\lambda}\right) + 20 \log r - 10 \log G_t - 10 \log G_r \quad (\text{dB}) \quad (2.12)$$

The path loss can be seen to increase with smaller wavelengths (higher frequencies), larger separation distances and lower antenna gains. The usefulness of the equation 2.12 is limited to those locations having Line-of-Sight (LoS) propagation from the transmitter to receiver, with no significant additional multipath components.

For many applications the concept of normalised power or normalised field strength is a useful concept. The normalisation process is achieved by defining unity received power at a distance of one metre. The received power at a distance of one metre is given by:

$$P_1 = P_t G_t G_r \left[\frac{\lambda}{4\pi}\right]^2 \quad (2.13)$$

The received power can now be expressed as a function of P_1 and the normalised received power P_N as shown in equation 2.14.

$$P_R = P_1 P_N \quad \text{where} \quad P_1 = P_t G_t G_r \left[\frac{\lambda}{4\pi}\right]^2 \quad \text{and} \quad P_N = \frac{P_t G_t G_r}{P_1} \left[\frac{\lambda}{4\pi r}\right]^2 = \left[\frac{1}{r}\right]^2 \quad (2.14)$$

The normalised field strength E_N can be computed from the normalised power density P_{DN} using equation 2.15 where $P_D = P_{D1}P_{DN}$ and P_{D1} represents the power density at 1 metre.

$$|E_N| = \sqrt{P_{DN}z_0} \quad (\text{volts/m}) \quad (2.15)$$

Equation 2.10 demonstrates that the received power is a function of range r , transmit power P_t and carrier wavelength λ . The term free space path loss can be defined to represent the loss in the radio channel resulting from distance and wavelength (for unity gain antennas).

$$L_f = \frac{(4\pi r)^2}{\lambda^2} \quad (2.16)$$

Figure 2.3 shows this path loss as a function of distance in metres for a range of typical carrier frequencies. At 1 metre, a loss of 53 dB is seen at 11.0 GHz and 57 dB at 17.0 GHz. At 10 metres, this path loss has increased to 72 dB and 76 dB respectively. At 100 metres, the path loss at these frequencies is well in excess of 90 dB.

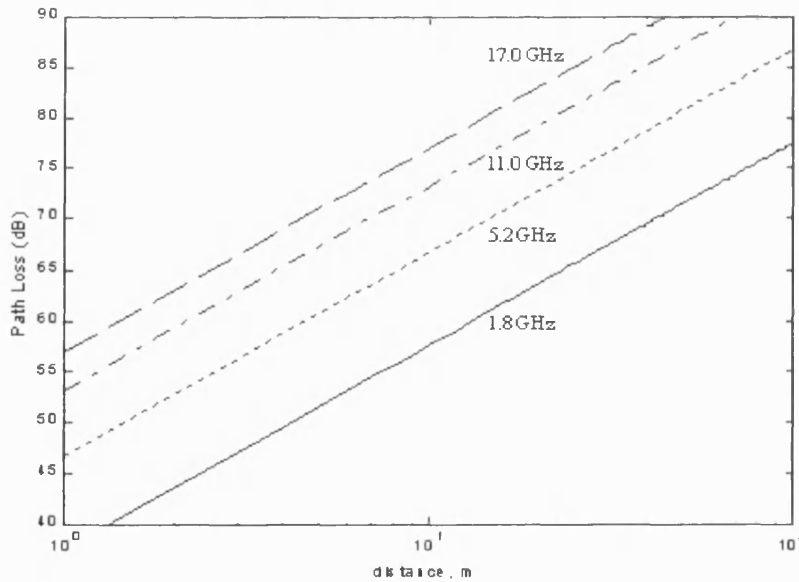


Figure 2.3: Path Loss as a function of centre frequency

Normalised path loss is similar to traditional path loss. The main difference is that the normalised value assumes the loss is 0dB (unity) at a distance of 1 metre. This normalisation can be performed by subtracting the path loss at 1 metre (in dB) from the standard equation (also in dB). The resulting value becomes insensitive to antenna gain and carrier frequency and is often used within ray models to produce a more general result. Figure 2.4 shows the normalised path loss for distances up to 100 metres.

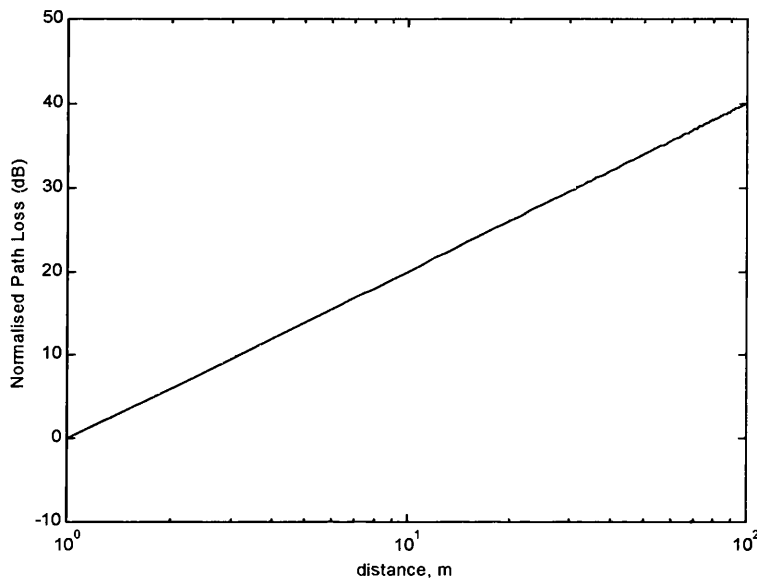


Figure 2.4: Normalized Path Loss versus distance

2.2.6 Signal to Noise Ratio

All radio receivers suffer from front-end noise introduced received by the antenna and introduced by the low noise amplifier. The ratio of the signal power to the noise power is a classical measure of performance. Many methods, including diversity combining studied in chapter 4, are used to improve the signal to noise ratio. The noise power depends on the receive antenna's equivalent noise temperature T_R (assumed to be 290 Kelvin) and the system's noise bandwidth B_n Hz [2][4]. The noise power referred to the terminals of the receive antenna is given by equation 2.17 where k represents Boltzmann's constant and η_f represents the receiver noise figure.

$$N = kT_R B_n \eta_f \quad (\text{watts}) \quad (2.17)$$

Given that the signal power is defined using equation 2.10, the received signal to noise ratio P_r/N is given by [4][7]:

$$\frac{P_r}{N} = \frac{P_t G_t G_r}{k T_r B_n \eta_f} \left(\frac{\lambda}{4\pi r} \right)^2 = \frac{P_t G_t A_r}{4\pi r^2 k T_r B_n \eta_f} \quad \text{since} \quad G_r = \frac{4\pi}{\lambda^2} A_r \quad (2.18)$$

2.3 Multipath Propagation

In reality, LoS communications is of little interest since the received signal at a mobile terminal is almost always composed from numerous attenuated, reflected, transmitted and diffracted versions of the original signal - see figure 2.5. This results in a phenomenon known as *multipath fast fading*.

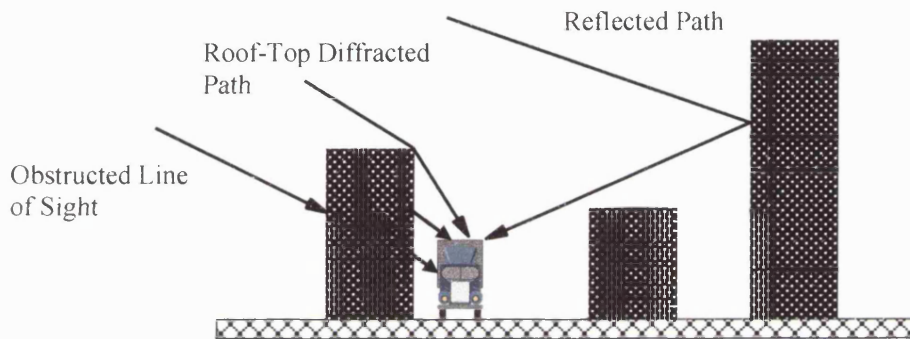


Figure 2.5: Typical Multipath Components in an outdoor Environment

Section 2.2 described signal attenuation with distance and wavelength for a LoS scenario. Once LoS is lost, a phenomenon known as shadowing (or slow fading) becomes important [6][15].

Shadowing is the term given to the slow additional variations¹ in the received signal power as the mobile terminal moves through the local environment. Usually this can be attributed to attenuation caused by walls, floors, ceilings and furniture. This extra attenuation ($\alpha(r)$ in equation 2.19), can be mathematically modelled by increasing the free space distance dependent exponent. As a result, the average signal strength is often assumed to follow an inverse n -th law with respect to distance (where for dense urban areas $n=4$), rather than the inverse square law ($n=2$) that is normally assumed for free space propagation – see equation 2.19.

¹ Slow fading represents additional losses in the local mean beyond that of free space spreading loss.

$$P_R = \alpha(r)P_T G_T G_R \left[\frac{\lambda}{4\pi r} \right]^2 = P_T G_T G_R \left[\frac{\lambda}{4\pi} \right]^2 \left[\frac{1}{r} \right]^n \quad (2.19)$$

Although shadowing can severely attenuate the received signal level, its rate of change is generally low (<2 times per second). A second form of attenuation is known as fast fading and this can be attributed to the phasor or vector addition of the various multipath signals.

2.3.1 Fast and Slow Fading

In the previous section the ideas of multipath fading were introduced. As shown in figure 2.6, the term fast fading is used to distinguish the rapid vector summation effects from the more long term shadowing variations resulting from object attenuations such as floors, walls and furniture.

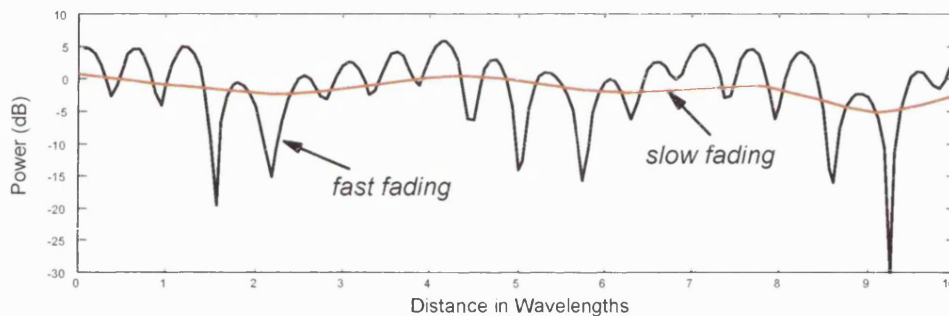


Figure 2.6: Combined fast and slow Fading

Figure 2.6 also demonstrates that fast and slow fading are multiplicative effects, i.e. their effect can be multiplied on top of the mean field strength predicted using equations such as 2.19.

2.3.2 Line of Sight (Rician) and Non-Line-of-Sight (Rayleigh) Fading

Fast fading can be characterised using two envelope distributions, known as Rayleigh and Rician [9-10]. Rayleigh is used to represent the worst case scenario where no dominant component exists in the vector multipath summation. Thus, extremely deep signal fades and phase fluctuations can occur in a Rayleigh scenario. Figure 2.7(i) shows the simulated fast fading envelope relative to the local mean for a Rayleigh scenario. The result was generated using a simple Matlab model to perform the vector

summation of eight equal amplitude rays over a ten wavelength route. Signal fades in excess of 30 dB relative to the mean are possible in the Rayleigh case.

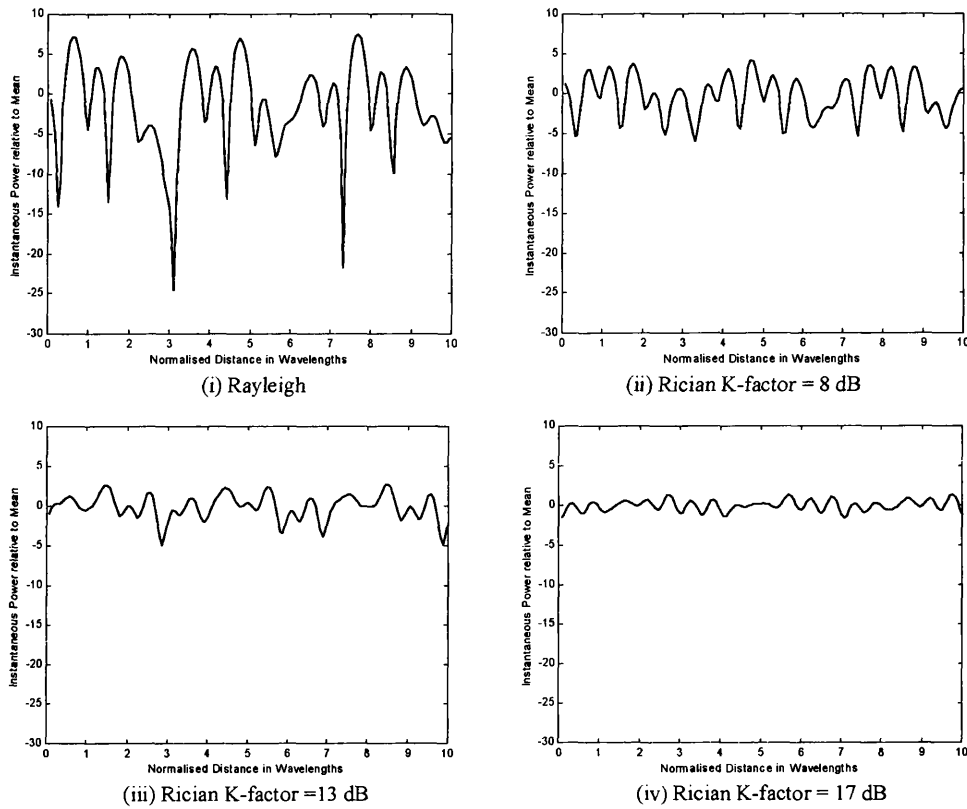


Figure 2.7: Typical Rayleigh & Rician Fading

When one of the ray amplitudes is increased to simulate a Rician channel, the severity of the fading reduces. As discussed in section 2.3.4, the ratio of the dominant power to the scattered power can be used to calculate the K-factor, which is a parameter that determines fading severity. In figure 2.7(ii), a K-factor of 8 dB is assumed. Fading envelopes for Rician K-factors of 13 dB and 17 dB are plotted in figures 2.7(iii) and (iv). The results show that the severity of fading reduces with increasing K-factor, and in the limit a simple non-fading AWGN channel is achieved [4][10][14].

2.3.3 Constructive and Destructive Interference

If a sinusoidal signal is received through two independent paths then the arrival phase for each of these rays will be different. Generally, the arrival phase of a ray is

determined by its electrical path length and the carrier frequency using the following equation, where θ_0 represents the initial phase of the ray.

$$\theta = \theta_0 - 2\pi r/\lambda \quad (2.20)$$

As the user moves relative to the transmitter, the electrical path length r varies and hence the phase of the ray will alter. If the two rays arrive in phase (left-hand side of figure 2.8) then constructive interference will occur resulting in a signal peak. However, if the phase of the two rays is in anti-phase (right hand side of figure 2.8) then destructive interference will occur and the two signals will cancel (fade). In practice there are usually many rays arriving at the receiver and the probability of total cancellation is very small [6][8].

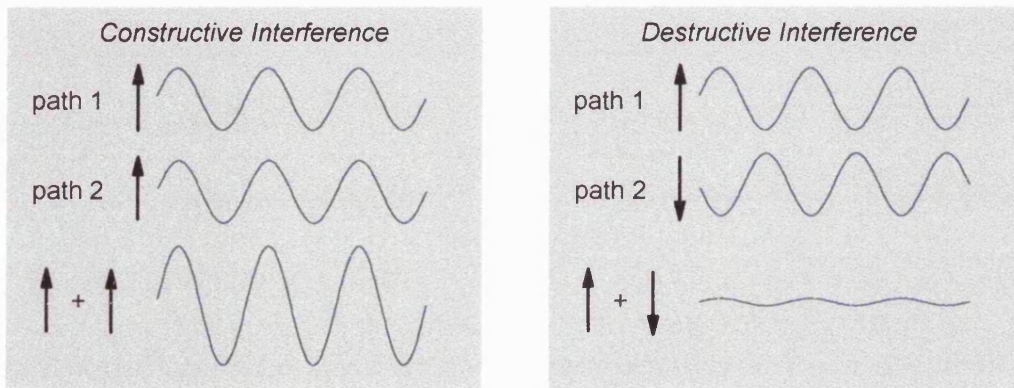


Figure 2.8: Constructive and Destructive Interference

From figure 2.8 it is clear that fast fading occurs due to the vector summation of the multipaths. Equation 2.21 shows that the resultant vector, V_{ff} , can be computed from the vector sum of N multipaths with unique amplitudes A_k and phases ϕ_k . In addition to fast fading, slow fading will also occur due to the additional attenuation resulting from blocking objects.

$$V_{ff} = \sum_{k=1}^N A_k \exp(j\phi_k) \quad (2.21)$$

Multipath propagation creates some of the most difficult problems associated with the radio environment. The three most important multipath issues for the digital radio designer are:

- Rapid amplitude fading and phase distortion
- Doppler shifts and random FM
- Delay Spread and Intersymbol interference

The rapid fast fading envelope variations are experienced as the mobile moves over very short distances (normally fractions of a wavelength) [2][8].

2.3.4 K-factor

As introduced in section 2.3.3, fast fading occurs as a result of the vector summation of multipaths. The K-factor is a parameter that describes the severity of the resulting fast fading. In channels with no dominant component, fading is severe and the K-factor will be low (and often negative when quoted in dB). For channels with a strong line-of-sight, fading will be less severe, as demonstrated in figure 2.7. Mathematically, the K-factor can be calculated using equation 2.22, where A represents the peak signal voltage in the line-of-sight path and $A^2/2$ and σ^2 represent the RMS power in the line-of-sight and random components respectively [7][16].

$$K = 10 \log \left(\frac{A^2}{2\sigma^2} \right) \quad (\text{dB}) \quad (2.22)$$

2.4 Wideband Channels

Section 2.3 provides a description of the narrowband properties of the radio channel. In this section, the wideband properties and parameters of a radio channel are introduced. These include, time delay spread, power delay profile, RMS delay spread and coherence bandwidth [9][17].

The multipath signals arriving at a mobile receiver each take a unique route and therefore suffer a unique time delay. This time delay will be different for each of the multipaths, particularly if the spread in path lengths is large (i.e. the ratio of the shortest path to the longest path). The Power Delay Profile (PDP) is obtained by plotting the square of the absolute field strength for each ray (to obtain power) against its time delay (which is often normalised relative to the first received ray). An example PDP or an indoor channel is shown in figure 2.9.

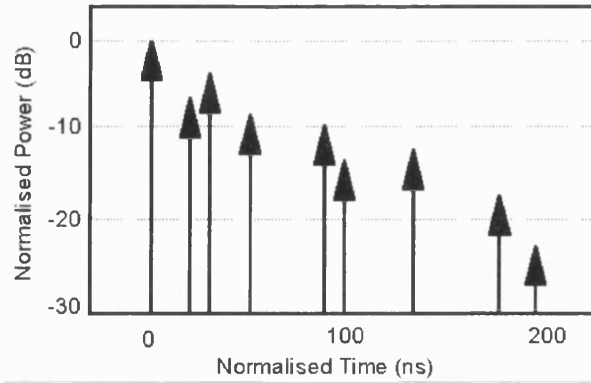


Figure 2.9: Typical Power Delay Profile [6]

Figure 2.9 shows graphically the degree of delay spread in the radio channel (i.e. the time difference between the first and last multipath). For channels with negligible delay spread, (i.e. appearing as a single impulse in the time domain), the resulting frequency domain response is flat (and this is known as frequency flat fading). The impact of time delay spread can be viewed in the frequency domain by performing a Fourier transform of the complex channel impulse response (Note: the Fourier transform of the power delay profile generates the frequency correlation function).

2.4.1 RMS Delay Spread

Usually the first rays to arrive at the radio receiver have the largest amplitude and the magnitudes of subsequent rays tend to fall away as the time delay increases (due to extra path loss and further reflections and diffractions). It is possible to quantify the degree of dispersion in a channel by evaluating its Root Mean Square (RMS) delay spread. This value can be calculated using equation 2.23, where α_k represents the amplitude of the received field strength for the k -th ray after a time delay of τ_k seconds. τ_a represents the time for half the power in the impulse response to arrive.

$$\tau_a = \frac{\sum_{k=1}^N \tau_k \alpha_k^2}{\sum_{k=1}^N \alpha_k^2}, \quad \tau_{rms} = \left[\frac{\sum_{k=1}^N [\tau_k - \tau_a]^2 \alpha_k^2}{\sum_{k=1}^N \alpha_k^2} \right]^{1/2} \quad (2.23)$$

The RMS delay spread value summarises the power and time spreading information from a power delay profile and expresses it as a single value whose magnitude allows

direct comparisons between differing areas and environments. The value of the RMS delay spread is important in a frequency diversity system since its value directly relates to the frequency separation required to achieve significant fast fading decorrelation. Diversity gain is only achieved when the diversity paths suffer uncorrelated fading, hence for small frequency separations little or no diversity gain would be seen [18-20].

2.4.2 Coherence Bandwidth

The coherence bandwidth represents the frequency spread over which the amplitude and phase distortion in the channel remains similar (correlated). Correlation coefficients of 0.9 and 0.5 are commonly used for this definition [21]. For a system to be considered narrowband, the frequency spectrum needs to be flat across the intended transmission band. In practice, the coherence bandwidth represents the maximum bandwidth that can be used for a narrowband transmission. The coherence bandwidth B_c for a 0.5 correlation can be estimated from the RMS delay spread using equation 2.24 [6].

$$B_c \approx \frac{1}{6\tau_{rms}} \quad (2.24)$$

The coherence bandwidth can be calculated from the normalised Fourier transform of the power delay profile [22-23]. Figure 2.10 shows the Fourier transform of the complex impulse response illustrated in figure 2.9. From this plot the frequency selective nature of the channel can clearly be observed with deep notches being seen with widths of approximately 5 to 7 MHz.

The coherence bandwidth is inversely proportional to the RMS delay spread, hence for small RMS delay spreads, the coherence bandwidth is large (and vice-versa).

Equation 2.24 can be used in conjunction with typical RMS delay spreads to estimate approximate values for the coherence bandwidth. For short-range indoor systems (operating ranges of 5m, 10m and 20m), typical RMS delay spreads would be in the order of 5ns, 10ns and 20ns respectively (chapter 3). Inserting these values into equation 2.24 reveals coherence bandwidth estimates of 33.3 MHz, 16.7 MHz and 8.3 MHz, the larger value corresponding to the low RMS delay spread.

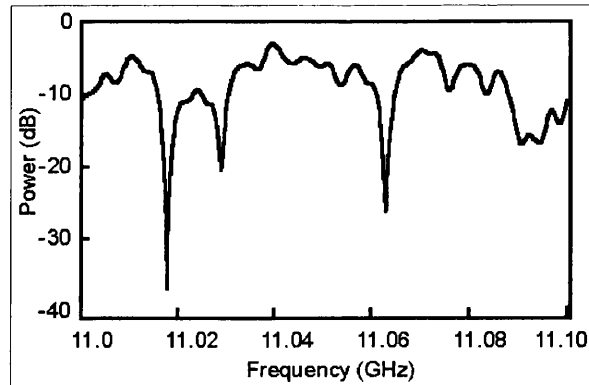


Figure 2.10: Frequency Response [6]

In summary, wideband transmission is the term used to describe systems that operate far in excess of the channel's coherence bandwidth B_c . All other systems are narrowband and suffer correlated fading in the frequency domain.

2.5 Indoor/Outdoor HAP

High Altitude Platforms (HAPs) are an emerging concept for next generation fixed and mobile communications [24-25]. To predict indoor field strength levels from such distant transmitters, modifications to the standard indoor ray-tracing concept are proposed. These modifications will be described in chapter 3 and require an array of virtual transmitters to be placed around the building under test.

Provision of telecommunication services by means of high-altitude platforms (HAPs) is becoming a relevant topic of interest for the research activities on future-generation systems. Mobility on demand and large coverage are only some examples of the expected benefits for personal communication systems based on the use of such platforms. They can act as augmentation infrastructure for global navigation satellite systems such as GPS and the future Galileo, easily performing direction of arrival estimation thanks to their high position, collecting and broadcasting position information [26]. Despite these interesting services, the real added value is in the fact that their payload can easily integrate both communication and navigation services, with mutual benefits for both systems.

The demand for high-capacity wireless services is bringing increasing challenges, especially for delivery of the "last mile". Terrestrially, the need for line-of-sight propagation paths represents a constraint unless very large numbers of base-station

masts are deployed, while satellite systems have capacity limitations. An emerging solution is offered by high-altitude platforms (HAPs) operating in the stratosphere at altitudes of up to 22 km to provide communication facilities that can exploit the best features of both terrestrial and satellite schemes [27-28]. Particular consideration is given to the use of HAPs for delivery of future broadband wireless communications.

2.6 Shannon Capacity equation

The standard formula for the Shannon capacity [4][29] expressed in bps/Hz is:

$$C = B \log_2(1 + \rho |H|^2) \quad (2.25)$$

where H represents the channel gain at a single frequency normalised over fading to an expected value of one. The normalised channel power transfer characteristic is $|H|^2$. In this single antenna case, H is simply a complex multiplier (for multiple antenna systems H become a complex matrix). This formula applies to a Single-Input Single-Output (SISO) system where B represents the system bandwidth, ρ the SNR and H the normalised complex channel transfer function.

It is evident that for high SNRs a 3dB increase in ρ offers an increase of one bit/Hz in capacity. The Shannon theorem states that if the required information transfer is less than the Shannon capacity limit C , then error free communication is possible. If information transfers at a rate greater than C is attempted, then errors in transmission will always occur no matter how well the equipment is designed [30]. For a SISO system, the Shannon equation can be written as:

$$\frac{C}{B} = \log_2 \left(1 + \frac{S}{N} \right) \quad (2.26)$$

The ratio C/B represents the bandwidth efficiency of the system in bits/s/Hz. The larger the ratio C/B , the greater the bandwidth efficiency is. The ratio S/N is a measure of the power efficiency of the system (i.e. it is desirable to achieve a given capacity at the lowest possible S/N in order to minimise transmit power). The Shannon theorem clearly shows that bandwidth efficiency can be traded for power efficiency, and vice versa [31].

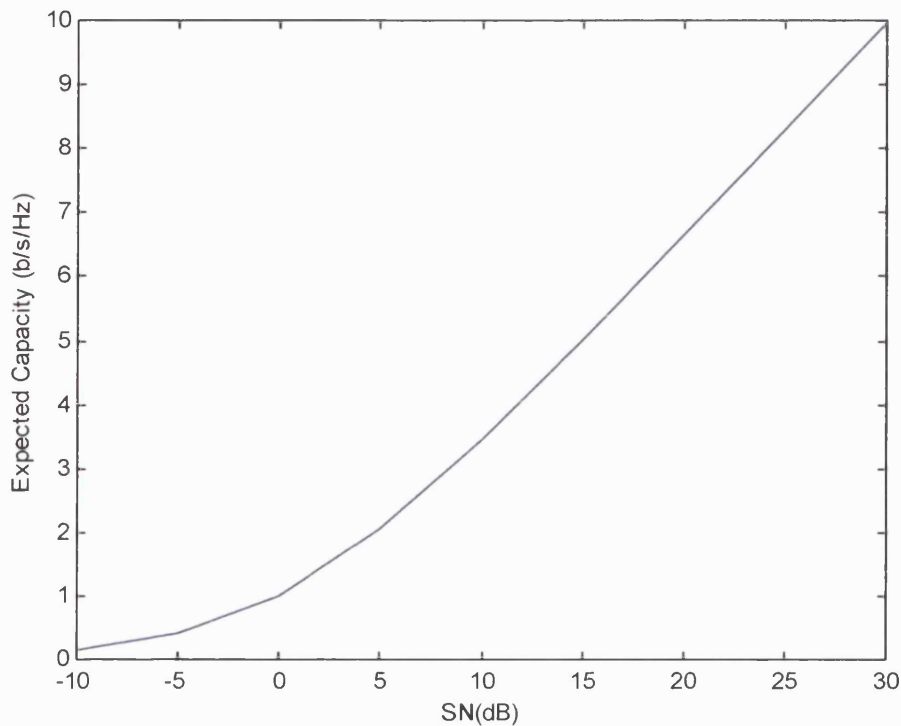


Figure 2.11: Normalized capacity as function of S/N

As can be seen from equation 2.26, the SISO link capacity can be increased by either expanding the system bandwidth or increasing the transmit power (or both). Increasing the transmit power may seem to be the easiest way to improve capacity. However, the capacity scales only logarithmically with SNR. Hence, for high SNR an increase of 3 dB in SNR can be seen from figure 2.11 to yield just a further increase in capacity of 1 bit/second/Hz. There are other practical obstacles for increasing the transmit power levels. Most cellular wireless systems are actually limited by self-interference. Scaling up the power of one user would automatically raise the level of interference for other users, which in turn would cause other users to increase transmit power to maintain the same link quality [30-32]. Clearly, in self-interference limited networks increasing the power above a certain limit does not pay-off. At the same time, increasing the power shortens the battery life. Last, but not least, electromagnetic hazard issues associated with wireless devices have recently sparked public unease. Regardless of how factual those fears are, increasing the transmit power will be welcomed neither by standardisation bodies nor consumers. In equation 2.26 a second possibility could be expanding the operational bandwidth B . Although the capacity scales linearly with bandwidth, there are also practical impediments. The

cost of the radio spectrum has become recently one of the most important factors. Also, increasing the bandwidth would expose a system to increased Inter-Symbol-Interference (ISI). Although in some cases the wideband channel characteristics can be desired and exploited, this has to be addressed in the form of an equaliser [32]. In light of the above comments, a dramatic increase in the capacity can only be achieved by some other means than those already discussed. In what follows, it is shown that Multiple-Input Multiple-Output (MIMO) configurations can provide a significant capacity increase. In this respect, MIMO is a unique approach to generating high capacity radio systems.

2.7 MIMO systems and the Foschini equation

The use of antenna arrays at both the transmitter and receiver gives rise to a multiple-Input Multiple-Output (MIMO) channel. This scenario is shown in figure 2.12.

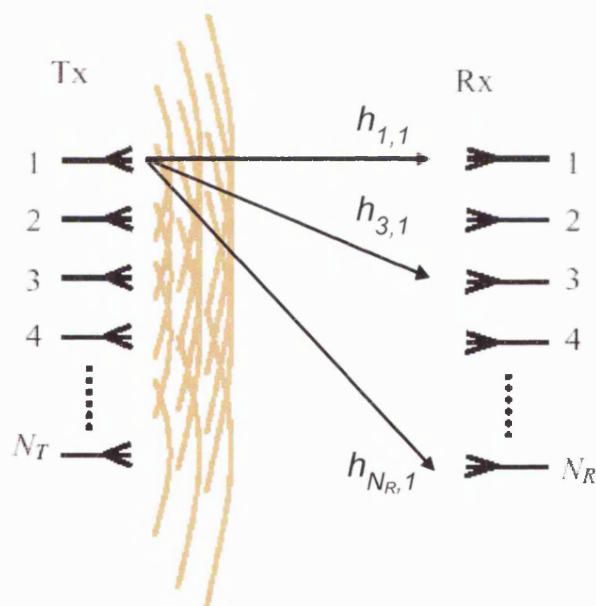


Figure 2.12: Concept of Multiple Input Multiple Output arrays

The performance of the MIMO channel created by N_T transmitter elements and N_R receiver elements can be analysed by calculating its information theoretical capacity. It has been shown in [29] and the references therein that Shannon's capacity theorem

can be extended to the MIMO [5][33] case using equation 2.27, where C now represents the normalised capacity in bits/s/Hz².

$$C = \log_2[\det(I_{n_r} + (\rho/n_T)\mathbf{H}\mathbf{H}')] \quad \text{bits/s/Hz} \quad (2.27)$$

where \mathbf{H} is the N_R by N_T complex channel matrix (with elements h_{ij} representing the channel transfer function between transmit element j and receiver element i), ρ is the average signal to noise ratio at each receiver branch, I is the identity matrix, \det is the determinant function and $(\cdot)'$ represents the complex conjugate transpose function. The channel response matrix, \mathbf{H} , is normalized so as to remove the average path loss and only show the relative variation in the path responses between all $N_R \times N_T$ elements. It can be seen that the value of the determinant in 2.27, and hence the channel capacity, will vary depending on the decorrelation between the elements of \mathbf{H} . In practical terms, this will be dependent on whether the channel experiences Rayleigh or Rician propagation. The more deterministic the propagation is, the higher the correlation between elements of \mathbf{H} , and the lower the channel capacity.

Most analysis of MIMO channels to date has assumed a perfect Rayleigh fading environment. This has been modelled by taking each element of \mathbf{H} to be complex samples of independently identically distributed (i.i.d) Gaussian processes, such that [34-35]:

$$h_{jk} = G(0,1/\sqrt{2}) + G(0,1/\sqrt{2})i \quad (2.28)$$

where i represents the complex operator $\sqrt{-1}$. MIMO architectures enable powerful techniques for improving the capacity of wireless communication systems, especially in rich multiple environments. In particular, it is now well known that in such rich scattering environments the attainable capacity of MIMO links increase approximately linearly with the *minimum* of the number of antennas at the transmitter and receiver (see figure 2.13). In the case where there are more transmitters than receivers (or vice versa), the system enjoys a diversity gain which improves performance at low SNRs. These potentially significant capacity improvements of MIMO systems become even more desirable as the next generation of wireless communication systems emerge. However, many technical challenges remain before

² Several attempts were made to obtain further information on the derivation of this equation from Dr Foschini; however at the time of writing no reply had been received.

the potential capacity gain is realized in practice. These challenges include some of the most intriguing problems in wireless communications and signal processing, such as space time coding and decoding, optimal multiple access techniques for systems equipped with multiple antennas, multi-user detection, and adaptive space-time beamforming.

New challenges also emerge within some classical signal processing problems, such as MIMO channel characterization, estimation and equalization. Meanwhile the associated practical implementation issues of MIMO systems, such as receiver complexity, power dissipation, cost and robust operation are critical in making MIMO transceivers viable.

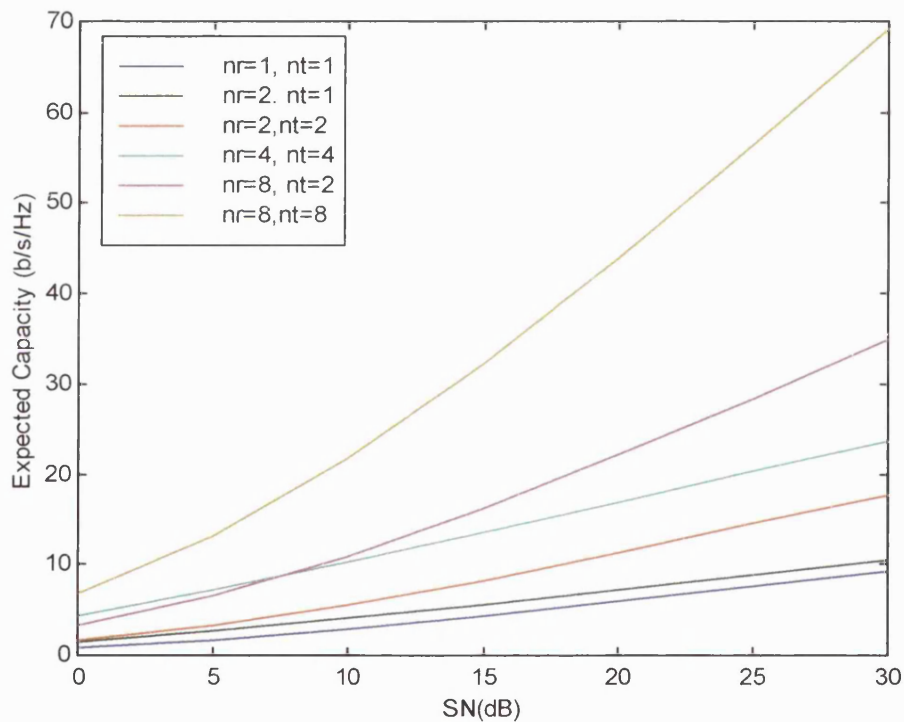


Figure 2.13: MIMO Capacity as function of S/N

As recently reported in the literature, the traditional smart antenna concept can be extended by employing multi-element arrays at both ends of the communication link in order to create a MIMO channel [5][36]. It has been shown analytically that when deployed in a suitably rich scattering environment, this architecture is capable of greatly increasing the spectral efficiency of such a system. It is this feature in particular that has aroused much interest in applying MIMO techniques to future

wireless communication standards in order to help meet the anticipated demand for high bit-rate, real-time services within limited bandwidths [29][37].

Given a suitable signal to noise ratio and knowledge of the \mathbf{H} matrix at the receiver, the performance of this system will therefore be dependent on the properties of the \mathbf{H} matrix.

2.8 Summary

This chapter introduced the basic concepts of radiowave propagation and has also explained the impact of multipath. Key narrowband and wideband parameters were covered and these will now be used to analyse radio systems in the subsequent chapters of this thesis. The work concluded with a discussion of multiple antenna communications systems and their unique ability to offer high capacities in a rich scatter environment. MIMO systems will be analysed in more detail in chapter 7.

2.9 References

- [1] B. Sklar, "Rayleigh Fading Channels in Mobile Digital Communication Systems Part I: Characterization", *Communications Engineering Services, IEE Communication Magazine*, July 1997.
- [2] J.G. Proakis, "Digital Communications", *McGraw-Hill Co., International Editions*, Third Edition, 1995.
- [3] K.G. Budden, "The propagation of radio waves", *Cambridge University Press*, 1st Edition, 1988.
- [4] H. Taub and D.L. Schilling, "Principles of Communication Systems", *McGraw-Hill Book Company, McGraw-Hill International Editions*, 2nd Edition, 1986.
- [5] Gerard J. Foschini, "Layered Space-Time Architecture for Wireless Communication in a Fading Environment when using Multi-Element Antennas", *Bell Labs Technical Journal (BLTJ)*, pp. 41-59, Autumn, 1996.
- [6] A.R. Nix, "Principles of Wideband Propagation", *IEE Eighth Residential Course on Radio Propagation*, Jan. 2000.
- [7] J.D. Parsons and J.G. Gardiner, "Mobile communication systems", *Glasgow & Blackie*, 1989.
- [8] A. Jagoda and M. de Villepin, "Mobile Communications", *John Wiley Ltd*, 1st Edition, April, 1993.
- [9] W.C.Y. Lee, "Mobile Communications Engineering", *McGraw-Hill Ltd*, 1st Edition, 1982.
- [10] W.C.Y. Lee, "Mobile Communication Design Fundamentals", *McGraw-Hill Ltd*, 2nd Edition, June, 1993.
- [11] S.R. Pennock and P.R. Shepherd, "Microwave Engineering", *Macmillan Press Ltd*, 1st Edition, ISBN 0-333-72801-7, 1998.
- [12] P.F. Panter, "Microwave Communication Systems", *McGraw-Hill Ltd*, 1st Edition, ISBN 0-07-048436-8, 1972.

- [13] C.A. Balanis, "Antenna theory analysis and design", *New York: Harper & Row*, 2nd Edition, ISBN 0-06-040458-2, 1982.
- [14] W.C. Jakes, "Microwave Mobile Communication", *John Wiley Inc.*, 1st Edition, ISBN 0-471-43720-4, 1974.
- [15] G.L. Turin et al., "A Statistical Model of Urban Multipath Propagation", *IEEE Trans. Vehicular Technology*, vol. 21, pp. 1-9, 1972.
- [16] A.J. Rustako, Jr., N. Amitay, G.J. Owens, and R.S. Roman, "Radio Propagation at microwave frequencies for line-of-sight microcellular mobile and personal communications", *IEEE Trans. Veh. Technol.*, vol. 40, pp. 203-210, Feb. 1991.
- [17] W.G. Duff, "Mobile Communications", *Don White consultants, Inc.*, First Edition, 1976.
- [18] F. Tila, SR. Pennock and PR. Shepherd, "Evaluation of Indoor Propagation Effects and Diversity Techniques", *Proc. IEE PREP*, pp. 23-25, 2001.
- [19] Ch. Ghobadi, S.R. Pennock and P.R. Shepherd, "Evaluation of Diversity Techniques in Complex Indoor Environments", *28th European Microwave Conference Amsterdam*, pp. 345-350, 1998.
- [20] R.C. Bernhardt, "Macroscopic Diversity in Frequency Reuse Systems", *IEEE J. Selected Areas in Comms.*, vol. 5, pp.862-878, 1987.
- [21] B. H. Fleury and P. E. Leuthold, "Radiowave Propagation in mobile communication: An Overview of European research", *IEEE Communication Magazine*, pp. 70-81, 1996.
- [22] W. C. Y. Lee, "Estimate of Local Average Power of a Mobile Radio Signal", *IEEE Transactions on Vehicular Technology*, Vol. 34, No. 1, pp. 22-27, 1985.
- [23] J.F. Ossanna, "A Model for Mobile Radio Fading due to Building Reflections: Theoretical and Experimental Fading Waveform Power Spectra", *Bell Syst. Technical Journal*, vol. 43, pp. 2935-2971, 1964.
- [24] F. Tila, PR. Shepherd and SR. Pennock, "2GHz Propagation and Diversity Evaluation for In-Building Communications up to 4MHz Using High Altitude Platforms (HAP)", *Vehicular Technology Conference, VTC 2001 Fall, IEEE VTS 54th*, vol. 1, pp. 121-125, October 2001.

- [25] T.C. Tozer and D. Grace, "High Altitude Platforms – The Future for Broadband Communications", *Communicate 2000 Online Conference (invited Paper)*, October 2000.
- [26] J. Thornton, D. Grace, C. Spillard, T. Konefal and T.C. Tozer, "Broadband Communications from a High Altitude Platform: The European Helinet Programme", *Electronics & Communication Engineering Journal*, pp. 138-144, June 2001.
- [27] W. Pawlowski, "Radio wave propagation effects in high-altitude platform systems", *13th International Conference on Microwaves, Radar and Wireless Communication, MIKON-2000*, vol. 1, pp. 185-188, 2000.
- [28] C. Spillard, D. Grace, J. Thornton, G.P. White, M. Mohorcic, E. Falletti and T.C. Tozer, "Broadband Communications from Helinet High Altitude Platforms", *DASIA, Dublin, Ireland*, May 2002.
- [29] G.J. Foschini and M.J. Gans, "On limits of wireless communications in a fading environment when using multiple antennas", *Wireless Personal Communications*, pp. 311 – 335, 1998.
- [30] C. Berrou, A. Glavieux, and P. Thitimajshima, "Near Shannon Limit Error-Correcting Coding and Decoding: Turbo Codes", *Proc. IEEE International Conference on Communications (ICC), Geneva*, pp. 1064-1070, 1993.
- [31] I.E. Telatar, "Capacity of Multi-Antenna Gaussian Channels, *Technical Report, Bell Labs internal memo*, 1995.
- [32] X. Li, H. Huang, A. Lozano, and G. Foschini, "Reduced Complexity Detection Algorithms for Systems Using Multi-Element Arrays", *IEEE Globecom 2000, San Francisco*, April 2000.
- [33] G.J. Foschini and R.K. Mueller, "The Capacity of Linear Channels with Additive Gaussian Noise", *Bell System Technical Journal*, pp. 81-94, Jan 1970.
- [34] G. Golden, G. Foschini, R. Valenzuela, and W. Wolniansky, "Detection Algorithm and Initial Laboratory Results Using the V-Blast Space-Time Communication Architecture", *IEE Electronics Letters*, pp.14-15, 1999.

- [35] D.P. McNamara, M.A. Beach, P.N. Fletcher and P. Karlsson, “Temporal Variation of Multiple-Input Multiple-Output (MIMO) Channels in Indoor Environment”, *11th International Antennas and propagation Professional Network ICAP*, pp. 578-582, Manchester, April 2001.
- [36] I.E. Telatar, “Capacity of Multi-antenna Gaussian Channels”, *Technical Report, Bell Labs internal memo*, 1995.
- [37] P.W. Wolniansky, G.J. Foschini, G.D. Golden, and R.A. Valenzuela, “V-Blast: An Architecture for Realizing very High Data Rates over the Rich-Scattering Wireless Channel”, *URSI International Symposium on Signals, Systems, and Electronics, ISSSE 98*, pp. 295-300, 1998.

Chapter 3: Ray Tracing Principles and Techniques

3.1 Introduction

The analysis performed in this thesis is based on predictions made using an automated propagation prediction tool. The program is divided into two main modules, 1) Ray Tracing and 2) Field Reconstruction. By launching two dimensional uniformly spaced rays inside an environment and then tracing these rays as they bounce and transmit throughout the environment, the various multipaths linking the transmitter and receiver can be identified.

The Ray Tracing algorithm performs a general analysis of launched ray paths from the transmitter as they reflect and/or transmit at a boundary and onward propagate through the indoor environment. The ray tracing module traces ray tubes from the source transmitter in a predetermined direction, based on azimuth start and stop angles and an angular launch resolution. Object intersections are identified for each ray path (by sensing a material discontinuity) and appropriate reflections and transmissions are calculated. Once the field strength of the ray has fallen below a predefined threshold level (known as the Cut-Off Power) then the process stops and a new source ray is initiated at the next launch angle. The ray tracing process is performed based on knowledge of the local environment and the location of the transmitter. The ray launching process is performed once for a given transmitter location to build an exhaustive ray tree that tracks launched rays as they reflect and transmit from planar surfaces.

The tracing of rays between the transmitter and receiver is accomplished using the second module, Field Reconstruction (see section 3.7), via an exhaustive analysis of the ray tracing image tree. A ray between the transmitter and receiver is said to occur if an image from the ray tracing tree illuminates the receiver. The total electromagnetic field strength at the receiver is then calculated from the vector sum of the individual fields from all launched paths illuminating the receiver point.

The computer program uses the above combination of ray tracing and field reconstruction to identify ray paths by which significant levels of energy radiate from the transmitter location to the receiver point. Multiple receiving locations can be

defined to form a route or coverage grid, with the field reconstruction procedure applied repeatedly at each receiving point.

The software is written in the 'C' programming language and runs on a UNIX platform [1-2]. Numerous ray-object intersection tests and the use of extensive data arrays place a considerable resource requirement on the computing platform. Although objects are used to reduce the number of intersection tests and intermediate data is disposed of as soon as possible, the computation and memory requirements still make a workstation the desired computing platform.

In this chapter the basic elements of the ray tracing process are discussed, including the mathematics behind the transmission and reflection process. Issues such as polarisation modelling and diffraction are also considered. Limitations in the current implementation of the ray model are discussed towards the end of the chapter. This chapter describes the structure of the ray launching software used in this thesis. The various input files required to operate the model are described. The main input file describes the physical and electrical properties of the operating environment and is generated by using the grid environment (see section 3.5.2). The various output files provide a formal record of the prediction results.

The chapter ends by predicting the received power and signal to noise ratio along a route for a 5GHz indoor transmission system. The use of normalised field strength and received power is explained and the methods required to compute received power for any transmit power and antenna gain are explained.

3.2 Literature review in ray tracing

This aim of this section is to review recent literature in the area of indoor and outdoor deterministic propagation modelling [3].

3.2.1 Deterministic Propagation Models

The increased availability of high resolution, electronic geographic databases, increased processing power and computer memory have made deterministic propagation modelling a more attractive research subject in recent years. These models are generally based on ray theory and are applied to indoor and outdoor

environments. Two main types of path searching technique are reported in the form of image theory and ray launching. These two methods will be explained in more detail in the following sections.

3.2.1.1 Image-based Technique

An image-based technique uses the electromagnetic theory of images [3-7]. It considers all objects as potential reflectors and calculates the location of transmitter images. Ray paths are formed based on the location of the receiver, the transmitter and its associated images as illustrated in Figure 3.1.

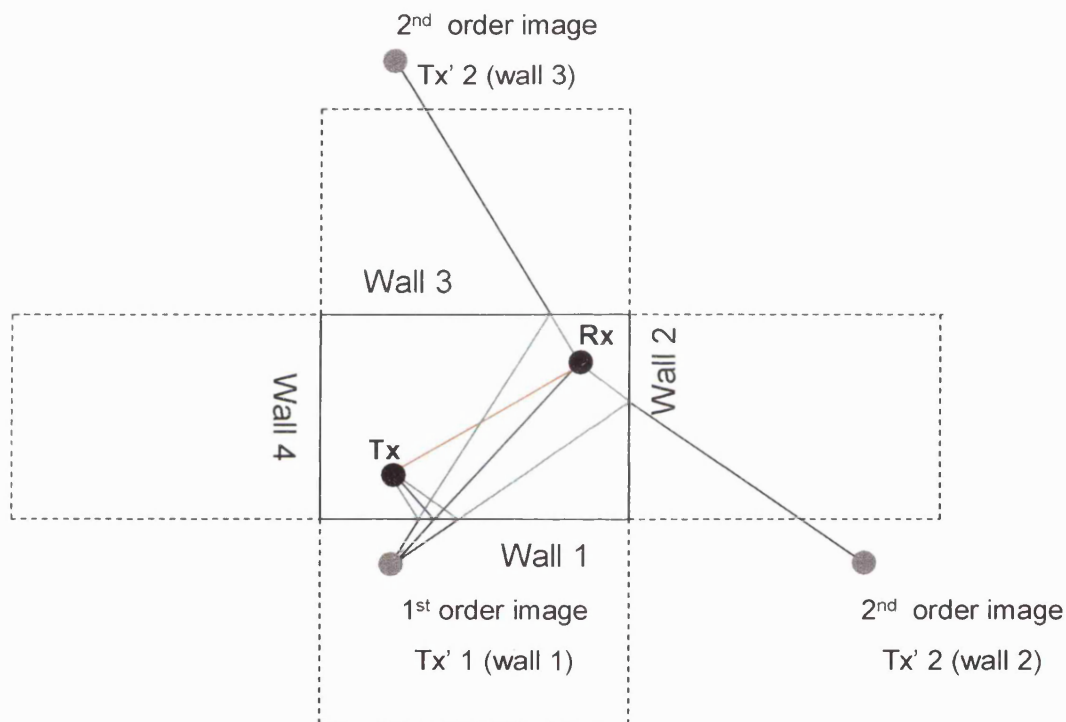


Figure 3.1: Two dimensional image-based ray tracing

Figure 3.1 illustrates how image based ray tracing can be applied to a simple rectangular room. From all the possible valid paths, four are shown for illustration purposes. The red line shows the direct path which is straightforward to calculate. The blue line shows the first-order reflected path due to reflection at the surface of wall 1. To determine this path, the point at which the line joining Rx and Tx' 1 (wall 1) intersects with wall 1 must be calculated [6]. The ray path then follows the line from Tx to the intersection point and from the intersection point to Rx. This idea can be extended to consider multiple reflections. Two intersection points are now required to

determine a second-order reflected path. The path starts at Tx, reaches the first intersection point (due to first order image), then moves on to the second intersection point (due to second order image) and finally terminates at Rx. The second intersection point is determined from the second order image that is formed using the appropriate wall and the first order image. Higher order paths can be determined using the same basic procedure. For image based models, an image tree is generated for all reflections (transmissions and diffractions) up to a maximum specified order. For very large environments, this approach requires very large amounts of storage memory. A key advantage of image based ray tracing is its geometric accuracy. Unlike ray launching (see section 3.2.1.2), image based ray tracing relies on calculating surface interactions via the solution of mathematical equations (i.e. the intersection of lines for 2-D geometry). This algorithm is therefore very unlikely to miss ray interactions even at long distances from the transmitter (for ray launching the accuracy at long distances from the transmitter depends critically on the launch angle step size).

An image tree is usually employed to hold all the images generated for a single location of Tx and a predefined order of reflection. Using such an image tree eliminates the repetitive generation of images for the same Tx location and hence increases the speed of the path-searching algorithm. With the employment of an image tree, the test to see whether an image is capable of providing a path usually starts from the highest order and works backwards towards the transmitter (backward tracing) [6].

3.2.1.2 Ray Launching Technique

The ray-launching technique [8-12] operates by sending out test rays at a number of discrete angles from the transmitter. As they propagate, the rays interact with objects present in the environment. The propagation of a ray is terminated when its power falls below a preset threshold.

The test for ray reception is critical in ray launching. Typically a reception sphere is placed around the receiver and a path from the transmitter is said to exist if a ray intersects with this reception sphere. The use of reception spheres can result in a double counting of certain rays, which is an additional complexity not encountered using the image based approach. The use of uniform launch angles can also be a

problem for directional antennas, where a high launch resolution may be desirable in the main beam of the antenna pattern. In the case of three dimensional ray launching, it may also be desirable to launch rays at a high resolution in the azimuth plane [13].

As mentioned in the above paragraph, the main disadvantage of ray launching is that it suffers from resolution problems and does not calculate the exact paths. The main cause of resolution problems is that not enough rays are launched from the transmitter (to reduce complexity and memory requirements). One solution to this problem is to increase the resolution of the launched ray; another is to split rays at some interval [9][11].

Ray launching does have advantage over the image-based ray tracing method. In the image-based method, the number of images increases significantly as additional reflecting surfaces are introduced (i.e. database complexity). The growth of the number of images is exponential because an image is capable of producing many higher order images depending on the number of reflectors. While in the case of ray launching, a ray interacting with an obstacle is only capable of producing two more rays (reflected and transmitted).

3.3 Basic Elements of Ray Tracing

When rays are traced in an environment they may undergo a number of primitive operations. In this thesis, the primitives considered include reflection and transmission at a medium discontinuity.

3.3.1 Single Reflection and Transmission

A single reflection is modelled as shown in figure 3.2 below (which also shows the transmission process). An incident ray falls on a medium discontinuity, in this case defined by the x-axis.

During the reflection process two major tasks must be performed. Firstly, the propagation direction of the ray must be modified after reflection based on Snell's law [14-16]. As shown in figure 3.2, if the incident angle (measured relative to the surface normal) prior to reflection is denoted by θ_i , then after the interaction the reflected wave will propagate at an angle θ_r , where $\theta_r = \theta_i$. In addition to

modifying the direction of propagation after reflection, in all practical situations additional attenuation must be applied to correctly model the losses associated with the reflection process. This additional attenuation is simulated mathematically by multiplying the received field strength by a reflection coefficient for each of the reflections present in the ray path [15-17].

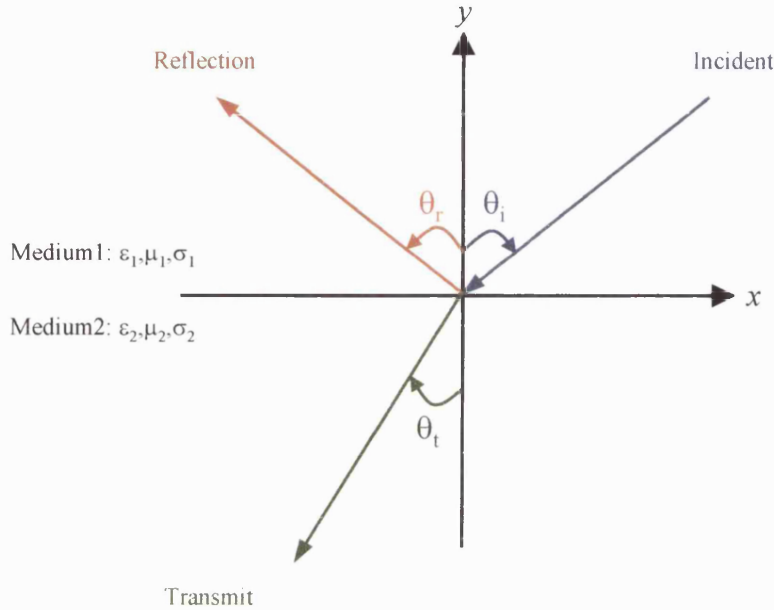


Figure 3.2: Reflection and Transmission in the x-axis

Figure 3.2 shows a linearly polarized plane wave obliquely incident on a boundary between two media. For a lossless medium ($\sigma = 0$, $\epsilon = \text{real}$), the refractive index is defined using equation 3.1.

$$\eta = \sqrt{(\mu_r \epsilon_r)} \quad (3.1)$$

For a non-ferrous media, $\mu_r = 1$ and equation 3.1 can be further simplified:

$$\eta = \sqrt{\epsilon_r} \quad (3.2)$$

For the case where the conductivity (σ) of the medium is finite, the permittivity is complex ($\epsilon = \epsilon' - j\epsilon''$), resulting in a complex refractive index as shown in equation 3.3 [15][17].

$$\eta = \sqrt{(\mu_r \epsilon_r)} = n' - jn'' \quad (3.3)$$

Figure 3.2 shows the incident; reflection and refraction ray angles are θ_i , θ_r with positive y-axis and θ_t with negative y-axis respectively. Snell's law defines the relationship between these angles. For reflection:

$$\theta_i = \theta_r \quad (3.4)$$

For transmission in a lossless medium:

$$\sin \theta_t = \eta_1 / \eta_2 (\sin \theta_i) = \sqrt{(\mu_1 \epsilon_1 / \mu_2 \epsilon_2)} \sin \theta_i \quad (3.5)$$

where η_1 , μ_1 and ϵ_1 are the refractive index, relative permeability and relative permittivity of medium 1 respectively and η_2 , μ_2 , ϵ_2 are the refractive index, relative permeability and relative permittivity of medium 2 respectively [18]. For a lossy medium, the complex refractive indices of the two media must be inserted in the equation.

While the modelling of a single reflection or transmission is simple to perform, the simulation of multiple interactions requires a more complicated process. In the following section, the theory of images is introduced to model multiple interactions in a number of surfaces.

3.3.2 Multi-Reflection using image theory

To simulate multiple combinations of reflection and transmission the theory of images has been applied. Figure 3.3 gives a simple example based on a direct wave reflecting and transmitting from the upper (surface 1) and lower (surface 2) horizontal surfaces of a single material structure. The source of the transmission is located at co-ordinates (x_t, y_t) . As explained in section 3.3.1 and figure 3.2, a single reflection from the top of surface 1 is modelled (path 2 in figure 3.3).

To simplify the modelling process, this reflected ray (ray 2) is now assumed to have propagated from a virtual image whose co-ordinates are based on a reflection in surface 1 of the original transmitter. Since the surfaces in the model are all assumed to be horizontal or vertical, this reflection calculation becomes trivial [19]. Equation 3.6 shows the calculation of the new image for path 2 after reflection in horizontal surface 1.

$$x_2 = x_t - 2\Delta x_1, \quad y_2 = y_t \quad (3.6)$$

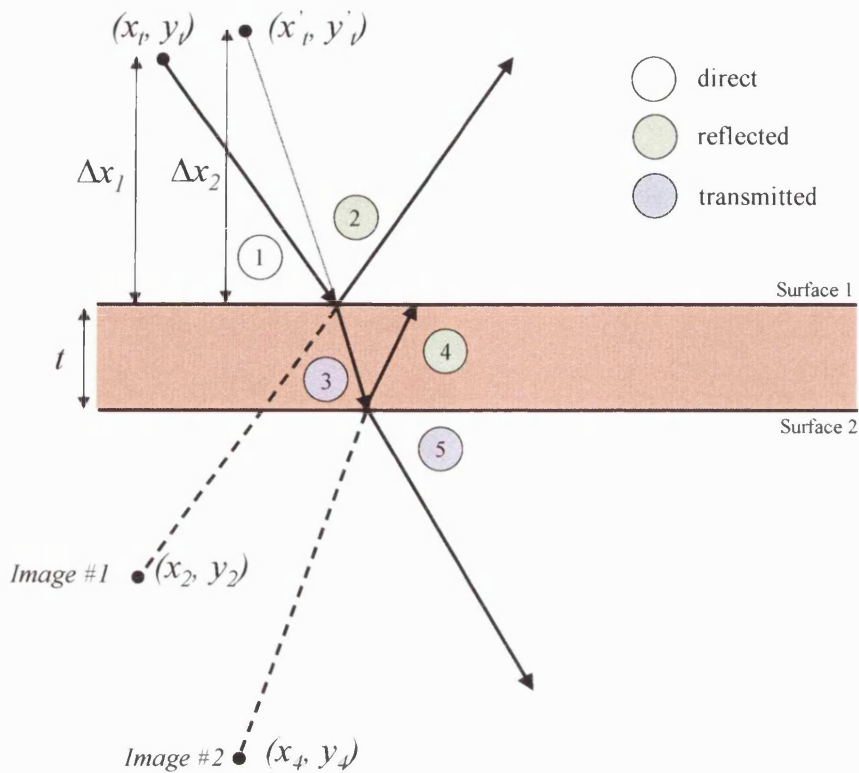


Figure 3.3: Multiple Reflections using image theory

This virtual image is labelled *Image #1* in figure 3.3 and has co-ordinates (x_2, y_2) . When combined with the additional attenuation of the reflection co-efficient, the image acts as an equivalent transmitting source that enables any subsequent calculations and interactions to be performed as if the ray were a direct path undergoing a further single transmission or reflection. The use of virtual images greatly simplifies the mathematical processes needed to simulate multiple reflection and transmission. In addition to the reflected wave at surface 1, the direct path also generates a transmitted ray, denoted as ray 3 in figure 3.3. Refraction during the transmission process will effectively ‘bend’ the transmitted ray and a new virtual image must be calculated to provide an effective straight-line source. This new virtual image is located at co-ordinates (x'_t, y'_t) . The refraction effect is an important part of the model’s illumination and shadowing process.

The transmitted ray (path 3) now interacts with surface 2. Two new rays are formed, a reflected ray (path 4) and a transmitted ray (path 5). The virtual image source for

the reflected ray (path 4) is calculated by reflecting the image source of path 3 in surface 2. For this ray the new image co-ordinates are denoted by (x_4, y_4) are calculated as shown in equation 3.7.

$$x_4 = x'_t - 2(\Delta x_2 + t), \quad y_4 = y'_t \quad (3.7)$$

This image approach lies at the heart of the ray-tracing module and the resulting output file contains a full list of image co-ordinates, attenuation coefficients, and propagation directions. This image file is used within the field reconstruction process to identify paths reaching the receiver and to enable the final field strength for each path to be calculated. It is the vector summation of the individual multipath field strengths that forms the overall field prediction at a receiver point.

3.3.3 Polarisation

The study of polarisation and polarisation diversity in particular, is of considerable interest in this thesis. With this in mind, it is necessary for the propagation model to simulate this effect. Polarisation can be split into two components: perpendicular or horizontal polarisation and parallel or vertical polarisation [17][20].

The first case, known as horizontal polarisation, occurs when the electric field vector is parallel to the boundary surface or perpendicular to the plane of incidence (see figure 3.4a). The plane of incidence is defined as the plane containing the incident ray and the normal to the surface.

In the second case, known as *vertical polarisation*, the electric field vector is perpendicular to the boundary surface and parallel to the plane of incidence (see figure 3.4b). The terms “horizontally and vertically polarised waves” refers to the fact that waves from horizontal and vertical antennas, respectively, would produce these particular orientations of electric and magnetic vectors in waves striking the surface of the earth [21-23].

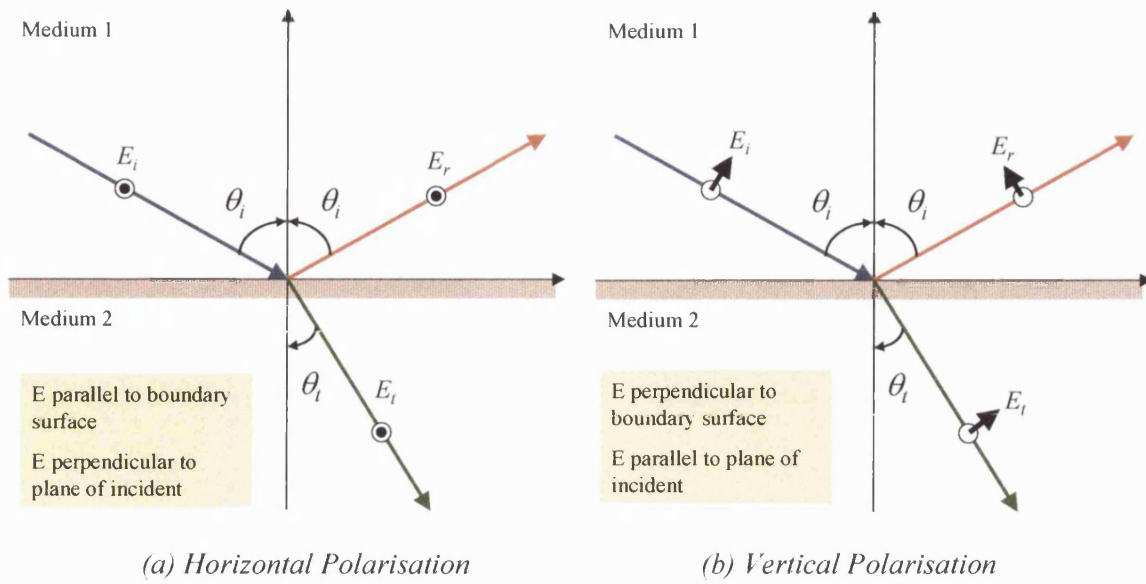


Figure 3.4: Reflection and Refraction waves having
(a) Horizontal Polarisation & (b) Vertical Polarisation

Perpendicular (horizontal) Polarisation: If medium 2 is a perfect conductor then the reflection coefficient is $\rho_{\perp} = -1$ and if both media are lossless non-magnetic dielectrics then the reflection coefficient is given by equation 3.8 [15][24-25].

$$\rho_{\perp} = \frac{\cos \theta_i - \sqrt{(\epsilon_2 / \epsilon_1) - \sin^2 \theta_i}}{\cos \theta_i + \sqrt{(\epsilon_2 / \epsilon_1) - \sin^2 \theta_i}} \quad (3.8)$$

Provided medium 2 has a higher dielectric constant than medium 1 (i.e. $\epsilon_2 > \epsilon_1$), then the value of the expression within the square root will be positive and the reflection coefficient will be real. If, however, the wave is incident from a medium with a larger value of permittivity (i.e. $\epsilon_1 > \epsilon_2$) and if $\sin^2 \theta_i \geq \epsilon_2 / \epsilon_1$ then the reflection coefficient becomes complex and its magnitude is equal to 1. Under this condition, the incident wave is totally internally reflected back into the higher ϵ medium.

The transmission coefficient, τ_{\perp} , of the electrical field is found from:

$$\tau_{\perp} = 1 + \rho_{\perp} \quad (3.9)$$

Parallel (vertical) Polarisation: The reflection and transmission coefficients, ρ_{\parallel} and τ_{\parallel} respectively, are related by equation 3.10.

$$1 + \rho_{\parallel} = \frac{\cos \theta_i}{\cos \theta_t} \tau_{\parallel} \quad (3.10)$$

For lossless non-magnetic dielectrics the reflection coefficient for parallel or vertical polarisation when the electric field is parallel to the plane of incidence becomes [15][24][25]:

$$\rho_{\parallel} = \frac{(\epsilon_2 / \epsilon_1) \cos \theta_i - \sqrt{(\epsilon_2 / \epsilon_1) - \sin^2 \theta_i}}{(\epsilon_2 / \epsilon_1) \cos \theta_i + \sqrt{(\epsilon_2 / \epsilon_1) - \sin^2 \theta_i}} \quad (3.11)$$

If medium 2 is a perfect conductor then the reflection coefficient becomes -1 .

3.3.4 Diffraction

Diffraction is a process that enables waves to bend around sharp edges or corners. This effect is particularly noticeable at lower frequencies and in large environments. For short-range high frequency indoor environments, diffraction is not normally considered to be as important as reflection and/or transmission. In this thesis, the diffraction process has not been considered in the ray-tracing model.

3.4 Limitations of Ray-Tracing Model

A number of limitations and assumptions have been made to simplify the ray modelling process. Perhaps the most significant assumption is the use of two-dimensional geometry in the model description and ray-launching algorithm. Environments are described in a 2-D plane, enabling horizontal cuts (x - y plane, figure 3.5a) or vertical cuts (y - z or x - z planes, figures 3.5b and 3.5c) to be analysed. Three dimensional interactions are not modelled in the current implementation and as such all reflections and transmissions are constrained to occur in a 2-D projection.

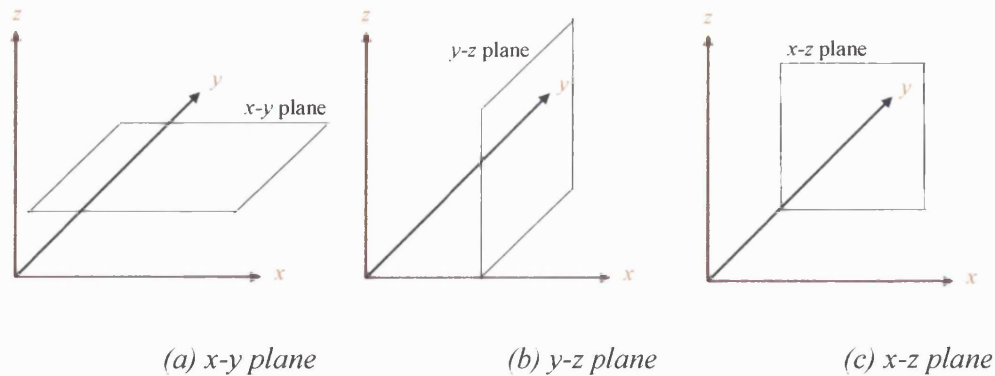


Figure 3.5: 2-D planes in a 3-D axis system

Further geometry limitations are placed on the two-dimensional database in that all surfaces are restricted to be either horizontal or vertical. Hence, all reflections and transmission must occur at a horizontal or vertical boundary, and this will introduce significant errors for curved surfaces or flat surfaces lying at arbitrary angles. This surface limitation partly arises from the use of a raster material grid, rather than a vector description, of the environment.

The modelling of reflection and transmission is dependent on an accurate knowledge of material parameters. In practice, simplified homogenous material parameters are used to model surfaces such as walls, floors and ceilings. Detailed in-building clutter such as tables, chairs, and bookcases etc. have not been included in the studies performed to date for simplicity, however this is easy to include given the availability of the data.

The electromagnetic analysis is based on normalised field strength (see section 2.2.1), and as such the effects of antenna gain do not need to be explicitly defined in the analysis [21][25]. While this simplification enhances the more generic value of the output data, it makes the modelling of practical, and particularly directional, antennas more difficult to incorporate. This could be performed by modifying the launched field strength based on the transmitter beam pattern (the receiver antenna beam pattern can be incorporated in the field reconstruction software).

3.5 Propagation Model: Program Structure and I/O

This part of the chapter describes the structure of the ray launching software used in this thesis. The various input files required to operate the model are described. The

main input file describes the physical and electrical properties of the operating environment and is generated by using the grid environment described in 3.5.2. The various output files provide a formal record of the final prediction results.

3.5.1 Definition of Input Database

The ray launching simulation engine operates in two-dimensional space. In the studies considered to date, the environment is defined using an input data file that includes the height and length of the building structures, as shown in the vertical x - z plane. It is also possible to define environments in the x - y plane (horizontal) or y - z plane (alternative vertical). More specifically, the input environment is defined using a two-dimensional cell raster [2][26]. A key parameter is the height and width used to represent each cell, since this defines the resolution of the input database and output grid predictions. The choice of cell size is a compromise between grid resolution and computer run-time. Once the cell size has been defined, the number of cells can be computed based on the width and height (assuming an x - y plane). Input environments can consist of many different material types. To accommodate this feature, each cell in the database can be assigned a particular set of permittivity and conductivity values. Each cell is assigned a single material number that effectively points to the set of material parameters assigned to that cell. Hence, the input database takes the form of a material pointer raster or array. An example of a simplified database is given in figure 3.6 and an annotated version in figure 3.7.

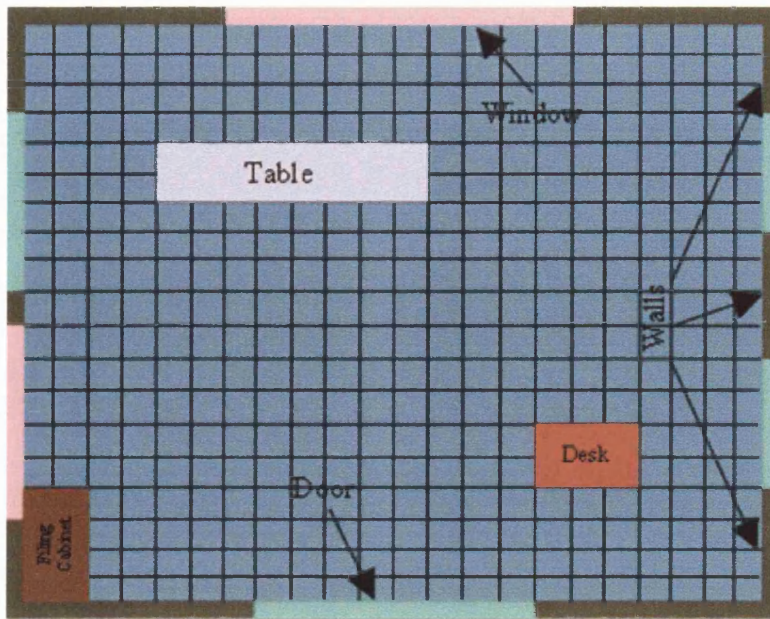


Figure 3.6: A simple environment showing on structure of the environment grid

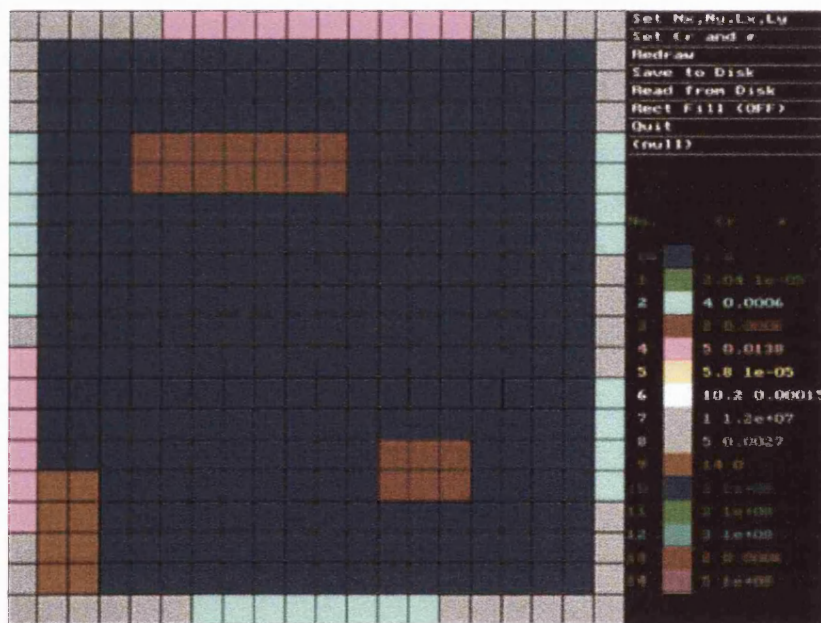


Figure 3.7: A simple environment showing on structure of the environment grid

Figure 3.7 shows a simple 20 cells (x-axis) by 20 cells (y-axis) environment. The area is defined with a width of 4 metres and a height of 4 metres. The cell resolution is therefore 0.2 metres by 0.2 metres (in a practical environment far smaller cell resolutions would be used). A single horizontal concrete wall is defined by appropriately assigning material pointers to a row of cells. The right hand side of

figure 3.7 shows two material relative permittivity / conductivity sets (air and concrete). These are assigned point values of 0 and 3 respectively (it is assumed that pointers 1 and 2 refer to material unused in this database). This database structure has been used to generate a number of realistic scenarios. Table 3.1 shows the material parameters of the test environments.

Env.	Material	Permittivity	Conductivity
Wall	Concrete	5.10	0.1380
Door	Wood	4.20	0.0007
Table / Desk	Wood	4.01	0.0006
Window	Glass	6.14	0.0310
Filing Cabinet	metal	0.00	0.00

Table 3.1: Permittivity and conductivity of common materials

To operate the ray-tracing algorithm the minimum and maximum launch angles at the transmitter must be defined. For typical indoor studies, a 360-degree spread of launch angles is normal. However, for High Altitude Platform (HAP) simulations, a far narrower set of launch angles can be defined (see chapter 5). The minimum and maximum launch angles define the angular spread of the launching process. In addition to the angular spread, a step-size is required to determine the total number of rays to be launched. This step size is used to determine the angular resolution of the ray tracing process.

The ray tracing software continues to trace rays in the environment until the normalised field strength falls below a predefined Cut-Off Power level (COP). This level is defined in the input file together with operating frequency, polarisation mode and the location of the transmitter. There are two polarisation modes: horizontal (perpendicular) and vertical (parallel) [18]. The transmitting or receiving antenna can be defined to operate in either the horizontal or vertical mode.

3.5.2 Environment Grid Software

This software is the initial program used in the simulation to produce rectangular input grid environments. First the size of the environment is specified, followed by the

required set of material types. Materials used in the environment are representative of structures such as walls, doors, ceilings etc. and are differentiated by their permittivity and conductivity values at the frequency. Finally, the shape and structure of the environment is defined by editing the material property of cells within the grid.

3.5.3 Program input/output

The input and output structure of the ray tracing software is summarised in figure 3.8. The input file ('Input') is generated as described in section 3.5.1 using a combination of the environment structure and material properties. The ray tracing software is split into two main modules, the first performs ray tracing (RT.c) and image generation while the second performs field reconstruction (FR.c) based on image data produced from the first module.

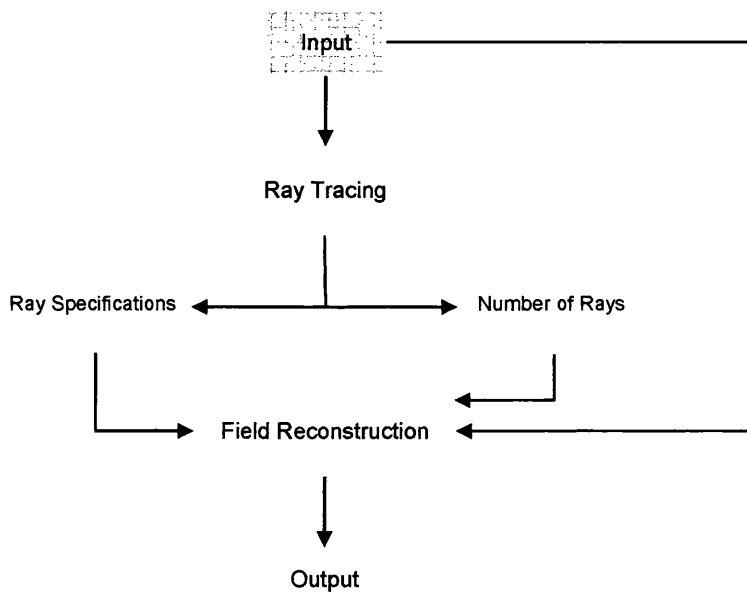


Figure 3.8: Ray Tracing Flow Diagram

The input database is vital to both the RT and FR modules since it defines the environment, material properties, transmitter location and receiver grid. The output from the RT module forms a further input to the FR software. This input takes the form of the total number of rays traced in the software and an image structure for each of these rays. The final field strength value for each receiver point in the grid is produced as the vector sum of all rays illuminating this point within the FR software.

3.5.4 Input File Format and Description

As mentioned in section 3.5.3, the ray-tracing program uses two software programs, referred to as ray tracing and field reconstruction. The output from the ray tracing code together with the original input file is passed to the field reconstruction software, as shown in figure 3.8. An example of the input data file is given in table 3.2.

20.0 20.0 4.0 4.0 0.2 0.2	xnum ynum, width height, delx dely
16	Material num
1.00 0.00 n	Perm. & Conduct. of 1 st material, non-conductor
2.04 0.001 c	Perm. & Conduct. of 2 nd material, conductor
6.14 0.001 n	Perm. & Conduct. of 3 rd material, non-conductor
....
6.14 0.001 n	Perm. & Conduct. Of 16 th material, non-conductor
0 2 3 1 0 0 ...	Raster of Material Points
-55.0 2.0	CoP (dB), Frequency (GHz)
1.0237 3.8257	Transmitter x & y co-ordinate (m)
0.0 6.0 0.0 8.0	Bounding rectangle for environment (m)
0.1 359.9 0.5	Min, Max & Step angles (degree)
1.0	Polarisation

Table 3.2: Example input data file (not including raster grid)

3.5.5 Output file formats and description

The ray-tracing module produces a number of output files (referred to as Ray Specification in figure 3.8) that are passed on to the field reconstruction block. There are two separate output files produced by the RT software, the first file is a text file which stores the number of images generated by the ray tracing code and the other is a binary file that stores the image information generated from the ray-tracing program. Each image structure contains the information listed in table 3.3.

Variable	Definition
Ang	Propagation direction of image source
X	Source x coordinate
Y	Source y coordinate
R	Path length from image source to last interaction
Betar	Cumulative phase
Refco * exp(-alfar)	Cumulative path loss
Atten	Reflection Attenuation
Refract	Refraction Attenuation

Table 3.3: Image information stored in the Ray Specification output

Every image represents a ray path. The direction of propagation is stored in *ang*. The wave propagates from a source at co-ordinate (*x,y*). The distance from the image source to the point of interaction (i.e. the point where the last transmission or reflection occurred) is stored in the variable *r*. The length, *r*, is critical since any path length less than this value represents an invalid path. Using the image co-ordinate, the propagation angle and the distance to the last interaction, the co-ordinates of the last interaction can be calculated. The image structure also includes four pieces of key electromagnetic information to enable the combined attenuation due to transmission and reflection to be calculated.

The two output files described above combined with the initial input file describing the building structure and transmitter details are used as input files in the second part of the software, known as field-reconstruction (FR.c). This code produces the final output grid prediction. The format of this file is shown in table 3.4 below.

X	Y	Field Amplitude	Phase (radians)	Field strength (dB)
0.175	0.025	0.015	0.572	-36.224
0.225	0.025	0.004	-2.390	-48.783
0.275	0.025	0.001	1.889	-60.078

Table 3.4: File format of final output

The first two columns provide the x and y co-ordinate for prediction. The third and fourth columns provide the field strength amplitude (normalised, 1V/m at 1m from the source) and phase in radians. The final column provides the normalised field strength in dB, i.e. $20\log_{10}$ (field amplitude).

3.5.6 Material Characteristics and Attenuation per Metre

Each material type is defined using a number of electromagnetic parameters. The relative permittivity or dielectric constant, ϵ_r , and the loss tangent, $\tan(\delta)$ can be used to represent the material. It is usual to characterise a dielectric in terms of the loss tangent rather than its conductivity σ , however the two are related via equation 3.12, where λ represents the wavelength.

$$\tan(\delta) = 60\sigma \lambda / \epsilon_r \tag{3.12}$$

Although most materials are quoted using permittivity and conductivity (or $\tan(\delta)$), it is far more useful to quote the attenuation coefficient (see equation 3.13), from which the loss per metre or loss per centimetre can be calculated [27].

$$\alpha = (\omega \tan(\delta/2) / \sqrt{(\mu_0 \epsilon_r \epsilon_0)}) \tag{3.13}$$

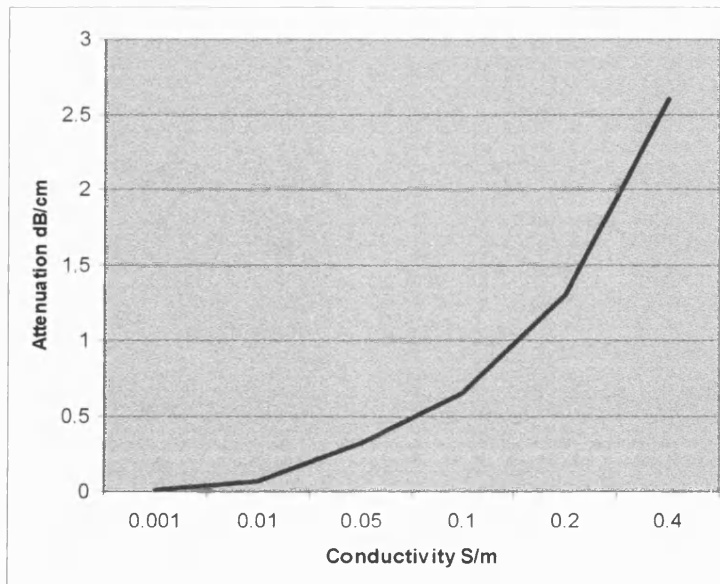


Figure 3.9: Relationship between conductivity and dB/cm (relative permittivity 6.14, $f= 2.0\text{GHz}$)

To convert equation 3.13 from nepers/metre to dB/cm (a more recognised value), the number must be divided by 8.686 dB. As an example, assume a carrier frequency of 2.0 GHz (i.e. a wavelength of 0.15 metres), a conductivity of 0.4 siemens/metre, and a relative permittivity of 6.14 [2][19]. Applying equation 3.12 the value of $\tan(\delta)$ is computed to be 0.5863. Inserting these values into equation 3.13 and adjusting to dB/cm, a value of 2.6 dB/cm is obtained. The transmission loss is very sensitive to the value of conductivity assumed, and figure 3.9 shows the loss in dB/cm as a function of conductivity. For a 15cm thick wall, the total attenuation can vary by 5-10 dB for conductivity values ranging between 0.01 to 0.1 S/m.

Results in the open literature quote various different values of ϵ_r and $\tan(\delta)$ for the same basic material type, and this reveals the variability and inaccuracy with which these parameters are measured. The accuracy of the propagation model can only ever be as good as the accuracy of the input material data. The calculation of attenuation in terms of dB/cm is a useful check to ensure that the loss for a particular material is in line with measured values. Transmission loss measurements are more commonly available for many materials at various thicknesses and frequencies. For concrete and brick walls in the 2 GHz range, a loss of 0.5-2.0 dB/cm is expected [19][27]. At higher frequencies such as 11 and 17 GHz, far higher attenuations are expected up to a worst case value of 8 dB/cm. Isolation between rooms will therefore depend quite critically on the type of material parameters and thickness assigned to the dividing walls [28-29].

3.6 Ray-Tracing program code

The main function of the ray tracing software has already been described earlier in the chapter. The ray-tracing model is based on the use of geometrical optics and uses combinations of direct, reflected and transmitted rays to calculate the field strength at the receiver. The code works together with the field reconstruction block to predict field strengths for a given environment description, source location and receiver point.

In the ray-tracing module, rays are uniformly launched from the source between a start and end angle with an angular resolution of $\delta\phi$. Each ray is traced and whenever it crosses a cell boundary, information concerning angle of incidence, path length, attenuation due to reflection and refraction during transmission etc is recorded in the

image structure described in table 3.2. The rays are traced until their amplitude decays below a pre-defined cut-off threshold. The main output file, out6, stores all the traced images for a given transmitter location and is used in the field reconstruction block to calculate the field strength at a given receiver point.

3.7 Field-Reconstruction program code

The field reconstruction code uses the images generated from the ray-tracing module to predict field strengths at an arbitrary receiver point. For each image in the out2 file, a test is performed to check whether the receiver falls in the illumination area of the ray image. Figure 3.10 shows the basic form of this test.

X_s, Y_s represent the location of the image source (obtained from the image structure) and X_{in}, Y_{in} represent the location of the last ray interaction. This latter co-ordinate is calculated from the source co-ordinate and the length, r_{ri} , obtained from within the image structure (denoted as r in table 3.2). The propagation direction of the illuminating ray is defined by the variable ang . The angle ($angrec$) and path length to the test point (r_{jt}) are now calculated. The test point is illuminated by the image if, and only if:

$$abs(angrec - ang) < dang \quad (3.14)$$

and

$$r_{jt} > r_{ri} \quad (3.15)$$

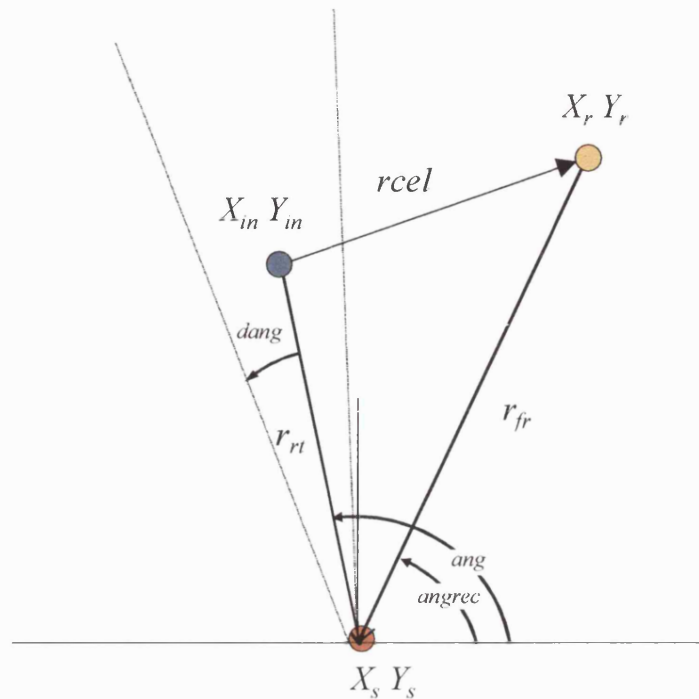


Figure 3.10: Image illumination test within Field Reconstruction

where $dang$ (related to the step angle) represents an acceptable angular error to overcome the coarse resolution of the input grid. Equation 3.14 ensures the image illuminates the test point, while equation 3.15 ensures that the test point is on the correct side of the boundary interaction.

The field strength at each receiver point is now calculated as the vector sum of the fields contributed by each illuminating image. Once this total field has been calculated, it is then written to the output file, *out2*, as defined in table 3.3.

3.8 Post-Processing Software

A number of software programs have been written during the course of this project to post-process the output data from the field reconstruction module. Further programs are used to produce the final coverage pictures.

One key piece of post-processing software loads in multiple coverage prediction grids and performs diversity combining based on selection, equal gain (vector) and equal gain (amplitude). In addition to diversity combining, this post processing software also calculates the minimum, maximum, mean, variance and standard deviation for each input branch and the resulting output signal. This software also calculates the

average diversity gain by comparing combined results with one of the input branches. Software to compute the field strength probability distribution function (PDF) and cumulative distribution function has also been written and the resulting data can be used to calculate diversity gain as a function of outage probability.

To display the output data in a pictorial form, the software program 'map_plot' is used. To use the map_plot program, two input data files (control and data) must be produced in the formats described in tables 3.5 and 3.6.

Line 1	Data file name
Line 2	Title for plot
Line 3	X-axis label
Line 4	Number of values shown on X-axis
Line 5	Y-axis label
Line 6	Number of values shown on Y-axis
Line 7	Number of contours
Line 8	Unit of contours
Line 9	Number of colours for palette

Table 3.5: Map_plot Control File Format

Line1	Min & Max. X value, No of X values
Line2	Min & Max. Y value, No of Y values
Line3	A real number
Line4	A little string line
Line5	Number of X values, The X values from min. to max
Line6	1 st Y value, Z at 1 st x and 1 st y, Z at 2 nd x and 1 st y
Line7	2ndY value, Z at 1st x and 2nd y, Z at 2nd x and 2nd y
Line...	...
Line N	Last Y value, Z at 1st x and last y, Z at 2nd x and last y

Table 3.6: Data File Format

3.9 Tracing of Rays

The ray-tracing program can only support reflection and transmission at horizontal and vertical boundaries due to the use of a raster environment description. Rays can propagate in the environment at any angle between 0 and 360 degrees. The motion of the ray is broken down into a large number of individual horizontal and vertical cell motions. For each iteration (or step) of the ray-tracer, the program must determine whether to propagate the ray in the vertical or horizontal direction.

Within the ray-tracing program, the angle of propagation is broken down into one of four quadrants. Based on the propagation angle, quantised versions of the horizontal and vertical motion components are generated. For example, if the angle of propagation lies in quadrant one, i.e. between 0 and 90 degrees measured anti-clockwise from right-hand x-axis, the ray is assumed to be moving upwards and to the right. Alternatively, in quadrant 3 (angles between 180 and 270 degrees), the ray is assumed to be moving downwards and to the left. These motions are expressed using two variables, i_x and i_y . If i_x is positive (left hand side of figure 3.11), the wave is moving to the right, otherwise if i_x is negative (the left-hand side of figure 3.11) the wave is moving to the left.

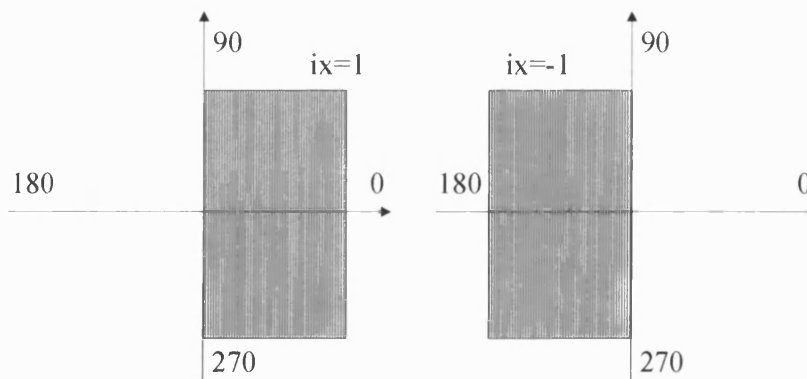


Figure 3.11: Motion Vector, i_x

Similarly, if i_y is positive (left-hand side of figure 3.12) the wave is moving upwards, otherwise (right hand side of figure 3.12) the wave is moving downwards.

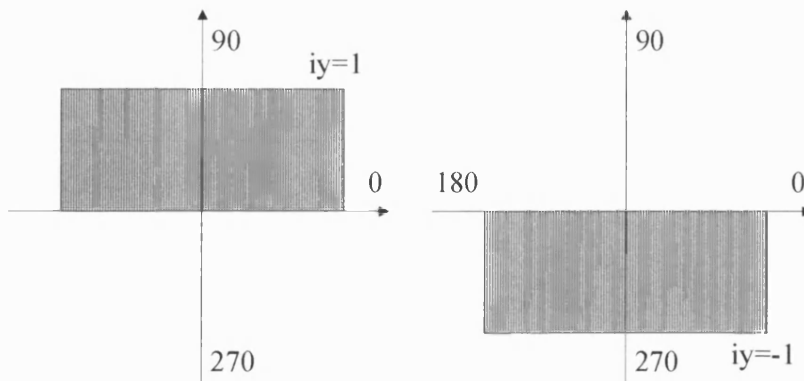


Figure 3.12: Motion Vector, i_y

The variables i_x and i_y are used to determine whether the ray is moving left or right and up or down. To determine whether the ray should move horizontally or vertically and whether the next boundary interaction will be horizontal or vertical, a simple mathematical test is performed to identify the direction that most closely approximates the true angular direction. The mathematical test is based on computing two distances r_1 and r_2 .

Table 3.7 shows the calculation of r_1 and r_2 based on the calculations in the software. Depending of the values of r_1 and r_2 , either i or j co-ordinates of the current ray location are adjusted based on the motion vectors shown in figures 3.11 and 3.12. In the table below, initially $r_2 < r_1$ and the x ordinate is decremented. However, when r_1 becomes less than r_2 , the y ordinate is decremented.

$R_2 \langle R_1 \Rightarrow \text{Motion in } X$	
$r_1 = 0.52$	$r_2 = 0.12$
$i = 4$	$j = 89$
$al = 0.39$	$\tan(al) = 0.42$
$x = 0.91$	$y = 18.0$
$x_1 = 0.43$	$yy_1 = 17.80$
$x_2 = 0.80$	$y_2 = 17.95$

$R_2 \rangle R_1 \Rightarrow \text{Motion in } Y$	
$r_1 = 0.18$	$r_2 = 0.22$
$i = 2$	$j = 89$
$al = 0.40$	$\tan(al) = 0.43$
$x = 0.60$	$y = 17.87$
$x_1 = 0.43$	$yy_1 = 17.80$
$x_2 = 0.40$	$y_2 = 17.78$

Table 3.7: Example of co-ordinate tracing along a ray

3.10 Average Power and Signal to Noise Calculations

In this section the method for calculating the instantaneous and average received power along a route is explained for any transmit power and antenna pair. For a known radio system, this data can be further processed to generate the signal to noise ratio (SNR).

This particular study is performed in the 5 GHz band for a WLAN system conforming to either the IEEE 802.11a or ETSI Hiperlan /2 [29] specification. The radio is assumed to operate with a transmit power of 100 μ W and a bandwidth of 20MHz. The transmitter and receiver antennas are assumed to have a gain of 0dBi in the azimuth plane.

The single room test environment is shown in figure 3.13. The Access Point (AP) is mounted in the bottom left hand corner of the room while the Mobile Terminal (MT) moves along route #1. The room includes a table, desk and several doors. The walls

are constructed from concrete (relative permittivity 5.0, conductivity 0.137) and the doors and furniture are made of wood (relative permittivity 2.0, conductivity 0.0006).

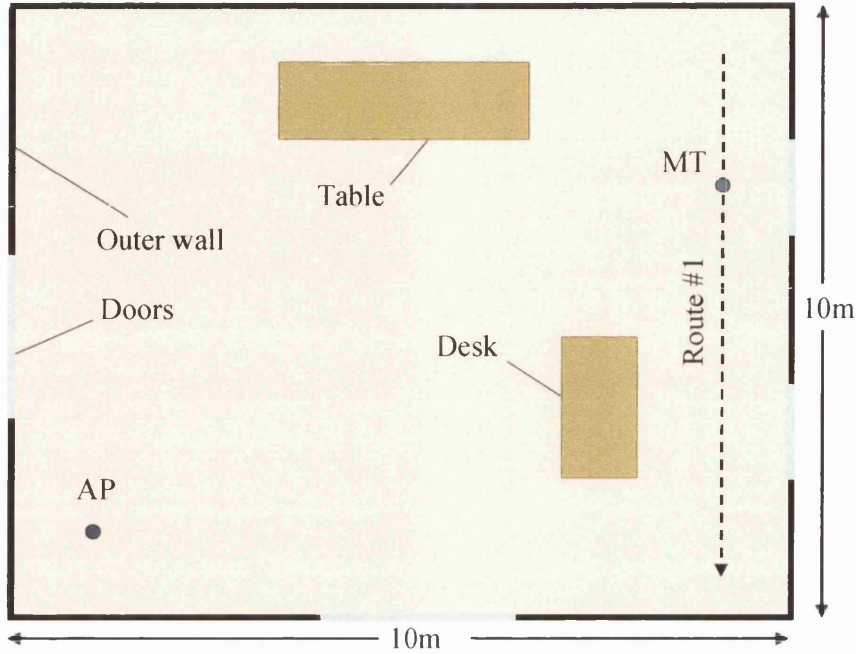


Figure 3.13: Indoor test environment with AP and MT locations

The ray tracing engine operates using normalised field strength. This normalisation is based on the received field strength having unity value at a distance of one metre from the transmitter. The concept of normalised field strength was discussed in section 2.2.5 (equations 2.13 and 2.14). Normalisation is useful since it removes the impact of transmit power and antenna gain (assuming omni directional antennas) in the ray calculations. Normalised field strength can easily be converted to normalised received power (see equation 2.15). The normalised received power is converted to actual received power by multiplying by the received power at one metre. This calculation requires the actual transmit power and transmit and receive antenna gains to be known. Conversion from normalised power to actual power was also discussed in chapter 2 (see equation 2.14).

The normalised instantaneous power $P_n(d)$ can be calculated as shown in equation 3.16 from the vector sum of the L multipaths ($V_k(d)$, $k=1..L$) arriving at the receiver. $V_k(d)$ represents the normalised complex field strength of the k -th multipath arriving at location d .

$$P_n(d) = \left(\sum_{k=1}^L V_k(d) \right)^2 / Z_l \quad (3.16)$$

To obtain an estimate of the local normalised received power centred at point d it is desirable to spatially average over some small section of the measurement route. This averaging helps to remove the fast fading to leave the underlying mean power. The average received normalised power over a section of the measurement route $\bar{P}_n(d)$ is given by equation 3.17, where $2K+1$ represents the number of measurement samples used in the averaging process (centred on point d) and Δ represents the spatial sampling step size.

$$\bar{P}_n(d) = \frac{1}{2K+1} \sum_{r=-K}^K P_n(d+r\Delta) \quad (3.17)$$

As explained in equation 2.14, the above expression can now be multiplied by P_t , the actual power received at one metre from the transmitter, to remove the normalisation and produce an expression for the actual received power for a given transmit power and antenna gain. The actual received power is therefore given by equation 3.18.

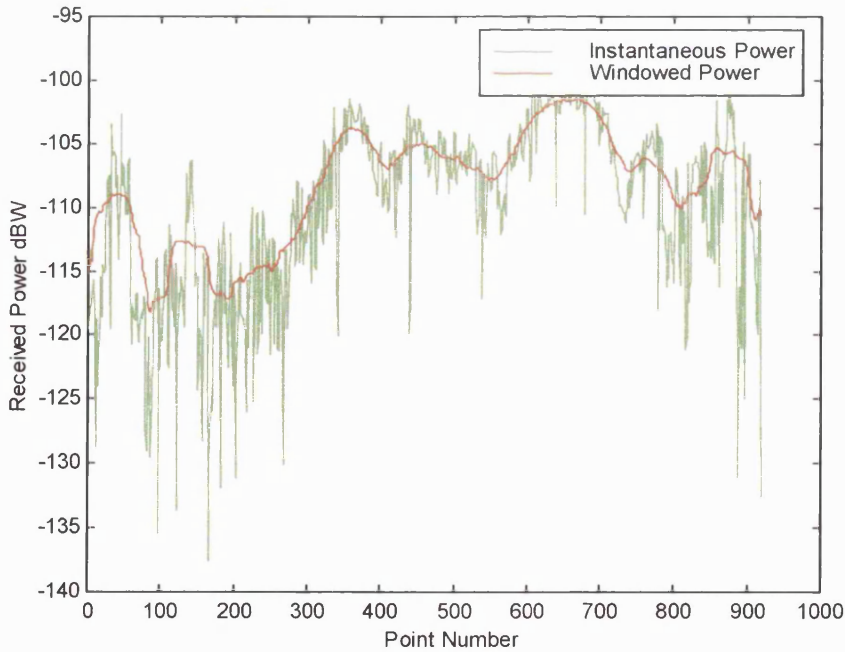


Figure 3.14: Actual received power along measurement route (see figure 3.13)

$$\bar{P}_r(d) = P_t G_t G_r \left[\frac{\lambda}{4\pi} \right]^2 \frac{1}{2K+1} \sum_{r=-K}^K P_n(d+r\Delta) \quad (3.18)$$

If required, the received power can be quoted in units of dBw by computing the expression $10 \log_{10} \bar{p}_r(d)$ and defining the transmit power in watts. The power can also be quoted in units of dBm by defining the transmit power in milliwatts.

Figure 3.14 shows the instantaneous received power (green) and the average received power (red) for an averaging window size K of 25 (which represents 8.6 wavelengths in this study). Samples are taken on the x-axis every 1 mm and the total route length is 9.2m. A transmit power of 100 μ W was assumed in the analysis. As expected, the instantaneous received power shows rapid fluctuations due to the high multipath activity in the room. The red line was produced using equation 3.18 and demonstrates the calculation of the local mean power along the route. Given knowledge of the receiver's noise floor N (see equation 2.17) and an expression for the average power, the average signal to noise ratio $\bar{\gamma}_i(d)$ at any point along the route can be calculated using equation 3.19.

$$\bar{\gamma}_i(d) = \frac{\bar{P}_r(d)}{N} \quad (3.19)$$

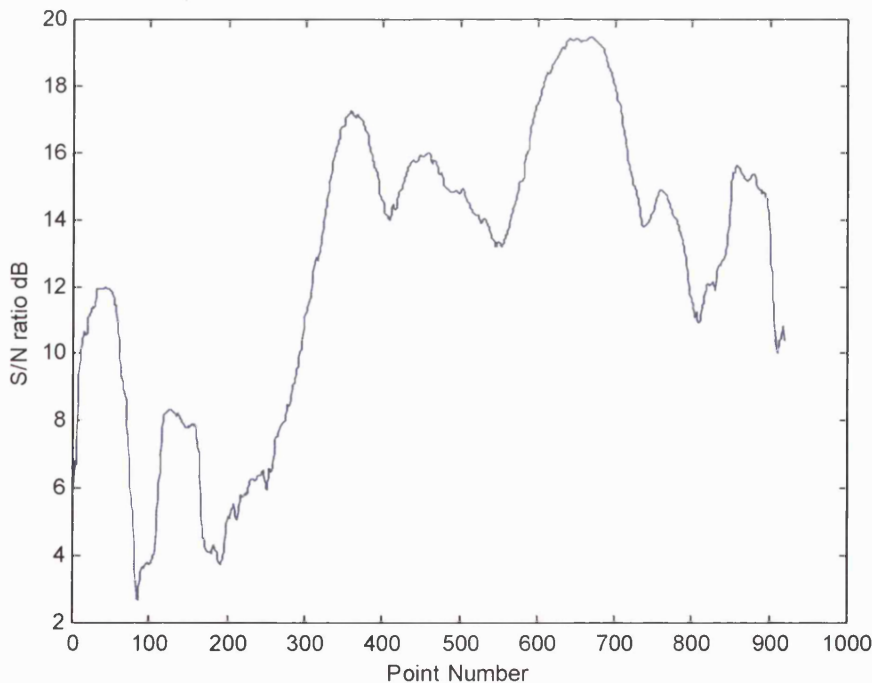


Figure 3.15: Signal to Noise Ratio along measurement route (see figure 3.13)

The value of N is given by equation 2.17 and as explained in chapter 7, for the radio parameter assumed $N = -121$ dBw. The average SNR calculated using equation 3.19 for the test route shown in given in figure 3.15.

3.11 Summary

This chapter has introduced the basic elements of the ray tracing process are discussed the underlying algorithms and mathematics involved. The structure of the ray launching software was explained and limitations in the current implementation discussed. The various input/output files required/produced by the model were defined and a number of examples given. The model was then applied to an example environment to predict the instantaneous and average received power and the signal to noise ratio along a defined measurement route at 5GHz. The use of normalised field strength and its conversion to received power was also explained for a given transmit power and antenna gain.

3.12 Reference

- [1] Ch. Ghobadi, P.R. Shepherd and S.R. Pennock, "2D Ray-Tracing Model for Indoor Radio Propagation at Millimetre Frequencies and the Study of Diversity Techniques", *IEE Proc.-Microw. Antennas Propagation*, vol. 145, no. 4, pp. 349-353, Aug. 1998.
- [2] F. Tila, P.R. Shepherd and S.R. Pennock, "Analysis of Indoor-Indoor and Satellite/Hap-Indoor Propagation Effects", *IEE 11th International conference on Antennas and propagation Professional Network ICAP, Manchester*, vol. 1, pp. 203-207, April 2001.
- [3] G.E. Athanasiadou, A.R. Nix and J.P. McGeehan, "A Microcellular Ray-Tracing Propagation Model and Evaluation of its Narrowband and Wideband Predictions", *IEEE Journal on Selected Areas in Communications*, vol. 18, no. 3, pp. 322-335, March 2000.
- [4] U. Dersch and E. Zollinger, "Propagation Mechanisms in Microcell and Indoor Environments", *IEEE Transaction Vehicular Technology*, vol. 43, no. 4, pp. 1058-1066, Nov. 1994.
- [5] K. Rizk, J-F Wagen and F. Gardiol, "Two-Dimensional Ray-Tracing Modelling for Propagation Prediction in Microcellular Environments", *IEEE Trans. Veh. Tech.*, vol. 46, no. 2, pp. 508-518, May 1997.
- [6] M.C. Lawton and J.P. McGeehan, "The Application of a Deterministic Ray Launching Algorithm for the Prediction of Radio Channel Characteristics in Small Cell Environments", *IEEE Trans. Veh. Tech.*, vol. 43, pp. 955-969, Nov. 1994.
- [7] R.P. Torres, L.Valle, M. Domingo, S. Loredó and M.C. Diez, "CINDOOR: An Engineering Tool for Planning and Design of Wireless Systems in Enclosed Spaces", *IEEE Antenna & Propagation Magazine*, vol. 41, no. 4, pp. 11-22, August 1999.

- [8] G. Durgin, N Patwari and T.S. Rappaport, "An Advanced 3D Ray Launching Method for Wireless Propagation Prediction", *47th IEEE Vehicular Technology Conference*, vol. 2, pp. 785-789, 1997.
- [9] P. Kreuzgruber, P. Unterberger and R. Gahleitner, "A Ray Splitting Model for Indoor Radio Propagation Associated with Complex Geometries", *43rd IEEE Vehicular Technology Conference*, pp. 227-230, 1993.
- [10] J.H. Tarng, W.R. Chang and B.J. Hsu, "Three-Dimensional Modeling of 900-MHz and 2.44-GHz Radio Propagation in Corridors", *IEEE Trans. Veh. Tech.*, vol. 46, no. 2, pp. 519-527, May 1997.
- [11] W. Honcharenko, H.L. Bertoni, J.L. Dailing, J. Qian and H.D. Yee, "Mechanisms Governing UHF Propagation on Single Floors in Modern Office Buildings", *IEEE Trans. Veh. Tech.*, vol. 41, no. 4, pp. 496-504, Nov. 1992.
- [12] S-H. Chen and S-K Jeng, "SBR Image Approach for Radio Wave Propagation in Tunnels with and Without Traffic", *IEEE Trans. Veh. Tech.*, vol. 45, no. 3, pp. 570-578, Aug. 1996.
- [13] B.S. Lee, A.R. Nix and J.P McGeehan, "Indoor Space-Time Propagation Modelling Using A Ray Launching Technique", *11th International conference on Antennas and propagation Professional Network ICAP, Manchester*, pp. 279-283, April 2001.
- [14] K.R. Schaubach, N.J.Davis IV, and T.S. Rappaport, "Propagation models for microcellular environments using a building database", *First Virginia Tech. Symp. on wireless Personal Communication*, Blacksburg, VA, vol. 2, pp. 932 - 935, June 1991.
- [15] W.C. Jakes, "Microwave Mobile Communication", *John Wiley Inc.*, 1st Edition, ISBN 0-471-43720-4, 1974.
- [16] P.F. Panter, "Microwave Communication Systems," *McGraw-Hill Ltd*, 1st Edition, ISBN 0-07-048436-8, 1972.
- [17] S.R. Pennock and P.R. Shepherd, "Microwave Engineering," *Macmillan Press Ltd*, 1st Edition, ISBN 0-333-72801-7, 1998.

- [18] Ch. Ghobadi, "Millimetre Wave Propagation and Diversity Techniques within Buildings and Around Human Bodies", *PhD Thesis, University of Bath*, July 1998.
- [19] C. Yang, B. Wu and C. Ko, "A Ray-Tracing Method for Modelling Indoor Wave Propagation and Penetration", *IEEE Transactions on Antennas and Propagation*, vol. 46, no. 6, pp. 907-919, Jun. 1998.
- [20] Ch. Ghobadi, S.R. Pennock and P.R. Shepherd, "Evaluation of Diversity Techniques in Complex Indoor Environments", *28th European Microwave Conference Amsterdam*, pp. 345-350, 1998.
- [21] E.C. Jordan, "Electromagnetic Waves and Radiating Systems", *Constable and company Ltd.*, 1st Edition, 1962.
- [22] B. Chatterjee, "Propagation of Radio Waves", *Asia Publishing House*, 1st Edition, 1963.
- [23] M.P. Hall, L.W. Barclay and M.T. Hewitt, "Propagation of Radiowave", *The Institution of Electrical Engineers*, 1st Edition, ISBN 0-85296-819-1, 1996.
- [24] K.G. Budden, "The Propagation of Radio Waves", *Cambridge University Press*, 1st Edition, ISBN 0-521-36952-2, 1988.
- [25] C.A. Balanis, "Antenna theory analysis and design", *New York: Harper & Row*, 2nd Edition, ISBN 0-06-040458-2, 1982.
- [26] Ch. Ghobadi, P.R. Shepherd and S.R. Pennock, "A 2D Ray-Tracing Model for Indoor Radio Propagation at MM Frequencies and the Study of Diversity Techniques", *High Frequency Postgraduate Student Colloquium, Leeds*, pp. 53-58, Sep. 1997.
- [27] L.M. Correia and P.O. Frances, "Transmission and Isolation of Signals in Building at 60 GHz", *IEEE Vehicular Technology Conf.*, pp. 1031-1034, 1995.
- [28] M.R. Williamson and A.R. Nix, "Investigating the effects of Antenna Directivity on Wireless Indoor Communications at 60 GHz", *8th IEEE Personal and Indoor Mobile Radio Conf.*, Helsinki, Finland, pp. 635-639, Sept. 1997.
- [29] D. Bull, N. Canagarajah and A.R. Nix, "Mobile Multimedia Communications", *Academic Press Ltd*, 1st Edition, ISBN 0-12-140310-6, 1999.

Chapter 4: Indoor Systems and Diversity

4.1 Introduction to Diversity

Diversity represents a common technique for mitigating the effects of fast fading in a radio environment. The principles of diversity combining have been known for many decades, with the first experiments being reported in 1927 [1-2]. The diversity method requires that a number of transmission paths be available, each carrying the same message but suffering independent fading statistics. The probability of experiencing deep signal fades on all diversity branches at the same time is low providing the fast fading on each branch is uncorrelated [1][3]. For diversity to be fully effective, the mean signal strength on all branches needs to be approximately equal. A number of common methods exist for generating and combining diversity signals. In this thesis frequency, polarisation and space diversity will be studied as methods for generating uncorrelated diversity paths. Combining techniques such as selection and equal gain combining [1][4] are then studied using ray tracing propagation prediction data from an indoor environment.

4.2 Generation Techniques

Space, frequency and polarisation diversity generation techniques are discussed in the following sections. Of these methods, space diversity is probably the most popular form of diversity generation. This method can be further split into transmit and receive space diversity, depending on the location of the spaced antennas.

4.2.1 Space Diversity

Space Diversity relies on generating uncorrelated fading paths through the use of spaced antennas at the receiver and/or transmitter. The method is relatively simple to implement and does not require additional frequency spectrum (a key issue given the growing importance of spectrum efficiency). Based on the above, space diversity is considered to be a strong contender for microwave mobile radio applications [5-7]. The spacing of the antennas at the receiving or transmitting array is chosen to increase the likelihood that the individual signals are suitably uncorrelated. In practice, the correlation of the antenna elements depends on the richness of the scattering in the

radio environment. In this thesis, spacings ranging from $\lambda/4$ to 4λ have been considered, where λ represents the operating wavelength. Two types of space diversity are considered in this thesis, namely receiver diversity and transmitter diversity. Receive diversity improves the likelihood of correct symbol detection (and hence capacity) by processing a number of independently faded observations. Transmit diversity relies on generating two or more uncorrelated signal paths, however this method relies on just a single observation antenna with multiple antennas used at the transmitter.

4.2.1.1 Receiver Space Diversity

Receiver space diversity relies on sensing the incoming transmission using an array of antennas or antenna elements. The basic concept is shown below in figure 4.1.

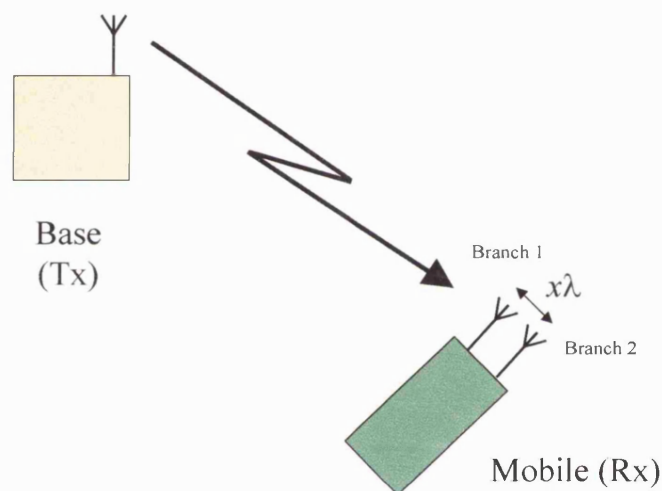


Figure 4.1: Receiver Space Diversity

Receive space diversity improves the reliability of signal detection in cases where the mean field is equal and the fast fading is uncorrelated on all antennas. Noise is also assumed to be uncorrelated over the receiver array. The precise antenna spacing depends on a number of factors, such as the wavelength of transmission, the azimuth distribution of the multipaths and the form factor of the receiver. In a high clutter environment, spacings as low as one quarter to one half of a wavelength can be used (i.e. 1-2 cm at 11 GHz or 0.5-1 cm at 17 GHz) [8-9]. In environments with narrow angle spreads, such as high mounted basestations, the antennas must be spaced much

further apart to increase the probability of decorrelation (5-10 wavelength separation is common).

4.2.1.2 Transmitter Space Diversity

Transmitter space diversity relies on transmitting the signal to a single receiver using an array of antennas or antenna elements. The basic concept is shown below in figure 4.2.

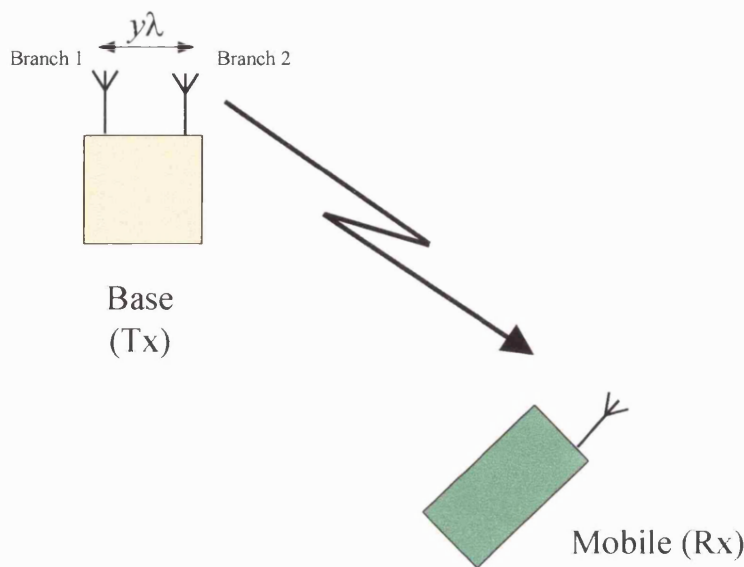


Figure 4.2: Transmitter Space Diversity

Providing the transmit antennas are suitably spaced in a rich scattering environment then two independently faded signal paths will arrive at the single receiver. The main problem associated with transmit diversity is the difficulty in controlling the array to exploit this benefit, given that the signal is received at a distant terminal. Some mechanism for transmitting information on the received signal strength back to the receiver is required in this simple case. Diversity combining techniques will be discussed in more detail in section 4.3.

A more complex form of transmit diversity exists that overcomes the need for a priori channel knowledge at the transmitter. This method is known as transmit delay diversity. The technique introduces a delay along the transmit array to enable the signals to be separated via temporal processing in the receiver (i.e. an equaliser). In this system, narrowband spatial diversity is converted into wideband time diversity.

This type of diversity exploitation is a simple form of space-time processing. The main disadvantage is the increase in signal processing required at the receiver. Given a priori knowledge of the radio channel, the transmit delay diversity data waveforms can be pre-processed into a form that greatly simplifies the required receive processing. This method (which is effectively coded transmit diversity) was first applied by Alamouti [10] who proposed a simple space-time block to perform the required pre-processing.

More recently there has been a trend to transmit time synchronised uncorrelated data from the transmit array. Signal processing is then applied to separate the data streams. If the multiple data streams are encoded from a common input source then the technique is known as space time coding (STC). If no spatial coding is applied, the method is referred to as spatial multiplexing. It should also be noted that the quality of transmit diversity can be enhanced by increasing the number of receive antennas. As seen in chapter 2, considerable capacity enhancement is achieved when multiple antenna elements are used at both the transmitter and the receiver. The resulting Multiple Input Multiple Output (MIMO) system exploits diversity across the arrays together with the ability to transmit multiple uncorrelated streams. MIMO systems are studied in detail in chapter 6.

4.2.2 Polarisation Diversity

Signals transmitted or received on two orthogonal polarisations in the radio environment will exhibit uncorrelated fading statistics [11-12]. These signals thus become candidates for use in diversity systems. In this case, however, only two diversity branches are available, since only two orthogonal polarisations are available [13-14]. One advantage of polarisation diversity is the possibility of supporting a compact antenna arrangement (important to fit in a small form factor), since physically spaced antennas are no longer required.

4.2.3 Frequency Diversity

Instead of transmitting the desired message over spatially separated paths, an alternative approach is to employ different frequencies to achieve independent diversity branches. This concept is illustrated in figure 4.3. The frequencies must be

separated enough so that the fading associated with these different frequencies is uncorrelated [15]. The coherence bandwidth is a convenient quantity that describes the required frequency spacing required to achieve a given degree of correlation (see section 2.4.2). The coherence bandwidth depends on the field strength and time delay of each ray in the multipath channel. In general, as the delay spread increases, the coherence bandwidth decreases (i.e. an inverse time-frequency relationship, equation 2.24).

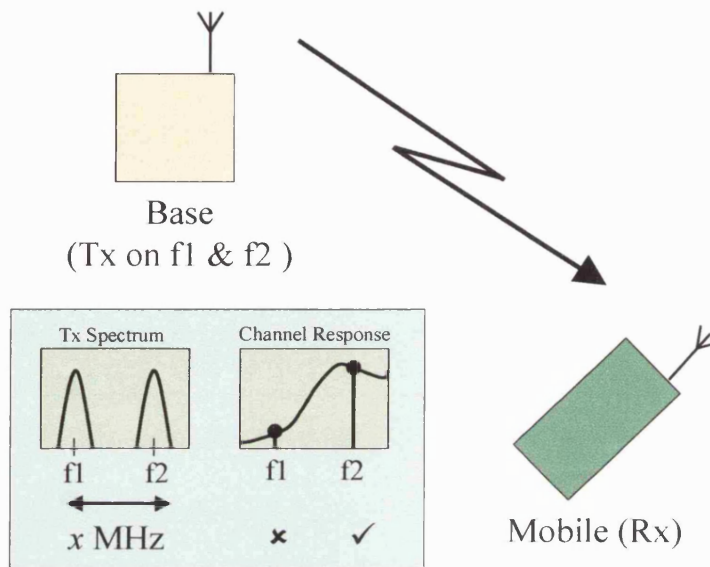


Figure 4.3: Frequency Diversity

Within the coherence bandwidth it is assumed that signals will suffer identical frequency-flat, or narrowband, fading. Hence, time delay spread will have no effect on transmission of the message itself. For frequency separations greater than the coherence bandwidth, signal fading becomes uncorrelated and diversity gain can be achieved [16-17]. Measurements indicate that a coherence bandwidth in the range 500 kHz to 5 MHz is typical for an indoor environment [18-20]. This implies that frequency diversity may require the branches to be separated by 5 MHz or more. For an outdoor channel larger values of delay spread are expected and hence smaller frequency separations would be viable.

The advantage of frequency diversity (relative to space diversity) is the reduction in the number of antennas to just one at both the transmitter and receiver. On the other hand, this method uses considerably more frequency spectrum and requires multiple

transmitter and receiver RF chains in the radio (which increases cost, size and power consumption).

4.3 Diversity Combining Methods

As discussed in section 4.2, the concept of diversity combining is useful for limiting the effects of multipath fading. Having generated two or more signal branches with uncorrelated fading, the process of diversity combining is now required to exploit the diversity gain. A number of methods exist, ranging from the relatively simple concept of selection combining, where the strongest branch is chosen for detection, to the more complex vector summation techniques of equal gain combining. The following section discusses the diversity combining techniques used in this thesis.

4.3.1 Selection Combining

Selection combining operates using two or more uncorrelated diversity branches. The method relies on selecting the *best* of the available diversity branches. The *best* branch is usually defined as the strongest branch at any given instant. The concept of selection diversity based on two input branches is shown in figure 4.4.

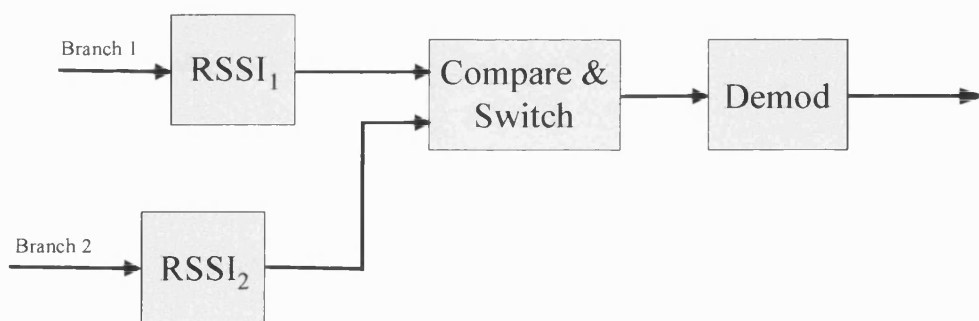


Figure 4.4: Selection combining of two uncorrelated branches

When implementing selection diversity, it is common to base the branch selection on the Received Signal Strength Indication (RSSI), which is a measure of the signal strength over a short time window. Selection diversity is also commonly known as switched diversity, since the strongest branch is switched to the detection device.

It should be noted that selection combining can also be used with transmit diversity schemes, in this approach the transmitting diversity branch is chosen to generate the

best received signal. As discussed in section 4.2.1, this requires the additional complexity of a return path to send back the RSSI information to the transmitting unit.

The movement of the mobile receiver through a multipath environment introduces rapid and extreme amplitude and phase distortions at the receiver. The mean signal strength per branch is calculated from an average over several tens of wavelengths and hence the rapid multipath effects are removed. The local mean signal is generally observed to obey a log-normal distribution as a function of receiver location, and the variance of the distribution is shown to depend on the general physical parameters of the environment.

4.3.2 Equal Gain Combining

In section 4.3.1, selection combining was introduced. Having selected a given branch, the energy associated with all the unselected branches is effectively lost in the detection process. This obviously results in a sub-optimal (i.e. wasted signal) solution. In equal gain combining, rather than choosing a single branch for detection, all the available diversity branches are summed to form a single signal for detection [1].

Two different forms of equal gain combining are considered in this thesis, namely amplitude and vector combining. The two techniques are discussed in the following sections.

4.3.2.1 Amplitude Summation

In this method, the amplitude of each diversity branch is simply summed to form a single diversity output. This process is shown mathematically in equation 4.1, where $|\cdot|$ represents the modulus process, m the message signal, and a and b the fading vectors of branches 1 and 2 respectively.

$$V = m \cdot |a| + m \cdot |b| \quad (\text{volts}) \quad (4.1)$$

In practice, the fading experienced per branch is a complex quantity made up of amplitude and phase. Given that equation 4.1 operates on the modulus of the fast fading component, a method must be found to remove the phase of the fast fading channel. The signal cannot be simply squared since this will remove the complex modulation of the message signal. In practice, amplitude summation is achieved

using a process known as cophasing. Cophasing aims to make the phase of a and b identical, thus enabling the signals to be summed as a modulus. The cophasing process requires the phase of each channel to be estimated prior to combining. Given that the channel phase is known, each branch can be multiplied by its unity gain conjugate to remove the channel phase component [1][4]. The method is therefore more complex than selection diversity and requires accurate channel estimation, which increases the cost of the combiner. Figure 4.5 shows the block diagram of an equal gain diversity combiner using amplitude selection.

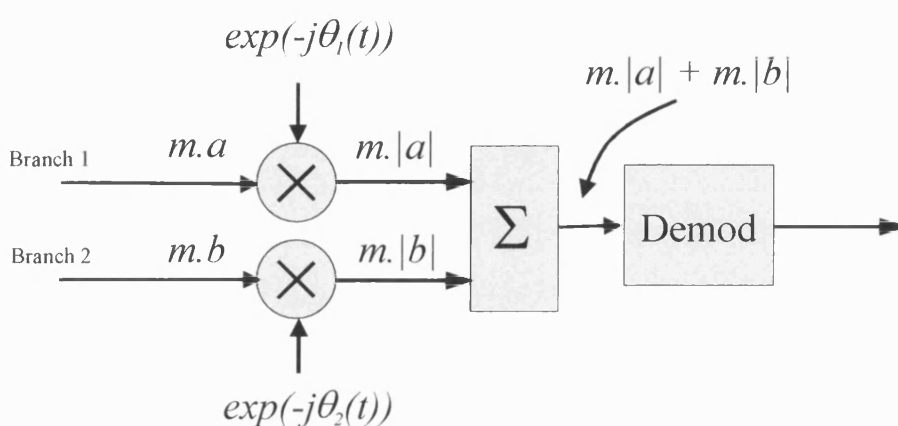


Figure 4.5: Equal Gain Combining: Amplitude Summation

Equal gain combining gets its name since each branch is summed with an equal gain, i.e. there is no bias towards a given branch. Mathematically it can be shown that the signal to noise ratio after combining is optimised if each branch is summed with a weight proportional to its signal to noise ratio [1][3]. This form of combining is known as maximal ratio combining, and is not considered further in this thesis due to its increased complexity and marginal gain over equal gain combining.

4.3.2.2 Vector Summation

In the previous section channel estimation was required to cophase the diversity signal prior to summation. The vector summation equal gain combiner simply sums the diversity vectors directly, without applying the cophasing process. Mathematically, the combined signal is described by equation 4.2.

$$v = m.a + m.b \quad (4.2)$$

While vector combining is a simpler method, the approach suffers from possible destructive combining of the branches. In some circumstances, the phase of the diversity branches can be in antiphase and their vector sum can result in an output signal smaller than any one of the input signals. Hence, unlike amplitude summation where the output will always be stronger than any of the inputs, in the vector summation case the combiner will not always produce a gain.

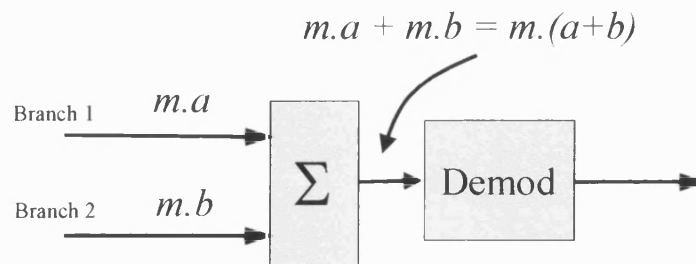


Figure 4.6: Equal Gain Combining: Vector Summation

The simpler block diagram for equal gain combining vector summation is shown in figure 4.6 [1]. Given the limitations of vector combining, the more complex amplitude summation approach is more commonly used. Results for both methods in an indoor environment are given in section 4.7.

4.4 Introduction to Frequency Diversity

The ray-tracing model described previously is used to generate a number of frequency diversity branches. Six branches are simulated in the 11GHz band with the frequency spacing between adjacent branches set at 1-100 MHz. For various branch combinations, two signals are then combined using one of three diversity combining techniques. Field strength improvement results are then produced as a function of a two branch frequency spacing and diversity combining strategy [14][21].

4.4.1 Single Branch Normalised Field Strength Results

In this section field strength grid plots and diversity combining results are given for various two-branch frequency separations and combining techniques. All results are generated for the same indoor environment.

Parameter	Value
Number of grid points in X and Y co-ordinate	50, 25
Room Width and Length	10m, 5m
Grid point spacing in x and y	0.2m, 0.2m
Transmitter co-ordinates	0.845m, 1.235m
Ray Tracing Launch Angles, Step Angles	0.1-359.9 , 0.5 degrees
Ray Tracing Cut off level	-55 dB
Frequency	11.0 GHz
Number of cells	1250

Table 4.1: Ray Tracing Simulation Parameters

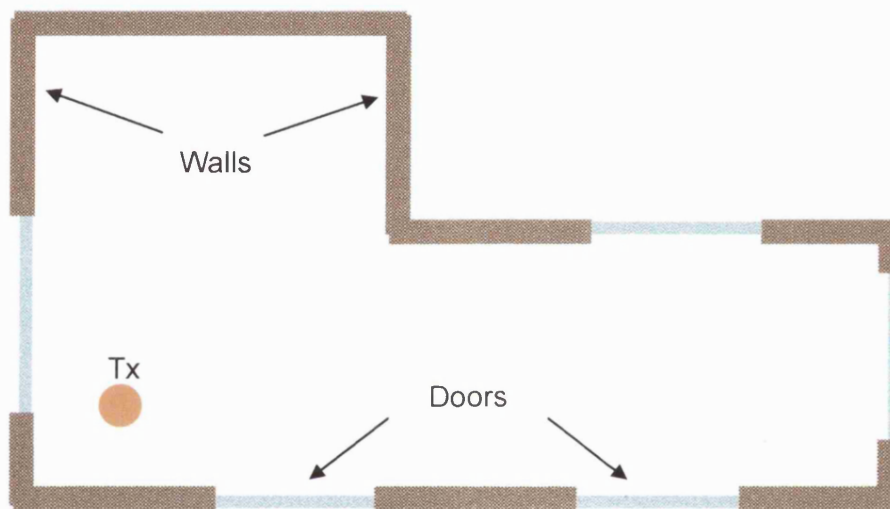


Figure 4.7: Plan of an indoor environment

For each simulation the transmitter is located in the bottom left-hand corner of the environment as illustrated in figure 4.7. A detailed set of simulation settings is given in table 4.1.

Nine simulated field strength grids were calculated at various centre frequencies as potential inputs into one of three diversity combining algorithms. Simulated results were generated at each of the centre frequencies defined in table 4.2.

Branch	Frequency (GHz)
1	11.00
2	11.001
3	11.01
4	11.05
5	11.10
6	11.20
7	11.30
8	11.40
9	11.50

Table 4.2: Diversity Branch Centre Frequencies

Figures 4.8 and 4.9 show the normalised field strength in 2-D and 3-D respectively for the first diversity branch at a simulated centre frequency of 11.0 GHz.

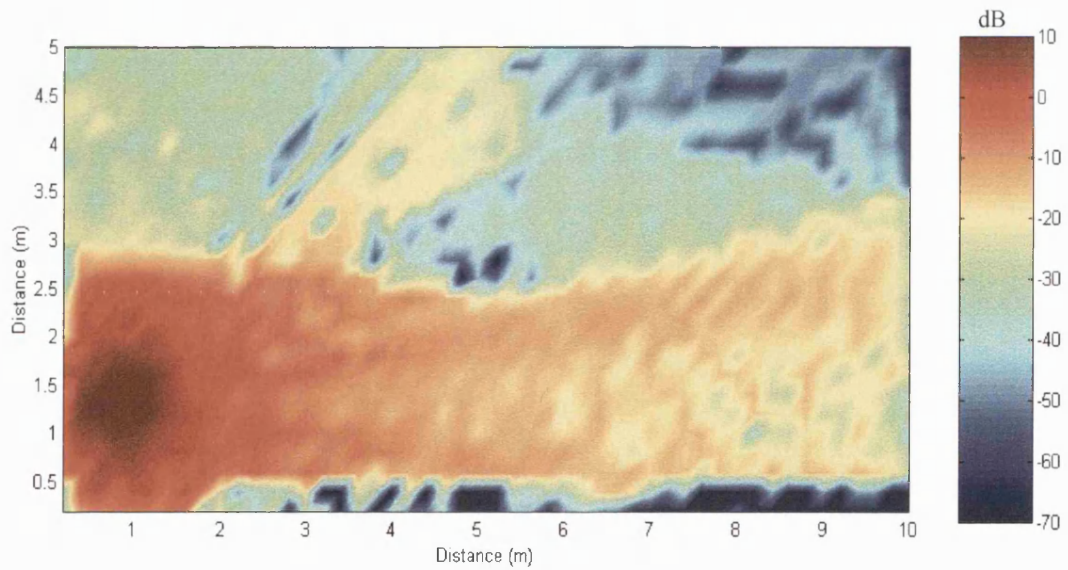


Figure 4.8: Normalised Field Strength for Branch 1(11.0 GHz) in 2-D plot

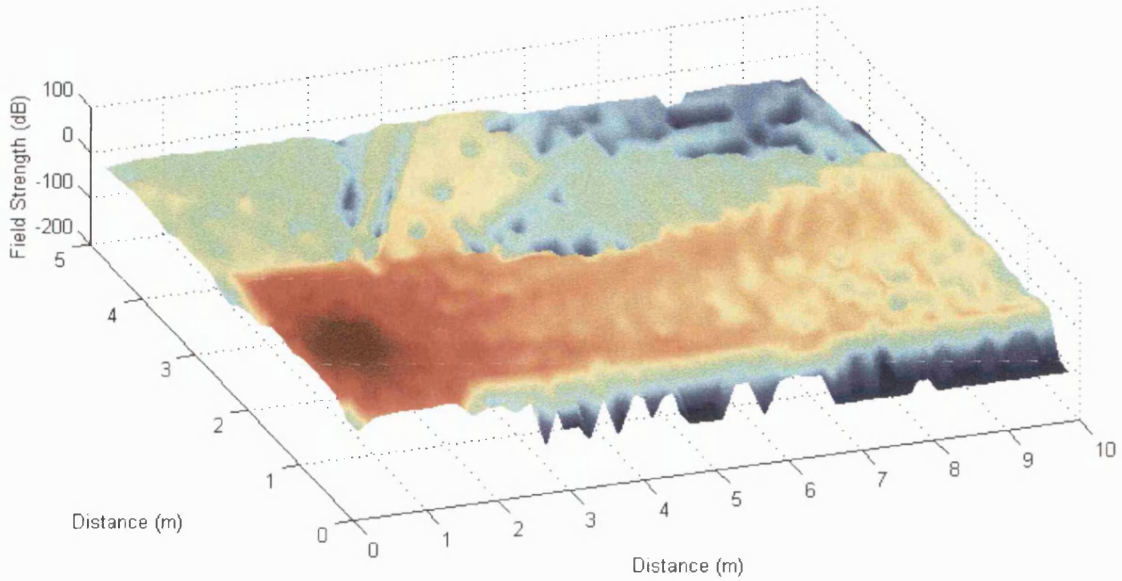


Figure 4.9: Normalised Field Strength for Branch 1 (11.0 GHz) in 3-D plot

High field strengths surrounding the transmitter are observed, however these fall rapidly with losses of 60-80dB on the far side of the test environment. Table 4.3 summarises the main numeric results.

Branch	Average (dB)	Mean (linear)	Variance	Standard deviation
1	-11.90	0.245	0.321	0.567
2	-11.91	0.245	0.322	0.567
3	-11.93	0.244	0.321	0.567
4	-12.22	0.236	0.307	0.554
5	-12.06	0.240	0.299	0.547
6	-11.50	0.256	0.329	0.574
7	-12.14	0.238	0.307	0.554
8	-11.66	0.252	0.325	0.572
9	-11.59	0.254	0.323	0.569

Table 4.3: Field Strength Summary: Frequency Diversity Branches 1-9

4.4.2 Frequency Diversity Combining

In order to produce the various diversity combining results shown in this subsection, branch 1 was chosen together with any one of the remaining four branches. By taking each of the four branches in turn, diversity gain as a function of frequency spacing could be determined [4][22]. A frequency spacing of 1-500 MHz between branches was chosen based on the expected values of RMS delay spread (5-10ns) and coherence bandwidth (1-500 MHz) for the single floor indoor environment.

For the following sections, frequency diversity combining was performed using each of the three techniques described in section 4.3. The first technique is referred to as Equal Gain Amplitude Combining (EG-AC), the second as Equal Gain Vector Combining (EG-VC) and the third as Switched Combining (SC).

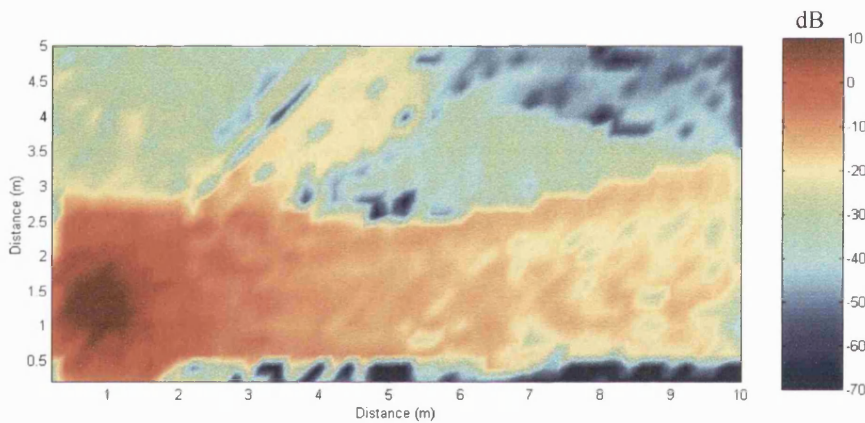


Figure 4.10: Normalised Field Strength for Branch 2(11.1 GHz)

While direct observations from the grid plot are difficult to achieve, it is obvious that generally lower received field strengths are achieved. For a more detailed understanding of the gains achieved, the statistical Cumulative Distribution Function (CDF) of the field strength can be generated. The mean, standard deviation and variance of the field strength before and after combining can also be used to determine diversity gain. In figure 4.11 below, the resulting field grid at the output of the SC combiner is shown for a diversity frequency spacing of 100 MHz (i.e. branches 1 and 5).

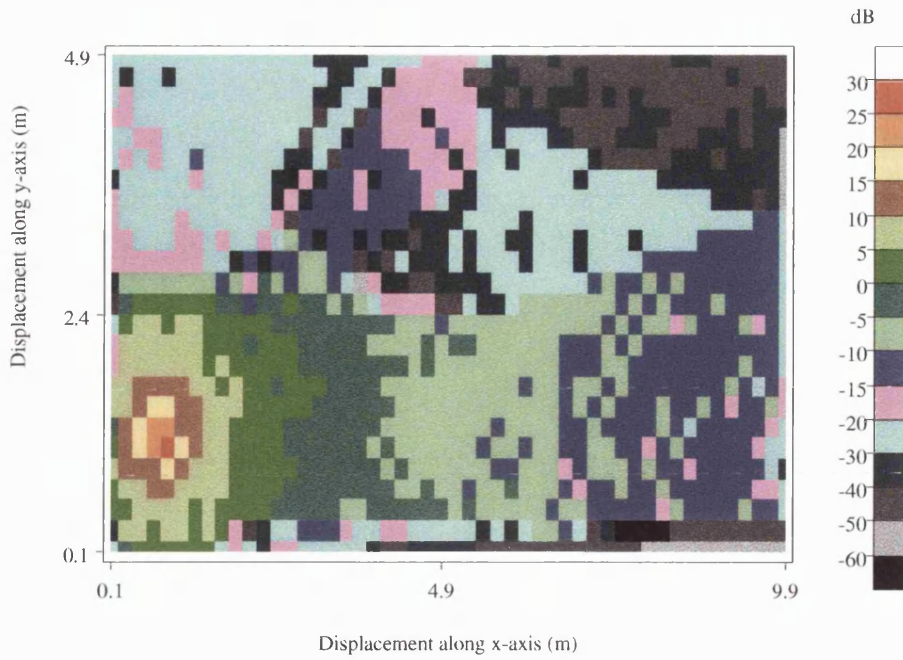


Figure 4.11: Diversity Gain Field Grid for EG-AC ($\Delta f = 100\text{MHz}$)

Rather than plotting the field strength at the output of the diversity combiner, it is more common to plot the diversity gain defined as the signal strength after combining divided by the signal strength of one of the branches before combining. This value is normally quoted as a dB ratio, as in figure 4.12 below for the EG-AC diversity case previously plotted in figure 4.11. In this figure the gain is quoted relative to branch 1.

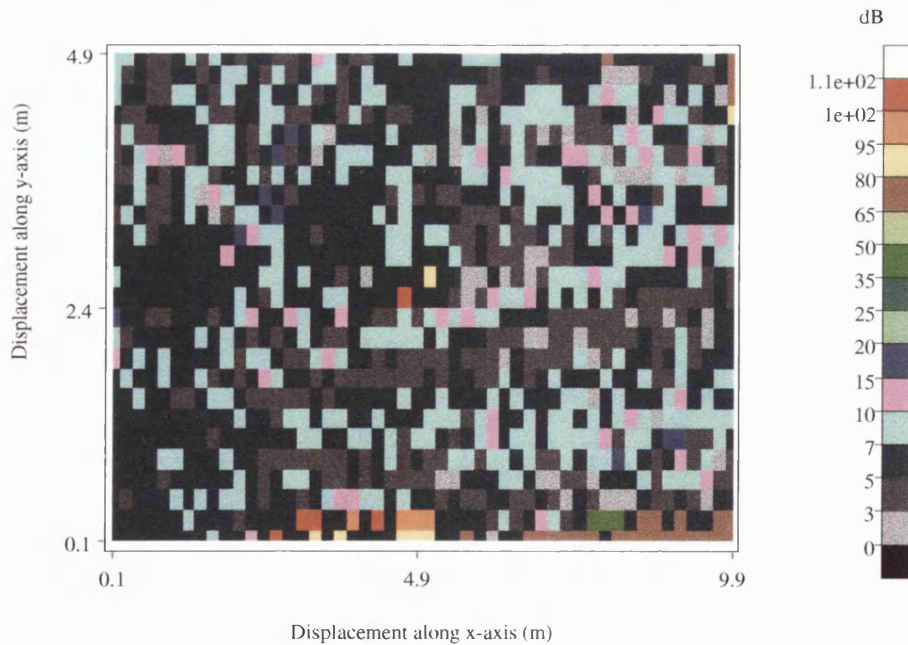


Figure 4.12: Diversity Gain relative to branch 1 for EG-AC ($\Delta f = 100\text{MHz}$)

Figure 4.13 shows the diversity gain obtained from branches 1 and 5 (relative to branch 1) using the EG-VC combining technique.

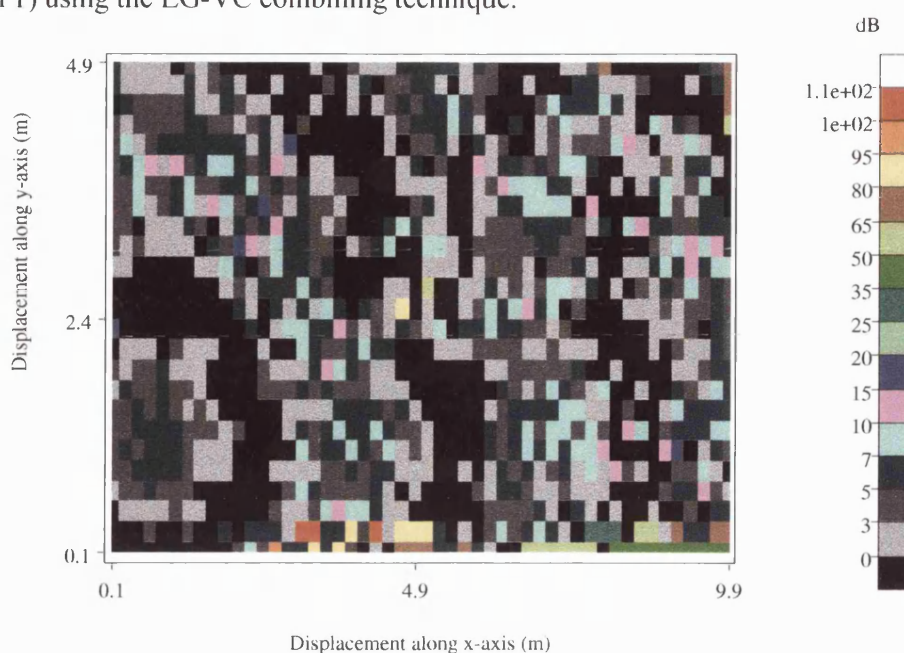


Figure 4.13: Diversity Gain relative to branch 1 for EG-VC ($\Delta f = 100\text{MHz}$)

Figure 4.13 demonstrates the main drawback of the EG-VC technique. When the two diversity signals are summed as vectors, it is possible for the signals to add constructively or destructively, depending on their relative phase. Unlike the EG-AC method, where the two signals are cophased before adding, in the EG-VC nulls can occur in the combiner output. Studying figure 4.13, these diversity nulls can clearly be seen spreading out across the environment. Hence, in many locations the output of the diversity combiner is actually worse than either of the two input signals.

Finally, figure 4.14 shows the diversity gain obtained from branches 1 and 5 (relative to branch 1) using the SC combining technique. Since gain is plotted relative to branch 1, no gain is seen when branch 1 is selected. A fairer diversity gain can be calculated by quoting the gain relative to the mean of branch 1 and branch 5 at each point.

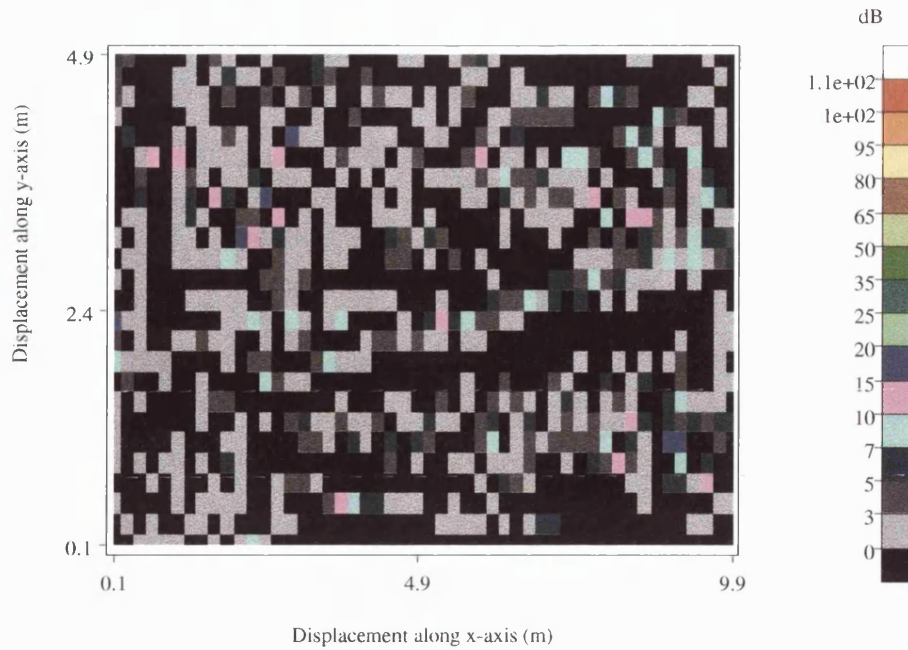


Figure 4.14: Diversity Gain relative to branch 1 for SC ($\Delta f = 100\text{MHz}$)

4.4.2.1 Comparison of EG-AC, EG-VC and SC results

Studying figures 4.12, 4.13 and 4.14 it can be seen that the EG-AC diversity technique generates the strongest field strengths and largest diversity gains. The EG-VC solution suffers from output nulls from the diversity combiner and would thus generate extremely poor performance in practice. The SC method is not as strong as the EG-AC approach, however the method is simpler and therefore cheaper to implement in most cases.

4.4.2.2 Detailed Combining Analysis: Branches 1 and 5

Table 4.4 shows the detailed field strength and diversity gain results for each of the three combining techniques using branches 1 and 5 as the input. An average gain of 6.54 dB (relative to branch 1) and 6.84 dB (relative to branch 5) was achieved using EG-AC. EG-VC showed an average gain in the region of 3 dB (see appendix A for other frequency separations); however a minimum value of -43.1 dB was observed when the branch inputs destructively combined. The SC technique achieved a gain in the region of 2 to 2.5 dB. Since gain is relative to branch 1 or branch 2, when this particular branch is selected then no gain is seen (hence, unlike the EG scheme the minimum gain is zero).

Method	Field Strength	Gain Relative to Branch 1	Gain Relative to Branch 5
EG-AC	-6.26	6.54	6.84
EG-VC	-9.43	3.06	3.50
SC	-11.04	1.98	2.45

Table 4.4: Field Strength and Combining Gains in dB for Frequency Diversity ($\Delta f = 100\text{MHz}$)

Table 4.5 shows the mean, maximum and minimum field strength values for frequency diversity with a spacing of 100 MHz. These results should be compared with table 4.3 for each of the individual branches. In all cases, improvements with diversity combining are observed. The final column in table 4.5 shows the number of points (out of 1250) where the diversity field strength is lower than either of the two input branches. For EG-AC this cannot occur, hence the number is zero. For the EG-VC solution, regular destructive combination results in 534 lowered output field strength samples. Using SC, the best signal should always be selected and the 80 samples reported are thought to arise due to problems with numeric accuracy in the 'less than or equal to' test within the code.

Method	Average	No Pts DIV < Branch 1 or 5
EG-AC	0.486	0
EG-VC	0.336	534
SC	0.270	80

Table 4.5: Mean, Maximum and Minimum field strength for Frequency Diversity ($\Delta f = 100\text{MHz}$)

For detailed combining analysis of branches 1 and 6-9 ($\Delta f = 200\text{MHz}-500\text{MHz}$) see appendix B.

4.4.3 Diversity Gain versus Frequency Separation

The numeric frequency diversity results given in sections 4.4.1 and 4.4.2 can be summarised using diversity gain versus frequency separation graphs for each of the three methods considered.

Figure 4.15 below shows the average diversity gain relative to branch 1 for each combining method in the indoor environment considered. EG-AC shows the highest gains (around 6.5 dB), as discussed in section 4.4.2. The gains are flat as a function of frequency, and this implies that the initial frequency separation of 100 MHz is large enough to completely decorrelate the input signals. The EG-VC method offers a gain in the region of 3 dB relative to branch 1. This drop of around 3dB relative to EG-AC is to be expected when vector combining is used. It is well known that the average power using coherent combining is the square of the sum of the input signals. Assuming the input branches have unity power, after coherent summation the power will increase by 6dB, as seen in the EG-AC case. However, for incoherent combining, the power is given as the sums of the squares, i.e. the power of the two branches merely add, resulting in a 3dB increase. The results obtained are in close agreement with these theoretical values.

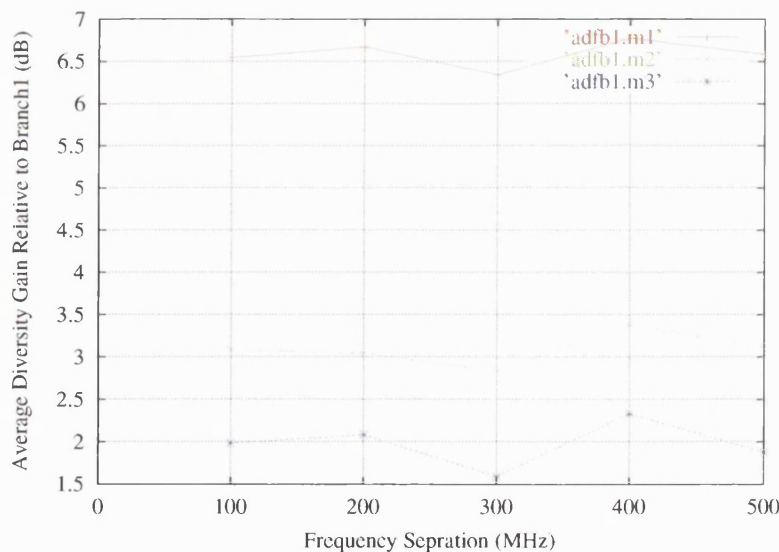


Figure 4.15: Average Diversity Gain vs Frequency Separation (relative to Branch 1)

The SC technique results in an average gain in the region of 2 to 2.5 dB, around 1 dB lower than EG-VC and 4 dB lower than EG-AC. Although the average gain is lower than EG-VC, as seen from table 4.7, the minimum signal value is far superior. This implies in a practical system, EG-AC would be preferred in terms of diversity performance, followed by SC and then EG-VC.

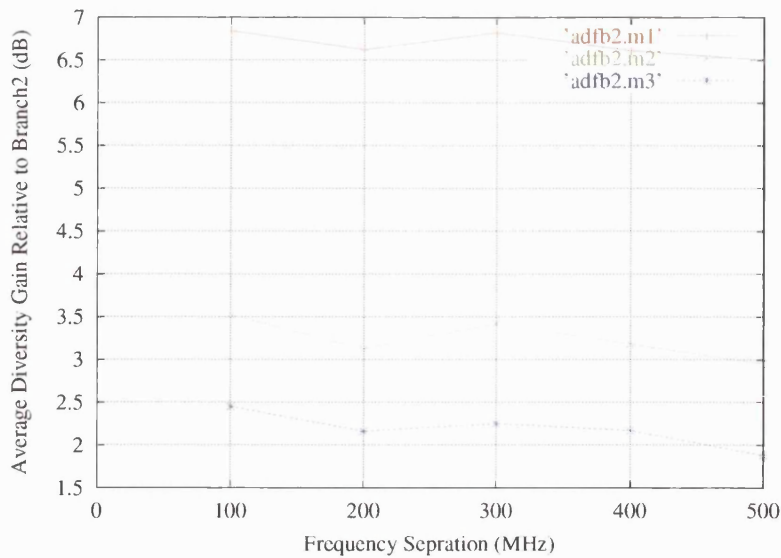


Figure 4.16: Average Diversity vs Frequency Separation (relative to Branch5)

To ensure that there was no bias in the simulation results or conclusions, the diversity gain results are now plotted relative to branch 2. Figure 4.16 shows that the absolute and relative gains are almost identical to the previous case, as would be expected for equal mean power input diversity signals.

4.4.4 Frequency Diversity CDF Results

To complete the analysis of the frequency diversity generation and combining strategies considered in the thesis, a set of diversity cumulative distribution function (CDF) results are plotted for the received field strength. A CDF plot can be used to determine the distribution of field strength in the indoor environment. More specifically, the data provides the probability of the field strength falling below a particular level. By defining an acceptable outage probability, an alternative measure of diversity gain can be generated. The outage probability can be obtained from the coverage requirements of the system. For example, assuming 95% coverage criteria, the outage probability would be 5%.

4.4.4.1 Comparison of Combining Strategies

Figure 4.17 shows the field strength CDF for branch 1 (generated at 11.0 GHz), branch 2 (generated at 11.1 GHz) and the combined output (using the EG-AC method,). The 50% CDF points results in a value of around -22.5 dB for branches 1

and 2 and -15 dB for the diversity output. Based on this probability (0.5), a field strength gain (relative to a single branch) of 7.5 dB is observed. This value is very similar to the gains reported in section 4.4.3. Assuming field strength in excess of -50 dB is required to ensure system operation for example, it can be seen the branch 1 and branch 2 signals would fail for around 8% of locations. However, using the EG-AC method, the resulting signal would fail for just 1-2% of locations. This last result demonstrates the significance of diversity combining in a radio system.

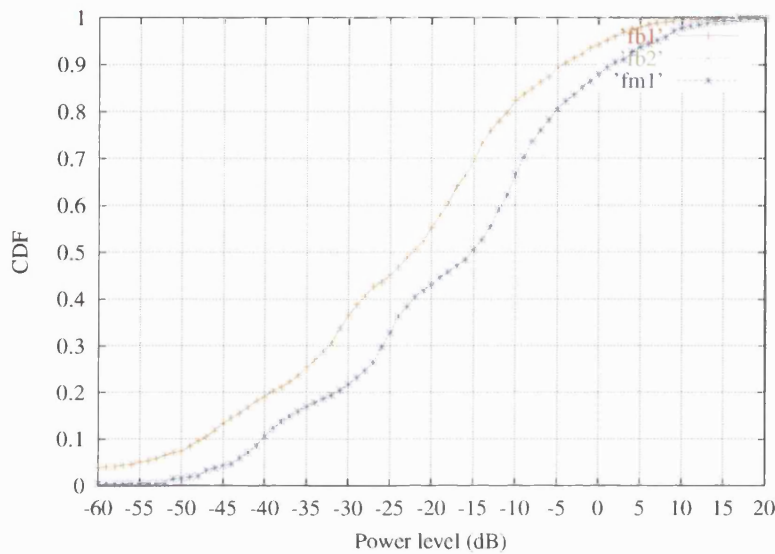


Figure 4.17: branch1 (11.0 GHz), branch 5 (11.1GHz) and Diversity (EG-AC) CDF

Figure 4.18 shows a similar CDF plot for the EG-VC technique assuming a 100 MHz separation in frequency diversity branch signals.

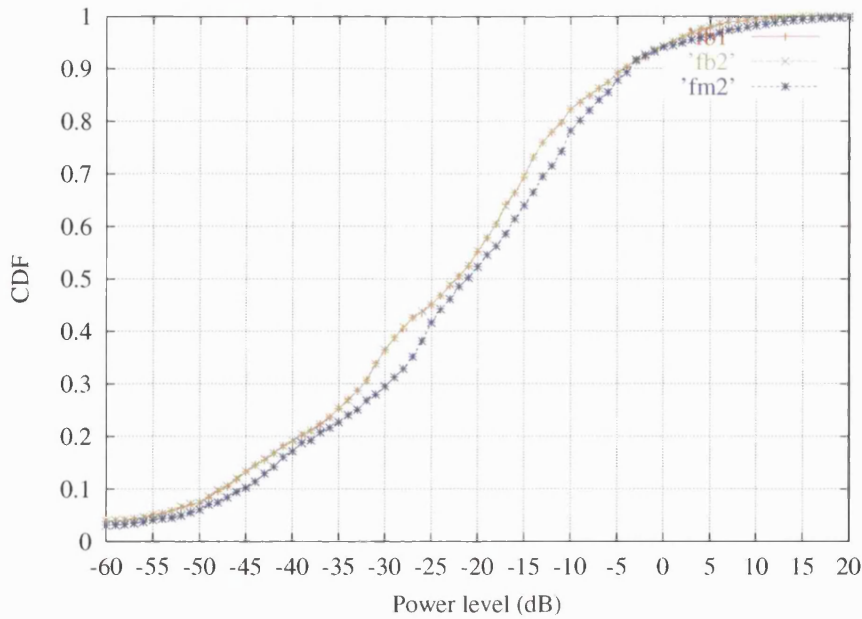


Figure 4.18: branch1 (11.0 GHz), branch 2 (11.1GHz) and Diversity (EG-VC) CDF

As expected from section 4.4.3, since the use of EG-VC results in a lower gain, the diversity combining CDF is now far closer to those of branches 1 and 2. At a threshold of -50 dB, failure would now be reduced from 8% to just 6%, a significant reduction in performance.

Figure 4.19 shows the CDF for the switched combining strategy. Here the lowest level of diversity gain is seen.

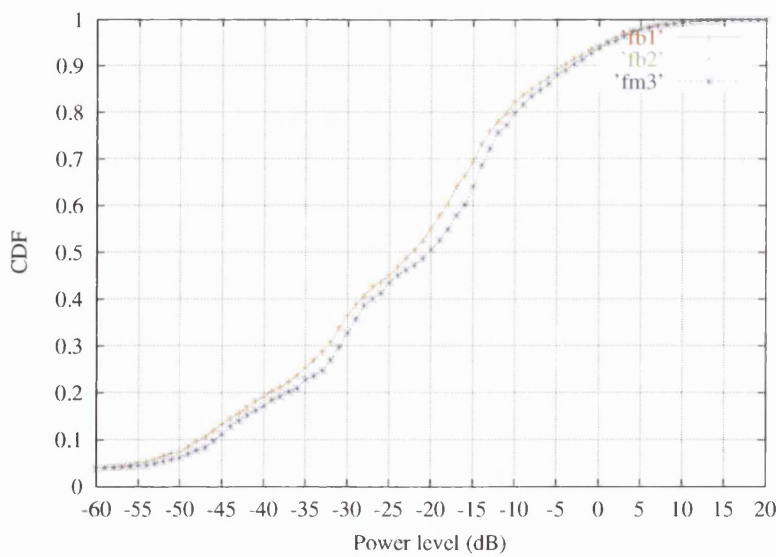


Figure 4.19: branch1 (11.0 GHz), branch 2 (11.1GHz) and Diversity (SC) CDF

As a final comparison, figure 4.20 shows the CDF of the three diversity combining strategies plotted on the same graph.

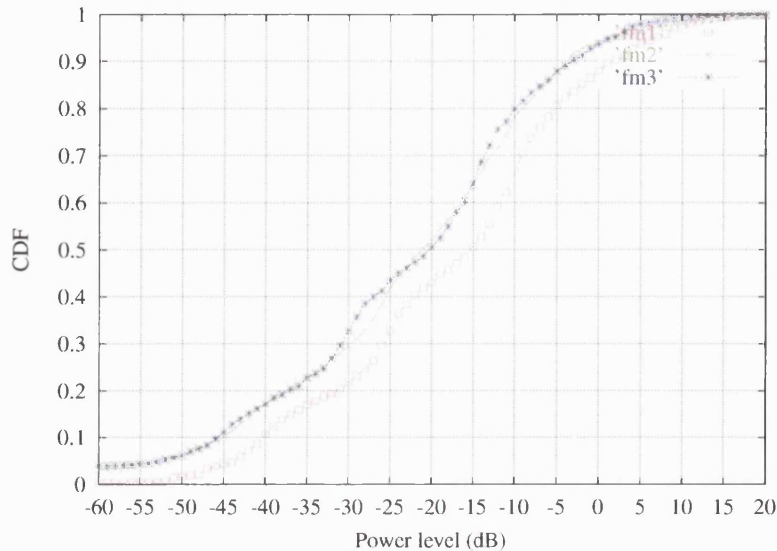


Figure 4.20: Field Strength CDF for each of the three combining methods ($\Delta f = 100\text{MHz}$)

Frequency separations ranging from 1 MHz to 500 MHz were considered, with diversity gain shown to increase for larger frequency spacings. For spacings well beyond the coherence bandwidth, no further significant diversity gain was observed.

While frequency diversity gains were impressive (assuming spacings beyond the channel coherence bandwidth), the method is not spectrally efficient since at least twice the operating bandwidth is required. Hence, given the importance of spectrum efficiency, frequency diversity is not likely to be viable for most indoor applications.

4.5 Introduction to Polarization Diversity

This part of the chapter presents indoor diversity results obtained using polarisation diversity. The same indoor environment as used in section 4.4 to study frequency diversity is applied. Polarisation diversity gain is studied as a function of two centre frequencies and the impact of the Cut Off Power (COP) with the ray tracing model is also investigated.

4.5.1 Polarisation Setup and Simulation Strategy

The polarisation simulations were performed using the parameters shown in table 4.6. Polarisation can be set to a value of 1 (vertical polarisation) or 0 (horizontal polarisation) [4][22]. Field strength prediction plots were produced for a fixed transmitter using both settings. The resulting diversity signals were then combined using EG-AC, EG-VC and SC techniques.

Parameter	Value
Number of grid points in X and Y	50, 25
Room Width and Length	10m, 5m
Grid point spacing in x and y	0.2m, 0.2m
Transmitter co-ordinates	0.7643m, 1.2357m
Ray Tracing Launch Angles – Step Angles	0.1, 359.9 - 0.5 degrees
Ray Tracing Cut off level	-55 dB or -155dB
Frequency	11.0 GHz
Polarisation	1 or 0
Number of grid points	1250

Table 4.6: Ray Tracing Simulation Parameters

The Cut Off Power (COP) is used within the software to prevent the onward launching of rays considered too weak for further interaction. The parameter allows a trade off between computing time and accuracy. Results are generated at the standard COP of -55 dB (normalised field strength) and a second value of -155 dB, where even extremely weak rays continue to propagate in the environment.

Six simulated field strength grids were calculated and these can be split into three different groups. The first group, referred to as group 1, produces branch 1 and branch 2 field strength outputs using vertical and horizontal polarisation settings respectively. A carrier centre frequency of 11.0 GHz was used (as with the frequency diversity results) together with a COP of -55 dB.

The second group of results was performed using a higher centre frequency for both branches. These results were produced to compare the performance of polarisation diversity at a higher frequency. A value of the 17 GHz was chosen for the second group of results.

In the third group of results as shown in table 4.7, the cut off power level was reduced to -155 dB (normalised field strength) to increase the ray launching sensitivity in the model. The results were produced to compare with earlier data generated from group one. For this final result of data, a centre frequency of 11.0 GHz was used [4][22].

Group	Branch 1			Branch 2		
No.	Freq (GHz)	COP (dB)	Pol	Freq (GHz)	COP (dB)	Pol
1	11.0	-55	Para.	11.0	-55	Perp.
2	17.0	-55	Para.	17.0	-55	Perp.
3	11.0	-155	Para.	11.0	-155	Perp.

Table 4.7: Simulation Summary and Group Definitions

4.5.2 Polarisation Results: Group 1

Figures 4.8 and 4.20 show the normalised field strength grid plots for vertical and horizontal polarisation respectively.

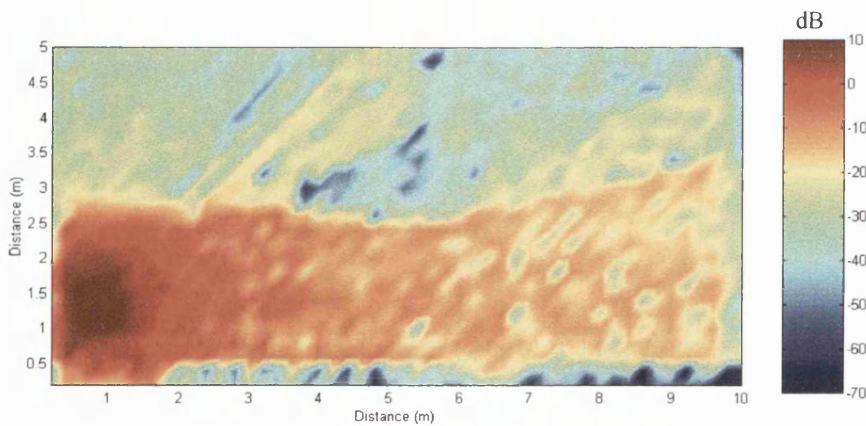


Figure 4.21: Normalised Field Strength Grid – Branch 2 (Horizontal Polarisation, Group 1)

Studying figure 4.21 clear differences in the field strength predictions can be seen. While predictions do not differ in terms of over all mean power at a given location, the fast fading effects are uncorrelated between the vertical and horizontal polarisations. Hence peaks and nulls occur at different spatial locations and the probability of encountering a weaker signal can be lowered via suitable combining. Table 4.8 below summarises the field strength values for the two group 1 branches. The statistical mean and variance are similar for both polarisations.

Branch	Average (dB)	Mean (Linear)	Standard Deviation	Variance
1	-11.90	0.245	0.321	0.567
2	-11.66	0.259	0.324	0.569

Table 4.8: Field Strength Summary: Polarisation Diversity Group 1

4.5.2.1 Diversity Combining: Group 1 (Polarisation Signals)

As in the previous diversity studies, three combining techniques have been considered. Two are based on equal gain combining (EG-AC and EG-VC) with the third using switched diversity (SC).

Diversity	Average (dB)	Mean (Linear)	Standard Deviation	Variance
EG-AC	-5.95	0.504	1.258	1.122
EG-VC	-6.30	0.484	1.240	1.114
SC	-10.54	0.297	0.369	0.608

Table 4.9: Diversity Combining Field Strength Summary: Polarisation Group 1

Table 4.9 lists the statistical values of the field strength *after* diversity combining using each of the three specified methods. For the equal gain techniques, the average and maximum value of field strength has increased by around 6 dB. Using SC, an increase of just 1 dB is seen in these values.

Table 4.10 shows the diversity gain (relative to branch 1 and branch 2) for each of the three diversity combining techniques. An average improvement in the range 6.2 – 9.3

dB is seen for the EG methods, while a gain of 3.9 - 6.3 dB is achieved using the SC approach.

Method of Diversity Improvement	Relative to Branch 1 (dB)	Relative to Branch 2 (dB)
EG-AC	9.29	7.28
EG-VC	8.28	6.25
SC	6.29	3.88

Table 4.10: Polarisation Diversity Gain versus Combining Technique – Group 1

4.5.2.2 Diversity Combining: Group 2 (higher centre frequency)

In this section the branch and combining results for polarisation diversity at a higher centre frequency of 17 GHz are considered. Table 4.11 summarises the field strength values for the two group 2 branches.

Branch	Average (dB)	Mean (Linear)	Standard Deviation	Variance
1	-11.51	0.256	0.315	0.561
2	-11.90	0.252	0.321	0.567

Table 4.11: Field Strength Summary: Polarisation Diversity Group 2

Table 4.12 lists the statistical values of the field strength *after* diversity combining using each of the three specified methods. Once again, for the equal gain techniques, the average and maximum value of field strength has increased by around 6 dB. Using SC, an approximate 1 dB rise is seen.

Diversity	Average (dB)	Mean (Linear)	Standard Deviation	Variance
EG-AC	-5.87	0.509	1.239	1.113
EG-VC	-6.22	0.489	1.219	1.104
SC	-10.46	0.300	0.368	0.606

Table 4.12: Diversity Combining Field Strength Summary: Polarisation Group 2

Table 4.13 shows the diversity gain (relative to branch 1 and branch 2 respectively) for each of the three diversity combining techniques. At this higher centre frequency an average improvement in the range 6.5 – 9.6 dB is seen for the EG methods, while a gain of 4.1 – 6.8 dB is achieved using the SC approach.

Method of Diversity Improvement	Relative to Branch 1 (dB)	Relative to Branch 2 (dB)
EG-AC	9.61	7.51
EG-VC	8.58	6.46
SC	6.80	4.12

Table 4.13: Polarisation Diversity Gain versus Combining Technique – Group 2

4.5.2.3 Diversity Combining: Group 3 (lower cut off level)

In this section the branch and combining results for polarisation diversity at a lower cut off level are considered. Table 4.14 summarises the field strength values for the group 3 branches.

Branch	Average (dB)	Mean (Linear)	Standard Deviation	Variance
1	-11.93	0.247	0.326	0.571
2	-11.61	0.258	0.325	0.570

Table 4.14: Field Strength Summary: Polarisation Diversity Group 2

Table 4.15 lists the statistical values of the field strength *after* diversity combining using each of the three specified methods with a COP of –155 dB.

Diversity	Average (dB)	Mean (Linear)	Standard Deviation	Variance
EG-AC	-5.81	0.505	1.268	1.126
EG-VC	-6.11	0.487	1.249	1.117
SC	-10.39	0.297	0.375	0.612

Table 4.15: Diversity Combining Field Strength Summary: Polarisation Group 2

Table 4.16 shows the diversity gain (relative to branch 1 and branch 2 respectively) for each of the three diversity combining techniques. At this higher centre frequency an average improvement in the range 5.7 – 9.2 dB is seen for the EG methods, while a gain of 2.9 – 7.2 dB is achieved using the SC approach.

Method of Diversity Improvement	Relative to Branch 1 (dB)	Relative to Branch 2 (dB)
EG-AC	9.92	6.79
EG-VC	9.02	5.73
SC	7.18	2.97

Table 4.16: Polarisation Diversity Gain versus Combining Technique – Group 2

4.5.3 Polarisation Diversity CDF Analysis

Figure 4.22 shows the field strength CDF for the first group of diversity combining results.

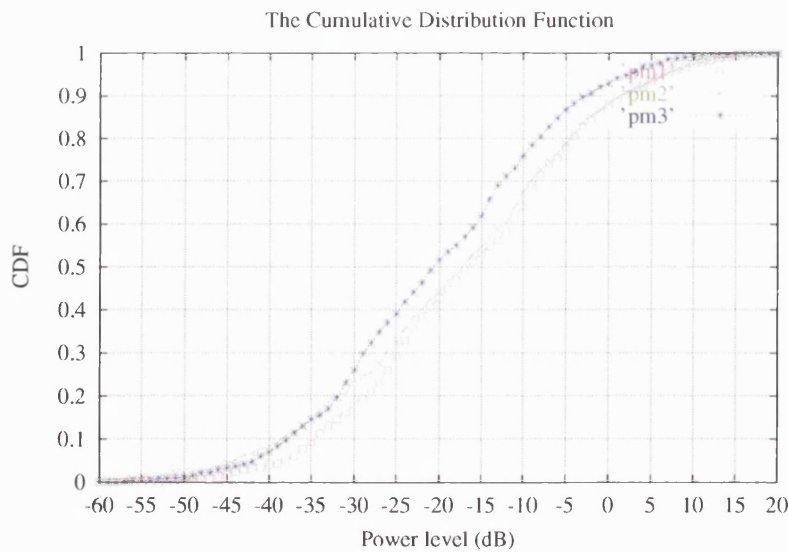


Figure 4.22: Polarisation Diversity for all three combining methods (Group 1)

Figures 4.23 and 4.24 show the field strength CDF for the second and third groups of polarisation diversity combining results respectively.

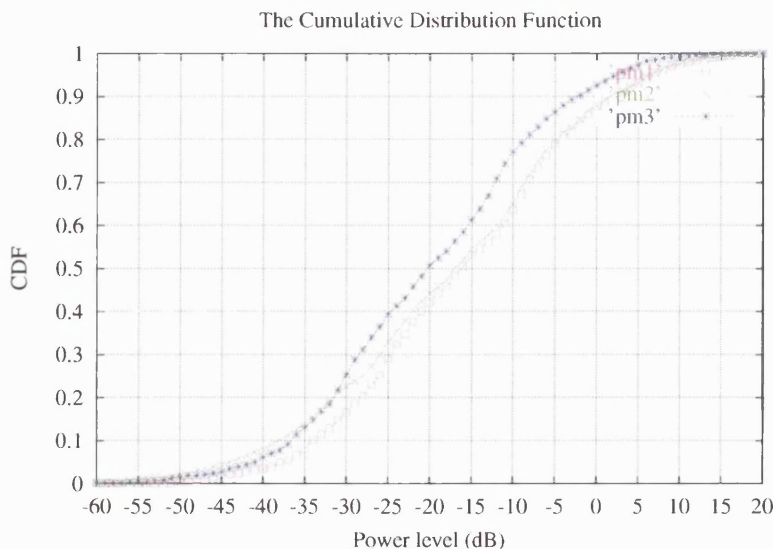


Figure 4.23: Polarisation Diversity for all three combining methods (Group 2)

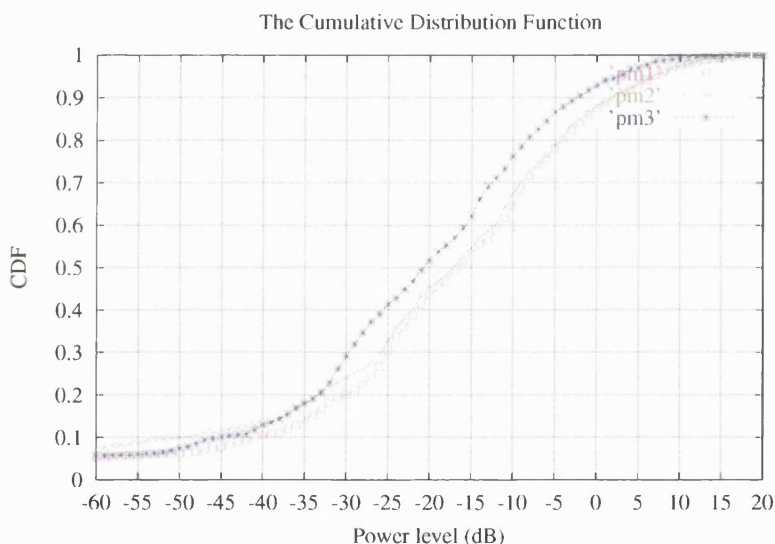


Figure 4.24: Polarisation Diversity for all three combining methods (Group 3)

As for frequency diversity, the EG-AC method yields the greatest gain, with values in the range of 8-10 dB being typical.

This section has explored the performance of polarisation diversity as a means to overcome the harmful effects of multipath. Field strength results for a single branch were provided together with an analysis of simulated polarisation diversity gain. Field strength predictions and diversity gain results were generated for each of the three diversity combining strategies defined in section 4.3.

Polarisation diversity has the major advantage of offering compact solutions (since spaced antennas are not required). This advantage is expected to be particularly important for hand-held portable terminals. While the frequency diversity gains (section 4.4) were impressive (assuming spacings beyond the channel coherence bandwidth), the method is not spectrally efficient since at least twice the operating bandwidth is required [23]. Results in this section have shown a diversity gain in excess of 9 dB (relative to branch 1) using the EG-AC technique. While this gain is amongst the highest seen in these diversity simulations, it should be remembered that the result is highly dependent on the fast fading correlation between simulated vertical and horizontal polarisations.

4.6 Introduction to Space Diversity

In this section two different methods of space diversity are considered: (i) receiver space diversity and (ii) transmitter space diversity [4][24]. The same indoor environment as used in sections 4.4 and 4.5 was applied. Predicted field strength grids using space transmitter and receiver diversity are generated for antenna spacings ranging from one quarter of a wavelength up to four wavelengths (3.5λ in Rx to prevent the receiver from leaving the test environment). Using the various combining schemes discussed in section 4.3, the diversity gain for the various techniques is evaluated as a function of antenna spacing.

4.6.1 Receiver Space Diversity

This subsection, presents indoor diversity combining results obtained using receiver space diversity. In this method, two spaced receivers [6] are used and the signals are combined using SC, EG-VC or EG-AC techniques (see section 4.3).

4.6.1.1 Receiver Spacing Setup and Simulation Strategy

The receiver space diversity simulations were performed using the parameters shown in Table 4.17. Space diversity was applied using two receiver antennas with spacing ranging from 0.25λ to 3.5λ ; 0.5λ spacings after 0.5λ ($0.25\lambda, 0.5\lambda, 1\lambda, \dots, 3.5\lambda$). Field strength prediction grids were produced for a single fixed transmitter antenna to each of the two receiving antennas. This was performed using two grid predictions,

with the co-ordinates of the second prediction grid offset by the required antenna spacing.

Parameter	Value
Number of grid points in X and Y	50, 25
Room Width and Length	10m, 5m
Grid point spacing in x and y	0.2m, 0.2m
Transmitter co-ordinates	0.764m, 1.236m
Ray Tracing Launch Angles	0.1, 359.9, 0.5 degrees
Ray Tracing Cut off level	-55 dB
Frequency	11 GHz
Antenna Spacing	$0.25\lambda - 3.5\lambda$.
Number of grid points	1250

Table 4.17: Ray Tracing Simulation Parameters

The resulting diversity signals were then combined using EG-AC, EG-VC and SC techniques. Nine simulated field strength patterns (Branch1 plus eight Branch2) were calculated and these are split into eight diversity groups (table 4.18). The first group, referred to as group 1, uses branch 1 and branch 2 field strength outputs, with a 0.25λ spacing between the two receiving antennas.

The second group of results was performed using 0.5λ spacings. All subsequent groups were produced with antenna spacings incremented by 0.5λ , resulting in the final group having an antenna spacing of 3.5λ . Care was taken to ensure that antenna pairs remain in the same room and that no grid wrap occurred (otherwise the receive antennas become located on different sides of the building). The results were processed to compare diversity gain as a function of combining technique and antenna spacing.

Group	Receiver Spacing
1	0.25λ
2	0.5λ
3	1.0λ
4	1.5λ
5	2.0λ
6	2.5λ
7	3.0λ
8	3.5λ

Table 4.18: Diversity Branch 2 Spacing: horizontal offset relative to branch 1

4.6.1.2 Receiver Space Diversity Results: Group 1

Figures 4.8 and 4.25 show the normalised field strength grid plots for branches 1 and 2 of group 1 (i.e. a receive antenna spacing of 0.25λ).

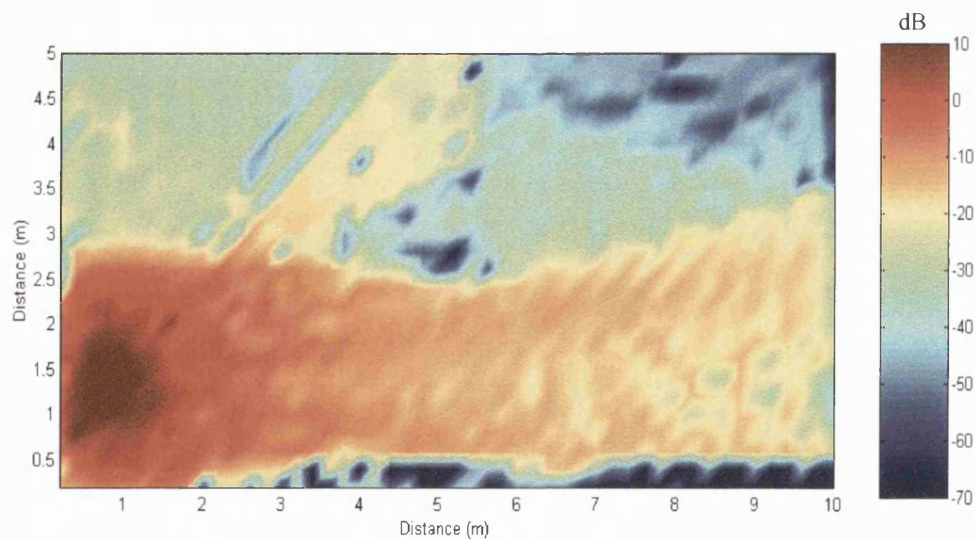


Figure 4.25: Normalised Field Strength - Branch 2 (0.5λ horizontal offset relative to Branch 1)

Figures 4.26 and 4.27 show the field strength and the relative improvement in the field strength grid when EG-AC combining is applied to the two branches. Comparing figure 4.26 with 4.25, the percentage of low field strength values (in

particular the areas (-40 to -60) mostly in the top right hand corner) can be seen to have reduced. Figure 4.27 confirms this observation by plotting the field strength improvement after EG-AC combining relative to branch 2.

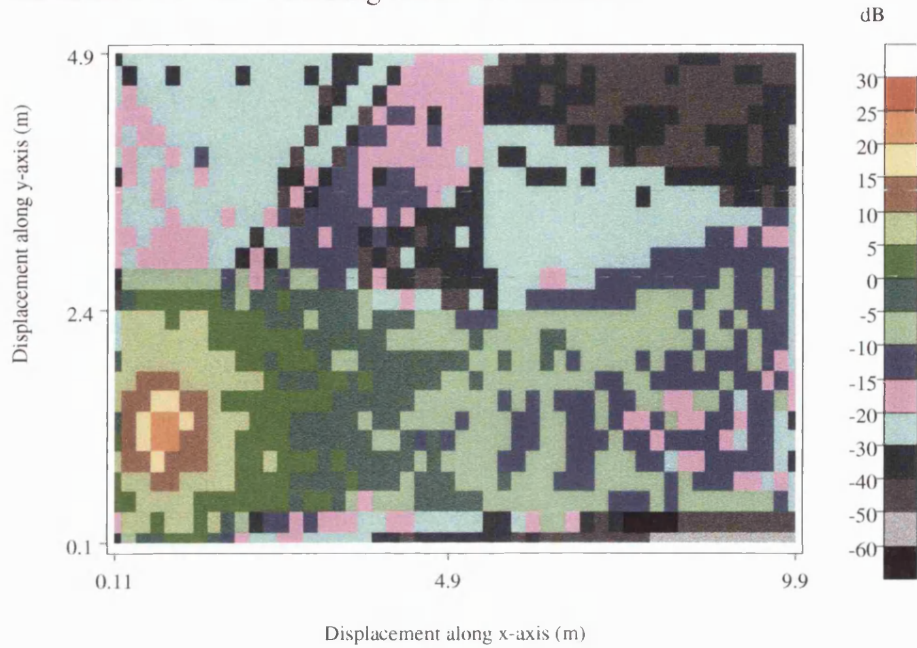


Figure 4.26: Receiver Space Diversity (EG-AC) Normalised Field Strength – Group 1

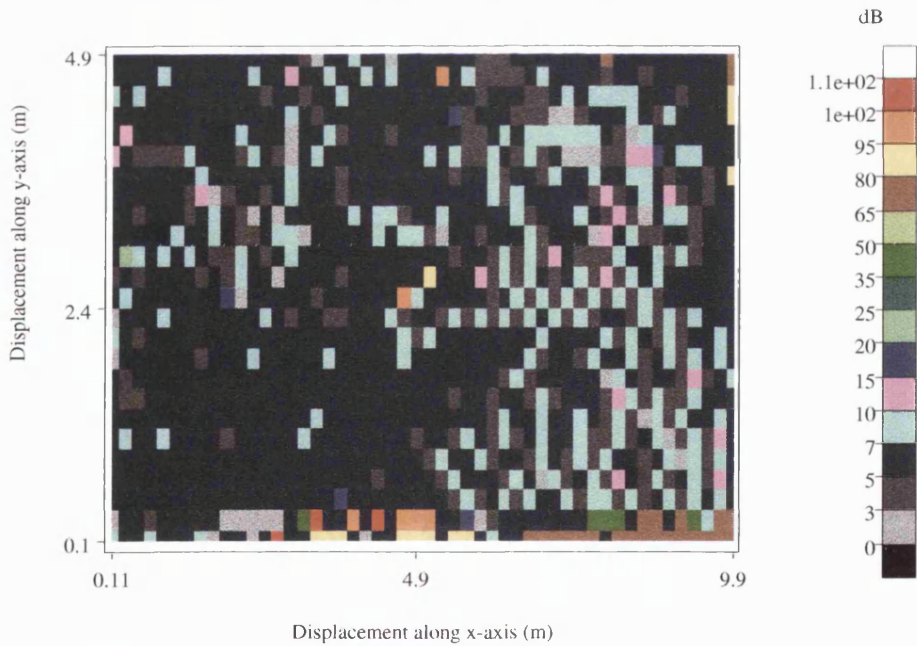


Figure 4.27: Receiver Space Diversity (EG-AC) - Diversity Gain relative to branch 2 ($\lambda 4$ spacing)

The relative field strength improvements for EG-VC and SC are shown in figures 4.28 and 4.29 respectively for group 1. The gain in figure 4.27 can be seen to be far lower than that shown in figure 4.28. In particular, a large region in the lower section of the environment suffers from poor diversity gain. While the gain for EG-VC is poor, as will be seen in section 4.27, the results oscillate depending on antenna separation distance. For antenna spacings of 0.5λ , 1.5λ , 2.5λ and 3.5λ the overall diversity gain is low. The diversity gain at 3.5λ is shown in figure 4.28 for EG-VC.

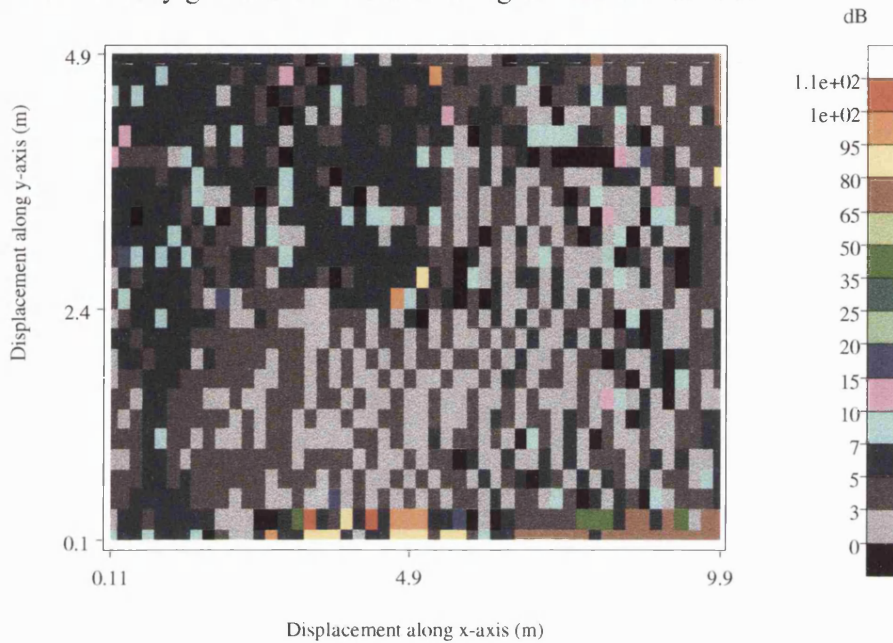


Figure 4.28: Receiver Space Diversity (EG-VC) - Diversity Gain relative to branch 2 ($\lambda/4$ spacing)

Figure 4.29 shows the diversity gain for SC. The figure shows many areas where effectively no diversity gain is offered. In those locations where gain is observed, this is still relatively low, in the region of 0-5 dB, with only a very small number of points seeing in excess of 5 dB.

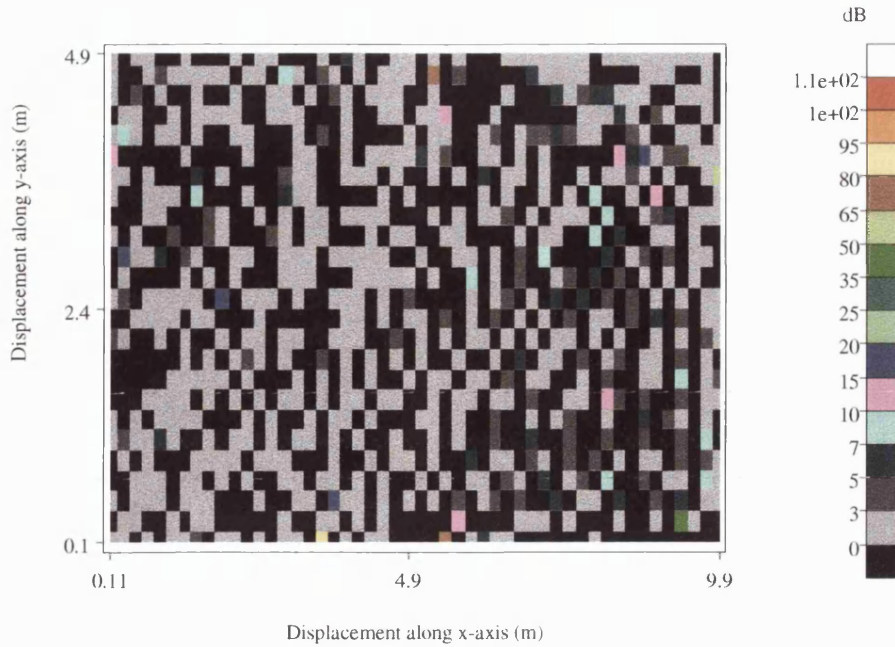


Figure 4.29: Receiver Space Diversity (SC) - Diversity Gain relative to branch 2 ($\lambda/4$ spacing)

4.6.1.3 Branch input statistics

Table 4.19 provides a statistical summary of the field strength predictions for each of the nine spatially separated branch signals. Predictions do not differ significantly in terms of average field strength (all results are within 0.1 dB), however as seen in figures 4.24 and 4.25, the fast fading effects (particularly the location of peaks and nulls) are different. The fast fading decorrelation is expected to increase with antenna spacing and should be completely decorrelated at the larger antenna spacings [25].

Branch	Average (dB)	Mean (Linear)	Standard Deviation	Variance
1	-11.90	0.245	0.567	0.321
2	-11.90	0.244	0.511	0.261
3	-11.81	0.248	0.523	0.274
4	-12.00	0.243	0.519	0.270
5	-11.97	0.244	0.518	0.269
6	-11.98	0.243	0.520	0.271
7	-11.96	0.243	0.517	0.267
8	-11.90	0.244	0.522	0.273
9	-11.99	0.242	0.518	0.268

Table 4.19: Field Strength Summary: Receiver Space Diversity Branch 1-9

4.6.1.4 Diversity Combining: Group 2

Group 2 combines branches 1 and 3 with a receiver separation distance of 0.5λ . Table 4.20 lists the statistical values of the field strength *after* diversity combining using each of the three specified methods.

Diversity	Average (dB)	Mean (Linear)	Variance	Standard Deviation
EG-AC	-6.14	0.493	1.156	1.075
EG-VC	-13.55	0.210	0.715	0.846
SC	-11.23	0.266	0.360	0.600

Table 4.20: Diversity Combining Field Strength Summary: Receiver Spacing Group 2 ($\lambda/2$ spacing)

Table 4.21 shows the receiver diversity gain (relative to branches 1 and branch 3 respectively) for each combining technique. At this larger antenna spacing, an average improvement in the range 0.43 - 7.3 dB is seen for the EG methods, while a gain of 2.37 - 2.87 dB is achieved using the SC approach. At this spacing, EG-VC performs extremely badly since the two signals have a high probability of being in antiphase (see chapter 2).

Method of Diversity Improvement	Relative to Branch 1 (dB)	Relative to Branch 2 (dB)
EG-AC	7.16	7.30
EG-VC	0.43	0.83
SC	2.37	2.87

Table 4.21: Receiver Space Diversity Gain versus Combining Technique – Group 2 ($\lambda/2$ spacing)

4.6.1.5 Receiver Space Diversity Gain versus Receiver Spacing

Figure 4.33 shows the average diversity gain relative to branch 1 for all three combining techniques ('EG-AC', 'EG-VC', 'SC'). The diversity gain was calculated from the linear average of the ratio of the field strength after combining to the field strength before combining (branch 1). The diversity gain is then quoted in dB using

$20\log$ (average ratio). Only locations where both the branch signals and the resulting diversity output are above a -90dB threshold are considered in the calculation.

Clearly the EG-AC technique produces the highest diversity gains, with values as high as 8 dB observed for antenna spacings of 3.5λ . At the largest antenna separation, the EG-VC technique produced a gain in the region of 6-7 dB. However, using VC the gain was seen to oscillate around a mean value similar to that of SC. Nulls were seen at half wavelength antenna separations and peaks at multiples of the wavelength. In practice, the spacing corresponding to a null is unpredictable and the method cannot be used to provide reliable diversity gains. When the branches are cophased to prevent destructive interference (i.e. EG-AC), a strong and reliable gain is obtained. The SC method provides a gain in the region of 4 dB for the largest antenna spacing, almost 4 dB below that of EG-AC.

For smaller antenna separations, less diversity gain is observed since the fast fading correlation between the branch signals increases [1][26]. For the EG-AC technique, the gain remains strong, with a value of almost 6 dB observed at an antenna spacing of 0.25λ . For SC, at 0.25λ the gain has dropped to just 2 dB (half the logarithmic gain seen at 4λ). For completeness, the diversity gains relative to branch 2 versus antenna spacing are shown in figure 4.31.

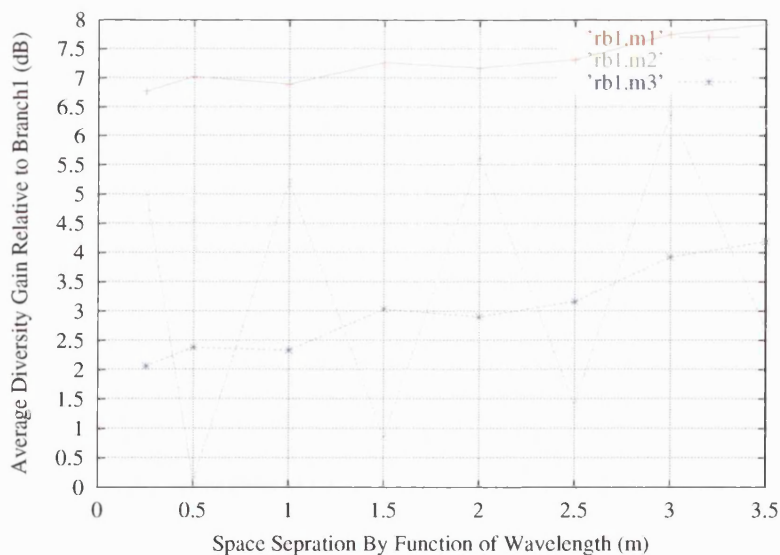


Figure 4.30: Average Diversity Gain vs Space Receiver Separation (relative to Branch 1)

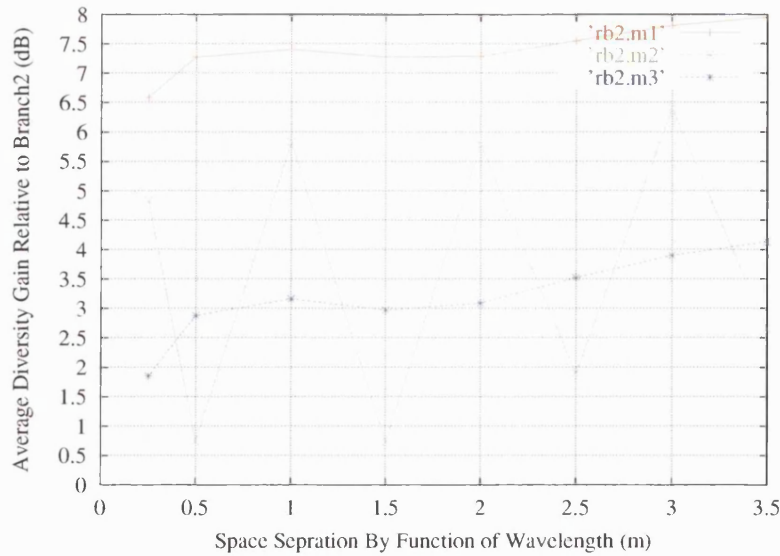


Figure 4.31: Average Diversity Gain vs Space Receiver Separation (relative to Branch 2)

The diversity gains seen relative to branch 2 are statistically similar to those relative to branch 1. The gain at 0.25λ is seen to fall off quite sharply, and at smaller spacing the diversity gain reduces significantly. This result corresponds well with previously published research [13], which states that an antenna spacing as low as 0.25λ can produce significant diversity gains in a high clutter environment.

4.6.1.6 Receiver Space Diversity CDF Analysis

Figure 4.32 shows the field strength CDF for the nine antenna branches that were used in the receiver space diversity study [1]. Statistically, the distribution of field strength on each branch is similar. At the 0.5 probability point, the field strength is approximately -16 dB. At the 0.1 probability point, the field strength has dropped to -40 dB. A number of differences are seen in the CDF tail, and given that this is where coverage failure occurs, such variations should be considered important.

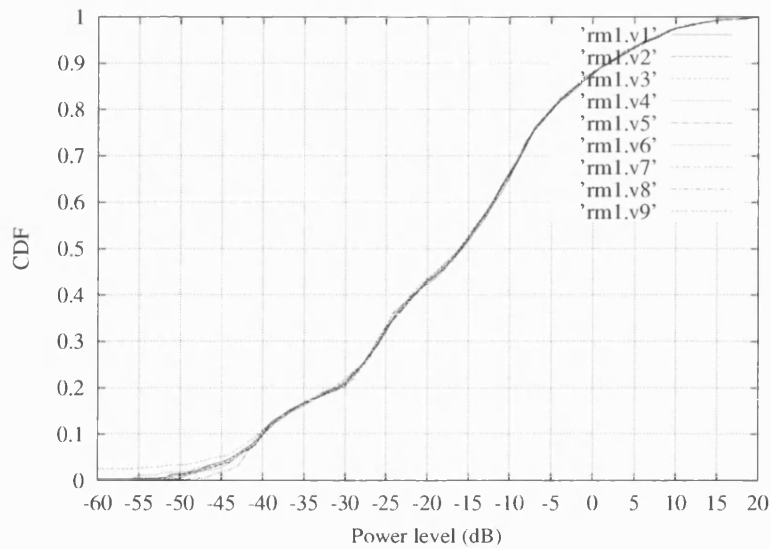


Figure 4.32: Field Strength CDF of the nine receive diversity input signals

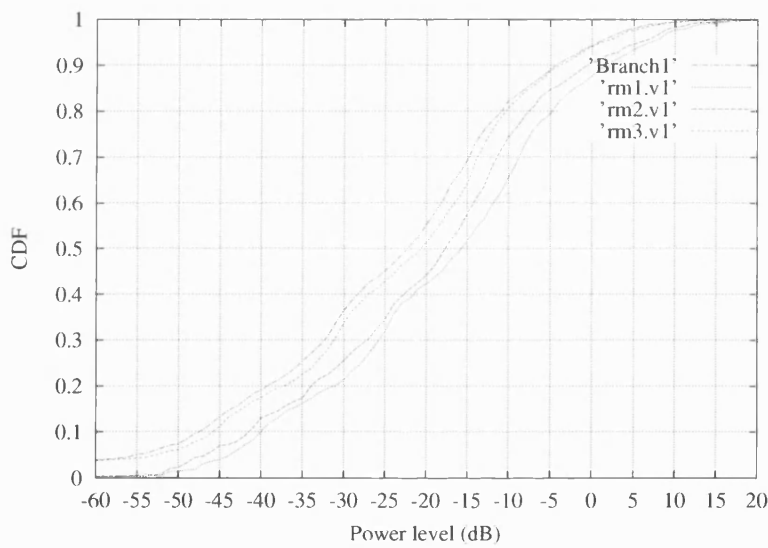


Figure 4.33: Receiver Space Diversity CDF plot for all three combining methods (group 1)

Figure 4.33 compares the field strength outputs for the three different combining techniques at the lowest antenna spacing of 0.25λ . At the 0.5 probability point, the approximate value of field strength is -16 dB for EG-AC, -18dB for EG-VC and -21 dB for EG-SC. At the 0.1 probability point, the field strengths are -40 dB for EG-AC, -42 dB for EG-VC and -46 dB for SC.

Figure 4.34 compares the field strength outputs for the three different combining techniques at the largest antenna spacing of 3.5λ . At the 0.5 probability point, the approximate value of field strength is -16 dB for EG-AC, -27 for EG-VC and -21 dB for EG-SC. At the 0.1 probability point, the field strengths are -40 dB for EG-AC, -47 dB for EG-VC and -45 dB for SC.

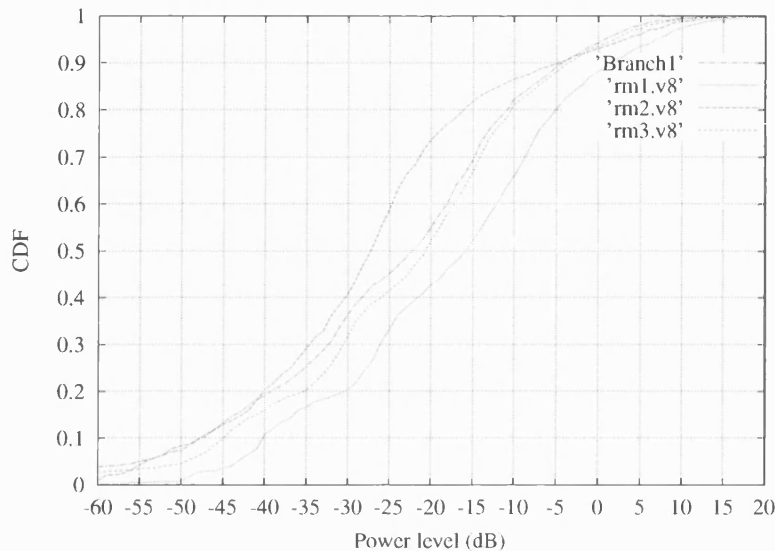


Figure 4.34: Receiver Space Diversity CDF plot for all three combining methods (group 8)

4.6.2 Transmitter Space Diversity

In this technique, two spaced transmitter antennas are used. Either the antenna that generates the strongest received signal is used, or both antennas are used to transmit the modulated signal with carrier phases that result in either VC or AC at the receiver. As discussed in section 4.2, transmitter diversity requires some form of feedback path to control the transmitter antenna switching or phasing.

In this section of the chapter, indoor diversity combining results are presented using Transmitter Space Diversity. Transmitter Space Diversity gain is studied by predicting a number of received field strength grids for a transmitting antenna that is placed in nine closely spaced locations. The closest transmit antenna spacing is 0.25λ , while the largest is 3.5λ . The first grid is taken together with one of the other eight grids to form the input to one of three diversity combining strategies. This method differs

from the earlier sections in this chapter since it is the transmitting antennas that are spaced, rather than the receiving antennas. In the following study, the practicality of feedback from the receiving antenna has been ignored and ideally combined signals are assumed.

4.6.2.1 Transmitter Space Diversity Setup and Simulation Strategy

The parameters described in table 4.20 are also used in this transmitter space diversity study. In this case, the antenna spacings given in table 4.21 are now applied to the transmitter antennas. Two field strength patterns were used for each diversity group study. These field strength grids were predicted for identical receiver points but using a transmitter with x-ordinate offsets as given by table 4.21. The two prediction grids are then processed using the EG-AC, EG-VC and SC combining algorithms (see section 4.3).

4.6.2.2 Transmitter Space Diversity Results: Group 1

Figure 4.35a shows the normalised field strength for branch 2. Figure 4.35b shows the grid plot after EG-AC combining of branches 1 and 2. A transmitter antenna spacing of 0.25λ was used in this group 1 study. Field strength grids for the input branches are not shown but are very similar to figures 4.24 and 4.25 given earlier in this chapter.

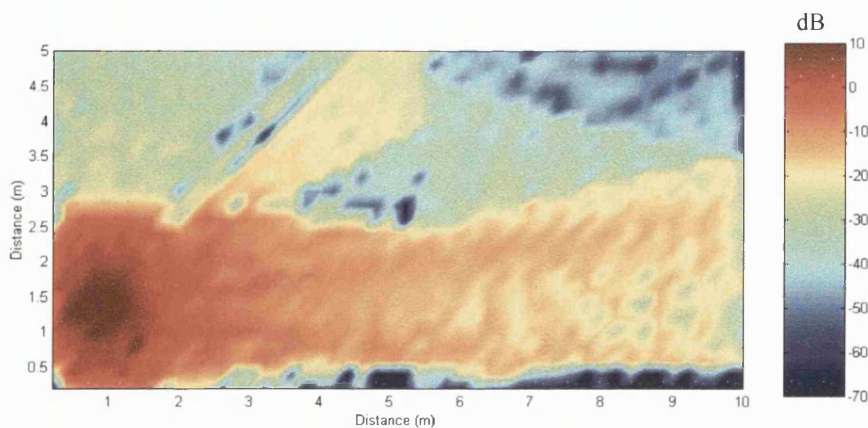


Figure 4.35a: Normalised Field Strength - Branch 2 (0.25λ horizontal offset relative to Branch 1)

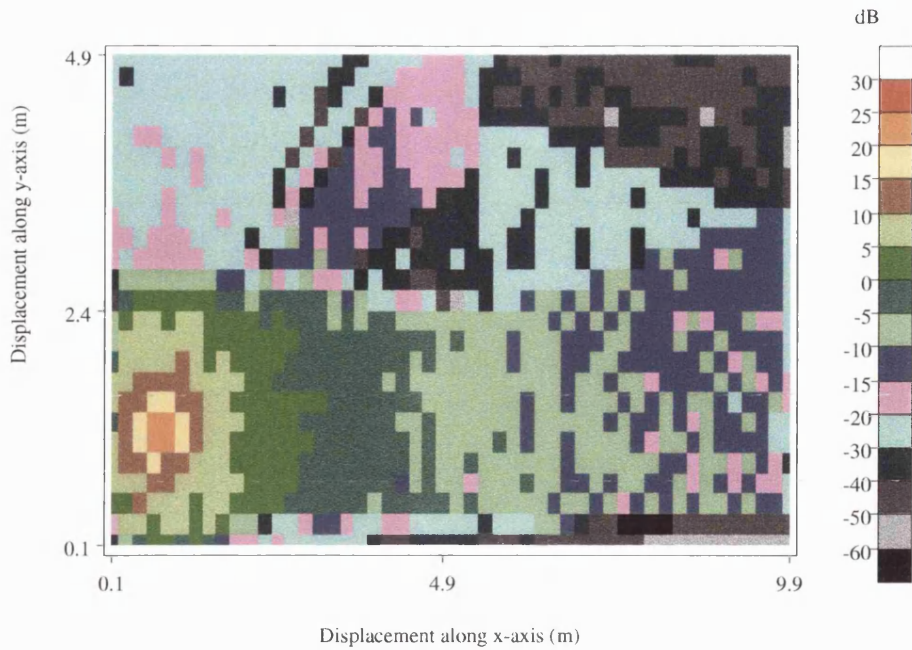


Figure 4.35b: Transmitter Space Diversity (EG-AC) Normalised Field Strength, Group 1 (0.25λ spacing)

Figure 4.36 shows the EG-AC diversity gain relative to branch 2 for the indoor environment under consideration. The figure shows that even at a transmitter spacing of just 0.25λ a reasonably high level of gain is achieved throughout the grid, with the majority of locations enjoying gains in excess of 5 dB.

Figure 4.37 shows the EG-VC diversity gain also relative to branch 2 for group 1. It can be seen by comparison with figure 4.36 that the overall gain is not as high. The results show some similarity with those seen in section 4.6.1.2 using receiver space diversity. In particular, large regions such as those in the bottom left-hand corner of the grid offer low degrees of diversity gain and this is thought to result from the destructive phase combining (when EG-VC is used) of the two input signals.

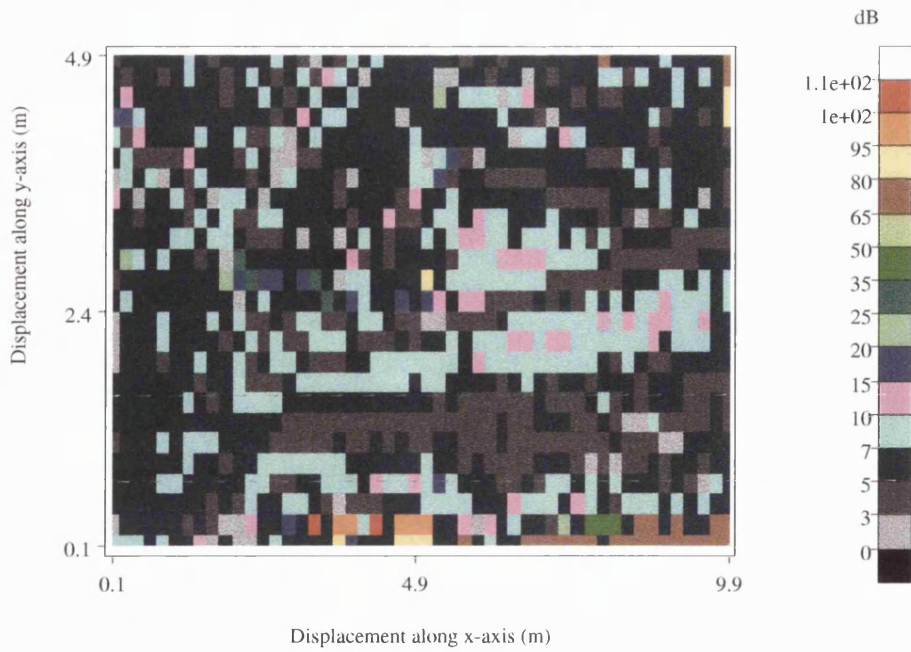


Figure 4.36: Improvement Transmitter Space Diversity (EG-AC) Normalised Field Strength, relative to Branch 2 – Group 1 (0.25λ spacing)

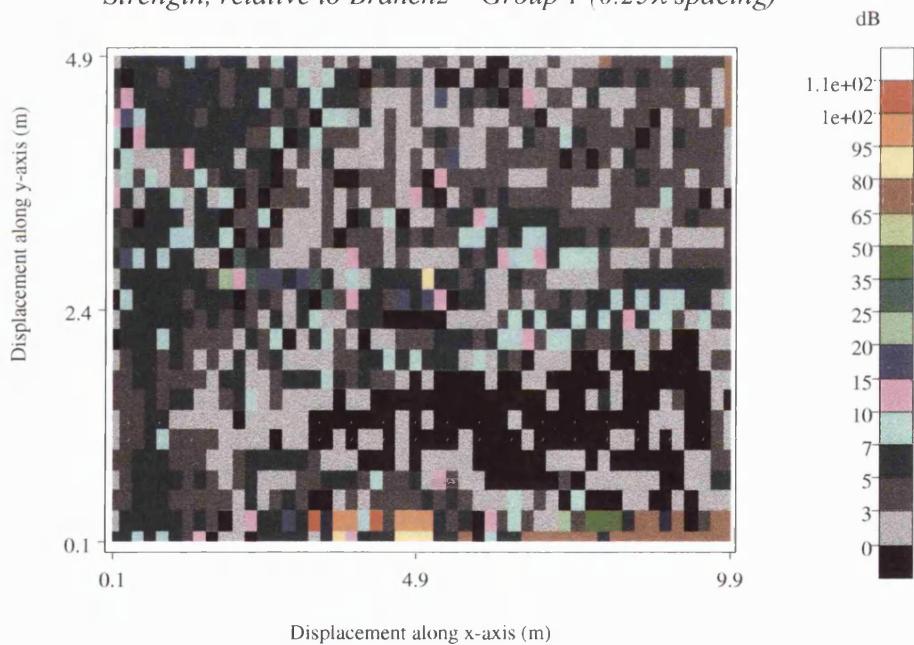


Figure 4.37: Improvement Transmitter Space Diversity (EG-VC) Normalised Field Strength, relative to Branch 2 – Group 1 (0.25λ spacing)

Figure 4.38 shows the group 1 diversity improvement using the SC technique. For large areas of the environment, little or no diversity improvement is observed. As will be seen in the later sections of this chapter, the degree of diversity improvement will increase as the spacing between the transmitter antennas is widened.

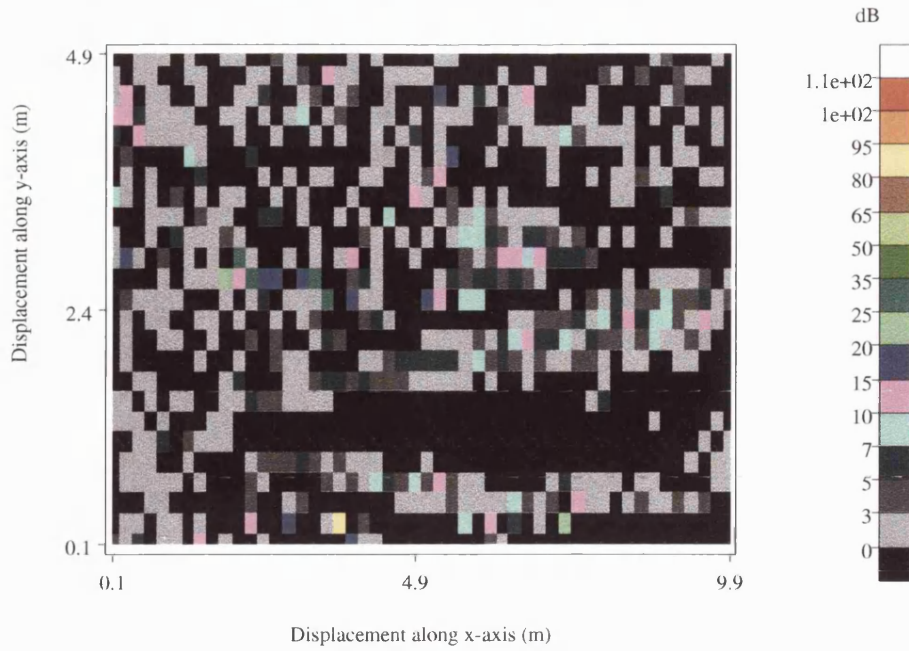


Figure 4.38: Improvement Transmitter Space Diversity (SC) Normalised Field Strength, relative to Branch 2 – Group 1 (0.25λ spacing)

4.6.2.3 Branch input statistics

Table 4.22 provides a statistical summary of the field strength predictions for each of the nine received branch signals. Predictions do not differ significantly in terms of average field strength (all results are within 0.3 dB). The received fast fading decorrelation is expected to increase with transmitter antenna spacing and complete decorrelation should occur at the larger antenna spacings.

Branch	Average (dB)	Mean (Linear)	Standard Deviation	Variance
1	-11.90	0.245	0.567	0.321
2	-11.86	0.247	0.509	0.259
3	-11.94	0.245	0.509	0.259
4	-11.80	0.248	0.525	0.275
5	-11.88	0.245	0.506	0.256
6	-11.76	0.251	0.520	0.270
7	-11.72	0.250	0.524	0.274
8	-11.81	0.249	0.522	0.272
9	-11.67	0.251	0.519	0.270

Table 4.22: Field Strength Summary: Transmitter Space Diversity Branch 1-9

4.6.2.4 Diversity Combining: Group 2

Table 4.23 lists the statistical values of the field strength *after* transmitter space diversity combining using each of the three specified methods. A transmitter antenna spacing of 0.5λ was used.

Diversity	Average (dB)	Mean (Linear)	Variance	Standard Deviation
EG-AC	-6.19	0.490	1.131	1.064
EG-VC	-13.76	0.205	0.727	0.852
SC	-11.32	0.264	0.347	0.589

Table 4.23: Diversity Combining Field Strength Summary: Transmitter Spacing Group 2 (0.5λ spacing)

Table 4.24 shows the transmitter diversity gain (relative to branch 1 and branch 3 respectively) for each of the three combining techniques. An average improvement in the range -1.77 - 7.42 dB is seen for the EG methods, while a gain of 1.77 - 3.08 dB is achieved using the SC approach. As was seen in the case of receiver diversity, the performance of EG-VC is extremely poor when half-wavelength antenna separations are used (i.e. far worse than either single antenna case).

Method of Diversity Improvement	Relative to Branch 1 (dB)	Relative to Branch 2 (dB)
EG-AC	7.42	6.61
EG-VC	-0.03	-1.77
SC	3.08	1.77

Table 4.24: Transmitter Space Diversity Gain versus Combining Technique – Group 2 (0.5λ spacing)

4.6.2.5 Transmitter Space Diversity Gain versus Antenna Spacing

Figure 4.39 shows the average diversity gain relative to branch 1 for all three combining techniques ('EG-AC', 'EG-VC', 'SC'). The diversity gain was calculated as in section 4.6.1.3.

Clearly the EG-AC technique produces the highest diversity gains, with values as high as 8 dB observed for antenna spacings of 3.5λ . At the largest antenna separation, the EG-VC technique produced a gain in the region of 6-7 dB. However, using VC the gain was seen to oscillate around a mean value similar to that of SC. Nulls were seen at half wavelength antenna separations and peaks at multiples of the wavelength. In practice, the spacing corresponding to a null is unpredictable and the method cannot be used to provide reliable diversity gains. When the branches are cophased to prevent destructive interference (i.e. EG-AC), a strong and reliable gain is obtained. The SC method provides a gain in the region of 4 dB for the largest antenna spacing, almost 4 dB below that of EG-AC.

For smaller antenna separations, less diversity gain is observed since the fast fading correlation between the branch signals increases. For the EG-AC technique, the gain remains strong, with a value of almost 6 dB observed at an antenna spacing of 0.25λ . For SC, at 0.25λ the gain has dropped to just 2 dB (half the logarithmic gain seen at 3.5λ). For completeness, the diversity gain relative to branch 2 versus antenna spacing is shown in figure 4.40.

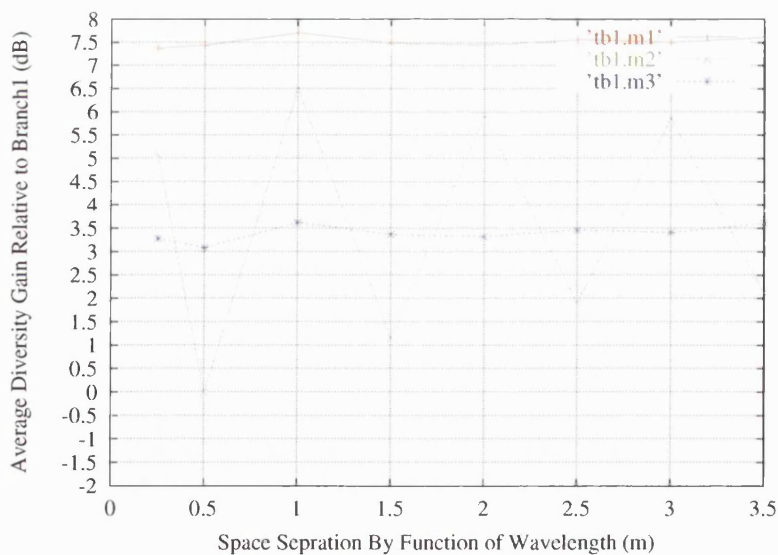


Figure 4.39: Average Diversity Gain vs Space Transmitter Separation (relative to Branch 1)

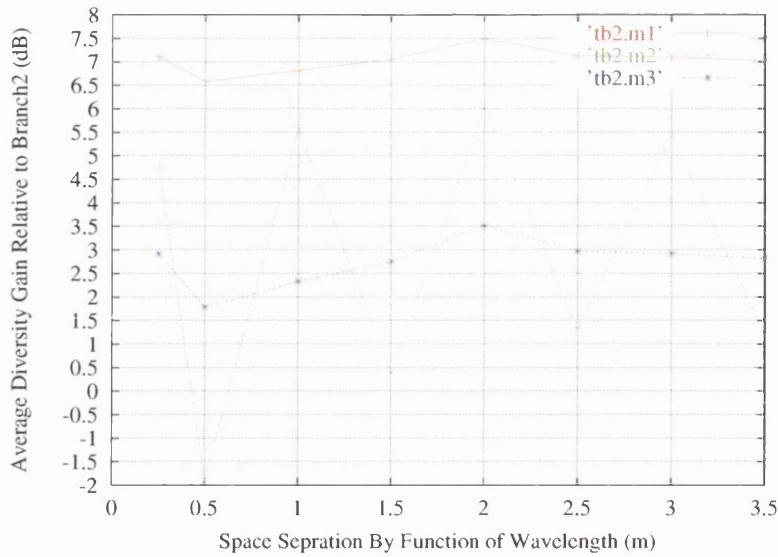


Figure 4.40: Average Diversity Gain vs Space Transmitter Separation (relative to Branch 2)

The diversity gains seen relative to branch 2 are statistically similar to those relative to branch 1. The gain at 0.25λ is seen to fall off quite sharply, and at smaller spacing the diversity gain reduces significantly. This result corresponds well with previously published literature that states that an antenna spacing as low as 0.25λ can produce significant diversity gains in a high clutter environment.

4.6.2.6 Transmitter Space Diversity CDF Analysis

Figure 4.41 shows the field strength CDF for the nine antenna branches that were used in the transmit space diversity study. Statistically, the distribution of field strength on each branch is similar, with only minor differences observed in the tail of the distribution [6]. At the 0.5 probability point, the field strength is approximately -16 dB. At the 0.1 probability point, the field strength has dropped to -40 dB.

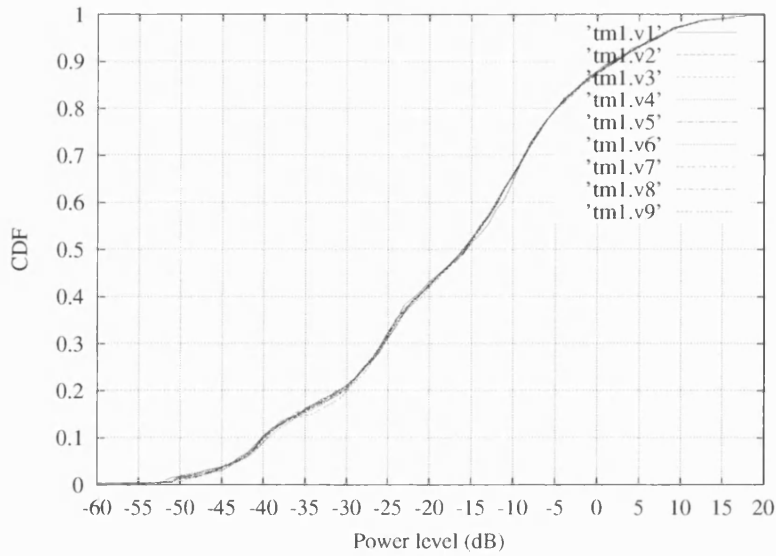


Figure 4.41: Field Strength CDF of the nine transmitter diversity input signals

Figure 4.42 compares the field strength outputs for the three different combining techniques at the lowest antenna spacing of 0.25λ ('EG-AC', 'EG-VC', 'SC'). At the 0.5 probability point, the approximate value of field strength is -15 dB for EG-AC, -19 dB for EG-VC and -21 dB for EG-SC. At the 0.1 probability point, the field strengths are -40 dB for EG-AC, -43 dB for EG-VC and -47 dB for SC.

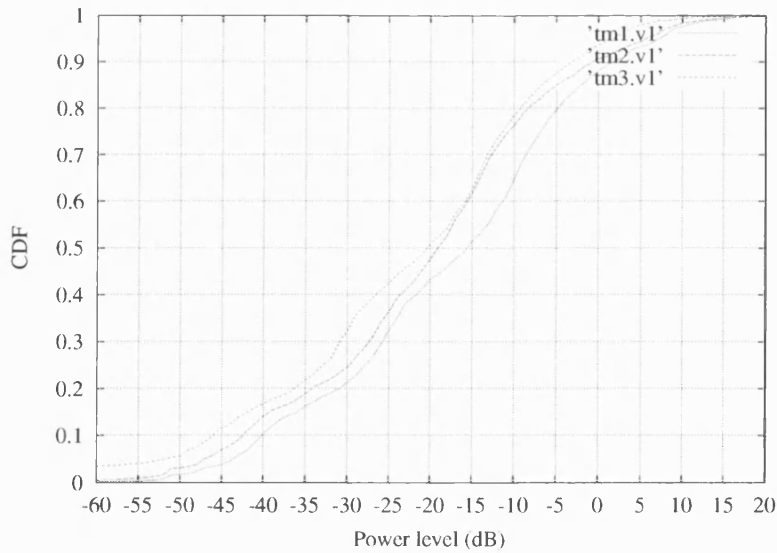


Figure 4.42: Transmitter Space Diversity for all three combining methods (group 1)

Figure 4.43 compares the field strength outputs for the three different combining techniques at the largest antenna spacing of 3.5λ . At the 0.5 probability point, the approximate value of field strength is -16 dB for EG-AC, -27 dB for EG-VC and -21 dB for EG-SC. At the 0.1 probability point, the field strengths are -40 dB for EG-AC, -47 dB for EG-VC and -45 dB for SC.

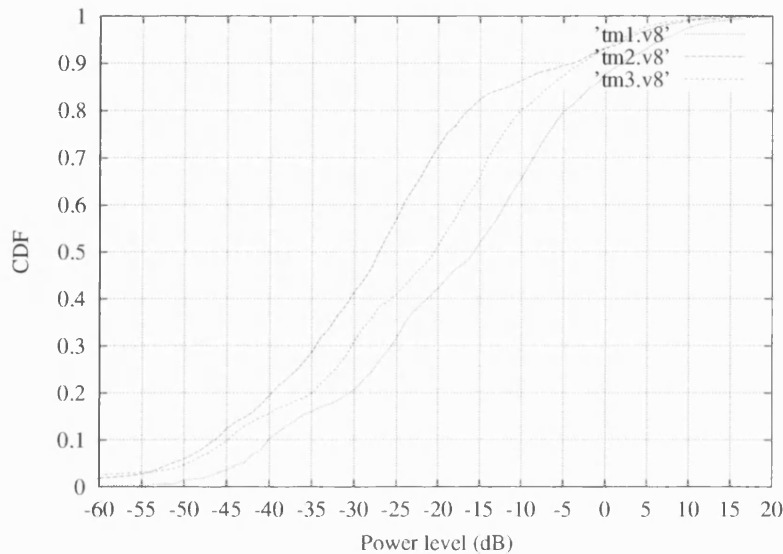


Figure 4.43: Transmitter Space Diversity for all three combining methods (group 8)

Section 4.6 in general has presented indoor diversity combining results obtained using receiver space diversity. Two different methods of space diversity were considered: (i) receiver space diversity and (ii) transmitter space diversity. In the first method, two spaced receivers were used and the signals combined using SC, EG-VC or EG-AC techniques. In the second technique, two spaced transmitter antennas were used. Transmitter diversity was shown to require some form of feedback path to control the transmitter antenna switching or phasing.

Predicted field strength grids were generated for antenna spacings ranging from one quarter of a wavelength up to four wavelengths. For the various combining schemes discussed in section 4.3, diversity gain as a function of antenna spacing was evaluated.

The results in this section have shown that the antenna spacing either at the transmitter or receiver is important when determining the expected diversity gain. Generally speaking, receiver diversity is easier to implement since combining

decisions can be made locally in the receiving radio. For transmitter diversity, information from the receiver must be sent back to the transmitter to support the combining process. For closely spaced antennas, the fast fading is more highly correlated and little diversity gain can be generated (i.e. for amplitude combining a gain in the order of 6 dB is observed). In a high clutter environment, antenna spacings of $\lambda/2$ and higher were significant to achieve high levels of decorrelation and more significant diversity gain can be achieved.

4.7 Summary

Diversity represents a common technique for mitigating the effects of fast fading in a radio environment. In this chapter three key methods for diversity signal generation were considered: i) two or more spaced antennas, ii) two orthogonally polarised antennas and iii) the use of two or more frequencies. The probability of experiencing deep signal fades on all diversity branches at the same time was shown to be low providing the fast fading on each branch is uncorrelated. For diversity to be fully effective, the mean signal strength on all branches needed to be similar. Using the indoor ray model discussed in chapter 3, field strength prediction grids were generated to enable a detailed diversity combining study to be performed. Table 4.25 summarises the diversity gain for each of the methods and combining strategies considered.

Diversity Technique	SC Gain (dB)	EG-VC Gain (dB)	EG-AC Gain (dB)
Space (Rx) - $\lambda/4$	3.06, 2.85	5.01, 4.83	6.77, 6.59
Space (Tx) - $\lambda/4$	4.28, 3.92	5.06, 4.78	7.37, 7.10
Space (Rx) - 3.5λ	5.38, 5.33	4.70, 4.65	9.91, 9.95
Space (Tx) - 3.5λ	4.60, 3.81	4.12, 4.19	9.60, 9.02
Frequency ($\Delta f = 1$ MHz)	0.06, 0.08	3.99, 4.01	6.01, 6.03
Frequency ($\Delta f = 500$ MHz)	1.87, 1.88	3.10, 2.95	6.58, 6.50
Polarisation	5.29, 2.92	5.28, 4.59	9.29, 6.65

Table 4.25: Average Diversity Gain Summary (dB relative to branch1, branch2)

4.8 References

- [1] W.C. Jakes, "Microwave Mobile Communication", *John Wiley Inc.*, 1st Edition, ISBN 0-471-43720-4, 1974.
- [2] P.F. Panter, "Microwave Communication Systems", *McGraw-Hill Ltd*, 1st Edition, ISBN 0-07-048436-8, 1972.
- [3] G. Corazza, V. Degli-Esposti, M. Frullone, C. Passerini, G. Riva, "Performance Evaluation of Space diversity in Indoor Communication Using a Ray-Tracing Propagation Model", *IEEE Trans.*, pp. 408-413, 1995.
- [4] F. Tila, S.R. Pennock and P.R. Shepherd, "Evaluation of Indoor Propagation Effects and Diversity Techniques", *IEE PREP Proc.*, pp. 23-25, 2001.
- [5] Ch. Ghobadi, S.R. Pennock and P.R. Shepherd, "Evaluation of Diversity Techniques in Complex Indoor Environments," *28th European Microwave Conference Amsterdam*, pp. 345-350, 1998.
- [6] G.E. Corazz, V. Degli-Esposti, M. Frullone and G. Riva, "Performance Evaluation of Space Diversity in Indoor Communications Using a Ray-Tracing Technique", *The sixth IEEE PIMRC*, Toronto, pp. 408-413, Sept. 1995.
- [7] G.A. Kalivas, M. El-Tanany and S. Mahmoud, "Millimetre Wave Channel Measurements with Space Diversity for Indoor Wireless Communications", *IEEE Trans. Veh. Tech.* vol. 44, no.3, pp. 494, August 1995.
- [8] W.G. Duff, "Mobile Communications," *Don White consultants, Inc.*, First Edition, 1976.
- [9] K. Fujimori and H. Arai, "Indoor Propagation Characteristics Including Radiation Pattern and Polarisation of Base Station," *IEEE Trans. Indoor Propagation*, pp. 2006-2009, 1997.
- [10] S.M. Alamouti, "A Simple Transmit Diversity Technique for Wireless Communications", *IEEE Journal on Selected Areas in Communications*, vol. 16, issue: 8, pp. 1451-1458, Oct. 1998.

- [11] J.P. Kermoal, A. Hammoudeh and C.J. Haslett, "An Evaluation of Frequency Diversity Performance in Microwave Frequency Mobile Radio Communication Systems," *10th International Conference on Antennas and Propagation, IEE Conference Publication*, no. 436, pp. 408-413, 2.123- 2.127, Apr. 1997.
- [12] A.R. Nix and J.P. McGeehan, "Modelling and Simulation of Frequency Selective Fading Using Switched Antenna Diversity," *IEE Electronic Letters*, vol. 26, no. 22, pp. 1868-1869, Oct. 1990.
- [13] A.J. Rustako, Jr., N. Amitay, G.J. Owens, and R.S. Roman, "Radio Propagation at microwave frequencies for line-of-sight microcellular mobile and personal communications", *IEEE Trans. Veh. Tech.*, vol. 40, pp. 203-210, Feb. 1991.
- [14] G.E. Corazza, V. Degli-Esposti, M. Frullone and G. Riva, "A Characteristic of Indoor Space Frequency Diversity by Ray-Tracing Modelling", *IEEE Journal on Selective Areas in Communications*, vol. 14, no. 3, pp. 411-419, April 1996.
- [15] W.C.Y. Lee, "Mobile Communications Engineering", *McGraw-Hill Inc*, 1982.
- [16] S. Stein and J. Jones, "Modern Communication Principles", *McGraw-Hill*, 1st Edition, 1967.
- [17] J.D. Parsons, M.Henze, P.A Ratliff and M.J. Withers, "Diversity Techniques for Mobile Radio Reception", *The Radio and Electronic Engineer*, Vol. 45, No. 7, pp. 357-367, July 1975.
- [18] F. Ikegami, T. Takeuchi, and S. Yoshida, "Theoretical predication of mean field strength for urban mobile radio", *IEEE Trans. Antennas Propagation*, vol. 39, pp.299-302, Mar. 1991.
- [19] J.M. Keenan and A.J. Motley, "Radio Coverage in Buildings", *British Telecom Technology Journal*, pp. 19-24, Jan. 1990.
- [20] K.R. Schaubach, N.J. Davis and T.S. Rappaport, "A Ray Tracing Method for Predication Path Loss and Delay Spread in Microcellular Environments", *42nd IEEE Veh. Tech. Conference*, pp. 932-935, May 1992.

- [21] S.Y. Seidel and T.S. Rappaport, "A Ray Tracing Technique to Predict Path Loss and Delay Spread Inside Buildings", *IEEE GLOBECOM Conference Proc.*, pp. 649-653, 1992.
- [22] Ch. Ghobadi, "Millimetre Wave Propagation and Diversity Techniques within Buildings and Around Human Bodies," *Thesis*, Jul. 1998.
- [23] Z. Zhao, S. Stapleton and J.K. Cavers, "Analysis of Polarization Diversity Scheme with Channel Codes", *IEEE Trans. Communication*, vol. 20, pp. 912-916, 1972.
- [24] V. Degli-Esposti, G. Falciasecca, M. Frullone, G. Riva and GE. Corazza, "Performance Evaluation of Space Diversity for 60 GHz Wireless LANs Using a Ray Model", *IEEE Veh. Tech. Conference*, vol. 2, pp. 984-988, 1997.
- [25] A.M. Saleh and R.A. Valenzuela, "A Statistical Model for Indoor Multipath Propagation", *IEEE Journal on Select Area Communications*, Vol. SAC-5, No. 2, pp. 128-137, Feb. 1987.
- [26] Ch. Ghobadi, P.R. Shepherd and S.R. Pennock, "2D Ray-Tracing Model for Indoor Radio Propagation at Millimetre Frequencies and the Study of Diversity Techniques," *IEE Proc.-Microw. Antennas Propagation*, vol. 145, no. 4, pp. 349-353, Aug. 1998.

Chapter 5: Sectorised Antenna Beam Patterns

5.1 Introduction

This chapter analyses field strength coverage predictions for high frequency indoor communications at 17 GHz using directional antennas at the basestation and 2 branch spaced antenna diversity at the terminal. Detailed propagation information is generated for a typical two-dimensional indoor environment using the ray-tracing propagation tool described in chapter 3. As a performance benchmark, initial field strength predictions are generated for omni-directional basestation and terminal antennas. Downlink performance is enhanced by the use of 2 branch spaced antenna diversity at the terminal. Factors such as antenna spacing and the choice of diversity combining algorithm are considered. At the basestation, a novel 3 branch phased array beam pattern diversity system is compared with an ideal six branch sectorised antenna. For each configuration, detailed propagation studies are performed to determine the relative (compared to omni-directional antennas) coverage improvement over the entire environment. Results indicate that the use of space diversity at the terminal can improve the expected coverage by as much as 10.7dB. Beam pattern and sector switching arrangements at the basestation result in a 7.2-10.4dB improvement. The most impressive gains were observed using directional antennas at the basestation and spaced antenna diversity at the terminal. Gains of 17.2dB and 19.4dB were observed for 3 (beam pattern) and 6 (sectorised) branch systems respectively at the basestation.

The need for high capacity indoor communications continues to escalate. Mobile and portable devices demand ever increasing bit rates. The majority of current indoor communications occur in the 2.4 GHz ISM (Industrial, Scientific and Medical) band. Technologies such as Bluetooth and 802.11 enable bit rates in the region 1-2 Mb/s [1]. Future enhancements of 802.11 are planned for use in the 5 GHz band offering bit rates as high as 54 Mb/s [2-3]. Looking to the future, even larger spectral allocations are available at higher frequencies. Systems such as AWA have been proposed in Japan for operation at 19 GHz [4-5]. ETSI are considering the use of 17 GHz [6-7] for future versions of their Hiperlan family of radio standards. In the US, spectrum has

been made available in the 59-64 GHz band for indoor short-range communications [8-9].

Section 5.2 explains how the ray tracing propagation tool was applied to the indoor environment of interest. Section 5.3 discusses the various basestation and terminal antenna structures and summarises the proposed diversity combining and selection algorithms. In section 5.4 a range of field strength coverage predictions are presented and analysed. Initial field strength predictions are generated for omni-directional basestation and terminal antennas. Downlink performance is enhanced by the use of 2 branch spaced antenna diversity at the terminal. Factors such as antenna spacing and the choice of diversity combining algorithm are considered. At the basestation, a novel 3 branch phased array beam pattern diversity antenna is compared with an ideal six branch sectorised antenna. For each configuration, detailed propagation studies are performed to determine the relative (compared to omni-directional antennas) coverage improvement averaged over the entire environment. Section 5.5 discusses a number of conclusions and ends with a set of recommendations.

5.2 Ray Model & Environment

The propagation model can be divided into two distinct modules. Firstly, a process of ray launching and tracing is performed from the basestation. Once complete, the resulting data structure is used to perform field reconstruction over the entire grid of receiver points. The ray tracing algorithm performs a general analysis of launched ray paths from the transmitter as they reflect and/or transmit at a boundary and onward propagate through the indoor environment [10]. The ray tracing module traces ray tubes from the source transmitter in a predetermined direction, based on azimuth start and stop angles and an angular launch resolution. Object intersections are identified for each ray path (by sensing a material discontinuity) and appropriate reflections and transmissions are calculated. The ray tracing process is performed based on knowledge of the local environment and the location of the transmitter.

Since the ray model is deterministic it requires a database for the environment of interest (including material properties). In practice, any two dimensional environment can be specified. Factors such as material thickness and complex permittivity are highly influential in such models, particularly when determining transmission loss.

The building material assumptions at 17 GHz (see equation 3.13) used in this study [2][11] are shown in Table 5.1.

Material Type	Relative permittivity	Conductivity	dB/cm	Thickness (cm)
Exterior Wall	2.7	0.05	0.5	20
Door	5.0	0.05	0.4	10
Desk	4.0	0.055	0.5	20
Partition Wall	2.7	0.05	0.5	20

Table 5.1: Material Properties

Once the database is generated, the ray model is able to trace the various path reflections and refractions at material boundaries to predefined signal strength. The received field strength at each grid point is then calculated by the vector summation of field strengths for all rays that illuminate that point. The indoor test environment is shown in figure 5.1.

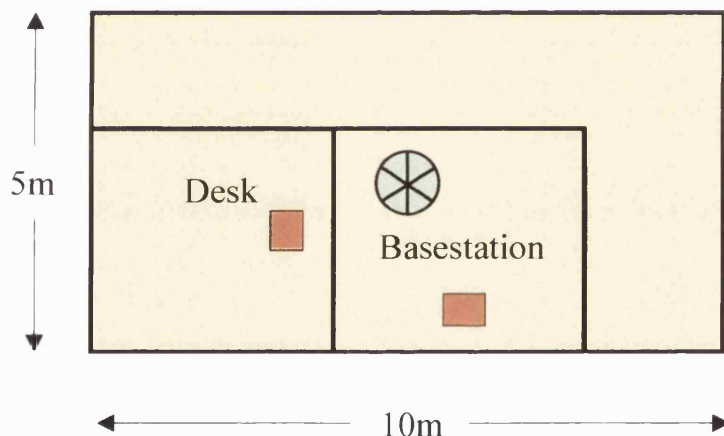


Figure 5.1: Example Environment

The environment consists of a main room surrounded by an L-shaped corridor. The basestation is placed in the main room. The environment is divided into a 50 x 25 grid, with receiver points spaced every 0.2m.

5.3 Diversity Generation and Combining

Wireless communications are known to suffer from fast fading and this can seriously disrupt the quality of the radio link (particularly in non-line-of-sight locations). Indoor

links, with the presence of walls, furniture, etc. are particularly susceptible. In addition to the use of directional transmit and receive antennas, in this section a number of diversity techniques are analysed to further enhance radio communication in an indoor environment. In particular, switched beam/sector and space diversity schemes are considered (see chapter 4) at the basestation and terminal respectively. In this analysis the two receiving omni-directional antennas are spaced at a distance of 3.5 wavelengths [12]. For the basestation, a 3 branch beam switching and a 6 branch sectorised arrangement are considered.

Space diversity is considered to be a strong contender for microwave mobile radio applications [12-13]. In this section, diversity signals are generated at the terminal using two spaced antennas. The spacing of the antennas at the receiver (see section 4.6.1) is chosen to ensure that the individual signals are suitably uncorrelated. Given the use of a 17 GHz carrier frequency, a spacing of 3.5 wavelengths translates to a separation distance of around 5 cm. In a high clutter environment, spacings as low as one quarter to one half of a wavelength can still offer good performance [12-13].

Two methods of diversity combining at the terminal are considered. The first technique, selection combining, simply selects the stronger of the two signals at any given time. The second technique, known as Equal Gain Combining (EGC), adds the amplitudes of the two signal branches [14]. Chapter 4 provides a detailed description of these methods.

5.3.1 Beam Pattern Diversity

At the basestation, two directive antenna strategies are explored. The first technique makes use of a linear phased array to implement beam pattern diversity. The basestation applies one of three sets of phase weights to the phased array to form one of three possible beam patterns. In practice, the number of beam patterns could be increased and depends on the number of individual antenna elements in the array. Figure 5.2(i) shows the amplitude of one of the three beam patterns considered in this study. Each beam pattern is assumed to have a 4.8 dBi boresight gain. This pattern was generated assuming a 7-element uniform linear array [15]. The second and third beam patterns are identical but rotated clockwise and anti-clockwise by 60 degrees. Using this strategy, all possible terminal locations will fall into the 3dB beamwidth of

one of the three beam patterns. For each terminal location, the best of the three beam patterns must be determined prior to data transmission (i.e. beam pattern selection diversity at the basestation). System performance can be further enhanced by applying space diversity at the terminal *in addition* to beam pattern diversity at the basestation. In this configuration, the beam pattern resulting in the best output from the terminal diversity combiner is chosen. In the case of switched terminal diversity, the algorithm will choose the best combination of basestation sector and terminal antenna element.

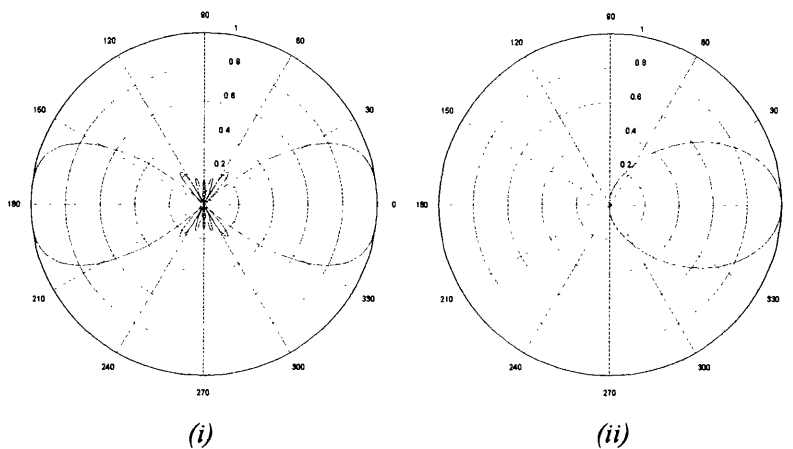


Figure 5.2: (i) 2 x 60 degree Phased Array Beam Pattern, (ii) 60 degree Sector Approximation

A sectorised antenna comprises a number of individual antenna units, each having a single main lobe covering a fraction of the full 360 degrees. In this chapter a six sector solution is considered, with each sector having a 60 degree 3-dB beamwidth. To ease the modelling process, idealized individual sector patterns based on a Gaussian pulse are assumed [16]. Figure 5.2(ii) shows the resulting beam pattern for a single sector. The other five sectors are identical, but rotated by 60, 120, 180, 240 and 300 degrees. Each sector is assumed to have a 7.8 dBi boresight gain.

5.4 System Analysis

The following 6 system configurations are analysed in this section:

1. Omni basestation antenna to omni terminal antenna
2. Omni basestation antenna to space diversity terminal
3. Phased array basestation with omni terminal antenna

4. Phased array basestation with space diversity terminal
5. Sectorised basestation with omni terminal antenna
6. Sectorised basestation with space diversity terminal

For each mode, beam pattern and sector, ray tracing field strength prediction grids are generated and the appropriate transmit and/or receive diversity processing applied. Figure 5.3 shows the field strength prediction grid for omni directional basestation and mobile antenna (mode 1).

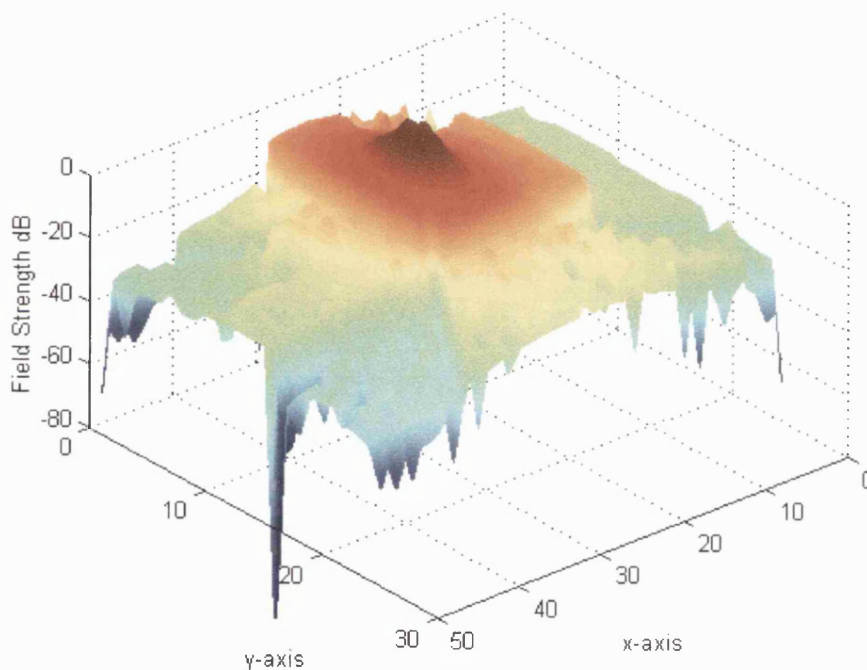


Figure 5.3: 3-D field strength grid plot

The received field can be seen to peak in the vicinity of the basestation and remains high in areas of direct line of sight. The field drops dramatically as the signal passes through dividing walls into the corridor. The omni-omni data was used as a reference to compare the coverage performance of the remaining diversity systems.

Figure 5.4 shows the Cumulative Distribution Function (CDF) of normalized fade depths for an omni basestation with and without space diversity at the terminal. The CDF for each scheme was generated by computing the instantaneous fade depth at each receive point. This fade depth was calculated as the difference between the mean field strength for an omni-omni configuration and the instantaneous field for the mode

of interest (calculated from the vector sum of rays). In the case of directional antennas, a normalized pattern with unity gain on the boresight was used. Hence, the impact of antenna gain needs to be incorporated in the final comparison.

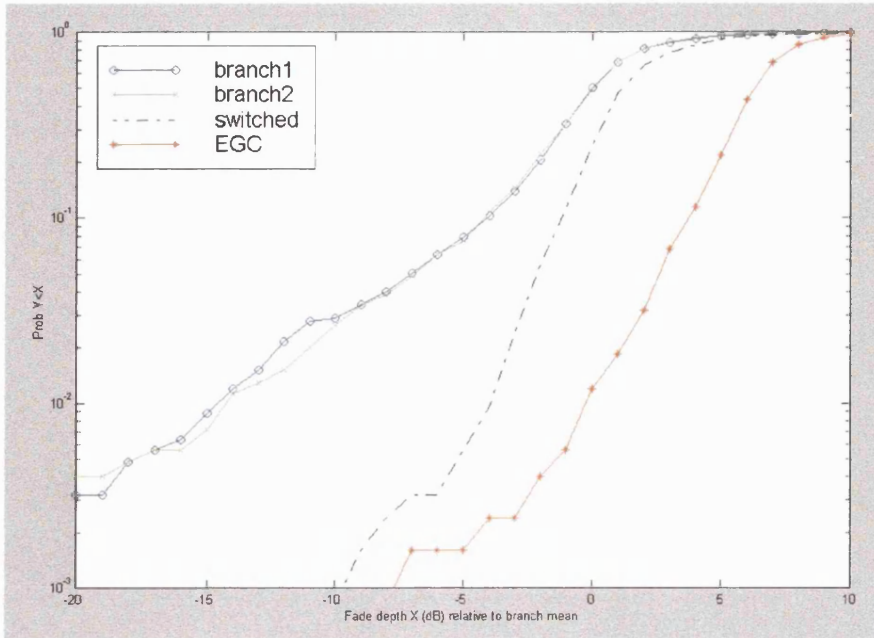


Figure 5.4: Fast Fading CDF for omni basestation (relative to single antenna mean)

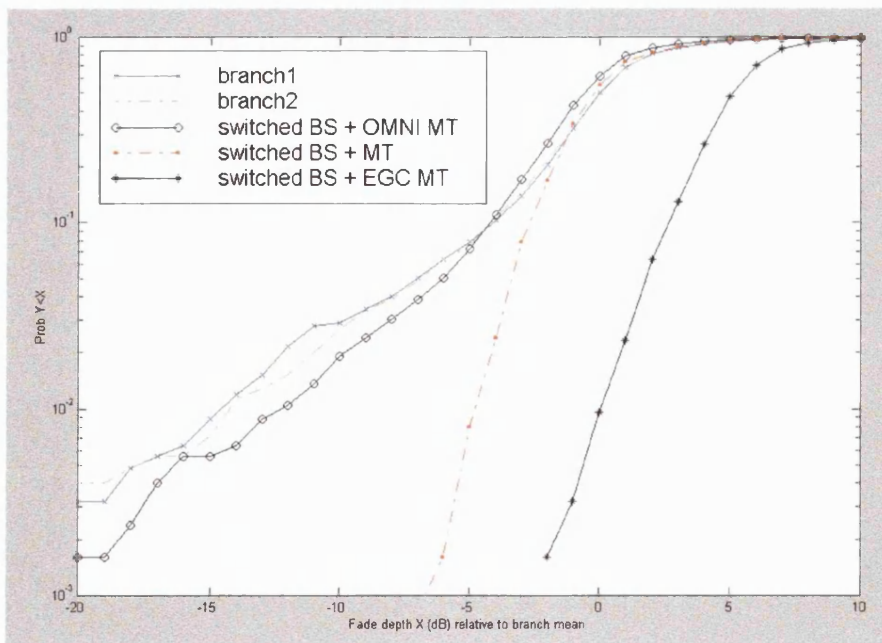


Figure 5.5: Fast Fading CDF for 3 branch beam pattern basestation (relative to single antenna mean)

Figure 5.4 shows the CDF for branch 1 and branch 2 at the terminal. As expected, the fading statistics for both antennas are nearly identical, with both experiencing a 14 dB fade margin (assuming a 1% outage). The first row in Table 5.2 summarizes the processed data for the omni-omni configuration. Application of switched space diversity can be seen dramatically to improve the resulting CDF. A fade margin of 4 dB is now observed and the overall mean of the combined signal is also seen to increase by 1.17 dB.

From a field strength coverage point of view, performance is improved by 8.83 dB. This improvement is calculated using the equation:

$$\text{Maximum Overall Gain} = (F_o - F_s) + (M_o - M_s) - (G_o - G_s) \quad (5.1)$$

Where F_o and F_s represents the fade margins, M_o and M_s the relative mean levels and G_o and G_s the antenna boresight gains for the reference omni and test system respectively.

System Type	Relative Mean (dB)	1% Fade Margin (dB)	Directive Gain (dBi)	Overall Improvement (dB)
Omni BS – Omni MT	0	14	0	0
Omni BS – SW MT	1.17	4	0	8.83
Omni BS – EGC MT	6.28	0	0	10.72
3 Branch BS – Omni MT	-0.40	12	4.78	7.18
3 Branch BS – SW MT	0.44	4	4.78	14.34
3 Branch BS – EGC MT	5.55	-1	4.78	17.23
6 Branch – Omni MT	-0.67	12	7.78	10.45
6 Branch – SW MT	0.02	5	7.78	16.76
6 Branch SW EGC	5.33	0	7.78	19.45

Table 5.2: System Gain versus BS/MT Antenna Strategy

It is important to note that in the case of EGC systems, 3 dB is subtracted from the difference in means to reflect the statistical doubling of the noise power in the combining process. The final graph in figure 5.4 shows the CDF for EGC combining at the terminal. The mean power has increased by 6.28 dB relative to the original single antenna configuration. This gain is consistent with EGC, where an approximate 6 dB increase in mean is expected. The summary data for the case of EGC combining

with an omni transmitter antenna is given in the third row of Table 5.2. A net gain of 10.72 dB is observed, which is almost 2 dB better than the simpler switched scenario.

Figure 5.5 shows the CDF results for 3 branch beam pattern diversity at the basestation. Assuming a single omni antenna at the terminal, the mean power drops by 0.4 dB and the fade margin improves to 12 dB. The beam pattern (see figure 5.2(i)) has a gain of 4.78 dBi.

As summarized in row 4 of Table 5.2, this configuration results in an overall gain of 7.18 dB. Switching beam patterns at the basestation does not result in a significant fade margin reduction since the beams do not overlap. This means that the directly illuminating beam pattern is always likely to be chosen, even when the beam suffers a deep fade. This observation is confirmed by figure 5.6, which shows the most likely beam selection as a function of terminal location. Generally, the beam that points in the direction of the terminal is nearly always chosen, irrespective of fade depth. The application of diversity at the terminal dramatically improves the fade margin.

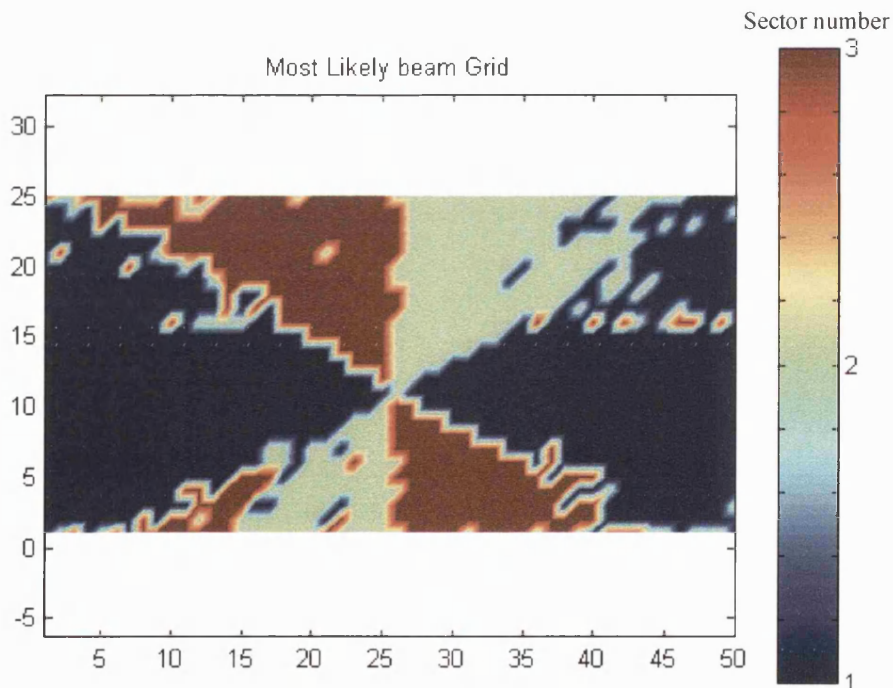


Figure 5.6: Most Likely Beam Pattern (1: 0 degrees, 2: +60 degrees, 3: -60 degrees – see figure 5.2(ii))

From figure 5.5 the fade margin drops to 4 dB (from 12 dB previously). Taking into account differences in mean power and antenna gain, the overall improvement for this

system is 14.34dB (row 5, Table 5.2). The final curve on figure 5.5 shows the impact of applying EGC at the terminal. The overall gain now increases to 17.23dB.

The final three rows in Table 5.2 consider the use of a 6 sectored antenna at the basestation. Field strength predictions for each of the six sectors are shown in figure 5.7. The diagram shows the orientation of each sector and confirms that the best coverage for each sector lies within its 3dB beamwidth. By switching to the sector offering the best coverage at a given point, indoor coverage can be greatly enhanced.

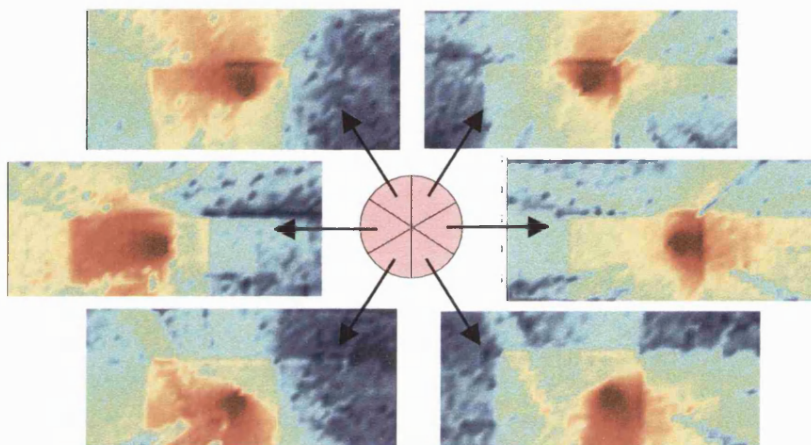


Figure 5.7: Individual Sector Plot (omni terminal antenna)

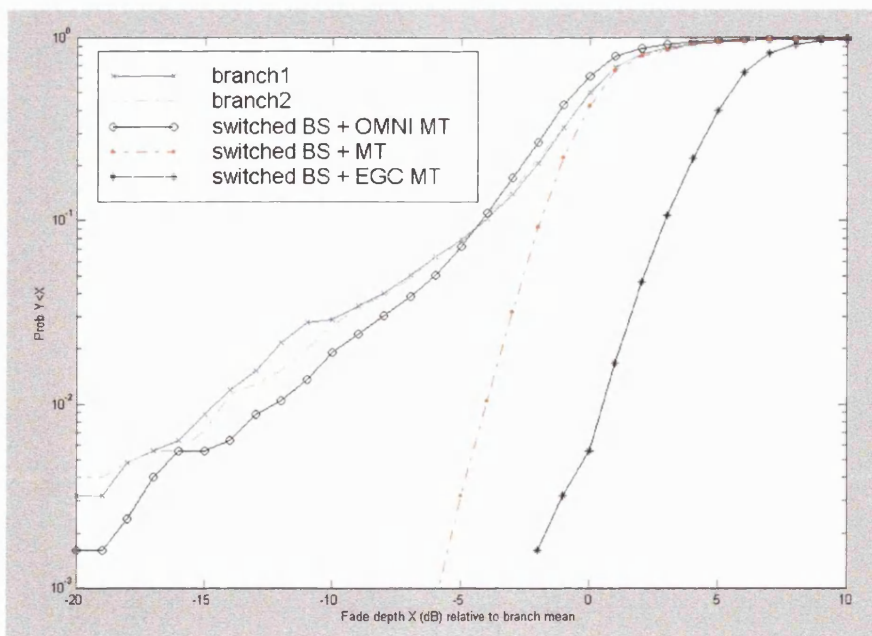


Figure 5.8: Fast Fading CDF for 3 branch beam pattern basestation (relative to single antenna mean)

Figure 5.8 shows the resulting CDF statistics for this case. As for the beam pattern scenario, little improvement in fade margin is seen when a single omni antenna is used at the terminal. An overall gain of 10.43 dB is observed (largely due to the high antenna gains associated with a 60 degree beamwidth antenna). The application of switched diversity at the terminal improves performance significantly, with an overall gain of 16.76 dB. The final system studied in this chapter considers EGC combining at the terminal with the 6 sector antenna at the basestation. For this system, an overall gain of 19.43 dB was observed.

5.5 Summary

In this chapter a range of diversity systems have been studied at the basestation and terminal. Results indicated that gains in the order of 8-11 dB are possible using spaced antenna diversity at the terminal. The use of 3 branch pattern diversity at the transmitter can improve performance by over 7 dB for a single omni antenna at the terminal and by as much as 17 dB if space diversity is also applied at the terminal. The final system considered used a six sectored basestation antenna. This configuration offered in excess of 10 dB gain for a single omni terminal antenna and almost 20 dB gain when combined with 2 branches EGC at the terminal. All gains were calculated for a 1% outage. The results showed that the performance of high frequency indoor systems can be improved by up to 20dB through the careful application of antenna diversity.

5.6 References

- [1] S. Souissi and E.F. Mehofer, "Performance Evaluation of a Bluetooth Network in the Presence of Adjacent and Co-Channel Interference", *IEEE Emerging Technologies Symposium: Broadband, Wireless Internet Access*, Sep. 2000.
- [2] A.R. Nix and J.P. McGeehan, "Predicted HIPERLAN Coverage and Outage Performance at 5.2 GHz and 17 GHz using Indoor 3D- Ray Tracing Techniques", *Wireless Personal Communication Journal HIPERLAN Special Edition, Kluwer, New York*, 1996.
- [3] S. Guerin, Y.J. Guo and S.K. Barton, "Indoor Propagation Measurements at 5 GHz for Hiperlan", *10th International Conference on Antennas and Propagation*, vol. 2, pp. 306-310, April 1997.
- [4] M. Umehira et al, "An ATM Wireless Access System for Tetherless Multimedia Services", *International Conference on Universal Personal Communications (ICUPC)*, April 1995.
- [5] V. Kvicera and P. Cejka, "First Results of a Long-Term Propagation Experiment at 19 GHz", *IEE 11th International Conference on Antennas and Propagation*, vol. 2, pp. 542-545, April 2001.
- [6] P. Nobles and F. Halsall, "Indoor Propagation at 17 GHz and 60 GHz- Measurements and Modelling", *IEE National Conference on Antennas and Propagation*, pp. 93-96, Aug. 1999.
- [7] P. Nobles, D. Ashworth and F. Halsall, "Propagation Measurements in an Indoor Radio Environment at 2, 5 and 17 GHz", *IEE Colloquium on High Bit Rate VHF/SHF Channel Sounders-Technology and Measurement*, pp. 41-46, Dec. 1993.
- [8] A. Plattner, N. Prediger and W. Herzig, "Indoor and Outdoor Propagation Measurements at 5 and 60 GHz for Radio LAN Application", *IEEE MTT-S International Microwave Symposium Digest*, pp. 853-856, June 1993.

- [9] H. Droste and G. Kadel, "Measurement and Analysis of Wide Band Indoor Propagation Characteristics at 17 GHz and 60 GHz", *9th International Conference on Antennas and Propagation*, vol. 2, pp. 288-291, April 1995.
- [10] F. Tila, P.R. Shepherd and S.R. Pennock, "Analysis of Indoor-Indoor and Satellite/Hap-Indoor Propagation Effects", *IEE 11th International Conference on Antennas and Propagation, ICAP*, pp. 203-207, April 2001.
- [11] M.R. Williamson and A.R. Nix, " Investigating the Effects of Antenna Directivity on Wireless Indoor Communications at 60 GHz", *8th IEEE Personal and Indoor Mobile Radio Conference (PIMRC), Helsinki, Finland*, pp. 635-639, Sept. 1997.
- [12] F. Tila, SR. Pennock and PR. Shepherd, "Evaluation of Indoor Propagation Effects and Diversity Techniques", *Proc. IEE PREP*, vol.2, pp. 23-25, April 2001.
- [13] Ch. Ghobadi, S.R. Pennock and P.R. Shepherd, "Evaluation of Diversity Techniques in Complex Indoor Environments", *28th European Microwave Conference Amsterdam*, pp. 345-350, 1998.
- [14] W.C. Jakes, "Microwave Mobile Communication", *John Wiley Inc.*, 1st Edition, ISBN 0-471-43720-4, 1974.
- [15] C.A. Balanis, "Antenna theory analysis and design", *New York: Harper & Row*, 2nd Edition, ISBN 0-06-040458-2, 1982.
- [16] F. Tila, P.R. Shepherd and S.R. Pennock, "Indoor Ray Tracing evaluation of enhanced High Frequency communications using Directional Antennas at the Basestation and Space Diversity at the Terminal", *31st IEEE European Microwave Conference (EuMC)*, pp. 351-355, Sep. 2001.

Chapter 6: High Altitude Platform (HAP)

6.1 Introduction

This chapter describes two methods to upgrade the indoor ray-tracing propagation model discussed in chapter 3 to simulate indoor reception from an overhead or offset High Altitude Platform (HAP). The first method represents a sub-optimum approximation used to minimise the changes required in the original code. This method has the advantage that the modification can be applied to existing results from the ray-tracing software.

Over the last 10-15 years a large number of indoor to indoor propagation models have been proposed in the literature [1]. Outdoor to indoor propagation models have also been developed, mainly to determine indoor penetration loss from terrestrial basestations [2]. Recently, the use of High Altitude Platforms (HAP) has been proposed as a means of offering broadband third and fourth generation services [1]. HAP basestations are located at a height of approximately 20km, thus avoiding the high path losses observed with satellite communications. The use of overhead platforms also reduces the path loss observed in dense urban terrestrial radio systems.

Traditionally, given the large separation distance between the HAP and the mobile terminal, ray-launching methods have been difficult to apply. In this chapter novel modifications to a previous indoor-only ray-tracing model [3-4] are described that enable HAP analysis to be performed. These enhancements involve the placing of an array of virtual transmitters around the building of interest. This array then enables indoor prediction from the HAP for any elevation angle and height.

In particular, the simplified method confines the software changes to the field reconstruction block, rather than both the ray tracing and field reconstruction blocks. The technique assumes that losses can be split into three basic multiplicative effects: spreading loss, material loss and fast fading loss [2]. The existing ray tracing software correctly computes material loss. However, fast fading loss (which requires accurate angle distributions) and spreading loss can only be correctly modelled if the distance to the transmitter is accurately modelled. To overcome this problem, the average spreading loss from the low mounted transmitter is removed (by division),

and the true spreading loss from the satellite is added to the result (by multiplication) [5].

The second and far more accurate method places a virtual array of transmitters above and to the side of the building under test. Rays are then launched from this virtual array to emulate the launching of rays from a distant HAP [2][5]. The accuracy of the first method is evaluated in section 6.4 and compared with the more accurate results obtained from the second and more detailed solution described in section 6.3. Testing of the new HAP model is described in section 6.5 and example results for a single building structure are generated in section 6.6.

The chapter ends with a detailed analysis of indoor HAP coverage in the 2GHz UMTS band using the newly modified model. A building database comprising two adjacent multi-storey homes is used as the basis for the study in section 6.7. Indoor coverage is generated with and without space diversity at the user terminal. The work is used to compute the level of transmit power required at the HAP for a given quality of area coverage and also the potential reduction in transmit power resulting from the application of diversity.

6.2 Modelling of HAP to Indoor Propagation

In this section two ray tracing methods for simulating indoor radio coverage from HAP are presented.

6.2.1 Approximating received in-building signal from a distant HAP

This section describes an approximate method for calculating the signal strength from an overhead HAP using results from the indoor propagation model presented in chapter 3. Figure 6.1 shows the basic configuration of the model. The diagram on the left hand side shows the real scenario, while the approximation on the right describes the simplified approximation. In reality, rays should be launched from a distant HAP such that near-perfect parallel waves would pass into the indoor structure [5]. In the approximation, rays are launched from a virtual transmitter placed above the building structure. The main cause of error in this approximation is the spreading loss, which must be corrected in order to obtain valid results. The method also suffers from the

fact that rays launched from the virtual transmitter are not emitted at the angles corresponding to a distant overhead satellite.

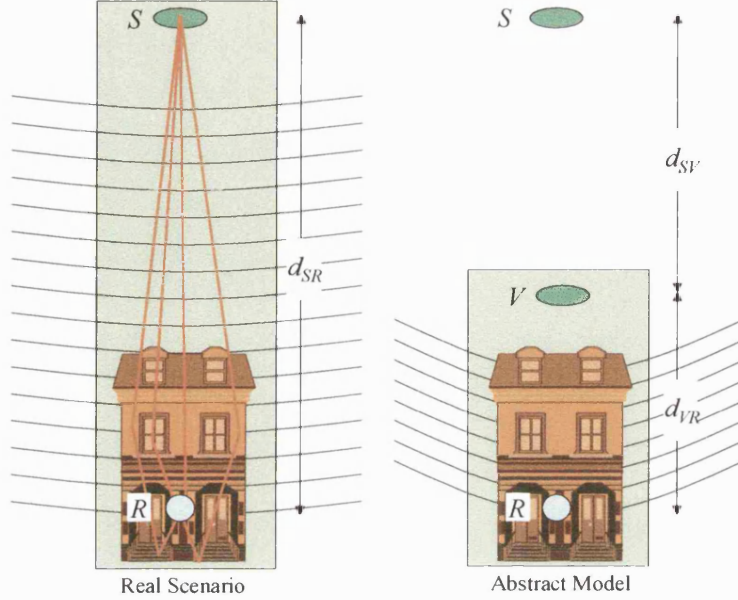


Figure 6.1: Real and Abstract HAP Models

6.2.2 Real Scenario

The signal is assumed to arrive at point R in the house from a distant overhead satellite. The received signal (assuming just a single line of sight path) can be mathematically modelled using the following equation:

$$P_R = P_T G_T G_R \frac{\lambda^2}{(4\pi d_{SR})^2} = \frac{P_T G_T G_R}{L_S} \quad (6.1)$$

where:

$$L_S = \text{Free Space Path Loss} = \frac{(4\pi d_{SR})^2}{\lambda^2} \quad (6.2)$$

It is common to model only the *loss* associated with a transmission path since this allows any transmit power and/or antenna gain to be applied at a later date [6-7]. So, assuming $P_T G_T G_R = 1$, we get:

$$P_R = \frac{\lambda^2}{(4\pi d)^2} = \frac{1}{L_S} \quad (6.3)$$

Some models normalise the free space path loss to equal 1 (0 dB) at a distance of 1 metre [3]. In this thesis we define this normalised loss by the variable, L'_s . In this special case we get:

$$L'_s = 1, d = 1 \text{ hence } L'_s = L_s \frac{\lambda^2}{(4\pi)^2} \text{ or } L_s = L'_s \frac{(4\pi)^2}{\lambda^2} \quad (6.4)$$

Hence, to calculate the true spreading loss from a normalised value, we must multiply the normalised loss by a factor $(4\pi)^2 / \lambda^2$.

For the real scenario shown in figure 6.1, the received signal would actually suffer from three independent losses [8]:

1. Free Space Path Loss , L_S
2. Building Penetration and Shadowing Loss (sometimes called slow fading), L_P
3. Fast Fading Loss (resulting from the vector summation of the various multipaths), L_F

The first loss has already been discussed previously. The second loss occurs due to attenuation as the waves pass through structures such as the roof, ceiling, walls and floors. The third loss occurs since we do not receive just a single path from the satellite, but a number of scattered, reflected and transmitted paths from within the building structure [9-10]. The actual signal is formed from the vector summation of these multipaths.

Hence, mathematically we can rewrite our earlier equation as shown below:

$$P_R = \frac{P_T G_T G_R}{L_S L_P L_F} \quad (6.5)$$

Again, assuming $P_T G_T G_R = 1$, we get:

$$P_R = \frac{1}{L_S L_P L_F} \quad (6.6)$$

Hence, to calculate the overall path loss (or received power assuming $P_T G_T G_R = 1$), we must multiply the three loss factors (losses are expressed in a linear rather than logarithm form). If the losses are in a logarithmic form then they should be summed.

The real scenario cannot be directly modelled using the existing ray-tracing software since it would require the creation of a huge grid (since the transmitter is more than 20 km away from the receiver). Hence, some form of approximation is required. The first of the two approximations proposed in this thesis is discussed in the following section.

6.2.3 Description of Approximation used

The ray-tracing model is used with a Virtual Transmitter (V) placed above the building at a distance manageable for the software (i.e. no more than tens of metres above the roof rather than thousands of metres). The distance above the roof must be sufficient to ensure approximately parallel waves at the rooftop (since the waves from the satellite are almost perfectly parallel). As the Virtual Transmitter is placed higher above the roof, the approximations associated with the method reduce. In the limit, when the Virtual Transmitter is placed at the same height as the HAP (S), the method will produce an ideal result. One aim of this study is to determine the degree of accuracy that can be obtained using this simplified method. This is achieved by comparing field strength predictions in section 6.6 of this chapter against a more accurate method described in section 6.3.

Placing the Virtual Transmitter at a height of say 5 metres, the ray tracer can be used to calculate the received signal over a grid within the building. The received power will be given by:

$$P_R = \frac{1}{L_S L_P L_F} \quad (6.7)$$

Since within the software we assume $P_T G_T G_R = 1$. The software also assumes the received signal is unity at 1 metre (normalised path loss as defined earlier) [3][11].

Since the Virtual Transmitter is far too close to the receiver, the value of the spreading loss is incorrect (since the separation distance is obviously far too small). However, assuming parallel waves are incident on the rooftop, the calculated values for the penetration loss and the fast fading loss will be a reasonable approximation. Hence, the method uses the simulated values of L_P and L_F , but needs to correct for the value of L_S .

First the incorrect spreading loss is removed from the ray-tracing result. This is performed by using equation 6.8:

$$P'_k = \frac{1}{L_S L_P L_F} \left(\frac{4\pi d_{VR}^2}{\lambda^2} \right) \quad (6.8)$$

In logarithmic terms, the spreading loss from the Virtual Transmitter to the Receiver is subtracted from the ray-tracing result. Having now removed the spreading loss associated with the virtual transmitter, the true spreading loss associated with transmissions from the satellite is added. The equation below shows how this HAP spreading loss is applied:

$$P''_k = \frac{1}{L_S L_P L_F} \left(\frac{4\pi d_{VR}^2}{\lambda^2} \right) \left(\frac{\lambda^2}{4\pi d_{SR}^2} \right) \quad (6.9)$$

$$P''_k = \left(L_S L_P L_F \left(\frac{\lambda^2}{4\pi d_{VR}^2} \right) \right)^{-1} \left(\frac{\lambda^2}{4\pi d_{SR}^2} \right) \quad (6.10)$$

In logarithmic terms, the spreading loss from the HAP is added to the previously modified value. This final expression now provides a good approximation for the required received signal inside the building from the distant satellite.

In summary, the received signal is calculated assuming a direct line-of-sight (LoS) spreading loss from the Satellite combined with the building penetration and fast fading loss values from the ray-tracing software. The spreading loss from the ray-tracing software is then removed using the mathematics described in the section.

6.3 Accurate Model for HAP-Indoor Propagation

The method described in section 6.2 only provides an approximate solution for indoor coverage from HAP. In order to generate the correct result rays should actually be launched from the distant transmitter. In this section, the novel use of a virtual transmit array placed just above the building under test is proposed to perfectly emulate this distant launch process.

6.3.1 Use of Virtual Transmitters

A number of modifications will now be made to the ray-tracing software described in chapter 3 to enable accurate propagation prediction from a distant HAP at any elevation angle. The method required modifications to the software within both the ray tracing and field reconstruction modules. Unlike the method described in section 6.2, the technique is accurate and does not rely on approximations. An explanation of the modifications is given, together with the testing procedures used to confirm the correct operation of the new software. Results using this new method are then given in section 6.4 and compared with results from the approximate method described in section 6.2.

We know that real waves traced from the HAP to the building under test will have virtually parallel wave fronts. In the approximate method described in section 6.2, a virtual transmitter was placed above the roof and a mathematical modification performed to correct for the incorrect spreading loss resulting from a spherical wave front. In this accurate method, an array of virtual transmitters is used, also located above the roof of the building in question [2]. However, unlike the earlier method, each virtual transmitter is now used to launch just a single ray. Using knowledge of the HAP and the virtual transmitter locations, a precise launch angle for each virtual transmitter is calculated. This angle is then used to launch a single ray that emulates the path that would have been traced from the distant HAP. By using an array of virtual transmitters, the software can simulate a number of uniformly launched rays from the HAP. To overcome the path length problem (i.e. the shorter distance to the virtual transmitter), modifications are made in both the ray tracing and field reconstruction modules to add the extra path length from the virtual array to the HAP. Using this technique, a number of rays can be launched from the array of virtual transmitters to mimic the set of rays that would have been launched from the HAP. By restricting each virtual transmitter to a single ray launch, by calculating the launch angle using knowledge of the HAP position and by modifying the path length to reflect the distance to the HAP, a novel and accurate simulation can be achieved for any point within the building [5].

The concept of this second technique is shown in figure 6.2. A simple indoor structure is shown comprising two floors (see figure 6.3). An array of N virtual

transmitters is shown at a small distance above the roof. The HAP is then placed above the building approximately 20 km above ground level.

The algorithm now calculates the angle to the first and last virtual transmitter, these are then denoted by the variables angmin and angmax (see figure 6.2). The ray-tracing algorithm now proceeds to trace rays uniformly between these two angles. The step size used in the algorithm is determined by the spacing of the virtual transmitters, which in turn is controlled by the width of the building and the number of transmitters in the virtual array (which can be adjusted to achieve any desired launch angle spacing). The spacing between the virtual transmitters must be smaller than the environmental grid spacing to ensure that the launched rays do not miss illuminating points in the grid.

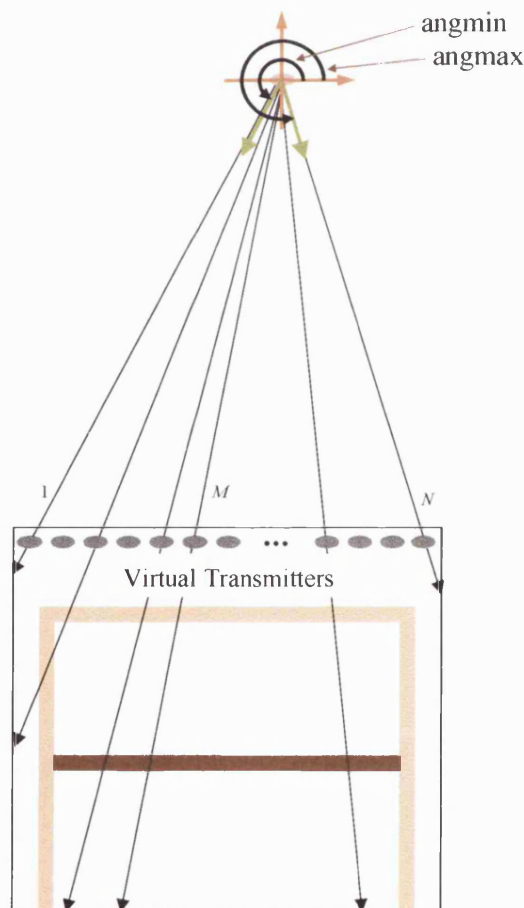


Figure 6.2: Concept of Virtual Transmitters to simulate propagation from distant satellite

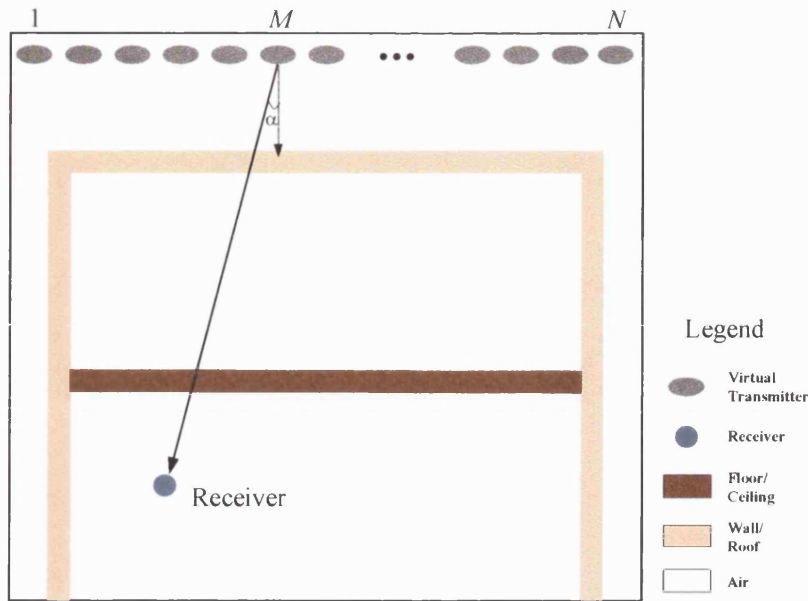


Figure 6.3: Ray-Tracing for a single ray from the M -th virtual transmitter

Figure 6.3 shows the process of a single ray launch for the M -th virtual transmitter. The launch angle, α , is based on the location of the HAP. The indoor environment is based on a 2-D grid structure; with the material property for each grid point defined using a building specific input file. In this simple example, two basic building materials are used, one for the floors and ceiling and another for the walls and roof. For simplicity, detailed furniture and clutter within the building is not included in the model.

6.4 HAP Environment Description and Model Modifications

The test environment used to evaluate the proposed HAP models is now described together with details of the ray model modifications required to support the virtual array method.

6.4.1 Environment Description

As described in section 6.3.2, any indoor environment can be used with the software. In this section, the following simulations are based on an empty (no furniture) two-floor building structure. This structure is shown in figure 6.4 together with the

lengths and widths of each surface. An air gap above the building has been left in which the virtual transmitter array can be located.

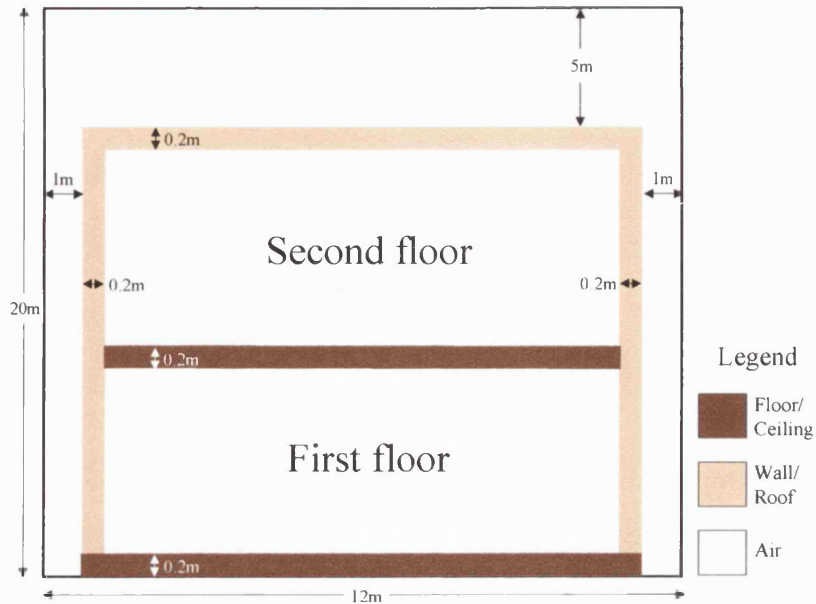


Figure 6.4: Environment structure used in satellite simulation

The roof and walls are constructed from solid concrete (as opposed to aerated concrete used in some structures) while the floor and ceilings are constructed from plaster. A full description of the material parameters is given in table 6.1.

Material	Conductivity (S/m)	Relative permittivity	Thickness (m)
Concrete	0.0014	6.14	0.20
Plaster	0.0006	5.00	0.20

Table 6.1: Material Properties for Satellite Test Structure [10]

6.4.2 Modification of the field reconstruction software

The original ray tracing software was written to study indoor 2-D environments [3][13]. In addition to modifying the software to support HAP illumination, an exhaustive set of tests were performed to confirm the correct operation of the code. In particular, a rigorous evaluation of the software was performed using symmetrical environments. For a symmetrical environment, the output prediction should also be symmetric. Faults in the code can easily be identified as errors in this output

symmetry. In total, there are sixteen blocks of code that must be correctly specified to enable transmission and reflection to be simulated at either a vertical or horizontal boundary. The verification of these code blocks is described in Appendix C.

Based on the above description, it is important to know whether the surface interaction is vertical or horizontal, whether the permittivity has increased or decreased, and the incident angle of the travelling ray. The boundary interaction is considered to be vertical if $r_2 \leq r_1$ and horizontal if $r_2 > r_1$ (see section 3.9 for definitions of r_1 and r_2).

6.5 HAP-Indoor Field Strength Predictions

Having completed a rigorous testing and verification programme for the ray tracing and field reconstruction software (see Appendix B), the new program is now used to analyse HAP coverage in an indoor environment. Two methods have been proposed in sections 6.2 and 6.3. The simplified method uses a version of the original indoor ray tracing software. The accurate method uses the modified virtual transmitter model developed in section 6.3. Results from both techniques will now be given and quality of their predictions compared.

6.5.1 Reconstructed Field Strength: Simplified Method

Figure 6.5 shows the field strength prediction for the indoor environment described in figure 6.4 using the simplified method. Typical field strength values in the region –77dB to –90dB are observed on the roof and –90dB to –100dB on the ground floor.

The result shows a considerable degree of fast fading, and this is thought to result from inaccurate vertical reflections resulting from the low simulated height of the transmitter. If true parallel waves were simulated from the satellite, horizontal reflections would not be observed and fast fading in the horizontal plane would not be observed.

The result implies that the mean field strength should be accurate, however fast fading effects are incorrectly modelled in the simplified approach.

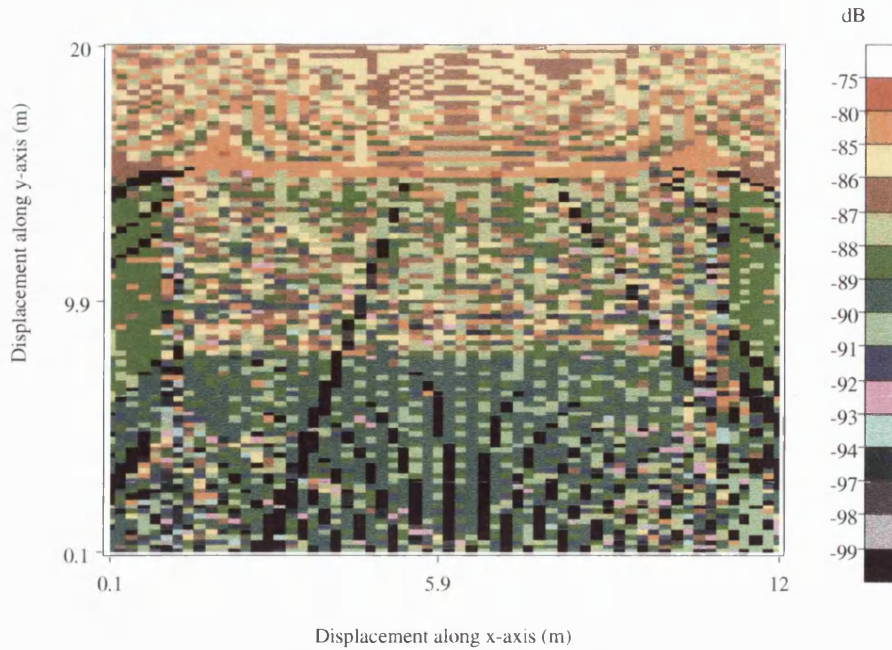


Figure 6.5: Reconstructed Field Strength: Simplified Method

6.5.2 Reconstructed Field Strength: Accurate Method

Figure 6.6 show the field strength prediction for the same environment using the accurate, virtual transmitter technique proposed in this thesis. Figure 6.6 was produced after performing the modifications described in section 6.3.

Typical field strength values in the region -82dB to -89dB are observed on the roof and -88dB to -92dB on the ground floor. These values are similar to those of the simplified method, however as discussed in section 6.6.1, the incorrect vertical reflections in the simplified method result in significant fast fading. This results in considerable variability in the simplified version's results, which show a greater gap between the weakest and strongest field strengths. The accurate modelling method shows predicted field strength is constant in the horizontal plane, since no horizontal reflections occur due to the near parallel nature of the waves from a distant satellite. However, fast fading is seen in the vertical plane due to reflections between the floors and ceilings.

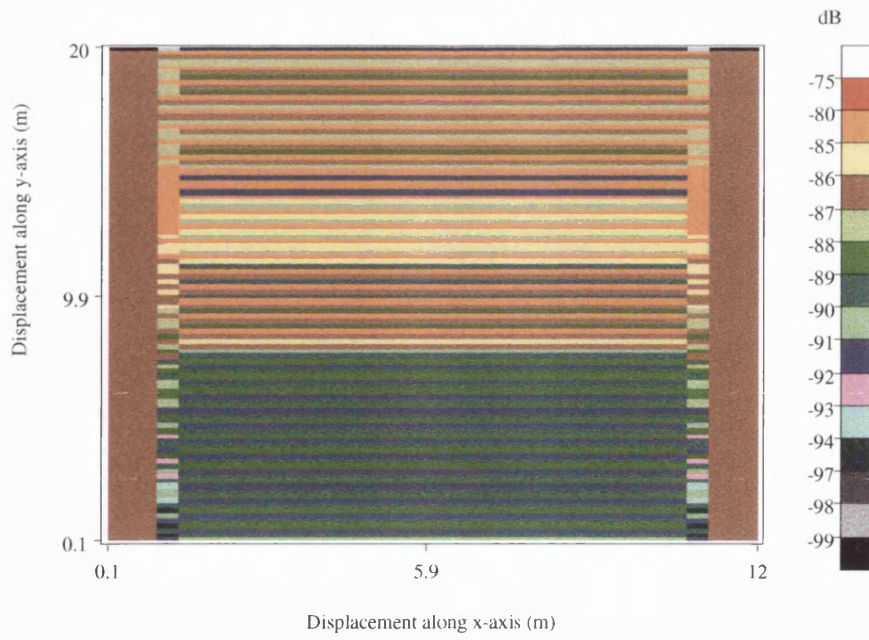


Figure 6.6: Reconstructed Field Strength: Accurate Method

6.5.3 Power CDF and PDF for the Simplified Method

The CDF and PDF of the field strength for the simplified model is shown in figures 6.7 and 6.8.

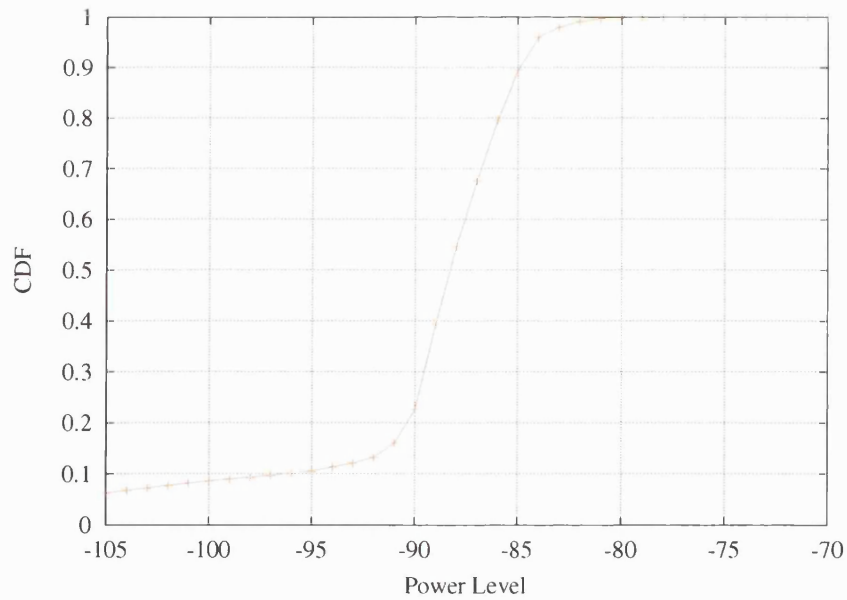


Figure 6.7: Power Cumulative Distribution Function of Simplified Method

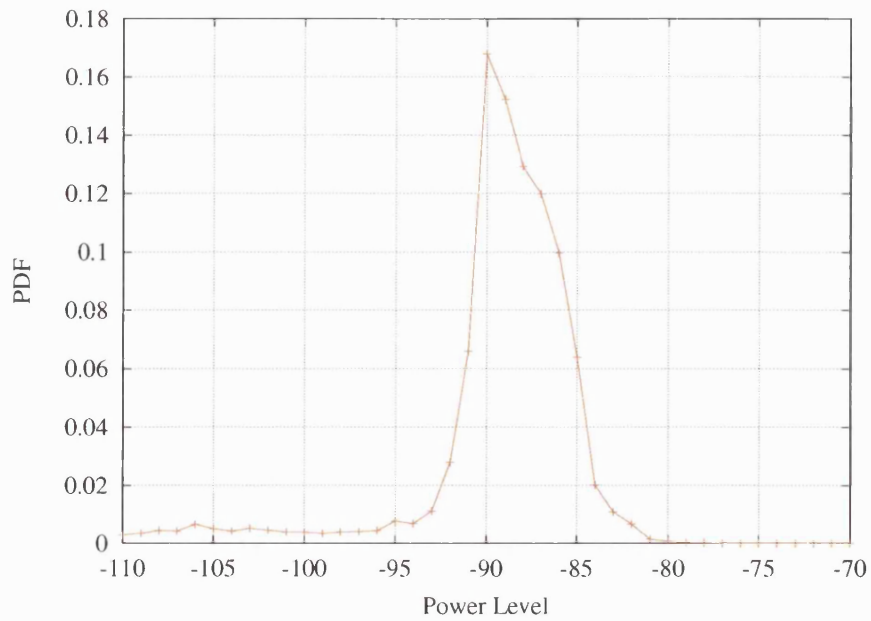


Figure 6.8: Power Probability Distribution Function of Simplified Method

6.5.4 Power CDF and PDF for the Accurate Method

The CDF and PDF of the field strength for the accurate model are shown in figures 6.9 and 6.10.

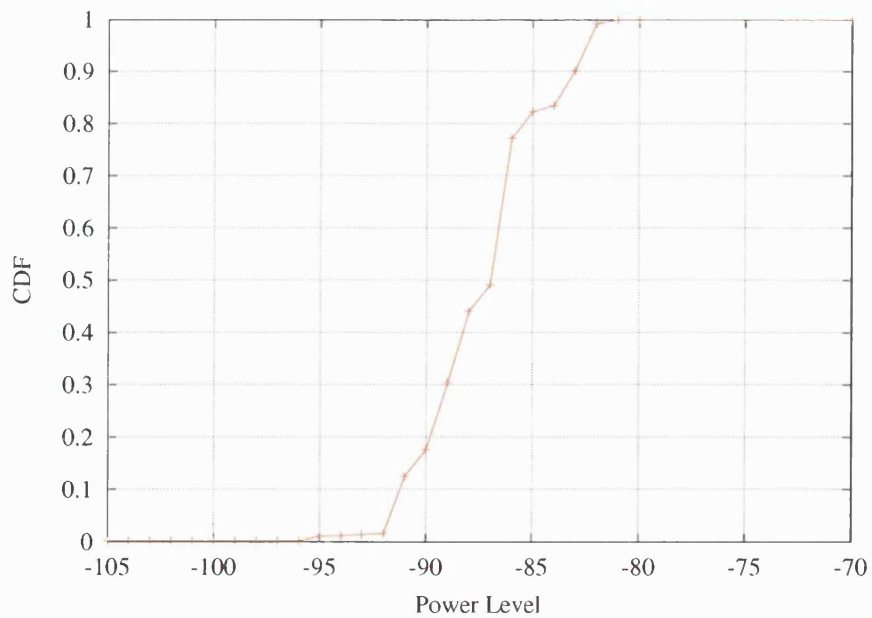


Figure 6.9: Power Cumulative Distribution Function of Accurate Method

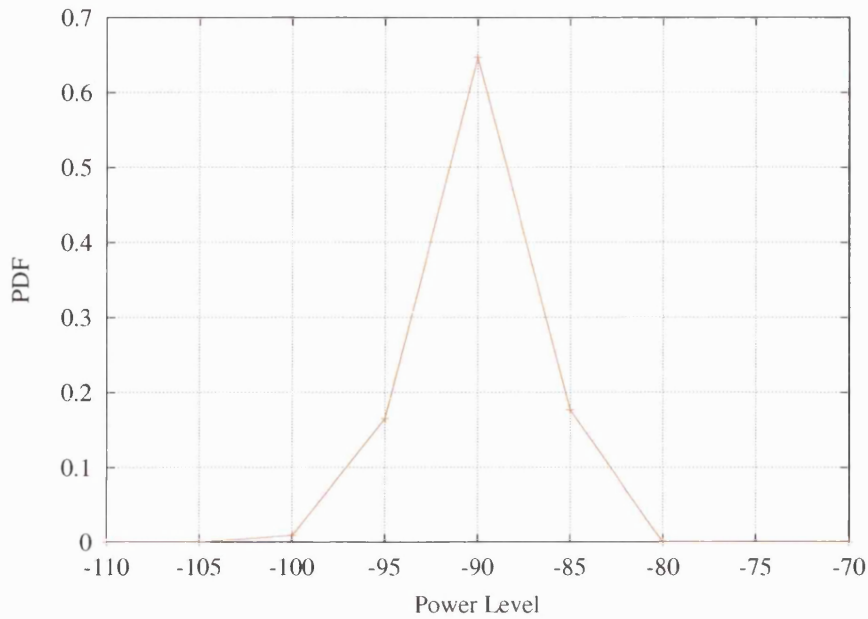


Figure 6.10: Power Probability Distribution Function of Accurate Method

6.5.5 Field Strength CDF comparison for Simplified and Accurate Methods

The CDF of the field strength for the simplified and accurate models are shown together in figure 6.11. This graph shows that the mean field strength is broadly similar for the two techniques, however the tail of the distribution is far higher in the case of the simplified model. This difference is thought to arise from incorrect vertically reflected multipath components in the simplified case. While the simplified method can be used to approximate the mean power in the indoor environment, the accurate method developed in this thesis is required to model accurately more detailed trends such as fast fading effects and the tail of the field strength CDF.

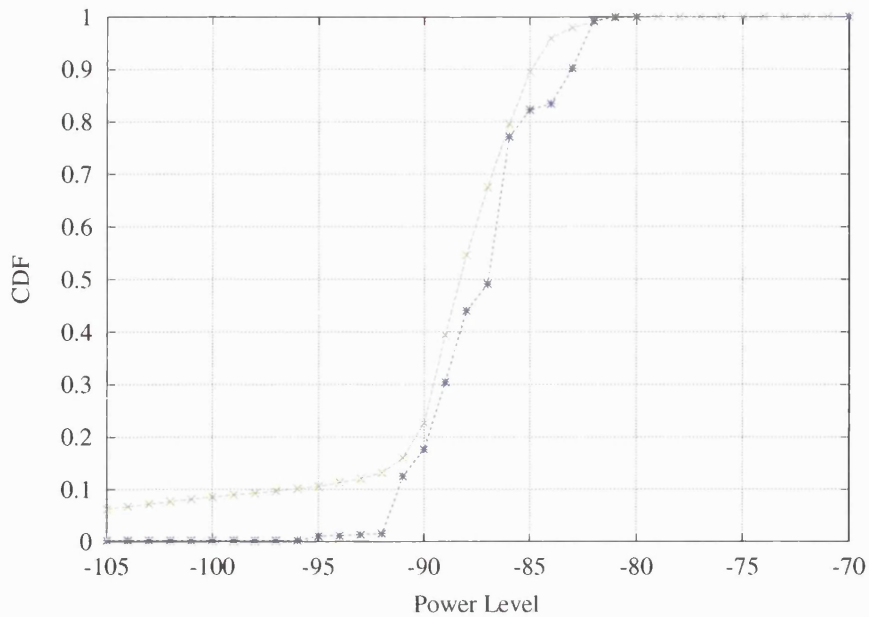


Figure 6.11: Power Cumulative Distribution Function of Simplified and Accurate Methods

6.6 Indoor Propagation and Diversity Evaluation using HAPs

In this section in-building radio coverage at 2GHz from a High Altitude Platform (HAP) is studied using the model developed earlier in this chapter. The HAP is located at a height of 20km above the earth [14]. To improve radio reception, two branch switched and equal gain diversity combining is applied at the mobile terminal. Propagation coverage grids are generated over a pair of multi-floor building structures [15-16]. Results include the calculation of in-building penetration loss and the derivation of link margins for 90% and 99% indoor area coverage. Using this data, the required HAP transmit power is calculated as a function of diversity technique, area coverage and operating bandwidth. The work assumes a 1km radius spot beam and a 3G compatible operating bandwidth of 4MHz. The results indicate that space diversity at the terminal can reduce the required HAP transmit power for a given service quality.

6.6.1 HAP path loss calculation

Wireless communications are known to suffer from fast fading and this can seriously disrupt the quality of the radio link (particularly in non-line-of-sight locations). Indoor

links, with the presence of walls, furniture, etc. are particularly susceptible to fading. The need to improve the link budget is vital in the case of broadband HAP communications.

In this section switched and equal gain diversity techniques are analysed to enhance the radio link for HAP to indoor communication. The analysis concentrates on the use of space diversity with antennas separated at half a wavelength (7.5 cm at 2 GHz). A range of antenna spacings have been analysed, the figure of half a wavelength providing a good compromise between high diversity gain and relatively small physical size.

Figure 6.12 shows the concept of HAP communication. Rather than using a terrestrially mounted basestation, the equipment is mounted, for example, in an unmanned airship (H) located approximately 20km above the surface of the earth [14][17].

Using highly directive spot beams from the HAP, communication occurs with mobile terminals on the ground. HAP systems do not suffer from the high path loss associated with satellite communications. They also avoid the high losses observed in dense urban environments when low mounted terrestrial basestations are used.

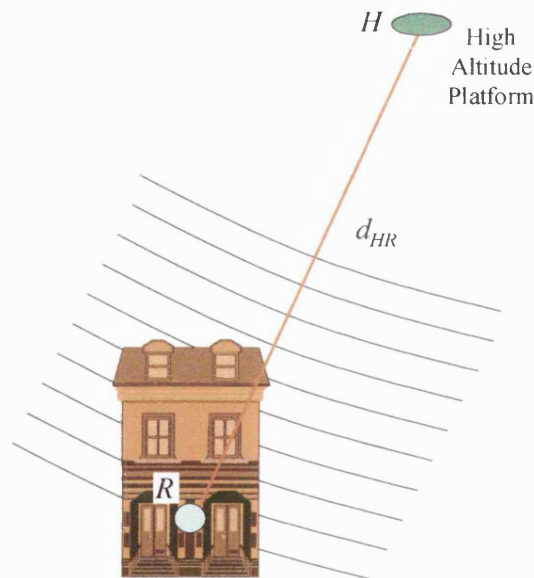


Figure 6.12: HAP Indoor Coverage

The HAP scenario shown in figure 6.22 suffers from three losses L_S , L_P and L_F as discussed in section 6.2.

In practice it is difficult to separate these mechanisms. The first two loss term were discussed back in section 6.2. A shadow loss margin is required to protect against these losses. The third loss occurs since we do not receive just a single path from the HAP, but a number of scattered, reflected and transmitted paths from within the building structure. The actual signal is formed from the vector sum of these multipaths and a fade margin is required to protect the quality of the system. We can write the following equation for the received power, P_{RM} , in a HAP environment:

$$P_{RM} = \frac{P_T G_T G_R}{L_S L_P L_F} \quad (6.11)$$

Again, assuming $P_T G_T G_R = 1$, we get:

$$P_{RM} = \frac{1}{L_S L_P L_F} = \frac{1}{L'_S L_P L_F} \frac{\lambda^2}{(4\pi)^2} \quad (6.12)$$

For the simple LoS example the spreading loss, L_S , at 2 GHz for a separation distance of 20,000 metres is 124.48 dB. The normalised spreading loss, L'_S , is 86.02 dB (a reduction of 38.46 dB due to the normalisation process described in section 6.2). To model the building penetration, shadowing and fast fading losses, a deterministic ray tracing model is used.

6.6.2 HAP ray modelling

It is known that real waves traced from the HAP to the building will have virtually parallel wave fronts. The method used to enhance the ray model places an array of virtual transmitters around the building under test (as shown in figure 6.13). Each virtual transmitter is now used to launch a single ray. This concept is shown in figure 6.13, where the virtual array is seen to traverse the roof and right hand side of the building structure.

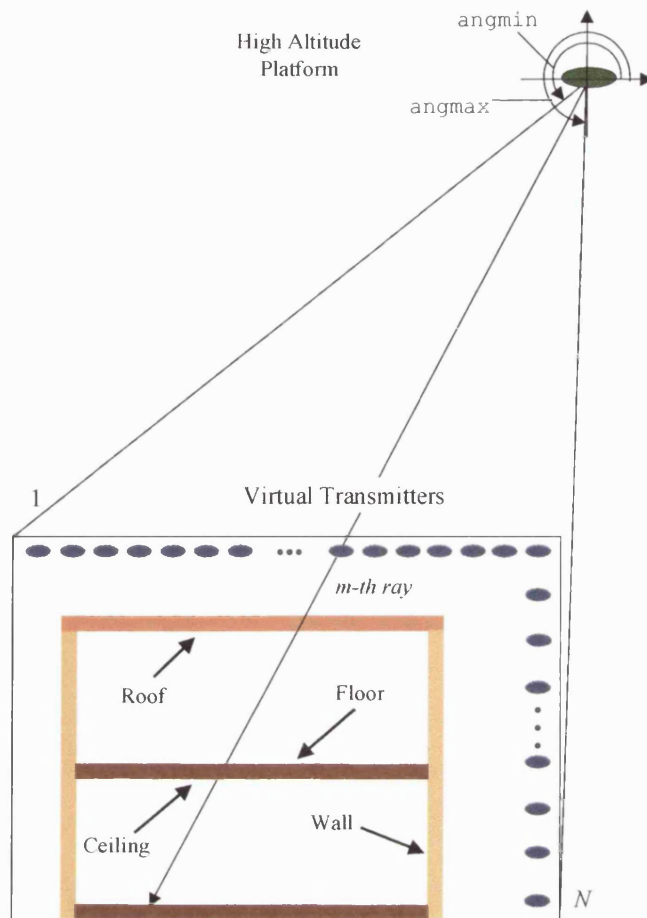


Figure 6.13: Concept of Virtual Transmitters (N = Number of virtual transmitters placed around the building to simulate propagation from a distant HAP)

The extension of the virtual array to the right hand wall (compared to figure 6.2 in section 6.3.2) allows HAP propagation modelling from any elevation angle. This is required since for non-overhead transmissions, the launched rays will impact of the side of the building as well as its roof.

In this study an array of N virtual transmitters is shown above the roof and to the side of the building. The HAP can be located at any height and elevation angle.

6.6.3 Test Environment

The test environment used in this section is shown in figure 6.14. Two multi-storey buildings placed side by side are assumed. The buildings comprise outer load bearing walls, windows, doors, partitions, ceilings, floors and a roof. The HAP is located at an elevation angle of around 60 degrees to the right of the buildings.

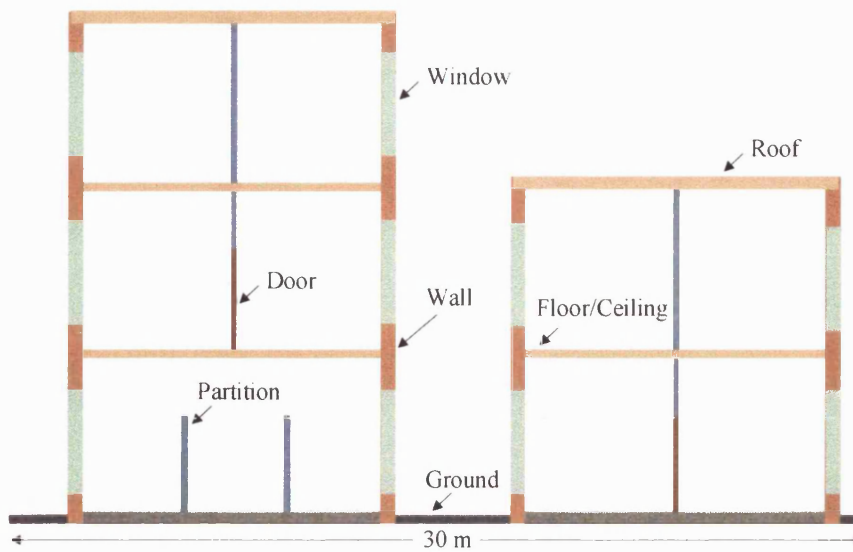


Figure 6.14: Description of Test Environment

Table 6.2 provides a list of the material types, thickness and transmission losses [18-19] assumed in the ray model. Each material in the database has a value of permittivity and conductivity. Using this information, angle dependent transmission and reflection coefficients are calculated in the modelling process [20-21].

Material Type (Env.)	Attenuation (dB/cm)	Thickness (cm)
Wall	0.6	20
Roof	0.5	20
Floor/Ceiling	0.3	20
Door	0.75	4
Partition	0.4	10
Window	2	1
Ground	0.3	20

Table 6.2: Assumed Material Parameters

6.6.4 Propagation results

Figure 6.15 shows the predicted normalised path loss (see section 6.7.2) for the entire grid area. Above each building, a path loss of approximately 87.3 dB is observed (86 dB due to the normalised free space path loss and 1.3 dB due to the use of a vertical

dipole pattern). In practice, fading is seen above the buildings due to the roof-top reflected path. As the rays enter each building, significant penetration is observed for all cases other than windows, where just 2 dB of attenuation is observed. Diffraction is not included in the analysis and as such the path loss may be overestimated in certain shadowed regions. For in building coverage the diffraction is not as critical as reflection and transmission and as such many models neglect the effect [22-24].

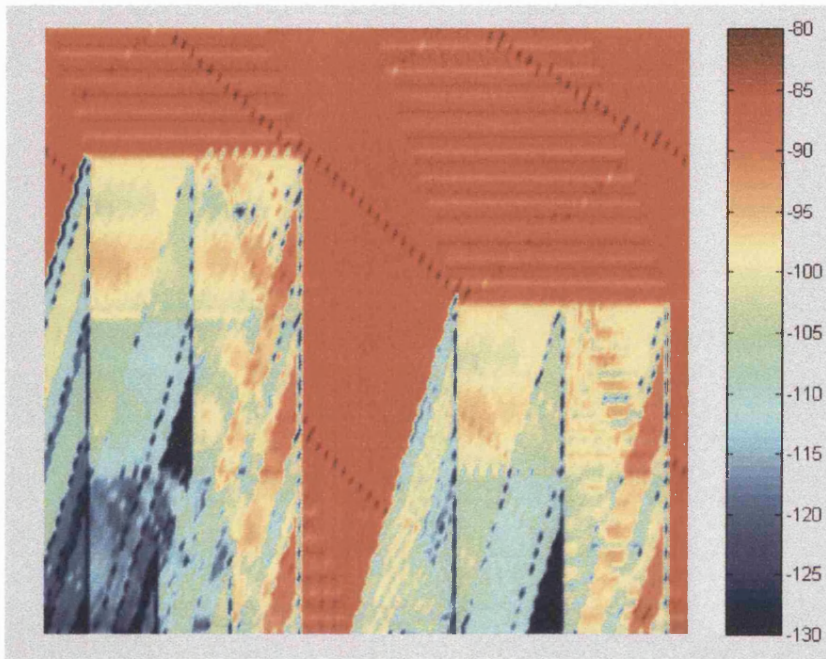


Figure 6.15: Instantaneous Normalised Path Loss (dB)

From figure 6.15 it can be seen that the left-hand side of the ground floor suffers the highest levels of attenuation. To analyse mathematically the in-building instantaneous normalised path loss statistics, the Cumulative Distribution Function (CDF) is shown in figure 6.16 for the case of a single antenna and two branch switched and EGC space diversity.

Figure 6.16 shows that the normalised instantaneous path loss for a single antenna varies from 80 dB to less than 160 dB.

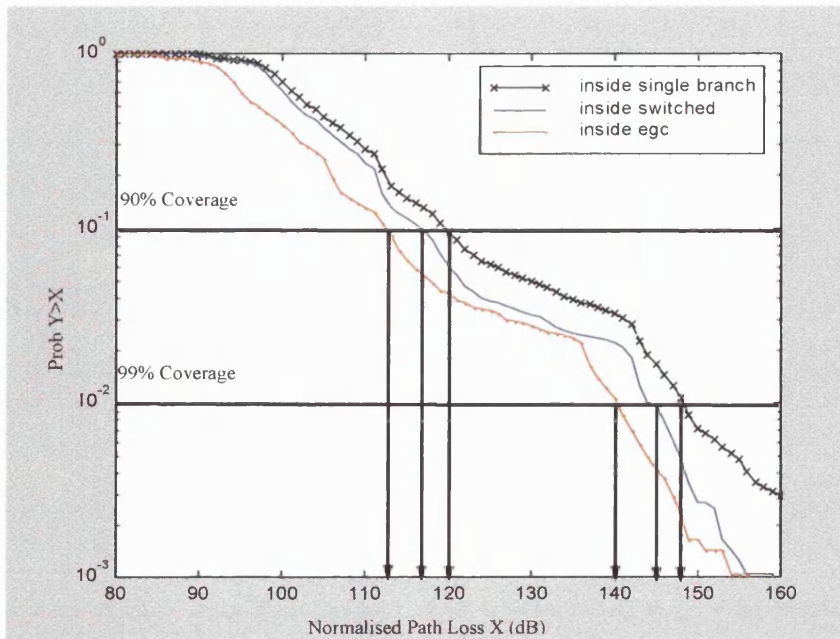


Figure 6.16: Normalised Path Loss CDF

Figure 6.16 can be used to determine the path loss margin required to achieve a given area coverage. Table 6.3 lists the normalised path loss values and margins assuming indoor area coverage requirements of 90% and 99%. The 90% and 99% values were obtained from the 0.1 and 0.01 probability thresholds in figure 6.16. Results are given for single antenna, switched diversity and EGC diversity solutions. Table 6.4 shows the additional path loss (or fade margin) that can be tolerated (relative to the average indoor loss of 97.82 dB). For 90% in-building coverage, for a single antenna an additional loss of 22.0 dB must be tolerated. For 99% coverage, this additional margin increases to 50.3 dB. The far larger 99% margin shows the difficulty of achieving high percentage coverage inside the building.

In the case of ideal equal gain combining, while the mean signal strength increases statistically by 6 dB, the noise floor will increase by 3 dB [25-26]. To compensate for this factor, the fade margin for EGC has been increased by 3 dB.

System	90% Coverage Margin (dB)	99% Coverage Margin (dB)
Single Branch	119.8	148.1
Switched	116.2	145.5
EGC	112.7	140.1

Table 6.3: Normalised Path Loss versus Percentage Area Coverage

System	90% Coverage Margin (dB)	99% Coverage Margin (dB)
Single Branch	22.0	50.3
Switched	18.4	47.7
EGC	17.9*	45.3*

Table 6.4: Path Loss Margin vs Percentage Area Coverage
(* includes an addition 3dB due to increase in noise floor for EGC)

6.6.5 HAP system performance

In this section the required HAP transmit power is calculated as a function of coverage quality, spot beam dimensions, system bandwidth (10 kHz to 4MHz) and diversity technique [27]. The shadow and fade margins given in tables 6.7 and 6.8 are used in the analysis. Table 6.5 shows the link budget for a system operating with 4MHz of bandwidth (similar to that required in 3G) using equal gain combining. From section 6.7.3, an in-building normalised path loss of 97.82 dB is assumed. The additional loss at 1 metre (38.46dB) is also added to the link budget. From table 6.4, the path loss margins for 90% and 99% area coverage are 22.0 dB and 50.3 dB respectively for a single antenna. For EGC, these margins reduce to 17.9 dB and 45.3 dB respectively.

For a bandwidth of 4MHz, the background noise power is given by kTB , where k represents Boltzmann's constant, T the temperature in kelvin and B the operating bandwidth in hertz [28-29]. A temperature of 290 kelvin is assumed in these calculations. Using these numbers, a noise floor of -137.95 dBw is obtained. After adding a 5 dB noise figure (a value compatible with 3G terminals [30-31]), the expected noise power rises to -132.95 dBw.

Assuming (conservatively) that a 10 dB signal to noise ratio is required for acceptable modem performance [32], this implies the received power after adjusting for margins must be -122.95 dBw. The Effective Isotropic Radiated Power ($P_e G_t$) for the HAP can now be computed. For 90% and 99% area coverage, an EIRP of 31.23 dBw and 58.63 dBw respectively is required to balance the link.

	90% Spatial	99% Spatial
Normalised Mean Indoor Loss (dB)	97.82	97.82
Denormalise Loss at 1m (dB)	38.46	38.46
EGC Path Loss Margin (dB)	17.9	45.3
Average Indoor Received Power (dBw)	-105.05	-77.65
Noise Power (5 dB noise figure) (dBw)	-132.95	-132.95
S/N Ratio	10	10
Indoor Power after margins (dBw)	-122.95	-122.95
PtGt (dBw)	31.23	58.63

Table 6.5: Link Budget Example with EGC and 4 MHz BW

The HAP antenna gain can be approximated using equation 6.13, where G_{HAP} , r_{HAP} and r_{SPOT} represent the HAP antenna gain in dBi [33-34], the distance to the HAP in metres and the radius of the spot beam in metres.

$$G_{HAP} \approx 10 \log_{10} \frac{4r_{HAP}^2}{r_{SPOT}^2} \quad (6.13)$$

Assuming the HAP is located 20km above the earth and illuminates the city with a 1km radius spot beam, a HAP antenna gain of 32 dBi is obtained. Under these assumptions, HAP transmit powers of -0.77 dBw (0.84 watts) and 26.63 dBw (460.3 watts) are required for 90% and 99% indoor coverage. This analysis was repeated for operating bandwidths between 10 kHz and 4 MHz with and without diversity at the mobile terminal. Figures 6.17 and 6.18 show the required EIRP at the HAP for 90% and 99% area coverage. These graphs can be used to compute the HAP transmit power for any given HAP antenna gain.

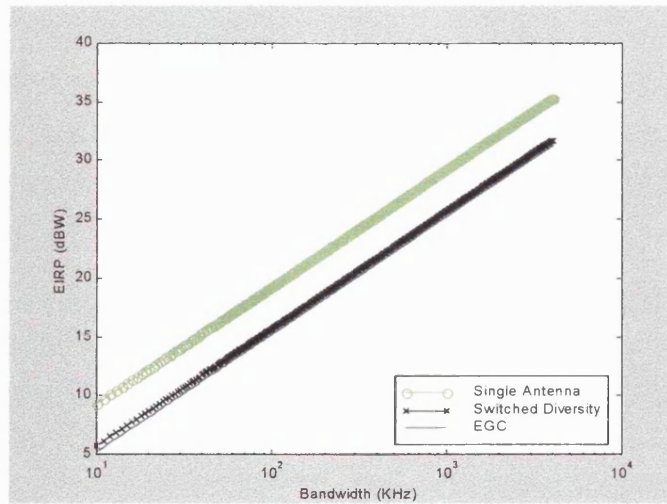


Figure 6.17: Require EIRP at HAP for 90% Area Coverage (10 dB S/N)

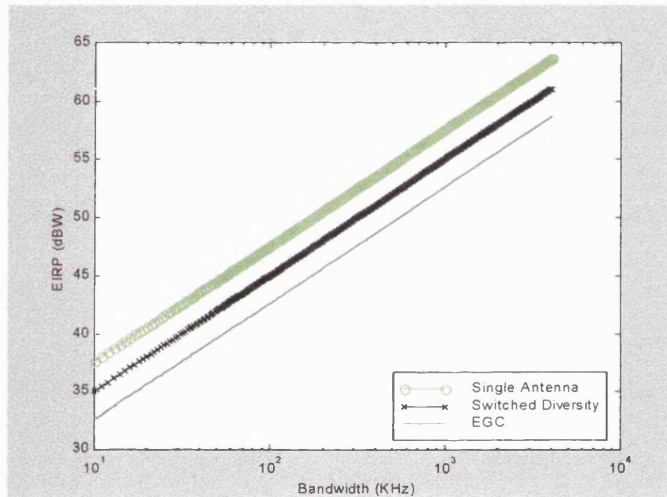


Figure 6.18: Require EIRP at HAP for 99% Area Coverage (10 dB S/N)

Tables 6.10 and 6.11 show the HAP transmit power required for a 32dBi antenna gain as a function of system bandwidth, antenna configuration and area coverage.

	Single Antenna	EGC Combining
10 kHz	-22.69	-26.79
100 kHz	-12.69	-16.79
500 kHz	-5.71	-9.81
4 MHz	3.33	-0.77

Table 6.6: HAP Transmit Power (dBw) for 32 dBi HAP gain and 90% Indoor Area Coverage

	Single Antenna	EGC Combining
10 kHz	5.61	0.61
100 kHz	15.61	10.61
500 kHz	22.59	17.59
4 MHz	31.63	26.63

Table 6.7: HAP Transmit Power (dBw) for 32 dBi HAP Gain and 99% Indoor Area Coverage

Using equal gain combining, for 90% area coverage, the HAP transmit power varies from 2.1 mW (10 kHz) to 0.84 W (4MHz). For 90% coverage the performance on the ground floor would be poor. To achieve 99% indoor area coverage, the HAP transmit power would need to vary between 1.15 W (10 kHz) and 460.3 W (4MHz).

Without the use of diversity, for 90% area coverage, the HAP transmit power would need to vary between 5.4 mW (10 kHz) and 2.15 W (4MHz).

99% area coverage using a single antenna requires HAP transmit powers between 3.64 W (10 kHz) and 1.45 kW (4 MHz). Such high values may be impractical.

6.6.6 Conclusions

This last section has analysed in-building propagation at 2GHz from a HAP. Assuming a 1km radius spot beam, a 3G compatible operating bandwidth of 4MHz and 90% in-building area coverage, the results indicate that space diversity at the terminal reduces the HAP transmit power from 2.15 watts to 0.84 watts. An area coverage of 99% was shown to require unreasonably high transmit powers at larger bandwidths (due to the large margin required) even with diversity at the terminal. For this level of in-building coverage, an outdoor-to-indoor repeater is possibly a more suitable solution.

6.7 Summary of HAP models

This chapter has explained two new modelling techniques for simulating indoor coverage from a distant HAP. The first method was shown to post process field strength results produced from the original indoor simulation software. The second technique used a novel virtual transmitter arrangement to simulate near parallel rays

entering the indoor environment from a distant HAP. A detailed description of the vertical and horizontal interactions has been given, together with an explanation of the angle definitions and formats used within the software. An indoor test environment was defined together with the material characteristics for the frequency of interest.

Results from the first method (where the field strength prediction was made using a single virtual transmitter placed just above the building structure and the distance dependent spreading loss was adjusted to a value based on the true terminal-satellite separation distance) were shown to produce an accurate mean power prediction. However factors such as fast fading and spatial multipath were not correctly modelled, and this was graphically demonstrated by comparing predictions with the second, more accurate method. The cause of error in the first technique was traced to vertical wall reflections resulting from the incorrect launch angles when a low mounted launch site was used to approximate the distant HAP. When ray tracing from a single virtual transmitter, it is not possible to recreate parallel waves accurately.

The second HAP modelling technique used an array of virtual transmitters, each launching a single ray at an angle corresponding to the equivalent that would have been sent from the HAP. This method allowed the HAP to be simulated at any angle in the sky and not just directly above the building. The method correctly modelled the near parallel waves expected, and also confined the analysis to a small grid surrounding the indoor environment (thus easing memory and run time computing constraints). For both techniques indoor coverage grids were produced and a statistical analysis of the modelled results performed.

Finally, a detailed analysis of indoor HAP coverage in the 2GHz UMTS band using the newly modified ray model was performed. Indoor coverage results were generated with and without space diversity at the user terminal. The analysis assumed a 1km radius spot beam, a 3G compatible operating bandwidth of 4MHz and 90% in-building area coverage. The link budget analysis showed that high quality indoor coverage from HAP was indeed possible at UMTS frequencies. In particular, the use of space diversity at the terminal reduces the HAP transmit power from 2.15 watts to 0.84 watts. An area coverage of 99% was shown to require unreasonably high transmit powers at larger bandwidths (due to the large margin required) even with diversity at the terminal.

6.8 References

- [1] J. Thornton, D. Grace, C. Spillard, T. Konefal and T. C. Tozer “Broadband communications from a high-altitude platform: the European HeliNet programme”, *Electronics & Communication Engineering Journal*, pp. 138-144, June 2001.
- [2] F. Tila, P.R. Shepherd and S.R. Pennock, “Analysis of Indoor-Indoor and Satellite/Hap-Indoor Propagation Effects”, *IEE 11th International Conference on Antennas and Propagation, ICAP*, pp. 203-207, April 2001.
- [3] F. Tila, SR. Pennock and PR. Shepherd, “Evaluation of Indoor Propagation Effects and Diversity Techniques”, *Proc. IEE PREP*, pp. 23-25, 2001.
- [4] Ch. Ghobadi, S.R. Pennock and P.R. Shepherd, “Evaluation of Diversity Techniques in Complex Indoor Environment”, *28th European Microwave Conference Amsterdam*, pp. 345-350, 1998.
- [5] F. Tila, PR. Shepherd and SR. Pennock, “2GHz Propagation and Diversity Evaluation for In-Building Communications up to 4MHz Using High Altitude Platforms (HAP)”, *Vehicular Technology Conference, VTC 2001 Fall. IEEE VTS 54th*, vol. 1, pp. 121-125, October 2001.
- [6] K.G. Budden, “The propagation of radio waves”, *Cambridge University Press*, 1st Edition, 1988.
- [7] J.D. Parsons and J.G. Gardiner, “Mobile communication systems”, *Glasgow & Blackie*, 1989.
- [8] A.R. Nix, “Principles of Wideband Propagation”, *IEE Eighth Residential Course on Radio Propagation*, Jan. 2000.
- [9] J.G. Proakis, “Digital Communications”, *McGraw-Hill Co., International Editions*, Third Edition, 1995.
- [10] J.F. Ossanna, “A Model for Mobile Radio Fading due to Building Reflections: Theoretical and Experimental Fading Waveform Power Spectra”, *Bell Syst. Technical Journal*, vol. 43, pp. 2935-2971, 1964.

- [11] Ch. Ghobadi, P.R. Shepherd and S.R. Pennock, "2D Ray-Tracing Model for Indoor Radio Propagation at Millimetre Frequencies and the Study of Diversity Techniques," *IEE Proc.-Microw. Antennas Propagation*, vol. 145, no. 4, pp. 349-353, Aug. 1998.
- [12] L.M. Correia and P.O. Frances, "Transmission and Isolation of Signals in Building at 60 GHz," *IEEE*, pp. 1031-1034, 1995.
- [13] Ch. Ghobadi, P.R. Shepherd and S.R. Pennock, "A 2D Ray-Tracing Model for Indoor Radio Propagation at MM Frequencies and the Study of Diversity Techniques," *High Frequency Postgraduate Student Colloquium, Leeds*, pp. 53-58, Sep. 1997.
- [14] D. Grace, N. E. Daly, T. C. Tozer, D. A. J. Pearce, and A. G. Burr, "Communications performance of High Altitude Platforms Networks operating in the mm-Wave Bands", *Airship Convention*, July 2000.
- [15] W. Pawlowski, "Radio wave propagation effects in high-altitude platform systems", *13th International Conference on Microwaves, Radar and Wireless Communication, MIKON-2000*, vol. 1, pp. 185-188, 2000.
- [16] T. Manabe, Y. Miura and T. Ihara, "Effect of Antenna Diversity on Indoor Multipath Propagation Characteristics at 60 GHz," *IEEE*, pp.1035-1039, 1995.
- [17] <http://www.york.ac.uk/admin/presspr/haps.htm>.
- [18] L.M. Correia and P.O. Frances, "Estimation of Materials Characteristics from power Measurements at 60GHz", *IEEE PIMRC*, pp. 510-513, 1995.
- [19] G.E Athanasiadou and A.R Nix, "A novel 3-D indoor ray-tracing propagation model: the path generator and evaluation of narrow-band and wide-band predictions", *IEEE Transactions on Vehicular Technology*, vol. 49, issue 4, pp. 1152 -1168, July 2000.
- [20] T. Harrold and A.R. Nix, "The indoor-outdoor radio environment", *Electronics & Communication Engineering Journal*, Vol. 12, Issue 6, pp. 249-261, Dec. 2000.
- [21] G.E. Athanasiadou, A.R. Nix and J.P. McGeehan, "A Microcellular Ray-Tracing Propagation Model and Evaluation of its Narrowband and Wideband

- Predictions”, *IEEE Transaction on Vehicular Technology*, vol. 18, no.3, pp. 322-335, March 2000.
- [22] O. Landron, R.S. Roman, R. Shafiei and R. A. Valenzuela, “Wise, A Wireless System Engineering Tool: Measuring Local Mean RF Signal Strength for Propagation Model Validation”, *Bell Labs internal memorandum*, 1994.
- [23] R.A. Valenzuela, “A Ray Tracing Approach to Predicting Indoor Wireless Transmission”, *IEEE Vehicular Technology Conference*, Secaucus NJ, pp. 214-218, May 1993.
- [24] O. Landron, R. A. Valenzuela and A. Houzouris, “A Simplified Method for Creating a Three-Dimensional Building Database for Indoor Site-Specific RF Propagation Modelling”, *Bell Labs internal memorandum*, June 1993.
- [25] A. Jagoda and M. de Villepin, “Mobile Communications,” *John Wiley Ltd*, First Edition, ISBN 0-471-93906-4, 1993.
- [26] Chiann Foo Yu, Lip Lim Woom, R. Tafazolli and L.W. Barclay, “Forward Link Power Control for High Altitude Platform Station W-CDMA System”, *Vehicular Technology Conference, VTC 2001 Fall. IEEE VTS 54th*, vol. 2, pp. 625-629, October 2001.
- [27] F. Tila, P.R. Shepherd and S.R. Pennock, “Indoor Ray Tracing evaluation of enhanced High Frequency communications using Directional Antennas at the Basestation and Space Diversity at the Terminal”, *31st IEEE European Microwave Conference (EuMC)*, pp. 351-355, Sep. 2001.
- [28] T.C. Tozer, D. Grace, “High Altitude Platforms - The future for Broadband Communications”, *Communicate 2000 Online Conference (Invited Paper)*, October 2000.
- [29] F. Dovis, R. Fantini, M. Mondin and P. Savi, “Small-Scale fading for High-Altitude Platform (HAP) Propagation Channels”, *IEEE Journal on Selected Areas in Communications*, vol. 20, no. 3, pp. 641-647, April 2002.
- [30] D. Bull, N. Canagarajah and A.R. Nix, “Mobile Multimedia Communications,” *Academic Press Ltd*, First Edition, ISBN 0-12-140310-6, 1999.

- [31] M.R. Williamson and A.R. Nix, "Investigating the effects of Antenna Directivity on Wireless Indoor Communications at 60 GHz", 8th IEEE Personal and Indoor Mobile Radio Conference, Helsinki, Finland, pp. 635-639, Sept. 1997.
- [32] J. Thornton, D. Grace, M. H. Capstick, T. C. Tozer, "Optimising an Array of Antennas for Cellular Coverage from a High Altitude Platform", *IEEE Transactions on Wireless Communications*,
- [33] J.J. Schlesak, A. Alden and T. Ohno, "A Microwave Powered High Altitude Platform", *IEEE MTT-S International Microwave Symposium Digest*, vol. 1, pp. 283-286, 1988.
- [34] A.M. Street, A.P. Jenkins, J. Thornton and D.J. Edwards, "Low Cost Adaptive Antenna Systems for Indoor Mobile Wireless Communications", *IEEE Antenna and Propagation Conference, Davos, Switzerland*, April 2000.

Chapter 7: Indoor MIMO Communications

7.1 Introduction

Multiple antennas located at the transmitter and receiver have the potential to significantly increase wireless communication capacity [1-2]. Using multiple-input multiple-output (MIMO) techniques, these antennas enable multiple independent channels to be supported in the same bandwidth, but only if the multipath scattering environment is rich enough. Recent research has shown that high theoretical capacities can be achieved in practice. For example in [3] channel capacities as high as 40 bits/s/Hz were demonstrated (in an indoor environment).

The chapter begins with a mathematical analysis of the MIMO channel capacity. Here the well known Foschini equation is applied to Rayleigh and Rician fading channels. The study is performed twice, firstly assuming ideal uncorrelated fading and secondly with perfectly correlated scattering components.

The remainder of the chapter makes use of the indoor deterministic ray tracing model developed in chapter 3. Here the impact of more realistic multipath fading and practical Access Point (AP) and Mobile Terminal (MT) configurations are studied. Importantly, instead of assuming identical and independent (i.i.d) Rayleigh fading statistics and perfect inter-element decorrelation, here capacity is obtained from a detailed ray tracing analysis [4] of the various element to element links in a site specific indoor environment. The work is performed in the 5 GHz band, where indoor systems such as 802.11a and Hiperlan /2 [5] are emerging and expected to operate widely in the near future.

The relationship between the inter-element spacing of a Uniform Linear Array (ULA) and the resulting MIMO capacity is explored via a number of simulation studies. At the AP, the use of micro and macro spaced elements are investigated for a typical indoor environment. The analysis is performed based on two orthogonal MT routes within the test environment. The micro and macro-MIMO analysis is then extended to cover the entire room.

For MIMO systems, capacity is shown to be a function of the received power (as in the single antenna case) and the inter-element fading statistics and correlations in the

H-matrix. The power distribution, capacity and effective rank of the **H**-matrix are computed and displayed as grids covering the entire room. The use of Eigen analysis is used to gain a greater insight into the channel behaviour. Results are generated for normalised and unnormalised MIMO channels (normalisation being applied to the **H**-matrix to generate a constant SNR at all points in the grid).

7.2 Theoretical MIMO Capacity

In this section, the theoretical MIMO capacity is calculated mathematically for a range of array dimensions. The **H**-matrix is initially assumed to consist of identical and independent Rayleigh fading samples. The resulting capacity is then shown to be a random variable whose expected value is used as a measure of average (or expected) capacity. The study is then extended to consider line of sight channels by incorporating Rician statistics. Finally, correlation is imposed in the Rayleigh component of the **H**-matrix and the resulting capacity loss determined.

The following section calculates the theoretical MIMO capacity for a generic communication system comprising N_T transmit antenna elements and N_R receive antenna elements. The analysis is based on the Foschini equation with a large number of realisations over **H** being used to generate a good statistical estimate for the expected capacity.

7.2.1 Ray Modelling and Calculation of the H-matrix

The mathematical study is performed using MATLAB and can be broken down into three main sections. Section 1 generates a set of normalised **H**-matrices, section 2 computes the average capacity and section 3 displays the results. Each of these sections is now described in detail.

7.2.2 Generating the normalised H-matrices (Step 1)

The software calculates average capacity by summing instantaneous capacity over a large number of channel realisations. The number of channels is a user defined variable and was set equal to 2000 for the results shown in this thesis. Beyond this value no further significant convergence was observed. The software requires the user to supply the number of transmit and receive antennas. The user can also define

whether the fading is Rayleigh or Rician distributed. If the latter distribution is chosen then the channel K-factor can be specified (see section 2.3.4). Next the user can specify whether the Rayleigh scatter in the MIMO channels is perfectly uncorrelated or perfectly correlated over the elements. The capacity will be at its highest when the scattering is perfectly uncorrelated. Finally, the user must supply the average SNR per element.

The program generates a deterministic (or line-of-sight) matrix, H_{LOS} and a non-deterministic (or scatter) matrix H_{RAY} . The entries in the deterministic matrix all have a magnitude of unity. The entries in the scatter matrix are taken from the Rayleigh distribution with an average power per sample of unity. In the case of uncorrelated fading, each of the required entries is taken from an identical and independent Rayleigh fading process. In the case of perfectly correlated fading only a single Rayleigh sample is generated per channel realisation and this value is used for all entries in the scatter matrix. The desired Rician \mathbf{H} -matrix is now generated using the expression shown below [6]:

$$H_{ric} = a_s H_{LOS} + b_s H_{RAY} \quad (7.1)$$

where a_s and b_s satisfy the following two equations:

$$a_s^2 + b_s^2 = 1 \quad (7.2)$$

$$K = 10 \log_{10} \left(\frac{a_s^2}{b_s^2} \right) \quad (\text{dB}) \quad (7.3)$$

Equation 7.2 is required to ensure that the average power per element remains at unity in the \mathbf{H} -matrix. Equation 7.3 ensures that the power in the deterministic matrix is set relative to the scatter matrix based on the desired K-factor. To generate the well known Rayleigh result, a large negative value must be entered for the K-factor in dB. This results in $a_s=0$ and $b_s=1$.

The software is now used to study the following MIMO configurations: $(N_T * N_R) = (1 \times 1)$, (2×2) and (4×4) . In practice, the software can analysis any combination of transmit and receive configuration.

7.2.3 Calculating Average Capacity (Step 2)

For each of the n channel realisations generated in Step 1, the capacity is now calculated from the Foschini equation (see section 2.7). The sum of all n instantaneous capacities is then computed and divided by n to generate an estimate of the average capacity. To illustrate the random nature of MIMO capacity, Figure 7.1 shows a plot of instantaneous capacity for a 4x4 MIMO system at an SNR of 16dB (this level is used for all normalised calculations later in the chapter) [7]. The analysis assumes uncorrelated Rayleigh fading and is performed for 2,000 independent channel realisations. The resulting average or expected capacity is 17.36 bits/s/Hz (denoted by the yellow line in figure 7.1). It should be noted that the instantaneous capacity fluctuates considerably around this value depending on each specific \mathbf{H} -matrix realisation.

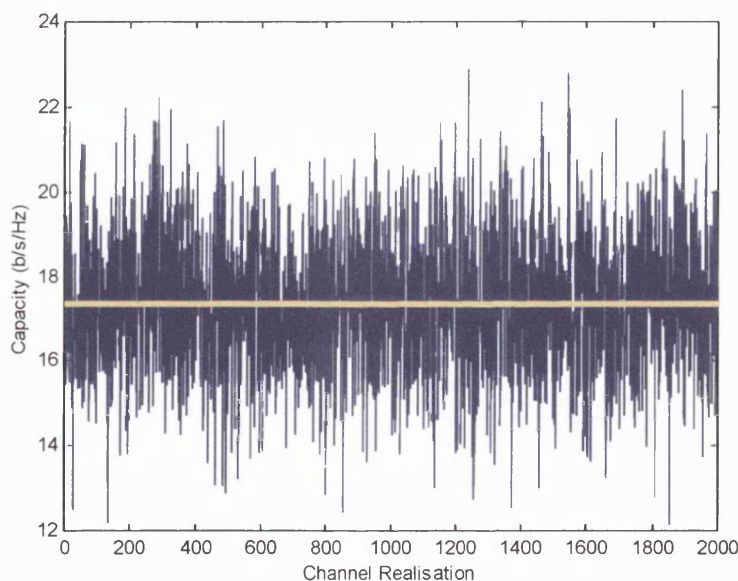


Figure 7.1: Theoretical instantaneous Rayleigh capacity for a 4x4 system, $S/N=16$ dB

7.2.4 Displaying the Results (Step 3)

Having calculated the average capacity for a range of K-factors and SNR values, the third and final step is to display these results in graphical form. Section 7.3 discusses the results for the three configurations defined in section 7.2.2.

7.3 Theoretical MIMO Results and Discussion

In this section the theoretical MIMO results are introduced and discussed. Results are generated and compared with perfectly uncorrelated and perfectly correlated scatter.

7.3.1 Single Antenna Configuration

Figures 7.2 and 7.3 show the resulting capacities for a single antenna communication system as a function of S/N ratio and Rician K-factor. From figure 7.2 it can be seen that the capacity rises with increasing signal to noise ratio. This is to be expected from the well-known Shannon equation, which was discussed in section 2.6.

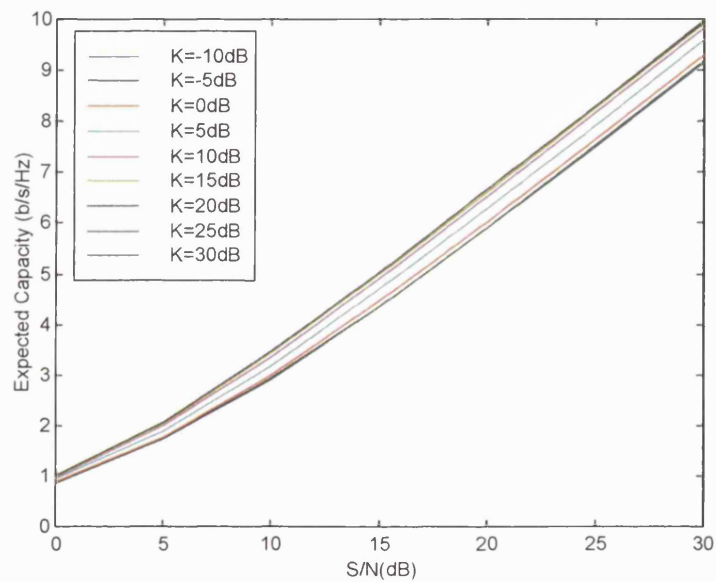


Figure 7.2: Capacity versus S/N ($1T_x - 1R_x$)

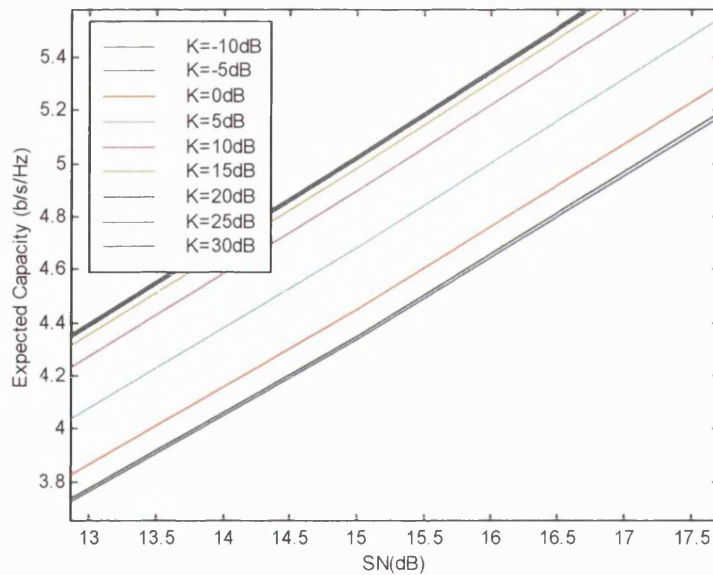


Figure 7.3: Capacity centred on 16dB SNR (1Tx-1Rx)

At an SNR of 16dB the resulting channel capacity is around 4.6 bits/s/Hz [8] for a Rayleigh channel and 5.2 bits/s/Hz for an AWGN channel (i.e. a dominant line-of-sight resulting in a high positive K-factor). For the single antenna case, the introduction of narrowband scattering is seen to lower the resulting channel capacity.

For single antennas, higher levels of capacity are best exploited using higher level modulation schemes. In channels with variable SNR, the use of adaptive modulation (i.e. BPSK, QPSK, 16-QAM, 64-QAM) is common with the higher constellation sets being used to take advantage of the greater channel capacity.

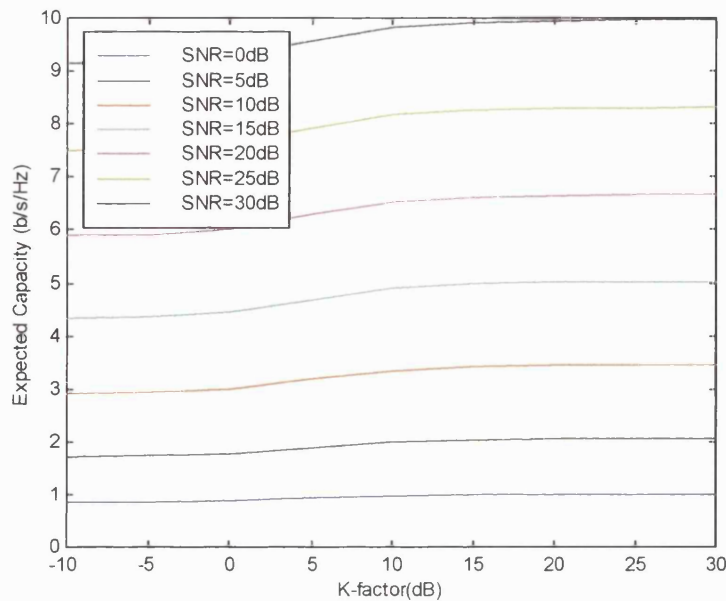


Figure 7.4: Capacity versus K -factor (1Tx-1Rx)

Figure 7.4 shows more clearly that in a Single Input Single Output (SISO) channel the average theoretical capacity drops under Rayleigh conditions (i.e. K -factor = -10 dB). As the channel K -factor increases, the capacity is seen to rise until it reaches a maximum level at around 20 dB. This graph explains why narrowband multipath is seen as a problem to be avoided in the single antenna case. Many techniques (such as antenna diversity) exist to combat the detrimental effects of Rayleigh fading. However, as will be seen in the later graphs, MIMO systems are able to exploit the multipath scatter significantly to improve capacity.

7.3.2 MIMO Configuration (2 transmit, 2 receive antennas)

Figures 7.5 and 7.6 show the MIMO capacities for uncorrelated scatter based on two transmit and two receive antennas. Figure 7.5 shows that capacity once again increases with increasing S/N ratio. However, figure 7.6 clearly shows that capacity now increases as the channel K -factor decreases, reaching a maximum under Rayleigh conditions.

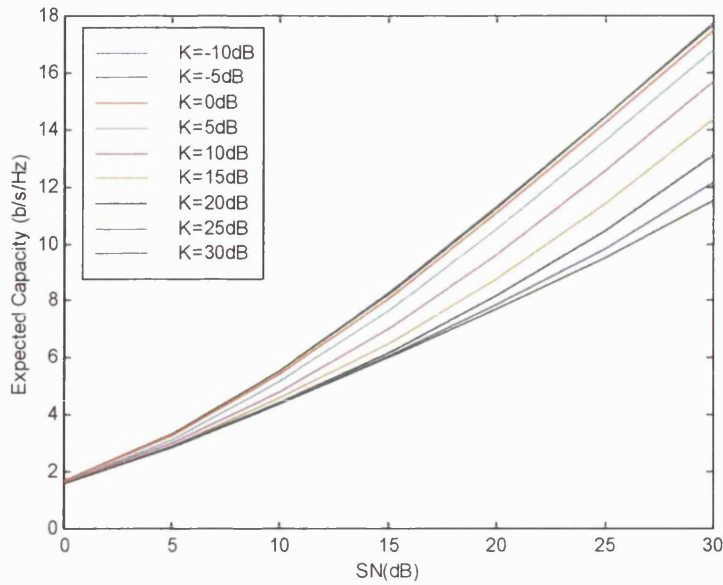


Figure 7.5: Capacity versus S/N (2Tx-2Rx ideal uncorrelated)

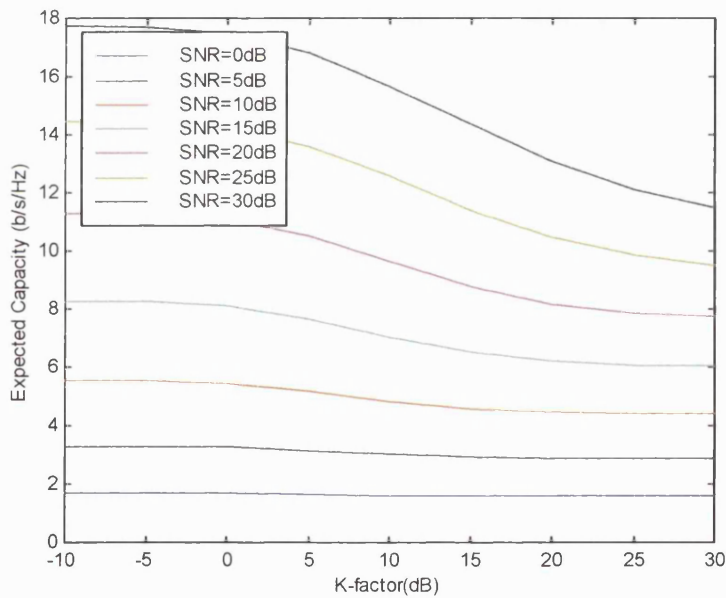


Figure 7.6: Capacity versus S/N and K -factor (2Tx-2Rx ideal uncorrelated)

For an SNR of 16dB, the capacity for a 2x2 MIMO system in uncorrelated scatter can be seen to lie between 6 and 8.5 bits/s/Hz [9]. From figure 7.6 it is clear that the highest values occur in a rich scatter Rayleigh fading environment. This result clearly demonstrates the power of a MIMO system compared with a SISO configuration (figure 7.3).

For MIMO systems it is important to deploy radio systems in such a way as to ensure a rich multipath scattering environment if capacity is to be maximised. From figure 7.6, at an SNR of 30dB, capacity is seen to rise from just under 12 bits/s/Hz in a strongly Rician channel to just under 18 bits/s/Hz in a Rayleigh channel. This compares for the SISO case to 10 bits/s/Hz in a Rician channel and just over 9 bits/s/Hz in a Rayleigh channel. Clearly, under Rayleigh conditions, for an SNR of 30 dB the 2x2 MIMO case (relative to SISO) offers around 100% more theoretical capacity. In strong Rician channels, the advantages of MIMO are less apparent (i.e. an increase of just 20%).

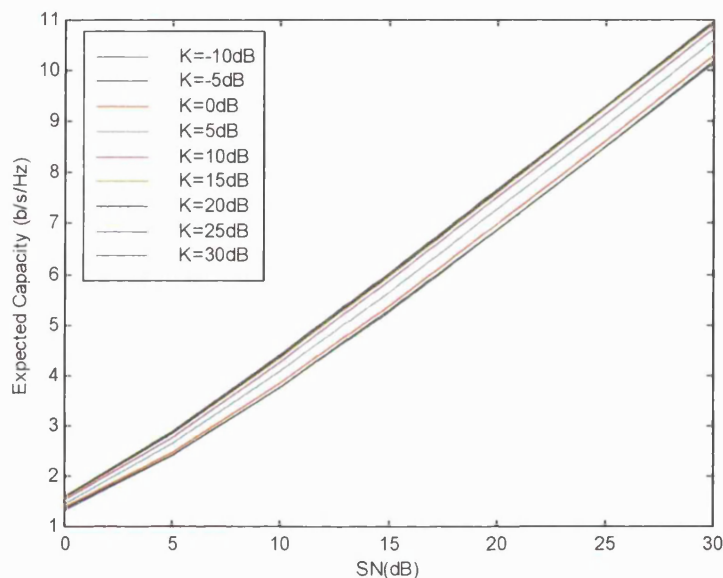


Figure 7.7: Capacity versus S/N (2Tx-2Rx perfectly correlated)

Figures 7.7 and 7.8 shows a similar set of graphs for the case of perfectly correlated scattering. Once again, capacity increases with increasing SNR (figure 7.7). However, in the case of correlated scattering, the capacity no longer improves with increasing scattering. The capacity in a Rayleigh fading channel can clearly be seen to fall relative to the Rician case. This is to be expected since in the case of correlated fading the array offers little benefit. From figure 7.8, at an S/N of 30dB, the capacity for a Rician channel remains at 11 bits/s/Hz, however this falls to just over 10 bits/s/Hz in a Rayleigh channel. While this is still better than the SISO case (10 bits/s/Hz in a Rician channel and just over 9 bits/s/Hz in a Rayleigh channel), the performance is clearly

very disappointing. These results show that the best MIMO performance is achieved in a strong uncorrelated scattering environment. However, for SISO systems the best performance is always achieved in a strong Rician channel.

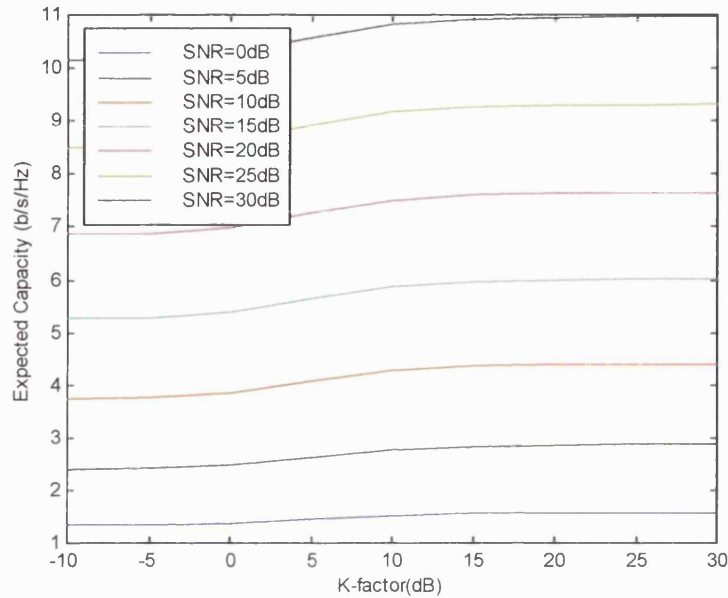


Figure 7.8: Capacity versus K-factor (2Tx-2Rx perfectly correlated)

7.3.3 MIMO Configuration (4 transmit, 4 receive antennas)

Figures 7.9 and 7.10 show the capacities for an uncorrelated MIMO configuration based on four transmit and four receive antennas. This type of configuration is expected to exploit further a multipath rich environment.

Figure 7.9 shows capacity increasing with enhanced SNR. Figure 7.10 shows once again that the capacity increases as the channel K-factor decreases. From figure 7.10, at an S/N of 30dB, capacity is seen to rise from 14 bits/s/Hz [10] in a strongly Rician channel to 35 bits/s/Hz in a Rayleigh channel. This compares with the SISO case to 10 bits/s/Hz in a Rician channel and just over 9 bits/s/Hz in a Rayleigh channel. For a 4x4 antenna configuration, the expected capacities are far higher than the 2x2 case and the improvement in Rayleigh (compared to Rician) to is also far higher, at around 150%.

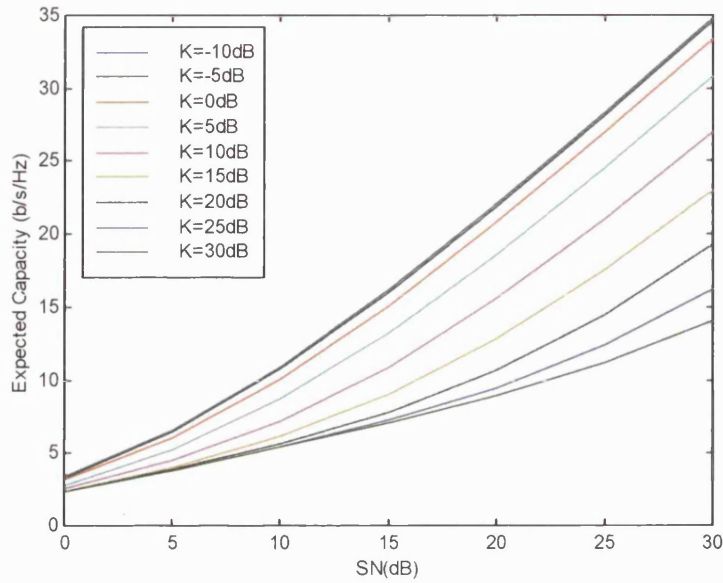


Figure 7.9: Capacity versus S/N and K -factor ($4T_x - 4R_x$ ideal uncorrelated)

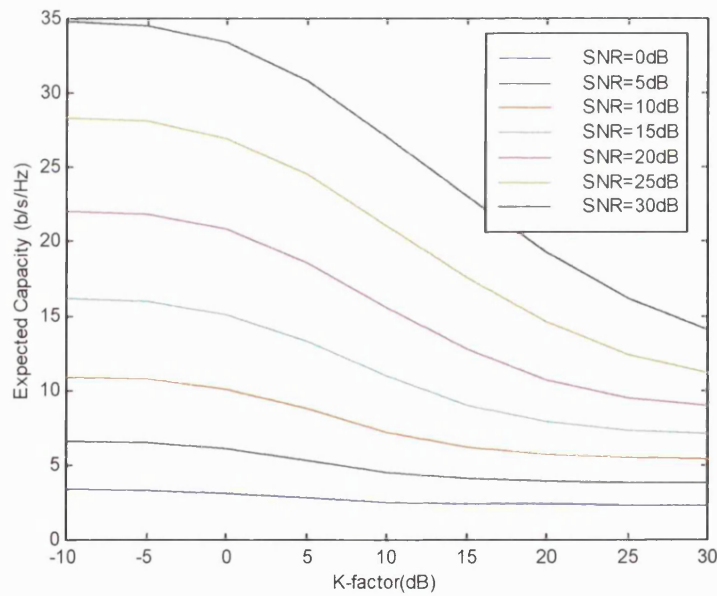


Figure 7.10: Capacity versus S/N and K -factor ($4T_x - 4R_x$ ideal uncorrelated)

Figures 7.11 and 7.12 show a similar set of graphs for the case of perfectly correlated scattering in the \mathbf{H} -matrix. Once again, capacity increases with increasing signal to noise ratio (figure 7.11). However, in the case of correlated fading, the capacity no longer improves with increasing scattering.

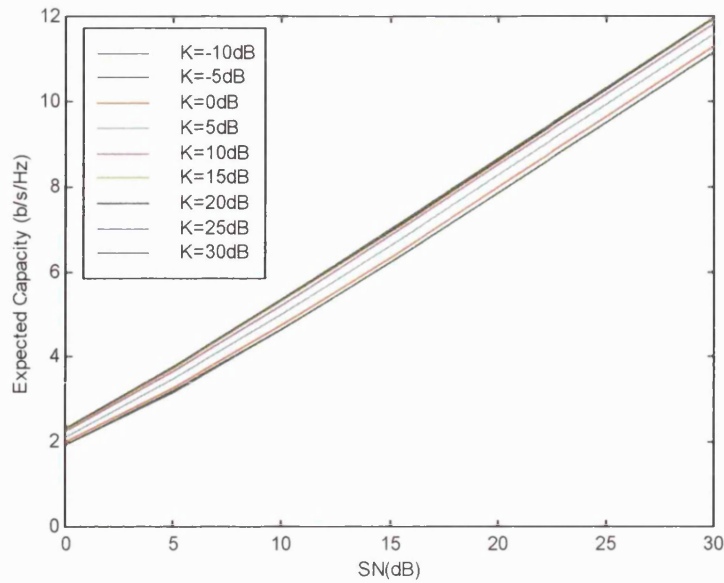


Figure 7.11: Capacity versus S/N ($4T_x - 4R_x$ perfectly correlated)

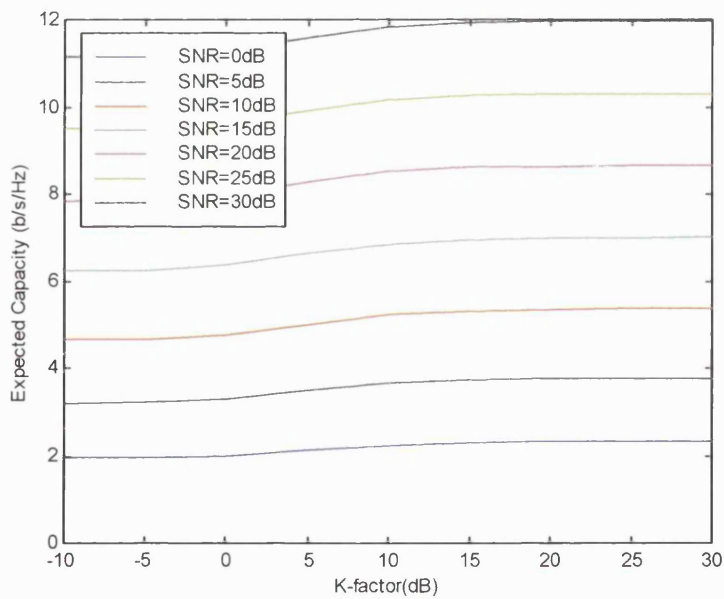


Figure 7.12: Capacity versus K -factor ($4T_x - 4R_x$ perfectly correlated)

From figure 7.12, the capacity in a Rayleigh fading channel can clearly be seen to fall relative to the Rician case. From figure 7.12, at an S/N of 30dB, the capacity for a Rician channel is 12 bits/s/Hz, however this falls to just over 11 bits/s/Hz in a Rayleigh channel. While this is still better than the SISO case, compared to the spectacular gains in uncorrelated scattering, the performance is clearly poor.

7.4 MIMO Deterministic Modelling

In sections 7.2 and 7.3 mathematical modelling was used to analyse the performance on SISO and MIMO communication systems. This work assumed certain statistical distributions for the fast fading component within the \mathbf{H} -matrix. In particular, the correlation of the scattering within the H-matrix was shown to have a dramatic effect of the potential capacity. In this section the ray tracing model described in chapter 3 is applied to perform propagation analysis for a MIMO system. The ray model is used to determine the magnitude of the received signal between any two elements in the MIMO system. By performing this analysis for all transmit/receive elements, the \mathbf{H} -matrix can be built up in an entirely deterministic manner. Rays are sent out in all directions from transmit antenna element k ($1..N_T$) and traced throughout the environment to determine those arriving at receive antenna element, n ($1..N_R$). Assuming $L_{n,k}$ rays are found between these two elements; the received signal $h[n,k]$ is calculated from the following vector sum:

$$h[n,k] = \sum_{m=1}^{L_{n,k}} T_m = \sum_{m=1}^{L_{n,k}} A_m \angle \theta_m \quad (7.4)$$

where A_m and θ_m represent the amplitude and phase of the m -th multipath component linking transmit element k to receive element n and T_m is transmission factor for the ray from transmitter to receiver. The \mathbf{H} -matrix is now constructed as shown in equation 7.5, where each element weight can be calculated from equation 7.4. To calculate the entries for each \mathbf{H} -matrix, a total of N_T by N_R ray tracing point-to-point studies must be performed.

$$\mathbf{H} = \begin{bmatrix} h[1,1] & \cdots & h[1,N_T] \\ \vdots & \ddots & \vdots \\ h[N_R,1] & \cdots & h[N_R,N_T] \end{bmatrix} \quad (7.5)$$

Using this approach, the \mathbf{H} -matrix can be calculated deterministically based on the location and structure of each transmit and receive array [11]. This enables the impact of factors such as array geometry (linear, circular etc), element placement and spacing to be determined for a MIMO system.

A new indoor environment (see figure 7.13) is generated that consists of walls, doors, tables and desks. The material properties for these objects are summarised in Table 7.1.

Part	Material	Permittivity	Conductivity
Wall	Concrete	5.01	0.1368
Door	Wood	2.03	0.0006
Table / Desk	Wood	2.01	0.0006

Table 7.1: Material conductivity & permittivity [12]

The environment dimensions are approximately 10 metres by 10 metres. The three doors are located on three different sides of the office.

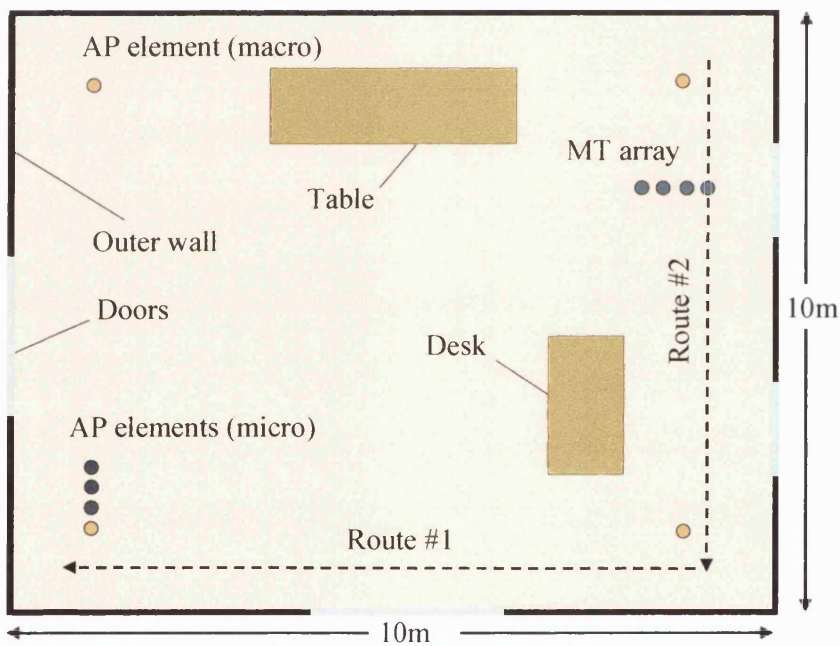


Figure 7.13: Indoor Environment with Micro and Macro MIMO configuration

For this environment the resulting multipath creates a high degree of decorrelation over the transmit and receive arrays. The Wireless LAN radio and array configuration is summarised in Table 7.2.

In section 7.4.2 the mathematical analysis required to extract the expected received power and signal to noise ratio along the test routes (shown in Figure 7.13) is

explained. This data is then inserted into the Foschini equation to generate capacity bounds for the chosen MIMO configurations and array spacings.

Parameter	Setting
Carrier Frequency	5.1 GHz
Carrier Wavelength	5.8 cm
Transmission Bandwidth	20 MHz
Noise Temperature and Figure	290°K, 10 dB
Transmit power per element	Fixed at 0.1mW (-40 dBw)
Transmit Antenna Array (micro)	4 element ULA – spacing varied from 0.1 to 1.0 wavelengths
Transmit Antenna Array (macro)	4 elements placed near corners of room
Receiver Antenna Array	4 element ULA = spacings varied from 0.1 to 1.0 wavelengths

Table 7.2: MIMO test parameters

7.4.1 Micro and Macro MIMO

In most theoretical studies the array elements are assumed to be perfectly decorrelated and to experience Rayleigh fading statistics. With the use of a ray tracing model the antenna decorrelation and fading statistics now depend on the site specific environment and the AP and MT array configurations and locations. In the following analysis the number of transmit and receive elements, N_T and N_R , are fixed at four (although the software supports any number of elements).

Two types of antenna system are explored. The first assumes a ULA of vertically polarised dipoles at both the AP and MT (shown as blue elements in Figure 7.13). For this scenario, the inter-element spacing is varied from 0.01λ to λ , where λ represents the carrier wavelength. This approach is referred to as micro-MIMO and is the standard deployment for this type of system. The second configuration explores the use of wide-area or macro-MIMO (shown as the yellow AP elements). Here, the AP

elements are distributed across the indoor environment. In this configuration the distance between the nearest transmitters is 110 times the wavelength. Since $N_T = 4$, a single transmit element is placed near each corner of the room as shown in Figure 7.13. In this second case the MT array and the inter-element spacings are identical to those used in the micro-MIMO study.

7.4.2 Average Received Power, Normalisation and Channel Capacity

At a point d along the measurement route the resulting \mathbf{H} -matrix can be denoted by $\mathbf{H}(d)$. The total instantaneous received power at this point $P_r(d)$ is given by:

$$P_r(d) = \sum_{n=1}^{N_T} \sum_{k=1}^{N_R} H(d)[n, k]H(d)[n, k]^* \quad (7.6)$$

where ‘*’ represents the complex conjugate. It now follows that the instantaneous average received power per element at point d is given by:

$$\bar{P}_e(d) = \frac{P_r(d)}{N_T N_R} \quad (7.7)$$

Although $\bar{P}_e(d)$ is calculated as an average of $N_T \times N_R$ samples, in cases where $N_T \times N_R$ is small (or where the $\mathbf{H}(d)$ matrix is correlated), then the averaging process is insufficient (since the expected power requires a large number of uncorrelated samples to converge) and the resulting value of $\bar{P}_e(d)$ is statistically inaccurate (i.e. the short ensemble average is not a good approximation of the expected value). To obtain a more accurate estimate of the average received power per element, it is desirable to spatially average over some small section of the measurement route. This form of averaging helps to remove any residual fast fading effects that still exist after averaging internally within the \mathbf{H} -matrix (i.e. over the $N_T \times N_R$ links at a single spatial point). The average received power per element calculated over a section of the measurement route $\bar{\bar{P}}_e(d)$ is now given by equation 7.8 where $2K+1$ represents the number of measurement samples used in the averaging process and d represents the location where the averaging is centred. The distance along the route is given by $(d + r\Delta)$, where d represents the point number and Δ the spatial step size between measurements. K is chosen so as to suitably average the residual fast fading in the \mathbf{H} -

matrix. Typically, K would be chosen such that the following inequality is satisfied $5\lambda < (2K+1)\Delta < 10\lambda$ [10] [13].

$$\bar{P}_e(d) = \frac{\bar{P}_r(d)}{N_T N_R} \quad \text{where} \quad \bar{P}_r(d) = \frac{1}{2K+1} \sum_{r=-K}^{K_i} P_r(d+r\Delta) \quad (7.8)$$

In the evaluation of the Foschini capacity bound [3] it is necessary to estimate the average signal to noise ratio. It is also vital to normalise correctly the $\mathbf{H}(d)$ matrix to ensure that the expected received power per element is unity. Failure to correctly normalise the $\mathbf{H}(d)$ matrix will result in a double counting of power (i.e. in both the \mathbf{H} -matrix and the SNR term).

Given knowledge of the receiver's noise floor (see equation 2.17) and the expression for average power from equation 7.8, the average signal to noise ratio $\bar{\gamma}_i(d)$ at any point along the route can be calculated from equation 7.9.

$$\bar{\gamma}_i(d) = \frac{\bar{P}_r(d)}{N} \quad (7.9)$$

Finally, the instantaneous $\mathbf{H}(d)$ samples are normalised as shown in equation 7.10, where $\mathbf{H}_n(d)$ represents the normalised $\mathbf{H}(d)$ matrix with unity average power per element.

$$\mathbf{H}_n(d) = \mathbf{H}(d) / \bar{P}_e(d) \quad (7.10)$$

From equations 7.9 and 7.10 the average MIMO capacity $C(d)$ can now be calculated at each point along the route using the well known Equation 7.11.

$$C(d) = \log_2 \left| \det \left(I + \bar{\gamma}_i(d) \mathbf{H}_n(d) \mathbf{H}_n^*(d) \right) \right| \quad (7.11)$$

7.4.3 Reference Graphs

Since the MIMO capacity depends on both the SNR and the scattering/correlation within the \mathbf{H} -matrix, two reference graphs are now defined to aid interpretation of the route results. The true capacity (i.e. the capacity based on the \mathbf{H} -matrix and the actual measured SNR) is calculated from equation 7.11 and is shown as a green line in the route results of section 7.5.

The first reference graph uses the ray-traced signal to noise ratio (equation 7.9) but ignores the ray traced \mathbf{H} -matrix and instead inserts perfect i.i.d Rayleigh fading

samples. The resulting theoretical \mathbf{H} -matrix is denoted \mathbf{H}_{ray} . All other parameters are as defined in equation 7.11. The resulting capacity equation for the first reference graph is given by equation 7.12. This first reference capacity graph represents the *maximum* capacity C_{Ray} that can be generated for the observed SNR along the route and is shown in black in the route results of section 7.5. If the simulated \mathbf{H} -matrix is correlated or does not exhibit Rayleigh fading statistics then the green line will fall below the black reference line.

$$C_{Ray}(d) = \log_2 \left| \det \left(I + \bar{\gamma}_i(d) \mathbf{H}_{ray}(d) \mathbf{H}_{ray}^*(d) \right) \right| \quad (7.12)$$

The second reference graph inserts a fixed SNR (calculated from the mean along the entire route) into Equation 7.11 rather than using the true value as calculated from the ray tracer. The resulting capacity C_{SNR} is used as a second reference curve and is represented by a blue line in section 7.5. For areas where the true capacity is high because of high SNR, the green line will lie above the blue line. Similarly, for areas where the capacity is low because of low SNR, the green line will fall below the blue line.

$$C_{SNR}(d) = \log_2 \left| \det \left(I + \bar{\gamma}_{fixed} \mathbf{H}_n(d) \mathbf{H}_n^*(d) \right) \right| \quad (7.13)$$

Finally, the normalised capacity for a fixed SNR of 16dB is also calculated for each point along the route. Here the calculation only uses the normalised \mathbf{H} -matrix entries from the ray tracing study. This form of normalised capacity is useful since it allows capacities to be compared based entirely on the structure of the \mathbf{H} -matrix, rather than on the level of SNR received.

7.5 Route Based MIMO Capacity Results using ULAs

As discussed in section 7.4, the theoretical MIMO capacity for the indoor test environment along the two routes shown in figure 7.13 is now evaluated. The routes are 9.2m in length and the ray tracing analysis is performed every centimetre between all Tx and Rx antenna elements. The output provides 920 \mathbf{H} -matrix samples which are then processed to determine the theoretical MIMO capacity bound. The local signal to noise ratio is calculated by averaging the received power per element [7][16] over a 0.5m window (approximately 8.6λ) as shown in equations 7.8 and 7.9.

7.5.1 Micro-MIMO

In this section the micro-MIMO results for four different array dimensions will be presented and discussed. For each point in the route, equations 7.9 and 7.10 are used to compute the SNR and normalised \mathbf{H} -matrix from the ray-tracing data.

Figure 7.14 shows the instantaneous MIMO capacity as a function of location along route #1 defined in figure 7.11. The AP and MT both used a ULA with inter-element spacing of 0.5 wavelengths (see section 4.6). As discussed in section 7.4.3, when the green and black lines lie on top of each other, this implies that the fading obtained from the ray tracer is both uncorrelated and Rayleigh. However, when the channel becomes correlated or experiences a strong line-of-sight component then the green line drops below the black line. When the green line is beneath the blue line, this implies that the average received power is lower than the route average and as such the capacity drop (which is why capacity is often normalised based on a fixed SNR). Alternatively, if the green line is above the blue line then this implies the average received power at this point is higher than the route average.

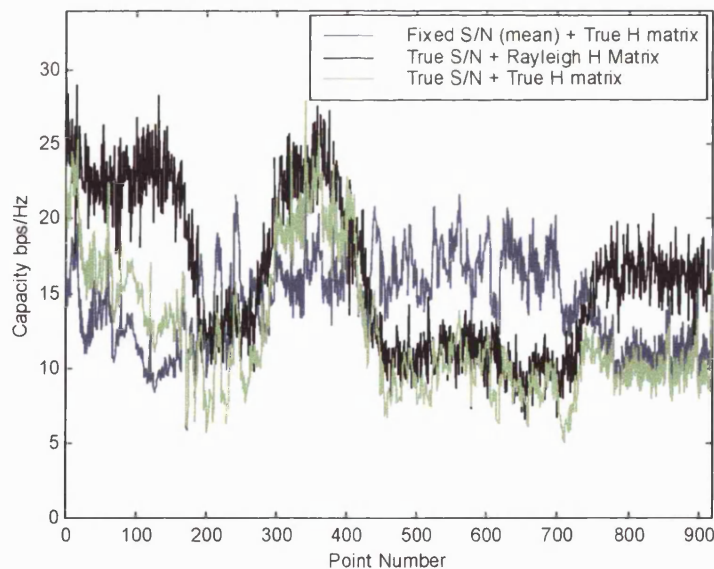


Figure 7.14: True and Reference Instantaneous Capacities (micro-MIMO, $\Delta x=0.5\lambda$)

As seen in figure 7.14, the instantaneous capacity is a random process with a given mean (expected value) and variance [14]. The green, black and blue lines vary significantly from point to point, however the local average is more stable and varies

slowly along the route. The trend of the green line is consistently below that of the black line, however due to the random nature of the instantaneous MIMO capacity estimate, there are a small number of specific locations where the green line exceeds the black line. This demonstrates the need to spatially average the data in order to better estimate the expected capacity. As discussed in section 7.4.2, a moving average window ($K=25$) centred on the point of interest is used to smooth the underlying received power and SNR estimates.

Figure 7.15 shows the instantaneous (equation 7.7) and windowed (equation 7.8) received power per element along the 920 sample route. The instantaneous value (green) can be seen to fluctuate rapidly from sample to sample due to the presence of residual fast fading after internal averaging within the \mathbf{H} -matrix. To remove this effect, the green data is windowed by spatially averaging using an 8 wavelength (approximately) moving average filter.

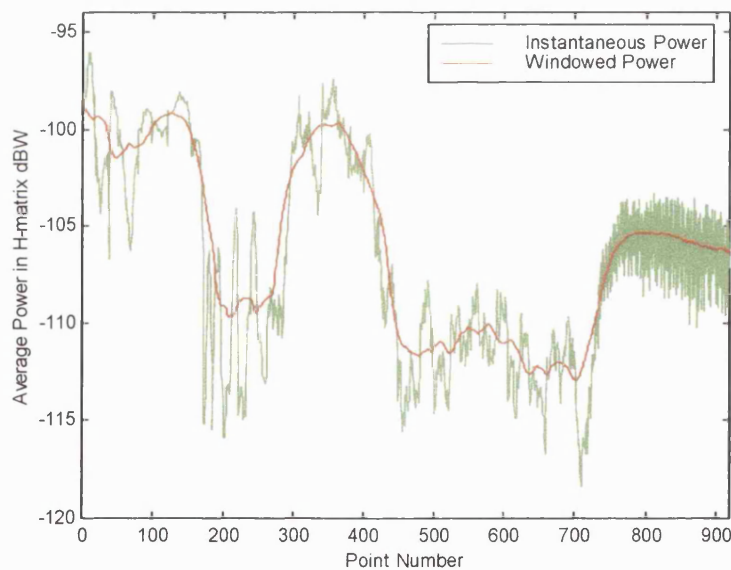


Figure 7.15: Instantaneous & Windowed Power for route 1 (micro-MIMO, $\Delta x=0.5\lambda$)

The resulting windowed data is plotted in red and now responds to the ‘slow’ fading along the route. The red line has effectively removed the instantaneous fluctuations in the green data that resulted due to poor statistical averaging.

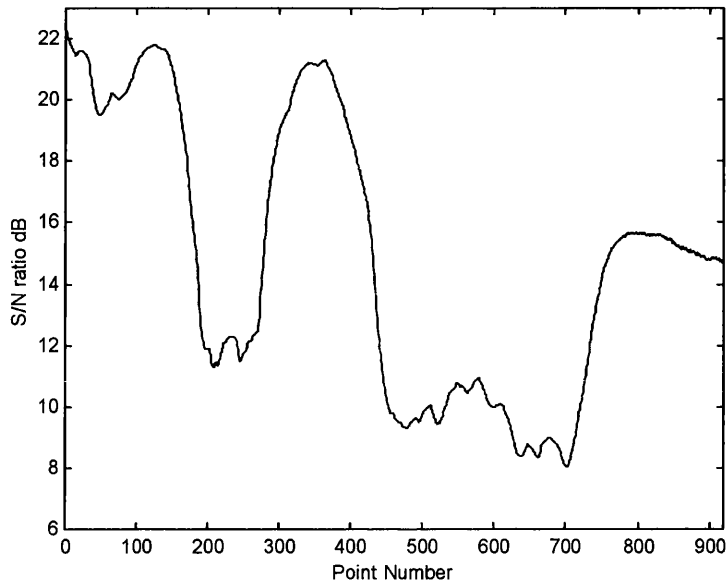


Figure 7.16: Windowed SNR for route 1 (micro-MIMO, $\Delta x=0.5\lambda$)

The windowed power shown in figure 7.15 is now used to calculate the expected SNR at each point along the route (figure 7.16). The noise floor was calculated using equation 2.x based on the parameters in table 7.2. For this analysis the noise floor was located at -121 dBw. From figure 7.15, the average received power per element starts at around -99 dBw (or -69 dBm). Given the level of the noise floor, this obviously translates into an SNR of 23 dB (which can be seen at the start of the plot in figure 7.16). The SNR values can be seen to vary significantly at the MT moves along the test route [15]. Initially, the MT is far from the AP and the resulting SNR is low. However, the as the MT travels along the route it moves closer to the AP and the resulting SNR improves. The presence of doors and tables is seen to generate spatial fluctuations in the received power and SNR. For the chosen power levels and system configuration the SNR varies from 8 to 23 dB.

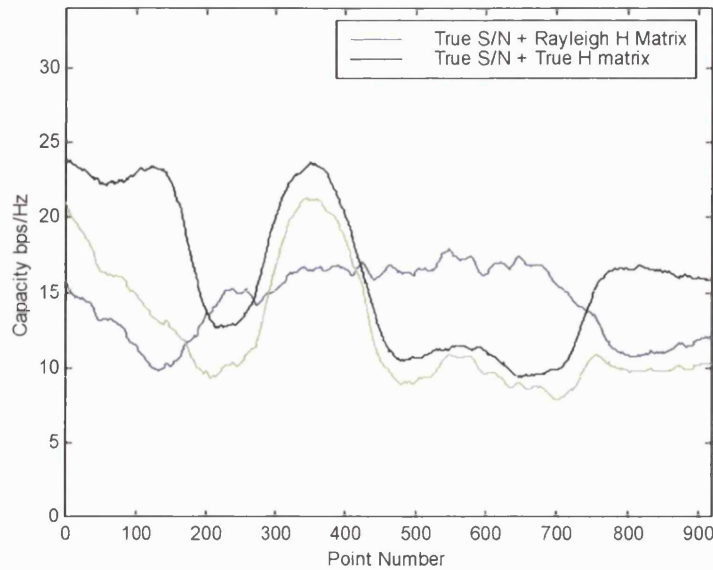


Figure 7.17: Windowed Capacities for route 1 (micro-MIMO, $\Delta x=0.5\lambda$)

Using the SNR data from figure 7.16 together with the normalised \mathbf{H} -matrix from the ray tracer equation 7.11 is now used to calculate the expected capacity for each point in the route. This capacity is shown using the green curve in figure 7.17. For illustrative purposes, the capacity assuming uncorrelated Rayleigh fading in the \mathbf{H} -matrix (black curve) and a fixed SNR based on the route average (blue curve) are also shown. All three capacity estimates can be seen to follow closely the trends shown in the original instantaneous capacity plot (figure 7.14). The spatial averaging procedure has significantly reduced the variance around each of the expected capacity values.

As expected, for most locations the practical capacity falls below that of the theoretical Rayleigh bound (due to dominant multipath components and correlation in the \mathbf{H} -matrix). For locations where the received power is high (i.e. points 300-400), the green curve rises above the blue curve indicating that high capacity is a result of high SNR). The average capacity along the route is calculated for the green and black lines and tabulated in table 7.3 for all experiments. For this graph, the average SNR was 17.0dB and the average capacity was 12.3 bits/s/Hz. From the black line, the maximum capacity assuming uncorrelated fading is 16.1 bits/s/Hz. The practical deployment therefore achieves a capacity that is 76.4% of the maximum achievable. The lost capacity can be attributed to non-Rayleigh fading and correlation in the \mathbf{H} -matrix. To aid comparison, the average capacity assuming a fixed SNR of 16dB at

each point along the route is also calculated (using the ray-traced \mathbf{H} -matrix) [16]. Here the resulting capacity was 13.4 bits/s/Hz. This normalised value can be compared with the mathematical bounds for a 4x4 MIMO system in section 7.3.3. Mathematically, the expected capacity for this configuration was around 17 bits/s/Hz for uncorrelated Rayleigh fading and 7 bits/s/Hz for a non-faded AWGN channel. The real deployment fails to reach the 17 bits/s/Hz i.i.d Rayleigh bound but is significantly higher than the 7 bits/s/Hz AWGN level.

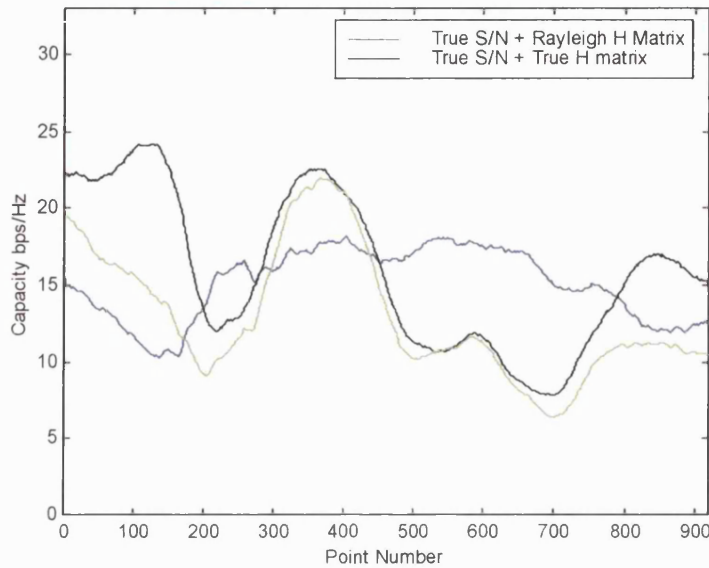


Figure 7.18: Windowed Capacities for route 1 (micro-MIMO, $\Delta x=1.0\lambda$)

Figure 7.17 was obtained using an inter-element spacing of 0.5 wavelengths. The remainder of this section now explores the impact of inter-element spacing on capacity and MIMO efficiency. Figure 7.18 shows the capacities generated for a ULA with one wavelength inter-element spacing. Generally, for larger element spacings the observed decorrelation in the H-matrix should increase resulting in higher levels of capacity. However, larger arrays are more difficult to deploy and it is therefore useful to determine the smallest array size that offers good MIMO performance. A visual comparison of figures 7.17 and 7.18 shows a very similar level of capacity. Numerically, the average capacity is 13.0 bits/s/Hz and the theoretical bound is 15.0 bits/s/Hz. These results in MIMO efficiency of 81.7%, which is slightly better than the 76.4% achieved using half wavelength spacings. The normalised capacity for an SNR of 16dB is 14.3 bits/s/Hz compared with 13.4 bits/s/Hz for the smaller array size.

The data indicates that the larger array is indeed more effective at exploiting the MIMO channel; however the levels of increase may not justify its greater physical size.

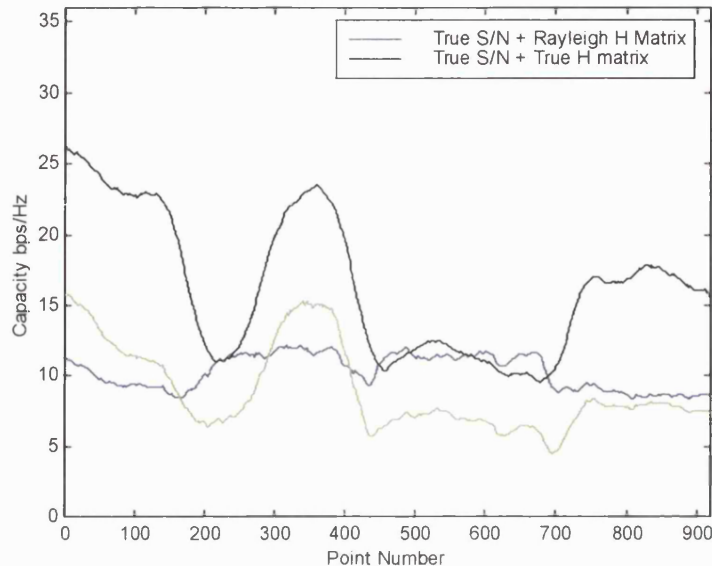


Figure 7.19: Windowed Capacities for route 1 (micro-MIMO, $\Delta x=0.1\lambda$)

Figure 7.19 now shows the same result for an inter-element array spacing of just 0.1 wavelengths. Visually, the green line can now be seen to have fallen considerably below the black Rayleigh fading bound for most points in the route. Overall, the average capacity has fallen to 8.9 bits/s/Hz and the resulting MIMO efficiency is now 54.6%, a significant drop from the earlier values. The normalised capacity for an SNR of 16 dB is now 9.5 bits/s/Hz, well below the theoretical value of 17 bits/s/Hz and approaching the AWGN value of 7 bits/s/Hz. This result indicates that such close inter-element spacings are inappropriate for MIMO communications since they fail to exploit the rich scatter present in a multipath channel.

Finally, to demonstrate the correct operation of the models, a final simulation was performed with an inter-element spacing of 0.01 wavelengths. Although not physically realisable, this experiment should generate almost perfectly correlated fading in the \mathbf{H} -matrix and therefore produces results that are in close alignment with the mathematical perfectly correlated graphs of section 7.3.3. The results are shown in figure 7.20. The capacity is now significantly reduced and rises only as a function of SNR. The average capacity was 6.4 bits/s/Hz and this translates to a MIMO efficiency

of 41.3%. The normalised capacity for an SNR of 16dB was just 7.1 bits/s/Hz, which is in agreement with the mathematical results shown in figure 7.11 for a 4x4 array in perfectly correlated Rayleigh fading.

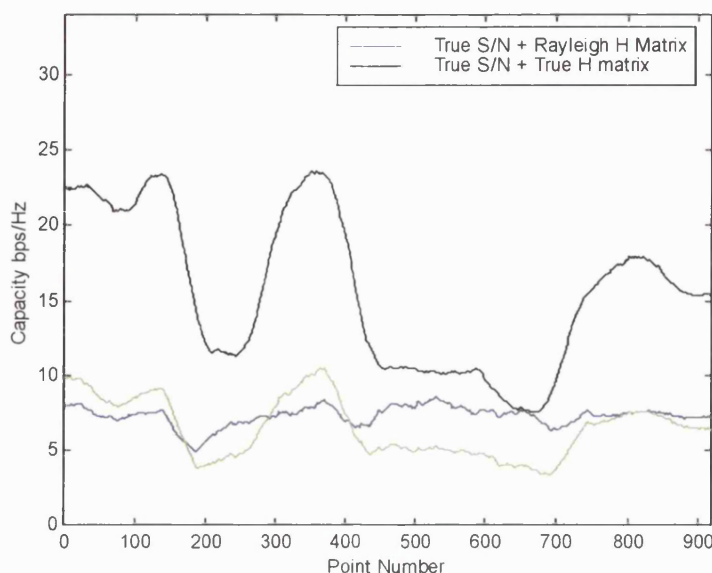


Figure 7.20: Windowed Capacities for route 1 (micro-MIMO, $\Delta x=0.01\lambda$)

A second set of micro-MIMO data is described in Appendix C for the second route defined in figure 7.13. The results for both routes are summarised later in table 7.3.

The ray tracing results for various array dimensions have compared well with earlier mathematical studies. An array size of 0.5 wavelengths achieved a MIMO efficiency of 76.4%. Although a larger array with one wavelength element separation was shown to improve performance, the gain was not considered to be significant given the increased bulk of the arrays [17]. Reducing the array size to an inter-element spacing of 0.1 wavelengths resulted in a considerable drop in performance, achieving a MIMO efficiency of 54.6%. This result indicates that such compact arrays are not suitable for developing high capacity systems. Finally, a study using 0.01 wavelength spaced arrays was performed as an academic study. Here the results were seen to agree well with mathematical estimates assuming perfectly correlated Rayleigh fading. This result is pleasing since it confirms the correct operating of the ray tracer and provides a strong physical link back to the earlier mathematical studies.

7.5.2 Macro-MIMO

In this section the macro-MIMO results for four different array dimensions will be presented and discussed. The analysis procedure is identical to that used in section 7.3.1, the only difference being the AP elements are now distributed towards each corner of the room.

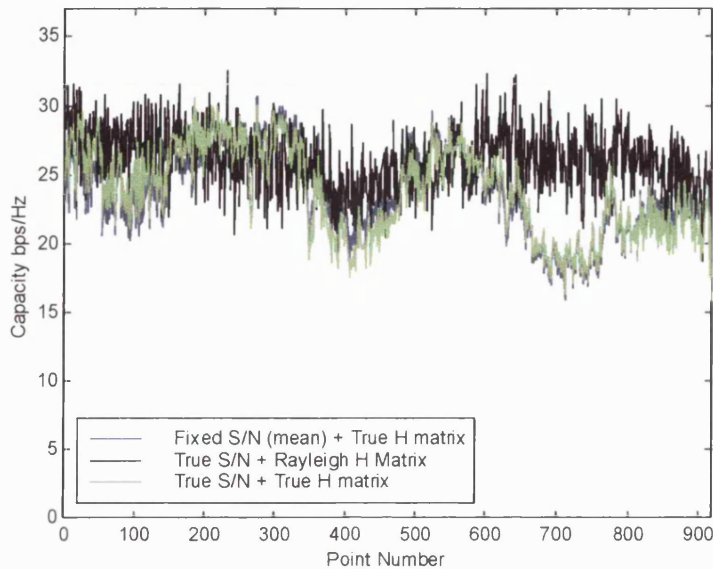


Figure 7.21: True and Reference Instantaneous Capacities (macro-MIMO, $\Delta x=0.5\lambda$)

Figure 7.21 shows the instantaneous MIMO capacity as a function of location along route #1 defined in figure 7.11. Generally speaking, the green line is now very close to the black line (indicated a high level of decorrelated fading in the ray traced results). The green line also closely follows the blue line, which indicates far less fluctuation in the received power over the route.

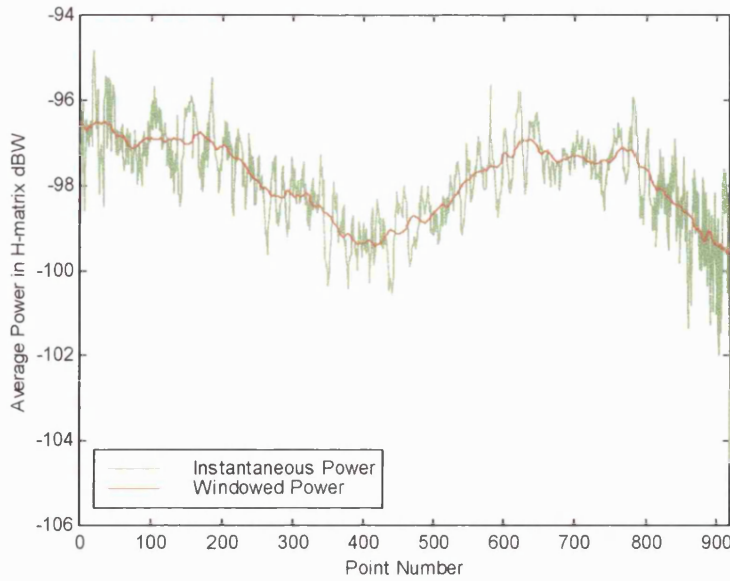


Figure 7.22: Instantaneous & Windowed Power for route 1 (macro-MIMO, $\Delta x=0.5\lambda$)

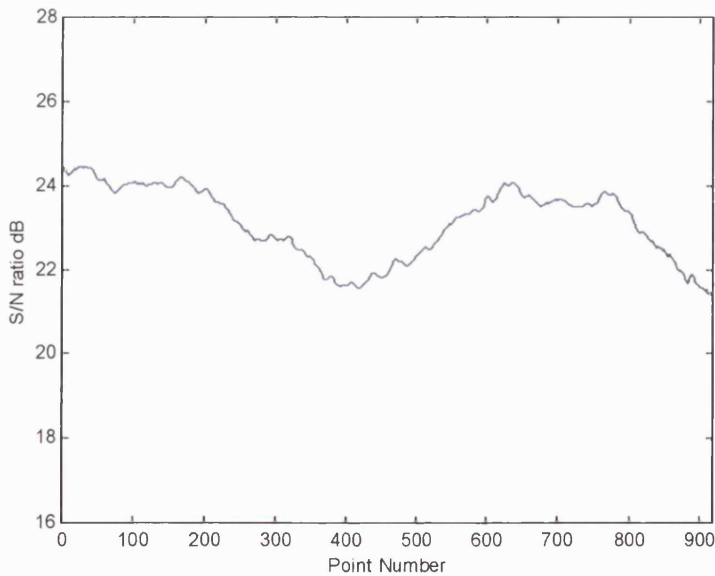


Figure 7.23: Windowed SNR for route 1 (macro-MIMO, $\Delta x=0.5\lambda$)

Figure 7.22 shows the instantaneous (equation 7.7) and windowed (equation 7.8) received power per element along the 920 sample route. The instantaneous value (green) can be seen to fluctuate from sample to sample, however the level of fluctuation is less than that seen for the micro-MIMO case (figure 7.15). The windowed power shown in figure 7.22 is now used to calculate the expected SNR at

each point along the route (figure 7.23). As described earlier, the noise floor was located at -121 dBw [18]. For the macro-MIMO case the variation in SNR is less severe than in the micro-MIMO case. This is to be expected since the AP elements are now more evenly distributed around the room. For the chosen power levels and system configuration the SNR varies from 21 to 25dB.

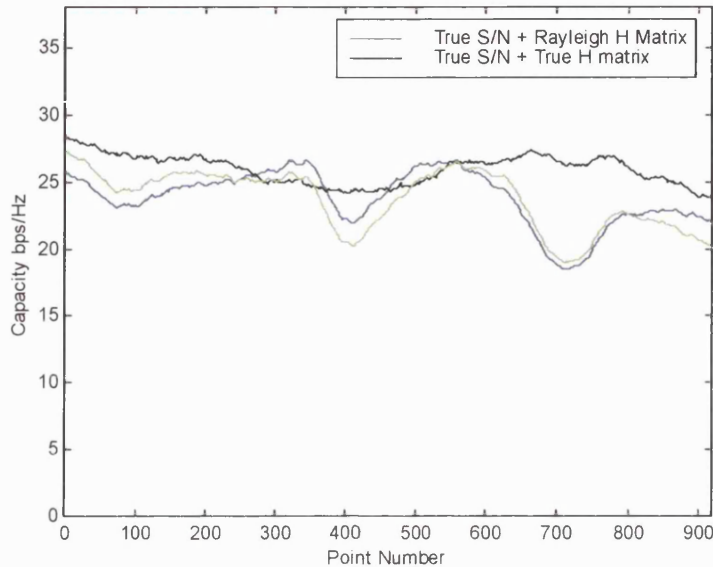


Figure 7.24: Windowed Capacity for route 1 (macro-MIMO, $\Delta x=0.5\lambda$)

Using the SNR data from figure 7.23 together with the normalised \mathbf{H} -matrix from the ray tracer equation 7.11 is now used to calculate the expected capacity for each point in the route. This capacity is shown using the green curve in figure 7.24. For illustrative purposes, the capacity assuming uncorrelated Rayleigh fading in the \mathbf{H} -matrix (black curve) and a fixed SNR based on the route average (blue curve) are also shown. All three capacity estimates can be seen to closely follow the trends shown in the original instantaneous capacity plot (figure 7.21).

Unlike the micro-MIMO case, for most locations the practical capacity is now very close to the theoretical Rayleigh bound. The average capacity along the route is calculated for the green and black lines and tabulated in table 7.3 for all experiments. For this graph, the average SNR was 23.2dB and the average capacity was 23.7 bits/s/Hz. From the black line, the maximum capacity assuming uncorrelated fading is 26.1 bits/s/Hz. The practical deployment therefore achieves a capacity that is now 90.8% of the maximum achievable. This result is considerable better than the micro-

MIMO case for identical transmit powers. To aid comparison, the average capacity assuming a fixed SNR of 16dB at each point along the route is also calculated (using the ray-traced \mathbf{H} -matrix). Here the resulting capacity was 15.6 bits/s/Hz (also considerably better than the micro-MIMO case). This normalised value can be compared with the mathematical bounds for a 4x4 MIMO system in section 7.3.3. For the macro-MIMO configuration the normalised capacity is now very close to the 17 bits/s/Hz i.i.d Rayleigh fading bound.

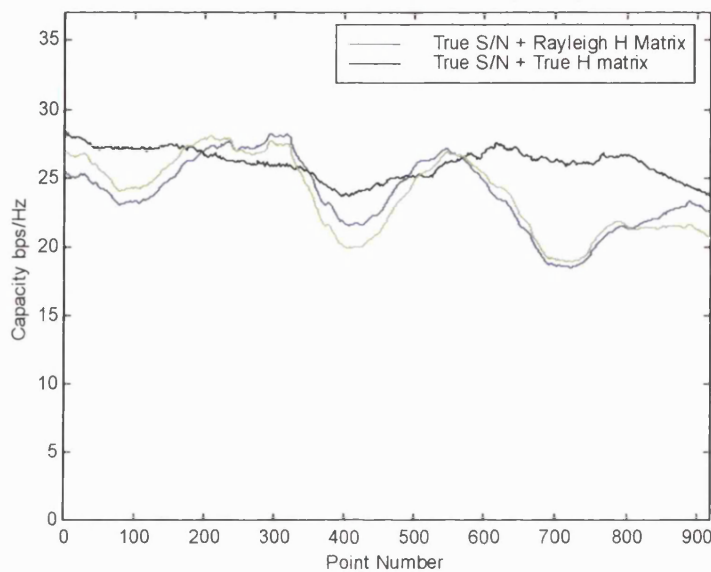


Figure 7.25: Windowed Capacities for route 1 (macro-MIMO, $\Delta x=1.0\lambda$)

Figure 7.24 was obtained using an MT inter-element spacing of 0.5 wavelengths. The remainder of this section now explores the impact of MT inter-element spacing on capacity and macro-MIMO efficiency [19]. Figure 7.25 shows the capacities generated for an MT ULA with one wavelength inter-element spacing. Generally, for larger element spacings the observed decorrelation in the \mathbf{H} -matrix is higher and this leads to better capacity. A visual comparison of figures 7.24 and 7.25 shows identical levels of capacity. The data indicates that the larger offers no benefit for this route study.

Figure 7.26 shows the macro-MIMO result for an MT inter-element array spacing of just 0.1 wavelengths. Visually, the green line can be seen to have fallen considerably below the black Rayleigh fading bound for all points in the route. Overall, the average capacity has fallen to 17.8 bits/s/Hz and the resulting MIMO efficiency is now 68.7%,

a significant drop from the earlier values. The normalised capacity for an SNR of 16 dB is now 12.1 bits/s/Hz, which is considerably better than the equivalent micro-MIMO results of 9.5 bits/s/Hz. In the macro-MIMO case the AP elements remain decorrelated and this results in some degree of enhanced capacity even when the MT array spacings are close together.

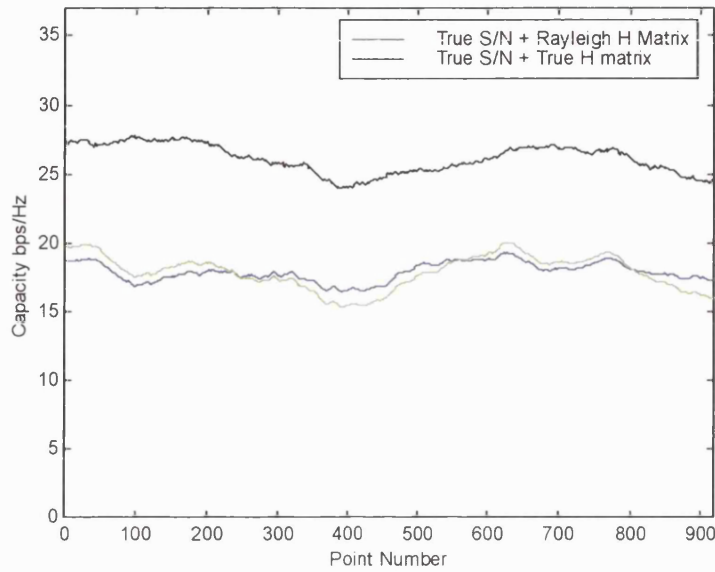


Figure 7.26: Windowed Capacities for route 1 (macro-MIMO, $\Delta x=0.1\lambda$)

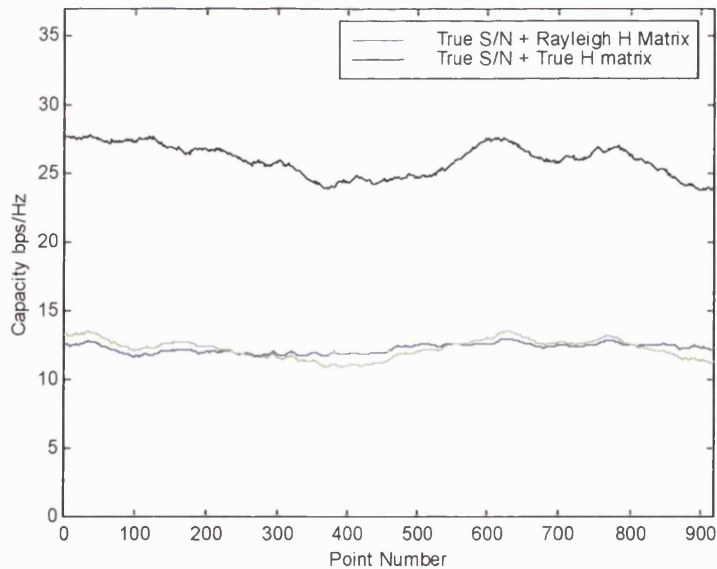


Figure 7.27: Windowed Capacities for route 1 (macro-MIMO, $\Delta x=0.01\lambda$)

Finally, as in the micro-MIMO study, a final simulation was performed with an inter-element spacing of 0.01 wavelengths. The results are shown in figure 7.27. The capacity is now significantly reduced. The average capacity is now 12.2 bits/s/Hz and the MIMO efficiency is just 47.1%. The normalised capacity for an SNR of 16dB is now 8.3 bits/s/Hz, which once again is approaching the mathematical results shown in figure 7.11 for a 4x4 array in perfectly correlated Rayleigh fading.

Appendix C includes a second set of results for the macro-MIMO configuration as the MT moves along the second route defined in figure 7.13. The results for micro and macro-MIMO along both routes are summarised in the following section.

7.5.3 Summary of Micro/Macro MIMO Capacities for routes 1 & 2

The results from sections 7.5.1 and 7.5.2 together with the second set of route data from Appendix C are now summarised in Table 7.3.

System	Average SNR (dB)	Simulated Capacity (b/s/Hz)	Capacity for i.i.d. Rayleigh H-matrix (b/s/Hz)	Normalised Capacity for SNR=16dB (b/s/Hz)	MIMO efficiency (relative to i.i.d Rayleigh)
Micro Route 1					
$\Delta x=1.0$	16.8	13.0	15.9	14.3	81.7%
$\Delta x=0.5$	17.0	12.3	16.1	13.4	76.4%
$\Delta x=0.1$	17.1	8.9	16.3	9.5	54.6%
$\Delta x=0.01$	16.5	6.4	15.5	7.1	41.3%
Macro Route 1					
$\Delta x=1.0$	23.2	23.7	26.1	15.6	90.8%
$\Delta x=0.5$	23.2	23.7	26.1	15.6	90.8%
$\Delta x=0.1$	23.2	17.8	25.9	12.1	68.7%
$\Delta x=0.01$	23.2	12.2	25.9	8.3	47.1%
Micro Route 2					
$\Delta x=1.0$	14.1	9.8	13.9	13.0	70.5%
$\Delta x=0.5$	14.3	9.5	14.1	12.3	67.4%
$\Delta x=0.1$	14.4	7.4	14.6	9.0	50.7%
$\Delta x=0.01$	14.4	6.0	14.1	7.2	42.6%
Macro Route 2					
$\Delta x=1.0$	26.3	22.4	28.4	12.8	78.9%
$\Delta x=0.5$	26.6	21.3	29.0	12.1	73.4%
$\Delta x=0.1$	26.9	15.3	29.3	8.8	52.2%
$\Delta x=0.01$	26.8	11.3	29.2	7.4	38.7%

Table 7.3: Summary of MIMO Route Capacity

When analysing the data in table 7.3 it should be remembered that a SISO communication system has a normalised Rayleigh capacity of 4.6 bits/s/Hz at an SNR of 16 dB. Mathematically, assuming perfectly uncorrelated i.i.d Rayleigh fading in the \mathbf{H} -matrix, a 4x4 MIMO configuration can increase this normalised capacity to 17.4 bits/s/Hz (see figure 7.9). For perfectly correlated Rayleigh fading, the normalised capacity drops to just 7.0 bits/s/Hz (see figure 7.10). For inter-element array spacings of 0.5 wavelengths or higher, the ray traced data showed MIMO capacities within 70-90% of the ideal upper bound. For smaller array spacings at either the AP or MT, the normalised capacity was seen to drop towards the ideally correlated value.

From the data produced along route 1, the use of macro-MIMO can be seen to result in an approximate 6 dB improvement in average SNR (for the same fixed transmit power per element). The normalised capacity was also seen to increase by around 16% when macro-MIMO was applied. More significantly, relative to micro-MIMO, the average capacity along the route is increased by 62% using macro-MIMO. The second route showed an even higher gain in average SNR. Here the improvement of macro-MIMO was more than 12 dB. The normalised capacity actually dropped by 1% with macro-MIMO along this route. However, when the gain in SNR is considered, the overall MIMO capacity was seen to rise by 105%.

As an alternative to large capacity gains, the use of macro-MIMO could be used as an effective method for reducing the transmit power required for a given capacity level. Given health concerns for indoor communications, this benefit could be of considerable future interest.

7.6 Grid Based MIMO Capacity Results using ULAs

In this section the MIMO analysis is now performed again over a grid covering the entire floor space of figure 7.13 [20]. For each grid location, the \mathbf{H} -matrix is predicted for one of two 4x4 antenna structures. As in section 7.3, the micro-MIMO configuration (with 0.5 wavelength spacing) is compared directly to the macro-MIMO case (with 0.5 wavelength spacing at the MT).

7.6.1 Micro-MIMO Study

Figure 7.28 shows the distribution of received power in dBm for the micro-MIMO case. Power is seen to peak in close vicinity to the transmit antenna, which is located in the bottom left-hand corner of the room. Due to the presence of tables, walls and doors, the flow of power shows a number of distinct fluctuations. Power drops sharply in the shadow region behind the tables. In the far corner the received power is around 30dB below the peaks observed in close vicinity to the transmit array. No transmit power control is assumed in this study; hence areas of low field strength result in low levels of SNR (and subsequently low capacity) [21]. Figure 7.29 maps the received power to SNR based on the calculation of noise power using parameters given earlier in table 7.2. With the micro configuration, the distribution of power and SNR is clearly biased to the corner containing the transmit array. MIMO capacity depends on SNR and scatter within the \mathbf{H} -matrix. In areas of strong line-of-sight, although the SNR is high, the scatter is likely to be low. Similarly, in areas of weak SNR, the scatter is more likely to be high.

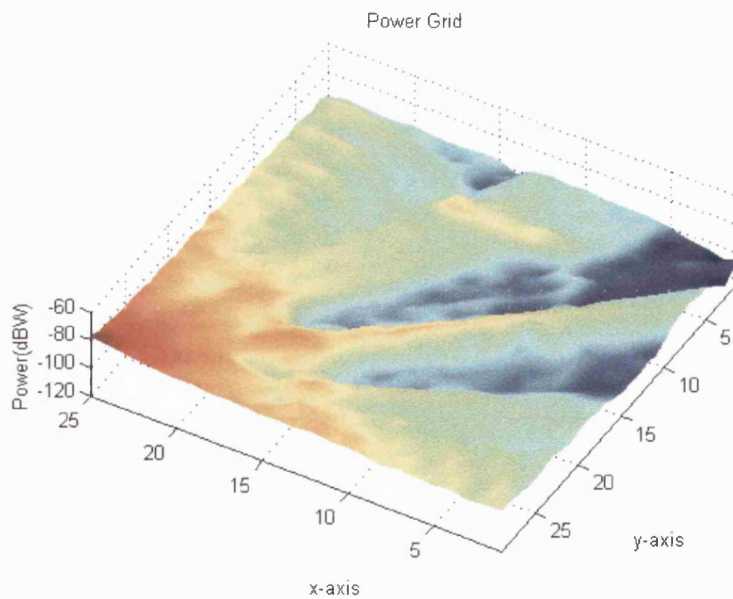


Figure 7.28: Received power grid for a 4x4 micro-MIMO configuration

For each grid point, the simulated \mathbf{H} -matrix and the predicted SNR is fed into the Foschini equation to compute the MIMO capacity bound. The resulting capacities are shown in figure 7.30.

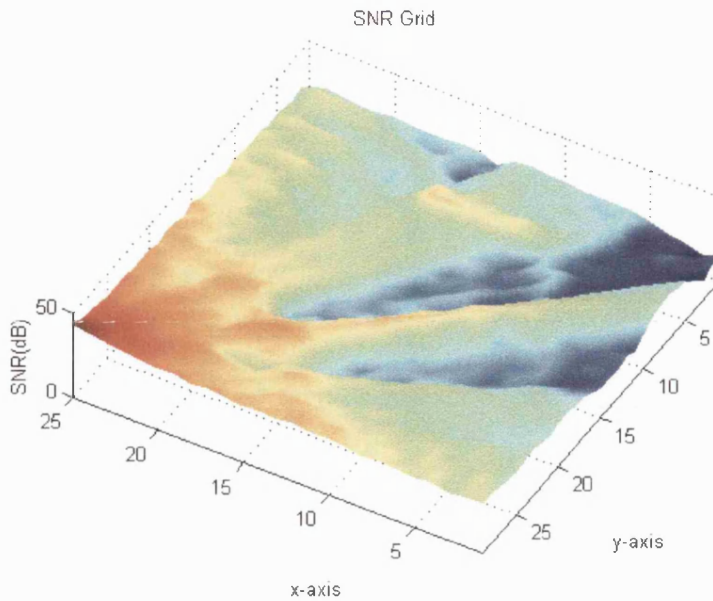


Figure 7.29: Received SNR grid for a 4x4 micro-MIMO configuration

Large capacity is seen in the vicinity of the transmitter and this implies that from a capacity viewpoint, the large SNR dominates over the low levels of scatter. However, for this capacity to be exploited in practice very high levels of modulation are required. Generally, in the far side of the room the overall capacity seems to be lower. The average capacity over the entire grid is 23.9 bits/s/Hz.

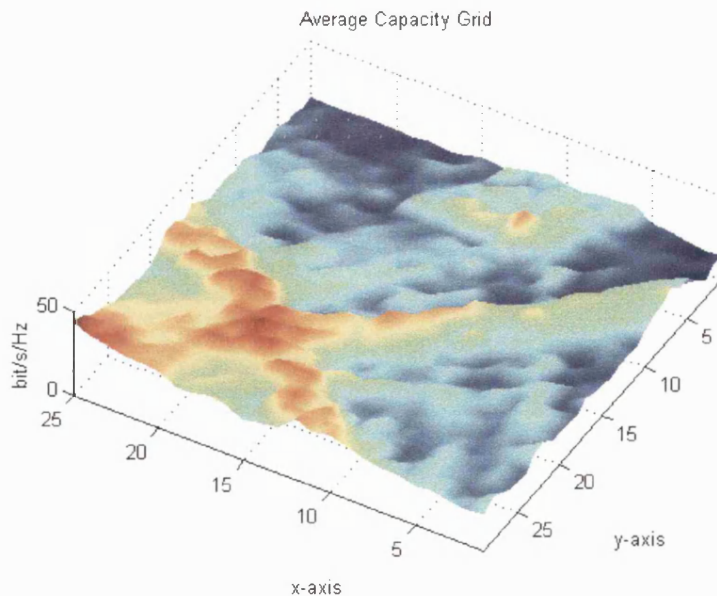


Figure 7.30: Average capacity grid for a 4x4 micro-MIMO configuration

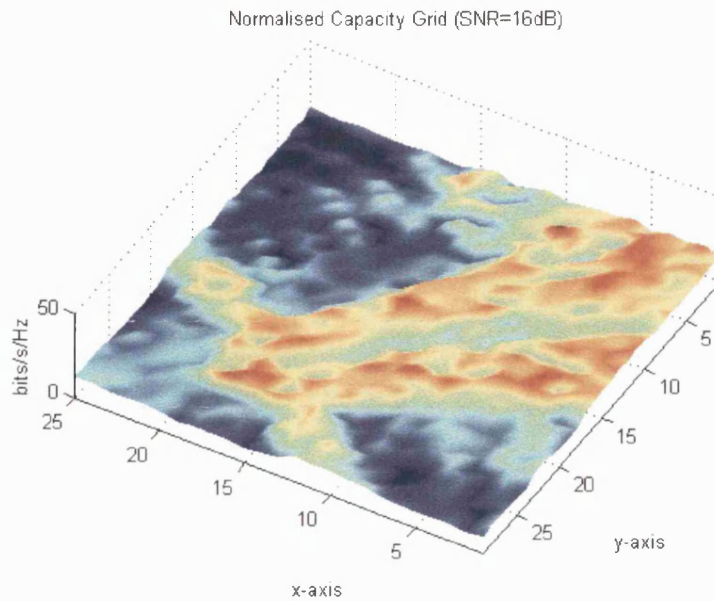


Figure 7.31: Normalised capacity grid for a 4x4 micro-MIMO configuration

To achieve a fair comparison, all the MIMO results in this chapter were obtained for a fixed level of transmit power. However, many authors overcome this problem by analysing the capacity for a fixed level of SNR [22]. It is common to fix the SNR at a desirable operating level (the idea here is that power control would be used to ensure a common target SNR is achieved at all points in the grid). In this study a fixed SNR of 16dB is achieved by varying the transmit point for each receive location. Figure 7.31 now shows a very different capacity picture to that seen in figure 7.30. With a fixed level of SNR, capacity variations are now a function of scattering and decorrelation in the channel. The highest capacities are now seen in the more distant non-line-of-sight locations at the far side of the room. This demonstrates that for a fixed SNR, locations in the far side of the room (from the transmitter) have a greater potential for MIMO capacity gain. Close to the transmitter, the received signals are dominated by the line-of-sight components and hence the fast fading is minimal (high K-factor) and the spatial correlation is high. The average normalised capacity is 12.8 bits/s/Hz.

In chapter 2 the MIMO channel capacity was seen to be related to the product $\mathbf{H}\mathbf{H}'$, where $(.)'$ represents the conjugate transpose. The Foschini capacity is derived from the sum of the individual Shannon capacity estimates for each of the Eigenvalues of $\mathbf{H}\mathbf{H}'$. These Eigenvalues give the power of each of the N orthogonal spatial channels; where $N=\min(N_t, N_r)$. For an \mathbf{H} -matrix resulting in N strong Eigenvalues, the matrix is

defined as full rank (in this thesis a strong Eigenvalue is one that lies within 10dB of the maximum). For channels with reduced scattering or correlation, a number of the Eigenvalues become weak and the \mathbf{H} -matrix is referred to as rank deficient. Clearly, as the Eigenvalues of $\mathbf{H}\mathbf{H}'$ become weaker, the total capacity will drop. In the remainder of this chapter, the capacity of micro and macro MIMO channels are analysed via a graphical depiction of the Eigen structure (namely Rank and Eigenvalue spread). It should be noted that in many MIMO papers the singular values of \mathbf{H} are calculated instead of the Eigenvalue of $\mathbf{H}\mathbf{H}'$. Mathematically it is well known that these singular values are simply the square root of the above Eigenvalues.

Figure 7.32 shows a grid plot of the number of Eigenvalues within 10 dB of the maximum. This parameter is sometimes referred to as effective rank [23] and the capacity is greater for channels with high rank. For a 4x4 channel matrix the maximum rank is four.

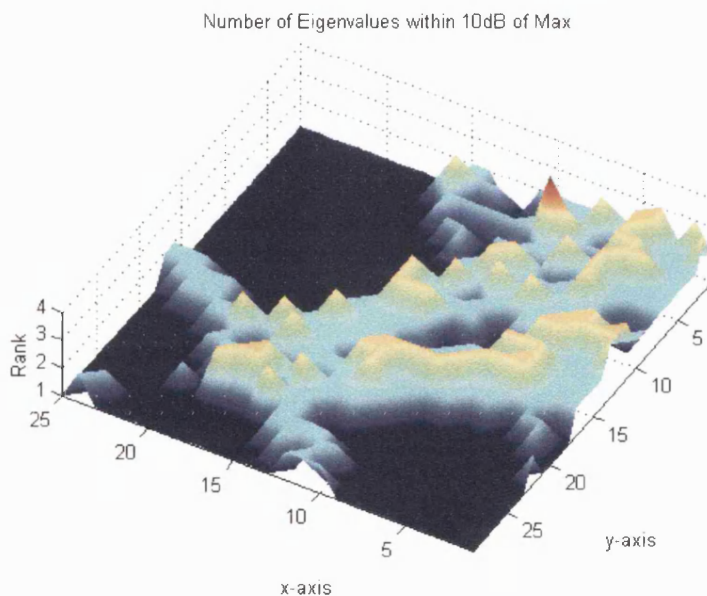


Figure 7.32: Effective rank for a 4x4 micro-MIMO configuration

From figure 7.32 this highest level of rank is seen just once, on the far side of the room in a location obstructed by the table. Rank is at its lowest for areas in direct line-of-sight from the transmitter. This figure shows the room is split into two regions, one where MIMO gain will be high (the high rank areas) and another where the MIMO gain will be minimal (areas with a rank of one).

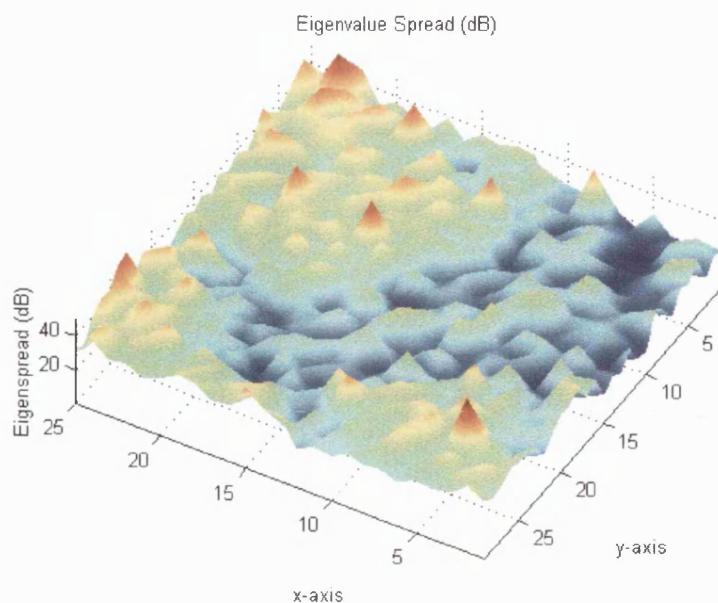


Figure 7.33: Eigenvalue spread for a 4x4 micro-MIMO configuration

Another useful indicator of MIMO channel capacity is the Eigenvalue spread [24], which is defined as the largest Eigenvalue divided by the lowest Eigenvalue. This measure is shown in Figure 7.33. Generally, capacity is lower for locations with high Eigenvalue spread (since the Eigenvalues are directly related to the power of the spatial channels created by a MIMO system).

Generally, the Eigenvalue spread is at its lowest in the regions corresponding to high rank. Areas having low rank clearly result in large Eigenvalue spreads. The highest spreads are seen directly around the transmitter and in the corner adjacent to the transmitter.

7.6.2 Macro-MIMO Study

Here the MIMO analysis of section 7.6.1 is repeated for the macro-MIMO configuration. The aim is to explore whether macro-MIMO is more desirable for an indoor communications system. The transmitter is now reconfigured with a single transmit element placed near each corner of the room.

Figure 7.34 shows the distribution of received power in dBm for the macro-MIMO case. The receive array is a ULA with half wavelength spacing. The power distribution is now very different to the micro-MIMO case seen in figure 7.28.

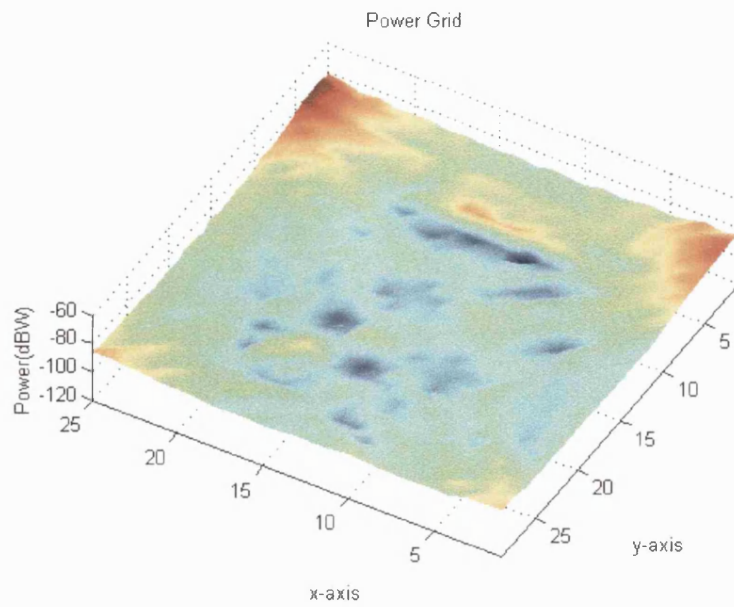


Figure 7.34: Received power grid for a 4x4 macro-MIMO configuration

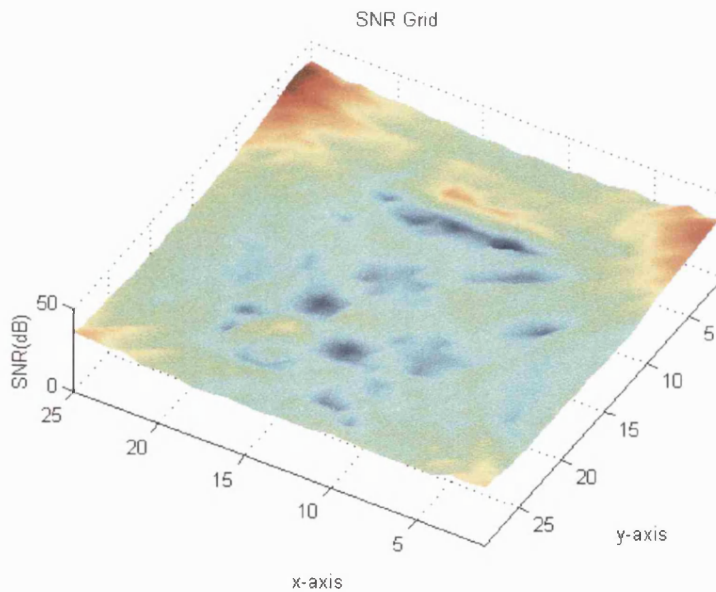


Figure 7.35: Received SNR grid for a 4x4 macro-MIMO configuration

Figure 7.35 maps the received power to SNR based on knowledge of the receive bandwidth, temperature and noise figure. Using the macro configuration, the power is now far more evenly distributed over the floor space (compared with the micro case). For a fixed transmit power, the distribution of SNR is also more even in the macro case. The main drawback with macro-MIMO is the potential dominance from one

transmitter location. This could reduce the rank of the \mathbf{H} -matrix and lower the potential MIMO capacity.

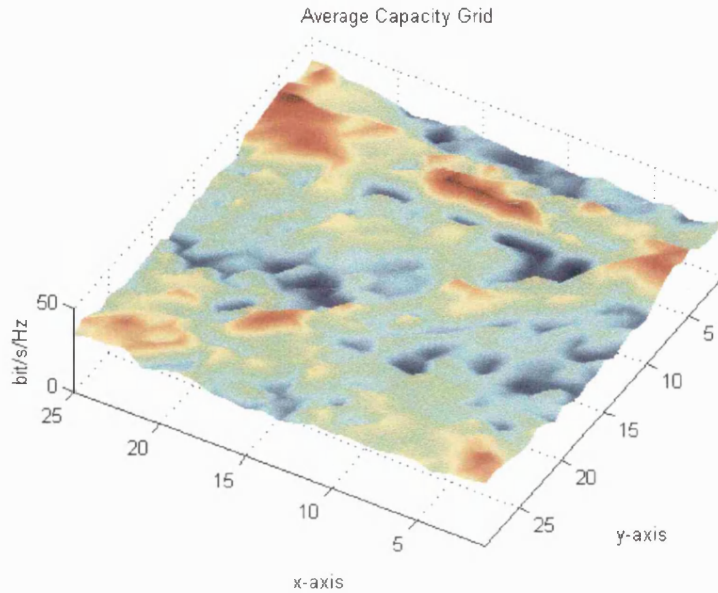


Figure 7.36: Received capacity grid for a 4x4 macro-MIMO configuration

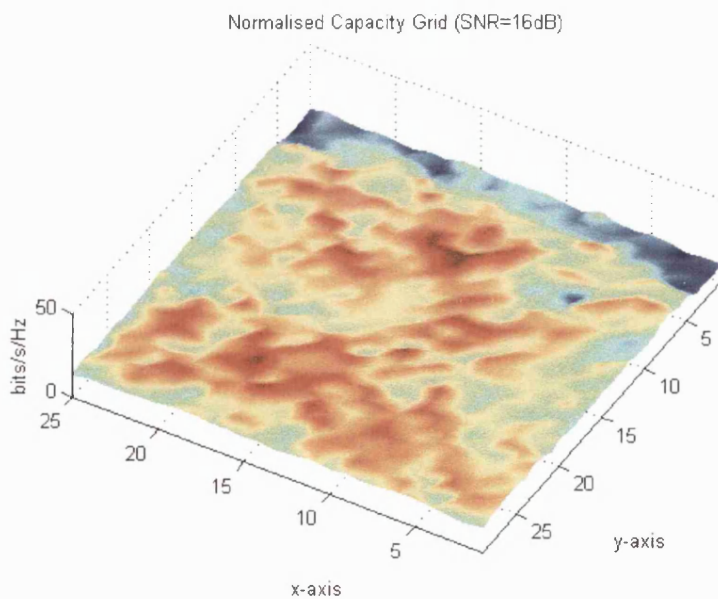


Figure 7.37: Normalised capacity grid for a 4x4 macro-MIMO configuration

The resulting macro MIMO capacity grid is shown in figure 7.36. Large capacities are seen to occur in the four corners (because of large values of SNR). However, there are a number of regions in the room that also show high levels of capacity and this is most

likely due to high degrees of scatter. The average capacity over the entire grid is 32.3 bits/s/Hz (which compares favourably with the micro capacity of 23.9 bits/s/Hz).

Figure 7.37 shows the resulting capacity for a normalised SNR of 16 dB. The plot shows a far more even level of capacity distribution throughout the environment. Interestingly, even in the corners (near a transmit element) the normalised capacity is high and this implies the \mathbf{H} -matrix retains a reasonable degree of scatter. The average normalised capacity over the grid area is 15.4 bits/s/Hz (compared with 12.8 bits/s/Hz).

Figure 7.38 shows a grid plot of the number of Eigenvalues within 10 dB of the maximum. The highest value of effective rank is 3 and the rank appears at its highest in the top half of the room. Compared to the micro-MIMO rank plot (figure 7.14-7.20) the locations of high rank are far more evenly distributed and this should greatly ease the design of an appropriate modulation and coding waveform [25].

Finally, Figure 7.39 shows the Eigenvalue spread. Unlike the micro-MIMO case, the Eigenvalue spread is now high in all the corners due to the use of distributed antennas.

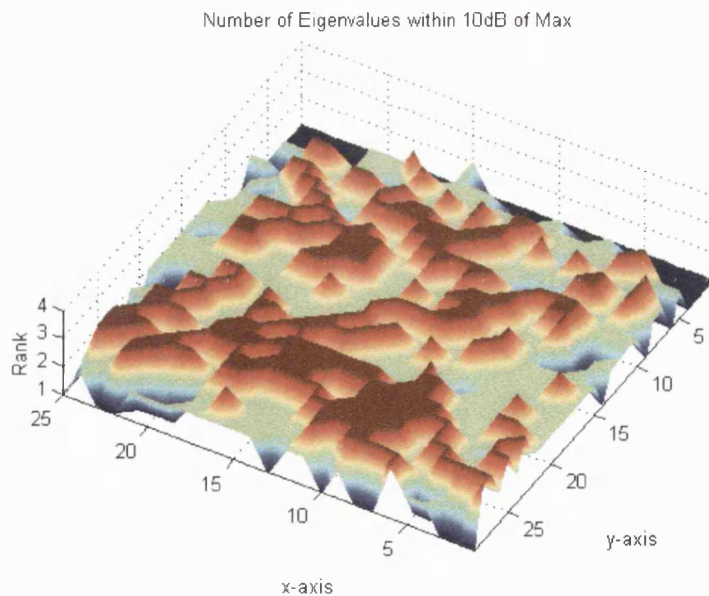


Figure 7.38: Effective rank for a 4x4 macro-MIMO configuration

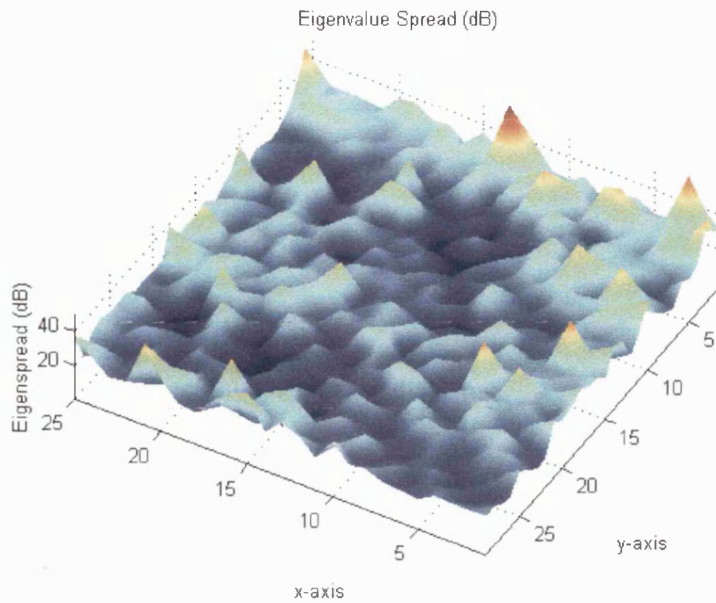


Figure 7.39: Eigenvalue spread for a 4x4 macro-MIMO configuration

Generally, the Eigenvalue spread is at its lowest in the middle of the room where the scatter is at its highest (hence maintaining a high degree of power in the lowest Eigenvalue). The Eigenvalue spread is at its highest in the corners of the room, where the dominant line-of-sight tends to concentrate power into a single Eigenvalue.

Overall, the macro-MIMO capacity is higher for both the normalised and un-normalised cases. In the normalised case, the average capacity is increased from 12.8 to 15.4 bits/s/Hz. This implied that macro-MIMO not only improved the distribution of power, but also the distribution of scatter and correlation. In the un-normalised case the micro-MIMO capacity was shown to improve from 23.9 to 32.3 bits/s/Hz. This substantial gain is largely due to the better distribution of power over the floor space.

7.7 Summary

A theoretical capacity analysis for SISO and MIMO communication systems has been presented for perfectly uncorrelated and correlated Rayleigh and Rician fading channels. The results confirm that MIMO communications systems can actually improve the theoretical capacity in a rich scatter environment, providing the fading over the array is uncorrelated. For correlated MIMO channels, the capacity drops with increasing scatter (although the absolute capacity is still superior to the SISO case).

For an SNR ratio of 16 dB, a SISO system was seen to offer a theoretical capacity of 4.6 bits/s/Hz in Rayleigh fading conditions. A 2x2 MIMO system improved this value to around 8.5 bits/s/Hz in uncorrelated fading (dropping to just over 6 bits/s/Hz in correlated fading). A 4x4 MIMO system offers around 18 bits/s/Hz in uncorrelated fading (dropping to around 7 bits/s/Hz in correlated fading).

This analysis confirms that MIMO processing is a powerful method for enhancing capacity (or reducing the S/N required to achieve a given capacity). For the method to be most effective it is important for the fading to be decorrelated and for the arrays to be placed in a rich scatter environment. A macro-MIMO configuration was shown to outperform a micro-MIMO configuration for the specific environment studied. Close inter-element spacings were shown to reduce MIMO capacity through the generation of correlation fading in the \mathbf{H} -matrix. Inter-element spacings of around 0.5 wavelengths offer a good compromise between MIMO capacity and physical bulk.

From the grid studies, the macro-MIMO capacity was shown to be higher for both the normalised and un-normalised cases. In the normalised case, the average capacity increased from 12.8 to 15.4 bits/s/Hz. In the un-normalised case, the use of macro-MIMO improved capacity from 23.9 to 32.3 bits/s/Hz. The benefits of macro-MIMO were also visually demonstrated using Eigen analysis.

7.8 References

- [1] Gerard J. Foschini, "Layered Space-Time Architecture for Wireless Communication in a Fading Environment When Using Multi-Element Antennas", *Bell Labs Technical Journal (BLTJ)*, pp. 41-59, Autumn, 1996.
- [2] G.J. Foschini and M.J. Gans, "On limits of wireless communications in a fading environment when using multiple antennas", *Wireless Personal Communications*, pp. 311 – 335, 1998.
- [3] C. Berrou, A. Glavieux, and P. Thitimajshima, "Near Shannon Limit Error-Correcting Coding and Decoding: Turbo Codes", *Proc. IEEE International Conference on Communications (ICC), Geneva*, pp. 1064-1070, 1993.
- [4] I.E. Telatar, "Capacity of Multi-Antenna Gaussian Channels, *Technical Report, Bell Labs internal memo*, 1995.
- [5] X. Li, H. Huang, A. Lozano, and G. Foschini, "Reduced Complexity Detection Algorithms for Systems Using Multi-Element Arrays", *IEEE Globecom 2000, San Francisco*, April 2000.
- [6] P.F. Driessen and G.J Foschini, "On the Capacity Formula for Multiple Input-Multiple Output Wireless Channels: A Geometric Interpretation", *IEEE Transactions on Communications*, vol. 47, no. 2, Feb. 1999.
- [6] G. Golden, G. Foschini, R. Valenzuela, and W. Wolniansky, "Detection Algorithm and Initial Laboratory Results Using the V-Blast Space-Time Communication Architecture", *IEE Electronics Letters*, pp.14-15, 1999.
- [7] D.P. McNamara, M.A. Beach, P.N. Fletcher and P. Karlsson, "Temporal Variation of Multiple-Input Multiple-Output (MIMO) Channels in Indoor Environment", *11th International Antennas and propagation Professional Network ICAP*, pp. 578-582, Manchester, April 2001.
- [8] I.E. Telatar, "Capacity of Multi-antenna Gaussian Channels", *Technical Report, Bell Labs internal memo*, 1995.
- [9] P.W. Wolniansky, G.J. Foschini, G.D. Golden, and R.A. Valenzuela, "V-Blast: An Architecture for Realizing Very High Data Rates over the Rich-Scattering

- Wireless Channel”, *URSI International Symposium on Signals, Systems, and Electronics, ISSSE-98*, pp. 295-300, 1998.
- [10] G.D. Golden, G.J. Foschini, R.A. Valenzuela and P.W. Wolniansky, “Detection algorithm and initial laboratory results using the V-BLAST space-time communication architecture”, *Electronic Letters*, Vol.35, no.1, pp. 14-15, Jan. 1999.
- [11] F. Tila, P.R. Shepherd and S.R. Pennock, “Analysis of Indoor-Indoor and Satellite/Hap-Indoor Propagation Effects”, *11th International Antennas and Propagation Professional Network ICAP*, pp. 203-7, Manchester, April 2001.
- [12] F. Tila, P.R. Shepherd and S.R. Pennock, “Indoor Ray Tracing evaluation of enhanced High Frequency communications using Directional Antennas at the Basestation and Space Diversity at the Terminal”, *31st IEEE European Microwave Conference (EuMC)*, pp. 351-355, Sep. 2001.
- [13] G.J. Foschini and R.K. Mueller, “The Capacity of Linear Channels with Additive Gaussian Noise”, *Bell System Technical Journal*, pp. 81-94, Jan 1970.
- [14] Ch. Ghobadi, S.R. Pennock and P.R. Shepherd, “Evaluation of Diversity Techniques in Complex Indoor Environments”, *28th European Microwave Conference Amsterdam*, pp. 345-350, 1998.
- [15] M.R. Williamson and A.R. Nix, “Investigating the effects of Antenna Directivity on Wireless Indoor Communications at 60 GHz”, *8th IEEE Personal and Indoor Mobile Radio Conference*, Helsinki, Finland, pp. 635-639, Sept. 1997.
- [16] D.P. McNamara, M.A. Beach, P. Karlsson and P.N. Fletcher, “Initial Characterisation of Multiple-Input Multiple-Output (MIMO) Channels for Space-Time Communication”, *IEEE Vehicular Transaction Conf.*, pp. 257-261.
- [17] M.A. Beach, D.P. McNamara, P. Karlsson and A.R. Nix, “Development of a Channel Measurement System for Multiple-Input Multiple-Output (MIMO) Applications”, *IST workshop*, Oct. 2000.
- [18] Robert W. Heath Jr. and Kapil R. Dandekar, “Characterization of Narrowband MIMO Channels”, *IEEE*, April 2002.

Chapter 8: Conclusions and Further Work

8.1 Introduction

The thesis has explored a range of methods for enhancing the quality of indoor wireless communications either from an in-building access point or from a distant High Altitude Platform (HAP). Highlights of the work include:

- The development of a novel deterministic propagation model for analysing field strength and multipath statistics in an indoor environment;
- A detailed analysis of diversity and diversity combining strategies for indoor communications at 11 GHz and 17 GHz;
- A comparison of sectorised and beam-switched solutions for indoor communications at 11 GHz and 17 GHz;
- The use of an array of virtual transmitter antennas to emulate propagation from a distant HAP at any elevation angle;
- A detailed analysis of W-CDMA coverage at 2GHz (with and without space diversity at the terminal) given transmission from a distant HAP;
- A theoretical (including ideally correlated and uncorrelated scatter components) and ray-model based analysis and comparison of capacity for MIMO communications;
- A comparison of micro and macro MIMO capacity (for various antenna spacings) over practical indoor communication channels at 5 GHz;
- A site specific grid based analysis of the effective rank and Eigen-structure of the \mathbf{H} -matrix for micro and macro-MIMO configurations.

The fundamentals of radiowave propagation theory were introduced in chapter 2. This chapter also demonstrated the theoretical capacity gains (assuming ideal and independently distributed Rayleigh fading) using multiple antenna elements at the transmitter and receiver. The development of the ray model for indoor use was described in chapter 3. All subsequent propagation and system analysis made use of

this newly developed ray tracing engine (or specially enhanced versions for HAP and MIMO analysis). The initial ray model was limited to the prediction of normalised path loss for omni directional antennas. The model was enhanced in chapter 3 to support directional antennas in addition to sectorised or beam switched antennas at the access point. The electromagnetics was also improved to provide field strength and power predictions for any transmit power, antenna gain pattern and operating frequency. Space, frequency, pattern and polarisation diversity were analysed in chapter 4 to enhance the communications quality of the indoor link. The work was further extended in chapter 5 to consider sectorised and beam switched antenna systems. Chapter 6 described modifications to the ray model to enable indoor coverage prediction from a distant (HAP). The modification made use of a unique array of virtual transmitters placed around the building under test. The extended model was then used to analyse indoor W-CDMA coverage at 2 GHz as a function of EIRP at the HAP and with space diversity at the mobile terminal. Finally chapter 7 was dedicated to the application of MIMO in an indoor environment. As well as providing theoretical capacity estimates for ideally correlated and uncorrelated fading channels, the ray model was further extended to analyse MIMO capacity as a function of antenna configuration and practical propagation conditions at 5GHz. The chapter also introduce the concepts of micro-macro MIMO systems and analysed and compared the performance of the micro and macro configurations for an example office structure. The work demonstrated the superior coverage and capacity potential of macro-MIMO configurations in the indoor environment.

8.2 Propagation Theory and Channel Capacity

The propagation environment plays an important role in the performance of any radio communication system. In chapter 2 the basics of propagation theory was introduced and parameters such as spreading loss, fast fading, K-factor and shadowing were introduced. The use of MIMO was first introduced in chapter 2 together with the well known Shannon and Foschini capacity bounds. MIMO was shown to enhance the capacity significantly in a rich scatter or multipath environment. For a single transmit and receive antenna configuration, the capacity was shown to be a simple function of the signal to noise ratio. However, in the case of multiple antenna systems, the

capacity was now seen to be a function of the signal to noise ratio, the degree of scattering in the communication channel and the number of antenna elements at both ends of the link. The motivation to develop an indoor propagation model was fuelled by the desire to generate MIMO capacity estimates from deterministic environments and antenna geometries (rather than ideal mathematical distributions).

8.3 Ray Tracing Principles and Techniques

A novel propagation prediction tool was developed based on a combination of two specific modules, 1) Ray Tracing and 2) Field Reconstruction. By launching two dimensional uniformly spaced rays inside an environment and then tracing these rays as they reflect and transmit throughout the environment, the various multipaths linking the transmitter and receiver were identified.

In chapter 3 the basic elements of the ray tracing process were discussed, including the mathematics behind the transmission and reflection process. Issues such as polarisation modelling also considered. Received power and signal to noise ratio were predicted at the end of chapter 3 for a 5GHz indoor transmission system. This analysis made use of the theory defined in chapter 2 to provide results in the form of normalised field strength and received power for a given transmit power and antenna gain.

8.4 Diversity Combining and Generation

Wireless communications were shown to suffer from fast fading (chapter 2) and this can seriously disrupt the quality of the radio link (particularly in non-line-of-sight locations). Diversity represents a common technique for mitigating the effects of fast fading in a radio environment. The principles of diversity combining have been known for many decades. Three main methods of diversity signal generation were considered: i) two or more spaced antennas, ii) two orthogonally polarised antennas and iii) the use of two or more frequencies.

The probability of experiencing deep signal fades on all diversity branches at the same time was shown to be low providing the fast fading on each branch is uncorrelated. For diversity to be fully effective, the mean signal strength on all branches also needed to be similar. Using the indoor ray model discussed in chapter 3, field strength

prediction grids were generated to enable a diversity combining study to be performed. Results were produced for different frequencies, polarisations, antenna spacings and receiver locations. Three diversity combining strategies were considered: i) switched diversity, ii) equal gain amplitude combining and iii) equal gain vector combining.

Based on the diversity gains quoted in chapter 5, the three diversity combining techniques can be ranked in order as follows, with the first being the best:

- 1 Space.
- 2 Polarisation.
- 3 Frequency.

Polarisation and space diversity achieved similar diversity performances, with EG-AC resulting in a diversity gain in the 7-9 dB range. The choice between these two schemes depends on the fading decorrelation and the choice of reference antenna. With closely spaced antennas, polarisation diversity will result in superior performance. However, when large antenna spacings are used, space diversity will offer superior performance in all environments other than those that result in strongly polarised signals with similar branch powers.

Polarisation and frequency diversity have the major advantage of offering compact solutions (since spaced antennas are not required). This advantage may be particularly important for hand-held portable terminals. While frequency diversity gains are impressive (assuming spacings beyond the channel coherence bandwidth), the method is not spectrally efficient since twice the operating bandwidth is required (assuming two-branch combining). Hence, given the importance of spectrum efficiency, frequency diversity is not likely to be viable for most indoor applications.

The three diversity combining strategies can also be ranked based on the results quoted in chapter 5. Once again, the first technique offers the better performance:

- 1 EG-AC.
- 2 EG-VC.
- 3 SC.

While equal gain combining offers the best performance, the method is expected to be more expensive to implement. Hence, for cost sensitive applications, the more simple switched solution may be more appropriate, despite its lower performance.

For space diversity, the results showed that antenna spacing at the transmitter or receiver is important when determining the expected diversity gain. Generally speaking, receiver diversity is easier to implement since combining decisions can be made locally in the receiving radio. For transmitter diversity, information from the receiver must be sent back to the transmitter to support the combining process. One exception is short-range radio systems using time division duplex. For these systems, channel reciprocity can be exploited with the transmit diversity combining process based on the channel estimate from the received signal. For closely spaced antennas, the fast fading is correlated and little diversity gain can be generated. In the different environments, such as those considered in these studies, for antenna spacings of $\lambda/2$ and higher, significant decorrelation, and hence significant diversity gain, can be achieved.

Fast fading correlation statistics are also important when determining the expected diversity gain using frequency diversity. When the frequency spacing is less than the coherence bandwidth, the fast fading is correlated and little diversity gain is seen. However, for larger frequency spacings the fading becomes decorrelated and the full diversity gain is seen.

8.5 Sectorised and beam switched antennas

Chapter 5 considers field strength prediction for high frequency indoor communications at 17 GHz using directional antennas at the basestation and 2 branch spaced antenna diversity at the terminal. Detailed propagation information is generated using the ray-tracing propagation tool described in chapter 3. As a performance benchmark, initial field strength predictions were generated for omnidirectional basestation and terminal antennas. Downlink performance was seen to improve with the use of 2 branch spaced antenna diversity at the terminal. Factors such as antenna spacing and the choice of diversity combining algorithm also had an impact on performance. At the basestation, a novel 3 branch phased array beam pattern diversity system was compared with an ideal six branch sectorised antenna.

For each configuration, detailed propagation studies were performed to determine the relative (compared to omni-directional antennas) coverage improvement over the entire environment. Results indicated that the use of space diversity at the terminal could improve the expected coverage by as much as 10.7dB. Beam pattern and sector switching arrangements at the basestation resulted in a 7.2-10.4dB improvement. The most impressive gains were observed using directional antennas at the basestation and spaced antenna diversity at the terminal. Here, gains of 17.2dB and 19.4dB were observed for 3 (beam pattern) and 6 (sectorised) branch systems respectively at the basestation.

8.6 High Altitude Platforms

The creation of a HAP-to-indoor coverage model formed a major and novel part of the work performed in this thesis. Traditionally, given the vast separation distance between the HAP and the mobile terminal, ray-launching methods have been very difficult to apply.

In chapter 6 two methods were introduced to simulate indoor reception from an overhead or offset High Altitude Platform (HAP). The first method represented a sub-optimum approximation and required minimal changes to the original ray tracing code. This simplified method assumed that losses could be split into three basic multiplicative effects: Free Space Path loss, material loss and fast fading loss. The existing ray tracing software correctly computes material loss. However, fast fading loss (which requires accurate angle distributions) and spreading loss can only be correctly modelled if the distance to the transmitter is accurately modelled. To overcome this problem, the average spreading loss from a single virtual transmitter was removed (by division), and the true spreading loss from the HAP added (by multiplication). The second and far more accurate method placed an array of virtual transmitters around the building under test. Rays were launched from this array to emulate the launching of rays from a distant HAP. Field strength grids were produced and compared with the simplified technique. Results from the first method (where the field strength prediction was made using a single virtual transmitter placed just above the building structure and the distance dependent free space path loss was adjusted to a value based on the true terminal-HAP separation distance) were shown to produce

an accurate mean power prediction. However factors such as fast fading and spatial multipath were not correctly modelled, and this was graphically demonstrated by comparing predictions with the second, more accurate method. The cause of error in the first technique was traced to vertical wall reflections resulting from the incorrect launch angles when a low mounted launch site was used to approximate the distant HAP. When ray tracing from a single virtual transmitter, it is not possible to recreate plane waves accurately.

The second HAP modelling technique used an array of virtual transmitters, each launching a single ray at an angle corresponding to the equivalent that would have been sent from the HAP. This method allowed the HAP to be simulated at any angle in the sky and not just directly above the building. The method correctly modelled the near parallel waves expected, and also confined the analysis to a small grid surrounding the indoor environment (thus easing memory and run time computing constraints). For both techniques indoor coverage grids were produced and a statistical analysis of the modelled results performed.

Finally, a detailed analysis of indoor HAP coverage in the 2GHz UMTS band using the newly modified ray model was performed. Indoor coverage results were generated with and without space diversity at the user terminal. The analysis assumed a 1km radius spot beam, a 3G compatible operating bandwidth of 4MHz and 90% in-building area coverage. The link budget analysis showed that high quality indoor coverage from a HAP was indeed possible at UMTS frequencies. In particular, the use of space diversity at the terminal was shown to reduced the HAP transmit power from 2.15 watts to 0.84 watts. An area coverage of 99% was shown to require unreasonably high transmit powers at larger bandwidths (due to the large margin required) even with diversity at the terminal.

8.7 MIMO Communications

Multiple antennas located at the transmitter and receiver have the potential to increase significantly wireless communication capacity but only if the multipath scattering environment is rich enough. In chapter 7 a theoretical capacity analysis was performed for SISO and MIMO communications assuming perfectly uncorrelated and perfectly correlated Rayleigh/Rician fading. The results confirmed that MIMO

communications systems improve the theoretical capacity in a rich scatter environment, providing the fading over the array is uncorrelated. For fully correlated MIMO channels, the capacity was seen to drop with increasing scatter (although the absolute capacity was still superior to the SISO case).

For an SNR ratio of 16 dB, a SISO system was seen to offer a theoretical capacity of 4.6 bits/s/Hz in Rayleigh fading conditions. A 2x2 MIMO system improved this value to around 8.5 bits/s/Hz in uncorrelated fading (dropping to just over 6 bits/s/Hz in correlated fading). A 4x4 MIMO system offers around 18 bits/s/Hz in uncorrelated fading (dropping to around 7 bits/s/Hz in fully correlated fading).

This analysis confirmed that MIMO processing is a powerful method for enhancing capacity (or reducing the S/N required to achieve a given capacity). For the method to be most effective it is important for the fading to be decorrelated and for the arrays to be placed in a rich scatter environment. Using a modified version of the ray tracing model, the channel matrix was predicted for two 4x4 MIMO configurations (the first being a standard micro-MIMO configuration while the second, referred to as macro-MIMO, distributed the AP antennas towards each corner of the room). For each point in a chosen route and also throughout the whole environment the theoretical capacity bound was analysed and compared with the case of ideal and independently distributed Rayleigh fading. For the first route, the use of macro-MIMO was seen to result in an approximate 6 dB improvement in average SNR (for the same fixed transmit power per element). The normalised capacity was also seen to increase by around 16% when macro-MIMO was applied. More significantly, relative to micro-MIMO, the average capacity along the route increased by 62% using macro-MIMO. The second route showed an even higher gain in average SNR. Here the improvement of macro-MIMO was more than 12 dB. The normalised capacity actually dropped by 1% with macro-MIMO along this route. However, when the gain in SNR is considered, the overall MIMO capacity was seen to rise by 105%.

As an alternative to large capacity gains, the use of macro-MIMO could be used as an effective method for reducing the transmit power required for a given capacity level. Given health concerns for indoor communications, this benefit could be of considerable future interest.

For all MIMO systems, close inter-element spacings were shown to reduce MIMO capacity through the generation of correlated fading in the \mathbf{H} -matrix. An inter-element spacing of around 0.5 wavelengths was shown to offer a good compromise between MIMO capacity and physical bulk.

The structure of the link matrix was analysed at each point in the grid by calculating the effective rank and Eigen-structure. The rank of the matrix can be used as an indicator of potential capacity. For rich scatter locations, the effective rank of the matrix was high and approached the number of transmit antennas. However, for locations with a dominant multipath the rank was seen to collapse. Generally, Eigenvalue spread was at its lowest in high scatter areas and showed high values where line-of-sight propagation tended to concentrate power into a single Eigenvalue. The total environment studies highlighted the benefits of macro-MIMO as a method of more evenly distributing power over the floor space. The results also showed that macro-MIMO maintained high rank and low Eigenvalue spread over the majority of the floor space.

From the total environment studies, the macro-MIMO capacity was shown to be higher for both the normalised and un-normalised SNR cases. In the normalised SNR case, the average capacity increased from 12.8 to 15.4 bits/s/Hz. In the un-normalised SNR case, the use of macro-MIMO improved capacity from 23.9 to 32.3 bits/s/Hz.

8.8 Future Work

The following areas have been identified as potential areas for further work:

- Perform indoor field strength measurements at a number of centre frequencies;
- Measure spatial, spectral and polarisation correlations;
- Measure material parameters at frequencies of interest;
- Model broadband effects such as RMS delay spread and coherence bandwidth in Outdoor - Indoor environments and vice versa;
- Enhance ray model to support a 3-D environment;
- Incorporation of diffraction model;
- Simulate MIMO physical layer and explore receiver complexity;

The first three points are based around a number of detailed measurements that could be performed to support the theoretical and simulation work described in this thesis. Ideally wideband measurements (enabling signal strength and RMS delay spread to be obtained) at two or more carrier frequencies would be performed. Spatial and spectral correlation measurements could be used to confirm the antenna and frequency spacings required to generate uncorrelated signals suitable for diversity combining. Measurements should also concentrate on determining typical attenuation levels through realistic building structures at the frequencies of interest. This data could be used to estimate the conductivity of the materials under test. This information would then be used to improve the accuracy of the propagation model.

Measurements using two antennas (spaced or dual polarised) would allow practical diversity gains to be generated by analysing the measured data. In addition to confirming the levels of diversity gain that are possible, measurements for each branch could be used to validate the accuracy of the prediction tool.

The ray model could be extended to support 3-D environments. This would enable the impact of height (both at the mobile terminal and access point) to be evaluated.

Finally, simulation work could be performed to analyse the physical layer performance of a MIMO communication system. Using channel data obtained from the ray model, simulated data transmissions could be used to determine the performance of a range of space time coded and spatially multiplexed solutions. In addition to quantifying the capacity for each scheme relative to the theoretical bound, the complexity of the required transmitters and receivers should also be studied and compared.

Appendix A: Boundary Analysis

A.1 Vertical and Horizontal Boundaries

In this section the ray interactions with vertical and horizontal boundaries are described. The analysis is broken down into four quadrants, with transmission and reflection possible in each case depending on permittivity values at the interface.

A.1.1 Relationship between `ang`, `al` and `alfa`

Internally within the ray-tracing algorithm three different angles (`ang`, `al` and `alfa`) are used to describe the direction in which a ray travels. These three angles are required to support full four-quadrant angle analysis. The following sections describe the relationship between `al` and `alfa` given the four-quadrant ray direction, `ang`.

A.1.1.1 Ang in Quadrant 1

The simplest case occurs when `ang` lies in quadrant 1 ($90 < \phi < 0$). In this case, `alfa` and `al` are simply assigned the same value as `ang`, as shown in figure A.1 below. This result is summarised in the table below, assuming `ang` travels at an angle, ϕ , defined in an anticlockwise direction from the x -axis.

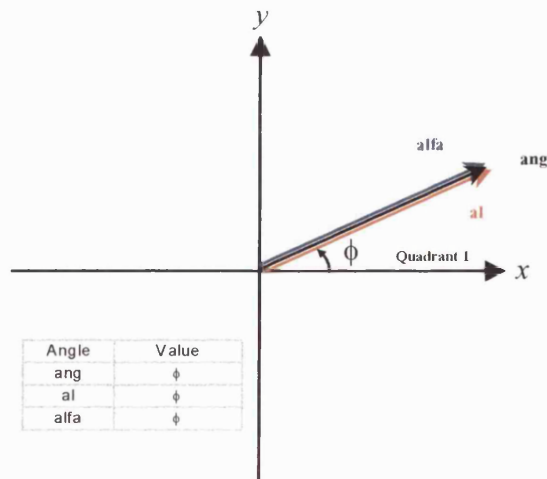


Figure A.1: Definition of `al` and `alfa` when `ang` lies in quadrant 1

A.1.1.2 Ang in Quadrant 2

Figure A.2 below shows ang and alfa when ang lies in quadrant 2 ($180 < \phi < 90$). In this case, alfa is obtained by mapping ang back into the first quadrant using the equation, $\text{alfa} = 180 - \text{ang}$. The variable al is obtained from the equation $180 + \text{ang}$. The angles are summarised in the table below, assuming ang travels at an angle, ϕ , defined in an anticlockwise direction from the x -axis.

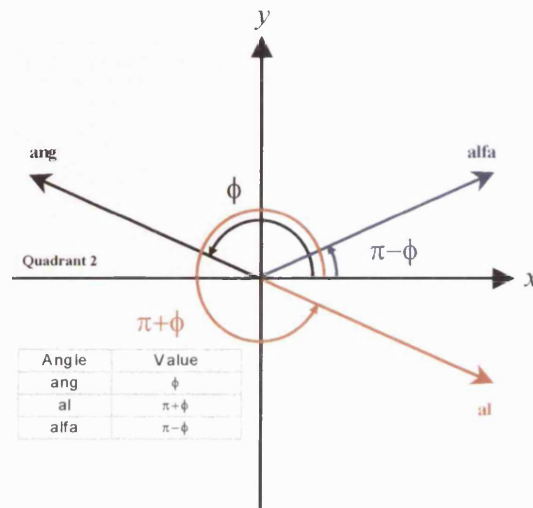


Figure A.2: Definition of al and alfa when ang lies in quadrant 2

A.1.1.3 Ang in Quadrant 3

Figure A.3 shows al and alfa when ang lies in quadrant 3 ($270 < \phi < 180$). In this case, alfa is obtained by mapping ang back into the first quadrant using the equation, $\text{alfa} = \text{ang} - 180$. In this quadrant al has the same value as ang . These angles are summarised in the table shown in figure A.3, assuming ang travels at an angle, ϕ , defined in an anticlockwise direction from the x -axis.

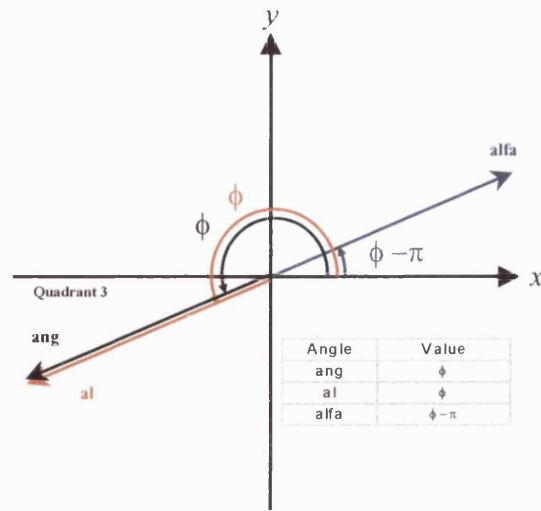


Figure A.3: Definition of al and alfa when ang lies in quadrant 3

A.1.1.4 Ang in Quadrant 4

Finally figure A.4 defines al and alfa when ang lies in quadrant 4 ($360 < \phi < 270$). In this case, alfa is obtained by mapping ang back into the first quadrant using the equation, $alfa = 360 - ang$. The variable al has the same value as ang. These angles are summarised in the associated table.

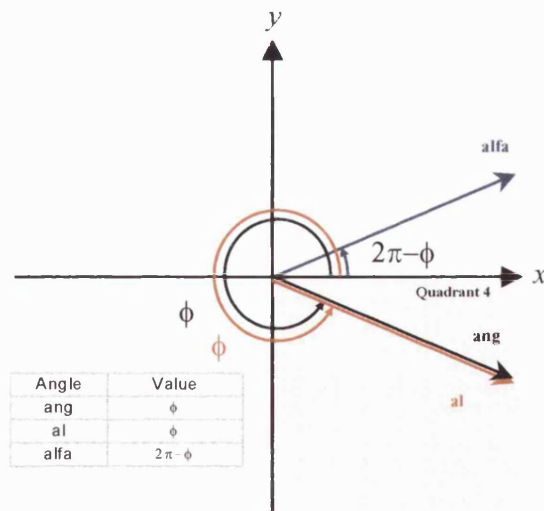


Figure A.4: Definition of al and alfa when ang lies in quadrant 4

A.1.2 Simulation of Transmission or Reflection

As mentioned previously, depending of the change in permittivity the ray may be transmitted and/or reflected. The permittivity of the first environment is denoted by e_1 and the second environment by e_2 . The following cases now apply.

A.2 Boundary Analysis

A.2.1 Vertical boundary, the case of $e_2 < e_1$

As the ray travels through the environment, the permittivity of the previous cell is denoted by the variable e_1 , while the permittivity of the current cell is denoted by the variable e_2 . When $e_2 < e_1$ the ray has encountered a boundary in the transmission medium and the signal will be transmitted, otherwise the ray will be reflected. The program now enters one of four cases, depending on the direction of the incident ray. The geometry for each of the four cases is now summarised under the assumption that the transmit ray travels at the same angle as the incident ray.

A.2.1.1 Geometry Case 1

In case 1 the incident ray is assumed to travel at an angle in the first quadrant. Figure A.5 shows the geometry associated with this vertical interaction. The incident ray (blue) travels in the direction of quadrant 1. The reflected ray travels in quadrant 2 while the transmitted ray travels in quadrant 1.

Figure A.5 shows the incident ray in quadrant one interacting with a vertical boundary. The ray is travelling upwards ($i_y=1$) and to the right ($i_x=1$), i.e. the incident angle, ang , lies in the range $0 \leq \alpha < 90$ degrees. Based on the material properties of the media, the direction of the transmitted and reflected rays can be calculated. Internally, four quadrant trigonometric functions are required in these calculations. To overcome this limitation, two further angles are defined, denoted by the variables $a1$ and alfa (see section A.1.1).

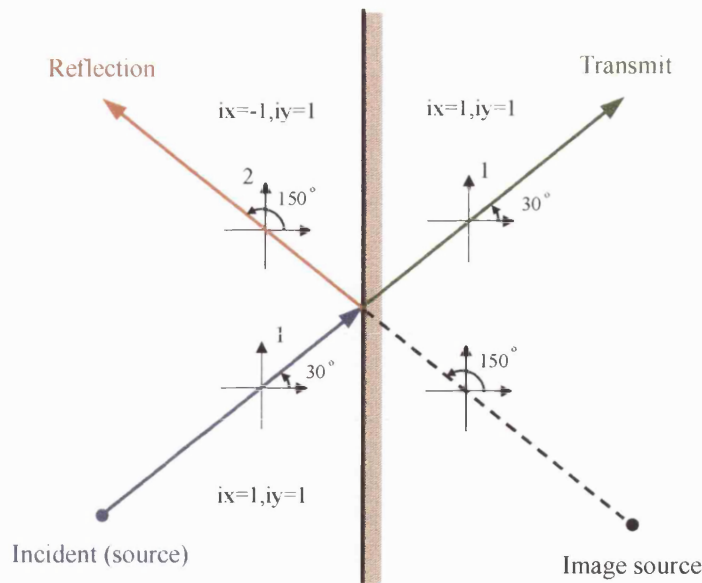


Figure A.5: transmission and reflection at a vertical boundary: case 1 ($ix=1, iy=1$)

The angle of incidence is denoted by ang and using a knowledge of the material characteristics at the boundary the transmission angle, tt , is calculated. This angle is then mapped to $p \rightarrow \alpha$, the first quadrant version of the angle after the boundary interaction. Next, using table A.1, the angles $p \rightarrow \alpha$, $p \rightarrow ang$ and ang (reflected angle after interaction) are calculated.

Angle	Equation	Value	Notes
Ang		30 degrees	Incident angle
Alfa	Figure A.6	30 degrees	Quadrant mapped incident angle
tt		30 degrees	Quadrant 1 transmission angle
$p \rightarrow \alpha$	tt	30 degrees	Stored quadrant 1 transmission angle
$p \rightarrow \alpha$	$p \rightarrow \alpha$	30 degrees	Intermediate angle
$p \rightarrow ang$	$p \rightarrow \alpha$	30 degrees	Transmission angle (green line in figure A.5)
Ang	$180 - \alpha$	150 degrees	Reflection Angle (red line in figure A.5)

Table A.1: Angle table for case 1

A.2.1.2 Geometry Case 2

In case 2 the incident ray is assumed to travel at an angle in the second quadrant. Figure A.6 shows the geometry associated with this vertical interaction. The incident

ray (blue) travels in the direction of quadrant 2. The reflected ray travels in quadrant 3 while the transmitted ray travels in quadrant 2.

Angle	Equation	Value	Notes
Ang		150 degrees	Incident angle
alfa	Figure A.7	30 degrees	Quadrant mapped incident angle
tt		30 degrees	Quadrant 1 transmission angle
p->alfa	tt	30 degrees	Stored quadrant 1 transmission angle
p->al	-p->alfa	330 degrees	Intermediate angle
p->ang	180-p->alfa	150 degrees	Transmission angle (green line in figure A.5)
Ang	Alfa	30 degrees	Reflection Angle (red line in figure A.5)

Table A.2: Angle table for case 2

Figure A.6 shows the incident ray in quadrant two interacting with a vertical boundary. The ray is travelling upwards ($iy=1$) and to the left ($ix=-1$), i.e. the incident angle, ang , lies in the range $90 \leq \alpha < 180$ degrees. Table A.2 defines the angles before and after the interaction.

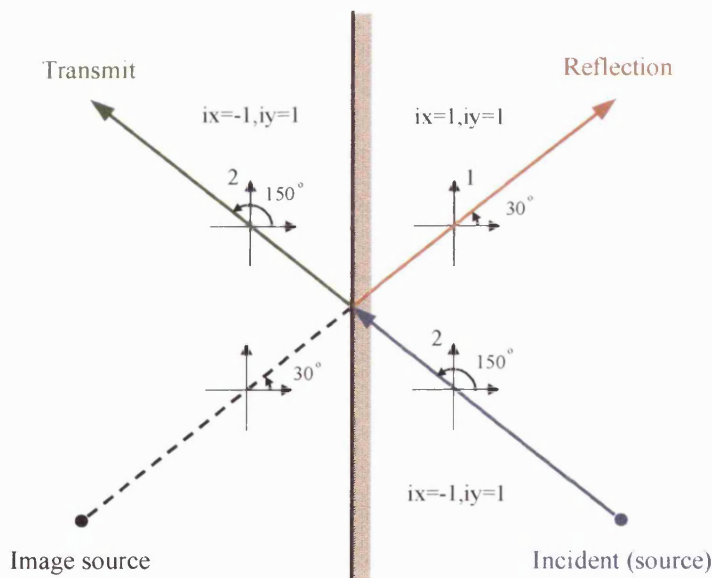


Figure A.6: transmission and reflection at a vertical boundary: case 2 ($ix=-1, iy=1$)

A.2.1.3 Geometry Case 3

In case 3 the incident ray is assumed to travel at an angle in the third quadrant. Figure A.7 shows the geometry associated with this vertical interaction. The incident ray

(blue) travels in the direction of quadrant 3. The reflected ray travels in quadrant 4 while the transmitted ray travels in quadrant 3.

Angle	Equation	Value	Notes
ang		210 degrees	Incident angle
alfa	Figure A.8	30 degrees	Quadrant mapped incident angle
tt		30 degrees	Quadrant I transmission angle
p->alfa	tt	30 degrees	Stored quadrant I transmission angle
p->al	p->alfa	30 degrees	Intermediate angle
p->ang	-180+p->alfa	210 degrees	Transmission angle (green line in figure A.5)
ang	-alfa	330 degrees	Reflection Angle (red line in figure A.5)

Table A.3: Angle table for case 3

Figure A.7 shows the incident ray in quadrant three interacting with a vertical boundary. The ray is travelling downwards ($i_y=-1$) and to the left ($i_x=-1$), i.e. the incident angle, ang , lies in the range $180 \leq \alpha < 270$ degrees. Table A.3 defines the angles before and after this interaction.

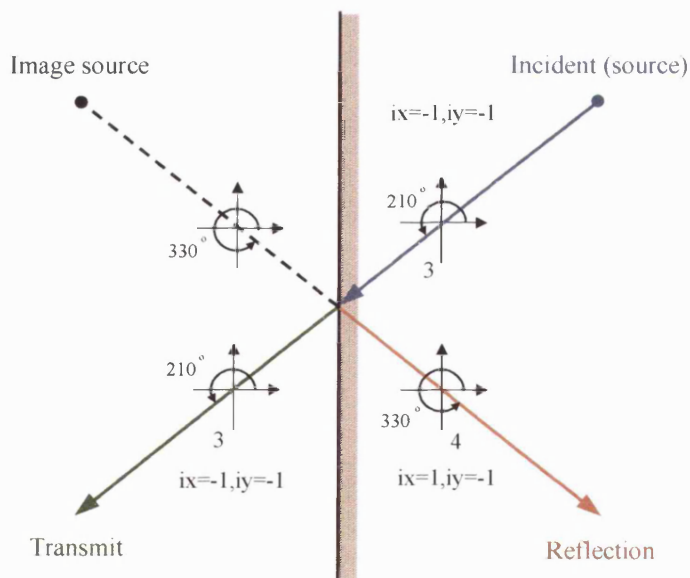


Figure A.7: transmission and reflection at a vertical boundary: case 3 ($i_x=-1, i_y=-1$)

A.2.1.4 Geometry Case 4

In case 4 the incident ray is assumed to travel at an angle in the fourth quadrant. Figure A.8 shows the geometry associated with this vertical interaction. The incident ray (blue) travels in the direction of quadrant 4. The reflected ray travels in quadrant 3 while the transmitted ray travels in quadrant 4.

Angle	Equation	Value	Notes
Ang		330 degrees	Incident angle
Alfa	Figure A.8	30 degrees	Quadrant mapped incident angle
tt		30 degrees	Quadrant I transmission angle
p->alfa	tt	30 degrees	Stored quadrant I transmission angle
p->al	-p->alfa	330 degrees	Intermediate angle
p->ang	p->al	330 degrees	Transmission angle (green line in figure A.5)
Ang	-180+alfa	210 degrees	Reflection Angle (red line in figure A.5)

Table A.4: Angle table for case 4

Figure A.8 shows the incident ray in quadrant four interacting with a vertical boundary. The ray is travelling downwards ($i_y=-1$) and to the right ($i_x=1$), i.e. the incident angle, ang , lies in the range $270 \leq \alpha < 360$ degrees. Table A.4 defines the angles before and after this interaction.

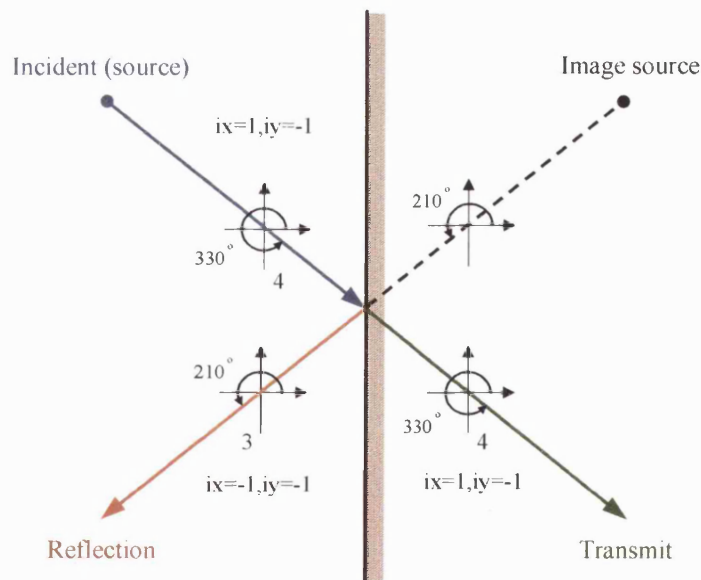


Figure A.8: transmission and reflection at a vertical boundary: case 4($i_x=1, i_y=-1$)

A.2.2 Horizontal Boundary, the case of $e_2 > e_1$

Ray interactions at the horizontal boundary are very similar to those described in section A.2.1. The incident, reflected and transmitted waves are shown for each of the four horizontal cases in figures A.9 - A.10. Tables similar to those given in A.2.1 can be calculated.

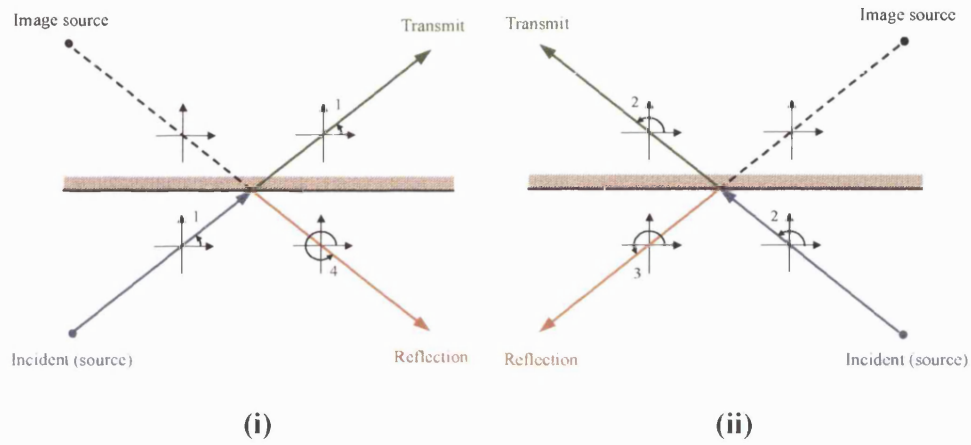


Figure A.9: transmission and reflection at a horizontal boundary
 (i) case 1 ($ix=1, iy=1$), (ii) case 2 ($ix=-1, iy=1$)

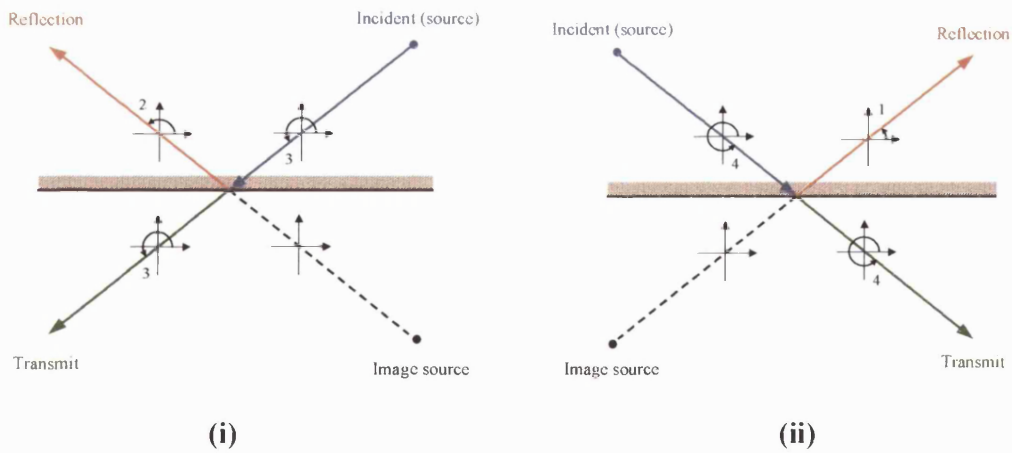


Figure 6.10: transmission and reflection at a horizontal boundary
 (i) case 3 ($ix=-1, iy=-1$), (ii) case 4 ($ix=1, iy=-1$)

Appendix B: Diversity Methods and Techniques

B.1 Detailed Combining Analysis

This appendix demonstrates the diversity combining results for different diversity techniques such as receiver and transmitter space diversity and frequency diversity.

B.1.1 Branches 1 and 2

Table B.1 shows a comparison of field strength and diversity combining gains for frequency diversity at a spacing of 1 MHz. For the SC case, an average gain of just 0.06 dB (relative to branch 1) and 0.08 dB (relative to branch 2) is observed.

Method	Field Strength	Gain Relative to Branch 1	Gain Relative to Branch 2
EG-AC	-6.19	6.01	6.03
EG-VC	-6.19	5.99	6.01
SC	-12.17	0.06	0.08

Table B.1: Average Field Strength and Combining Gains in dB for Frequency Diversity ($\delta f = 1\text{MHz}$)

The small gains seen in the above table result from the small frequency diversity spacing, in this case it is well below the channel's coherence bandwidth. In this scenario, the fast fading is correlated on both branches, resulting in very small switched diversity gain. As seen in later tables, the diversity gains increases as the frequency separation is increased.

In the EG-VC and EG-AC cases, the average field strength will increase by a factor of two, or 6dB, since the output from the two diversity branches are summed. Hence, even in the highly correlated diversity case, the signal field strength will increase statistically by a factor of 2 (although in the EG-VC case destructive phase summation at certain points can worsen performance). For EG schemes it is common to remove this 6 dB improvement from the quoted gain. If this were applied then no significant diversity gain is observed.

B.1.2 Branches 1 and 3

Table B.2 shows a comparison of field strength and diversity combining gains for frequency diversity at a spacing of 10 MHz. For the SC case, an average gain of 0.62 dB (relative to branch 1) and 0.83 dB (relative to branch 3) is observed.

Method	Field Strength	Gain Relative to Branch 1	Gain Relative to Branch 3
EG-AC	-6.19	6.09	6.22
EG-VC	-6.72	3.88	4.02
SC	-11.96	0.62	0.83

Table B.2: Average Field Strength and Combining Gains in dB for Frequency Diversity ($\delta f = 10\text{MHz}$)

The diversity gain has now increased relative to the 1 MHz case (see section 4.4 in chapter 4); however the gain is still low since the fast fading remains highly correlated in the two branches.

In the EG-VC and EG-AC cases, the average field strength can be seen to increase by approximately 4 to 6 dB (since the outputs from the two diversity branches are summed). Given that a 6 dB improvement is expected even for branches with correlated fast fading, the gains observed are disappointing. In the EG-VC case the gain is less than the minimum expected 6 dB due to destructive summation of the two branches. For EG-AC co-phasing is used to prevent this problem and a small additional gain is observed. The magnitude of this gain is expected to rise as the frequency spacing is further increased.

B.1.3 Branches 1 and 4

Table B.3 shows a comparison of field strength and diversity combining gains for frequency diversity at a spacing of 50 MHz. For the SC case, an average gain of 1.47 dB (relative to branch 1) and 1.83 dB (relative to branch 4) is observed. The decorrelation of the fast fading on the two branches is now becoming high and this has resulted in an increased diversity gain.

Method	Field Strength	Gain Relative to Branch 1	Gain Relative to Branch 4
EG-AC	-6.34	6.31	6.59
EG-VC	-8.66	2.56	2.93
SC	-11.64	1.47	1.83

Table B.3: Field Strength and Combining Gains in dB for Frequency Diversity ($\delta f = 50\text{MHz}$)

In the EG-AC case, the average field strength can be seen to increase by approximately 6 dB. Average diversity gains of 6.31 dB and 6.59 dB are now seen to occur. EG-VC results in disappointing gains of 2.56 dB and 2.93 dB. This is well below the minimum 6 dB to be expected in an equal gain combining scheme.

B.2 Receiver Space Diversity Gain versus Antenna Spacing

B.2.1 Group 8 relative to Branch 2

Figures B.1, B.2 and B.3 show the diversity gains relative to branch 2 for group 8 (i.e. where the largest antenna spacing, 3.5λ , applied). The results are in contrast to figures 4.27-4.29 in chapter 4, where the lowest antenna separation, 0.25λ , was used.

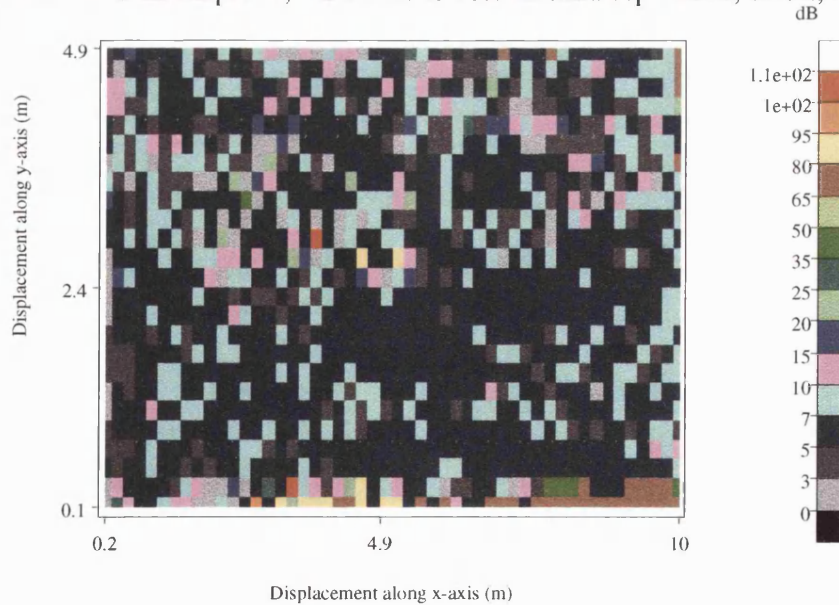


Figure B.1: Receiver Space Diversity (EG-AC) - Diversity Gain relative to branch 2 (3.5λ spacing)

Figure B.1 confirms the superiority of EG-AC, offering strong diversity gains throughout the indoor environment. Figure B.2 shows the gain for EG-VC. At this particular antenna spacing, the overall gain using this method is very low. This results from destructive interference between the two input signals and results in a diversity output that is potentially weaker than either branch input. Figure B.2 shows no gain for a significant section of the indoor grid.

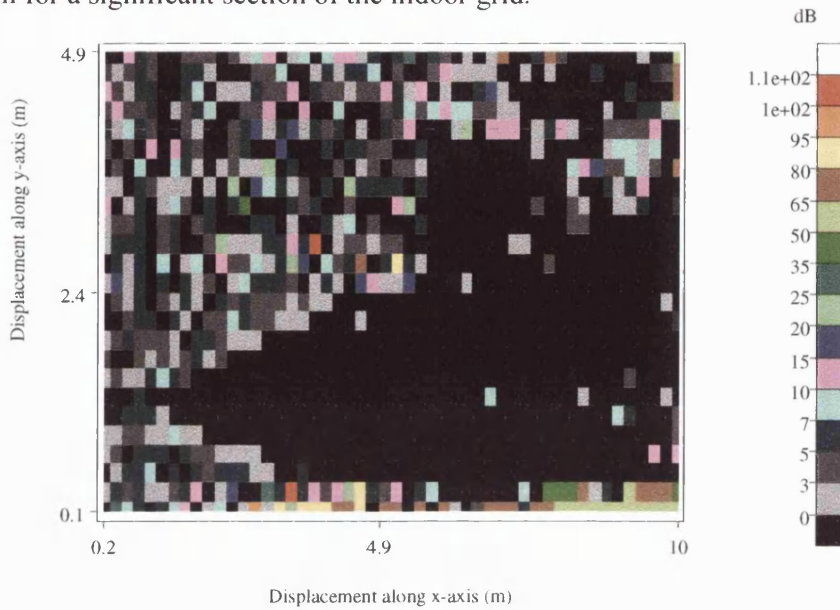


Figure B.2: Receiver Space Diversity (EG-VC) - Diversity Gain relative to branch 2 (3.5λ spacing)

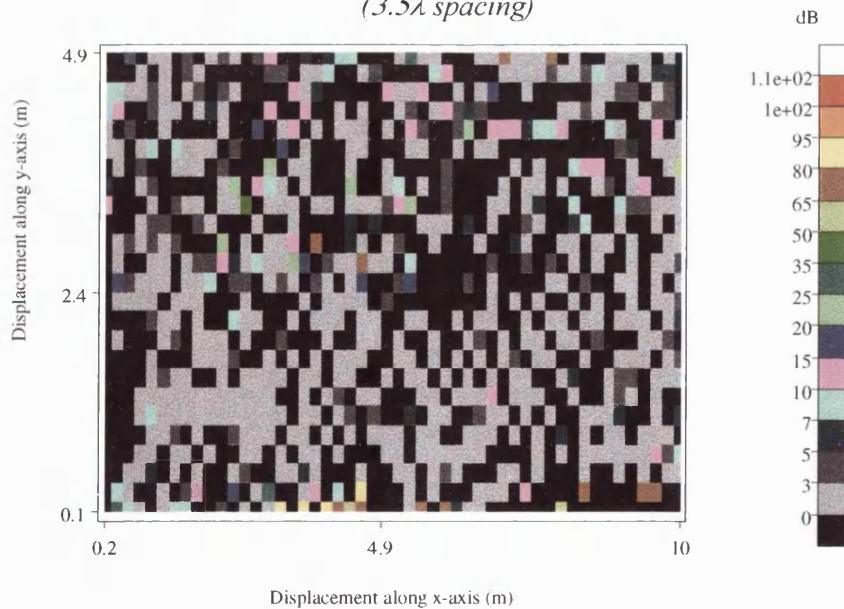


Figure B.3: Receiver Space Diversity (SC) - Diversity Gain relative to branch 2 (3.5λ spacing)

Figure B.3 shows the diversity gain using SC with an antenna spacing of 3.5λ . Overall, at this antenna spacing (and in fact at all the half wavelength spacings considered) the average gain for SC in this environment is higher than the previous EG-VC method. For other antenna spacings (where in this case constructive addition occurred) the EG-VC technique resulted in a higher gain than SC.

B.3 Receiver Space Diversity Combining

B.3.1 Group 1: 0.25λ Spacing

As in the previous diversity studies, three combining techniques were considered. Two are based on equal gain combining (EG-AC and EG-VC) with the third using switched diversity (SC).

Diversity	Average (dB)	Mean (Linear)	Variance	Standard Deviation
EG-AC	-6.19	0.490	1.134	1.065
EG-VC	-7.86	0.404	0.942	0.970
SC	-11.23	0.265	0.343	0.585

Table B.4: Diversity Combining Field Strength Summary: Receiver Spacing Group 1 (0.25λ spacing)

Table B.4 lists the statistical values of the field strength *after* diversity combining using each of the three specified methods. For the equal gain techniques, the average value of field strength has increased by around 6 dB. Using SC, a small decrease in the average is observed. Care must be taken when comparing the average values since different averaging methods are applied for the diversity calculations. In particular, if the antenna field strength falls below -90 dB on either of the two branches the point is excluded from the cumulative sum. If a large number of locations fall into this category then the average values in table B.4 become significantly lowered. For the average values shown in table B.4, no averaging thresholds were used.

To obtain a true value for the receiver diversity gain, the results shown in table B.5 should be used. These results were obtained by averaging the diversity gain (relative to branch 1) on a point by point basis for locations where the branch 1, branch 2 and diversity fields are greater than -90 dB. An average improvement in the range 5.05 - 6.89 dB is seen for the EG methods, while a gain of 1.85 - 2.06 dB is achieved using the SC approach.

Method of Diversity Improvement	Relative to Branch 1 (dB)	Relative to Branch 2 (dB)
EG-AC	6.89	6.78
EG-VC	5.15	5.05
SC	2.06	1.85

Table B.5: Receiver Space Diversity Gain versus Combining Technique – Group 1 (0.25λ spacing)

B.3.2 Group 3: λ Spacing

Table B.6 lists the statistical values of the field strength after diversity combining using λ antenna spacing.

Diversity	Average (dB)	Mean (Linear)	Variance	Standard Deviation
EG-AC	-6.23	0.488	1.147	1.071
EG-VC	-8.00	0.398	0.774	0.880
SC	-11.29	0.265	0.349	0.591

Table B.6: Diversity Combining Field Strength Summary: Receiver Spacing Group 3 (λ spacing)

Table B.7 shows the receiver diversity gain (relative to branches 1 and branch 4 respectively) for each combining technique. At this higher antenna spacing, an average improvement in the range 5.35 - 7.53 dB is seen for the EG methods, while a gain of 2.32 - 3.14 dB is achieved using the SC approach. As expected, the diversity gains are seen to increase with greater antenna spacing (see section 4.6 in chapter 4).

Method of Diversity Improvement	Relative to Branch 1 (dB)	Relative to Branch 4 (dB)
EG-AC	7.02	7.53
EG-VC	5.35	5.97
SC	2.32	3.14

Table B.7: Receiver Space Diversity Gain versus Combining Technique – Group 3 (λ spacing)

B.3.3 Group 4: 1.5λ Spacing

Table B.8 lists the statistical values of the field strength after diversity combining using 1.5λ antenna spacing.

Diversity	Average (dB)	Mean (Linear)	Variance	Standard Deviation
EG-AC	-6.21	0.489	1.144	1.070
EG-VC	-12.91	0.226	0.686	0.828
SC	-11.23	0.268	0.354	0.599

Table B.8: Diversity Combining Field Strength Summary: Receiver Spacing Group 4 (1.5λ spacing)

Table B.9 shows the receiver diversity gain (relative to branches 1 and branch 5 respectively) for each combining technique. An average improvement in the range 0.95 - 7.43 dB is seen for the EG methods, while a gain of 2.94 - 3.01 dB is achieved using the SC approach. Once again, for half wavelength antenna spacings, the gains for vector combining are poor.

Method of Diversity Improvement	Relative to Branch 1 (dB)	Relative to Branch 5 (dB)
EG-AC	7.30	7.43
EG-VC	0.95	1.09
SC	3.01	2.94

Table B.9: Receiver Space Diversity Gain versus Combining Technique – Group 4 (1.5λ spacing)

B.3.4 Group 5: 2λ Spacing

Table B.10 lists the statistical values of the field strength *after* diversity combining using each of the three specified methods with 2λ spacing.

Diversity	Average (dB)	Mean (Linear)	Variance	Standard Deviation
EG-AC	-6.22	0.489	1.146	1.071
EG-VC	-7.95	0.400	0.842	0.917
SC	-11.20	0.269	0.355	0.596

Table B.10: Diversity Combining Field Strength Summary: Receiver Spacing Group 5 (2λ spacing)

Table B.11 shows the receiver diversity gain (relative to branch 1 and branch 6 respectively) for each of the three combining techniques. An average improvement in the range 5.69 - 7.44 dB is seen for the EG methods, while a gain of 2.89 - 3.06 dB is achieved using the SC approach.

Method of Diversity Improvement	Relative to Branch 1 (dB)	Relative to Branch 6 (dB)
EG-AC	7.22	7.44
EG-VC	5.69	5.95
SC	2.87	3.06

Table B.11: Receiver Space Diversity Gain versus Combining Technique – Group 5 (2λ spacing)

B.3.5 Group 6: 2.5λ Spacing

Table B.12 lists the statistical values of the field strength after diversity combining using each of the three specified methods with 2.5λ spacing.

Diversity	Average (dB)	Mean (Linear)	Variance	Standard Deviation
EG-AC	-6.21	0.489	1.131	1.064
EG-VC	-12.69	0.232	0.547	0.739
SC	-11.15	0.270	0.367	0.605

Table B.12: Diversity Combining Field Strength Summary: Receiver Spacing Group 6 (2.5λ spacing)

Table B.13 shows the receiver diversity gain (relative to branch 1 and branch 7 respectively) for each of the three combining techniques. An average improvement in the range 1.42 - 7.73 dB is seen for the EG methods, while a gain of 3.13 - 3.49 dB is achieved using the SC approach. At the 2.5 wavelength spacing, diversity gains are seen to improve to new highs for the EG-AC and SC techniques. Once again, at half wavelength spacings, the results for EG-VC are poor.

Method of Diversity Improvement	Relative to Branch 1 (dB)	Relative to Branch 7 (dB)
EG-AC	7.31	7.73
EG-VC	1.42	2.25
SC	3.13	3.49

Table B.13: Receiver Space Diversity Gain versus Combining Technique – Group 6 (2.5λ spacing)

B.3.6 Group 7: 3λ Spacing

Table B.14 lists the statistical values of the field strength *after* diversity combining using each of the three specified methods with 3λ spacing.

Diversity	Average (dB)	Mean (Linear)	Variance	Standard Deviation
EG-AC	-6.21	0.489	1.139	1.067
EG-VC	-8.13	0.392	0.796	0.892
SC	-11.05	0.273	0.371	0.609

Table B.14: Diversity Combining Field Strength Summary: Receiver Spacing Group 7 (3λ spacing)

Table B.15 shows the receiver diversity gain (relative to branch 1 and branch 8 respectively) for each of the three combining techniques. An average improvement in the range 6.47 - 8.13 dB is seen for the EG methods, while a gain of 3.86 dB is achieved using the SC approach.

Method of Diversity Improvement	Relative to Branch 1 (dB)	Relative to Branch 8 (dB)
EG-AC	7.83	8.13
EG-VC	6.47	6.76
SC	3.86	3.86

Table B.15: Receiver Space Diversity Gain versus Combining Technique – Group 7 (3λ spacing)

B.3.7 Group 8: 3.5λ Spacing

Table B.18 lists the statistical values of the field strength *after* diversity combining using each of the three specified methods with the maximum 3.5λ spacing.

Diversity	Average (dB)	Mean (Linear)	Variance	Standard Deviation
EG-AC	-6.24	0.488	1.124	1.060
EG-VC	-11.85	0.256	0.601	0.775
SC	-11.10	0.272	0.375	0.612

Table B.18: Diversity Combining Field Strength Summary: Receiver Spacing Group 8 (3.5λ spacing)

Table B.19 shows the receiver diversity gain (relative to branch 1 and branch 9 respectively) for each of the three combining techniques. At this maximum spacing, an average improvement in the range 2.87 - 8.26 dB is seen for the EG methods, while a gain of 4.09 - 4.13 dB is achieved using the SC approach. These gains are now similar to those seen using frequency (separation much greater than coherence bandwidth) and polarisation diversity.

Method of Diversity Improvement	Relative to Branch 1 (dB)	Relative to Branch 9 (dB)
EG-AC	7.98	8.26
EG-VC	2.87	3.26
SC	4.13	4.09

Table B.19: Receiver Space Diversity Gain versus Combining Technique – Group 8 (3.5λ spacing)

B.4 Transmitter Space Diversity Combining

B.4.1 Group 1: 0.25λ Spacing

Results are based on equal gain (EG-AC and EG-VC) and selection combining diversity (SC).

Diversity	Average (dB)	Mean (Linear)	Variance	Standard Deviation
EG-AC	-6.15	0.492	1.126	1.061
EG-VC	-8.15	0.391	0.949	0.974
SC	-10.89	0.276	0.347	0.589

Table B.20: Diversity Combining Field Strength Summary: Transmitter Spacing Group 1 (0.25λ spacing)

Table B.20 lists the statistical values of the field strength *after* diversity combining using each of the three specified methods. For the equal gain techniques, the average field strength has increased by around 5.5 dB. Using SC, an increase of around 1 dB is seen in these values. As mentioned earlier, due to different filters in the averaging process, diversity gains cannot be directly calculated from these tables.

Table B.21 shows the transmitter diversity gain (relative to branch 1 and branch 2) for each of the three combining techniques. An average improvement in the range 4.80 - 7.37 dB is seen for the EG methods, while a gain of 2.91 - 3.28 is achieved using the SC approach. Interestingly, these values are slightly higher than the corresponding values for receiver space diversity.

Method of Diversity Improvement	Relative to Branch 1 (dB)	Relative to Branch 2 (dB)
EG-AC	7.37	7.12
EG-VC	5.06	4.80
SC	3.28	2.91

Table B.21: Transmitter Space Diversity Gain versus Combining Technique – Group 1 (0.25λ spacing)

B.4.2 Group 3: λ Spacing

Table B.22 lists the statistical values of the field strength *after* space transmitter diversity combining using each of the three specified methods. A transmitter antenna spacing of 1λ was used.

Diversity	Average (dB)	Mean (Linear)	Variance	Standard Deviation
EG-AC	-6.12	0.494	1.162	1.078
EG-VC	-7.71	0.411	0.909	0.953
SC	-11.16	0.269	0.353	0.594

Table B.22: Diversity Combining Field Strength Summary: Transmitter Spacing Group 3 (1λ spacing)

Table B.23 shows the transmitter diversity gain (relative to branch 1 and branch 4 respectively) for each of the three combining techniques. An average improvement in the range 5.75 - 7.70 dB is seen for the EG methods, while a gain of 2.31 - 3.61 dB is achieved using the SC approach.

Method of Diversity Improvement	Relative to Branch 1 (dB)	Relative to Branch 4 (dB)
EG-AC	7.70	6.98
EG-VC	6.50	5.75
SC	3.61	2.31

Table B.23: Transmitter Space Diversity Gain versus Combining Technique – Group 3 (1λ spacing)

B.4.3 Group 4: 1.5λ Spacing

Table B.24 lists the statistical values of the field strength *after* space transmitter diversity combining using each of the three specified methods. A transmitter antenna spacing of 1.5λ was used.

Diversity	Average (dB)	Mean (Linear)	Variance	Standard Deviation
EG-AC	-6.17	0.491	1.124	1.060
EG-VC	-12.95	0.224	0.675	0.821
SC	-11.19	0.268	0.349	0.591

Table B.24: Diversity Combining Field Strength Summary: Transmitter Spacing Group 4 (1.5λ spacing)

Table B.25 shows the transmitter diversity gain (relative to branch 1 and branch 5 respectively) for each of the three combining techniques. An average improvement in the range 0.86 - 7.61 dB is seen for the EG methods, while a gain of 2.72 - 3.34 dB is achieved using the SC approach.

Method of Diversity Improvement	Relative to Branch 1 (dB)	Relative to Branch 5 (dB)
EG-AC	7.61	7.29
EG-VC	1.44	0.86
SC	3.34	2.72

Table B.25: Transmitter Space Diversity Gain versus Combining Technique – Group 4 (1.5λ spacing)

B.4.4 Group 5: 2λ Spacing

Table B.26 lists the statistical values of the field strength *after* space transmitter diversity combining using each of the three specified methods. A transmitter antenna spacing of 2λ was used.

Diversity	Average (dB)	Mean (Linear)	Variance	Standard Deviation
EG-AC	-6.07	0.497	1.149	1.072
EG-VC	-12.10	0.248	0.744	0.863
SC	-11.04	0.274	0.360	0.360

Table B.26: Diversity Combining Field Strength Summary: Transmitter Spacing Group 5 (2λ spacing)

Table B.27 shows the transmitter diversity gain (relative to branch 1 and branch 6 respectively) for each of the three combining techniques. An average improvement in the range 1.36 - 7.61 dB is seen for the EG methods, while a gain of 2.93 - 3.44 dB is achieved using the SC approach.

Method of Diversity Improvement	Relative to Branch 1 (dB)	Relative to Branch 6 (dB)
EG-AC	7.61	7.13
EG-VC	2.05	1.36
SC	3.44	2.93

Table B.27: Transmitter Space Diversity Gain versus Combining Technique – Group 5 (2λ spacing)

B.4.5 Group 6: 2.5λ Spacing

Table B.28 lists the statistical values of the field strength *after* space transmitter diversity combining using each of the three specified methods. A transmitter antenna spacing of 2.5λ was used.

Diversity	Average (dB)	Mean (Linear)	Variance	Standard Deviation
EG-AC	-6.09	0.496	1.158	1.076
EG-VC	-8.16	0.391	0.844	0.918
SC	-11.06	0.273	0.356	0.597

Table B.28: Diversity Combining Field Strength Summary: Transmitter Spacing Group 6 (2.5λ spacing)

Table B.29 shows the transmitter diversity gain (relative to branch 1 and branch 7 respectively) for each of the three combining techniques. An average improvement in the range 5.95 - 8.40 dB is seen for the EG methods, while a gain of 3.29 - 3.48 dB is achieved using the SC approach.

Method of Diversity Improvement	Relative to Branch 1 (dB)	Relative to Branch 7 (dB)
EG-AC	7.46	8.40
EG-VC	5.95	7.08
SC	3.29	3.48

Table B.29: Transmitter Space Diversity Gain versus Combining Technique – Group 6 (2.5λ spacing)

B.4.6 Group 7: 3λ Spacing

Table B.30 lists the statistical values of the field strength *after* space transmitter diversity combining using each of the three specified methods. A transmitter antenna spacing of 3λ was used.

Diversity	Average (dB)	Mean (Linear)	Variance	Standard Deviation
EG-AC	-6.11	0.495	1.149	1.072
EG-VC	-8.10	0.394	0.900	0.950
SC	-11.03	0.275	0.361	0.601

Table B.30: Diversity Combining Field Strength Summary: Transmitter Spacing Group 7 (3λ spacing)

Table B.31 shows the transmitter diversity gain (relative to branch 1 and branch 8 respectively) for each of the three combining techniques. An average improvement in the range 5.44 - 7.49 dB is seen for the EG methods, while a gain of 2.88 - 3.39 dB is achieved using the SC approach.

Method of Diversity Improvement	Relative to Branch 1 (dB)	Relative to Branch 8 (dB)
EG-AC	7.49	7.10
EG-VC	5.83	5.44
SC	3.39	2.88

Table B.31: Transmitter Space Diversity Gain versus Combining Technique – Group 7 (3λ spacing)

B.4.7 Group 8: 3.5λ Spacing

Table B.32 lists the statistical values of the field strength *after* space transmitter diversity combining using each of the three specified methods. A transmitter antenna spacing of 3.5λ was used.

Diversity	Average (dB)	Mean (Linear)	Variance	Standard Deviation
EG-AC	0.497	1.144	1.070	0.497
EG-VC	0.252	0.686	0.828	0.252
SC	0.277	0.366	0.605	0.277

Table B.32: Diversity Combining Field Strength Summary: Transmitter Spacing Group 8 (3.5λ spacing)

Table B.33 shows the transmitter diversity gain (relative to branch 1 and branch 9 respectively) for each of the three combining techniques. An average improvement in the range 1.35 - 7.62 dB is seen for the EG methods, while a gain of 2.77 - 3.56 dB is achieved using the SC approach.

Method of Diversity Improvement	Relative to Branch 1 (dB)	Relative to Branch 9 (dB)
EG-AC	7.62	7.09
EG-VC	2.19	1.35
SC	3.56	2.77

Table B.33: Transmitter Space Diversity Gain versus Combining Technique – Group 8 (3.5λ spacing) Diversity ($\delta f = 1\text{MHz}$)

Appendix C: HAP Ray Tracing Symmetry Tests

C.1 Introduction

This appendix describes a set of ray tracing symmetry tests that fully examine the operation of the HAP enhanced ray-tracing program. In particular, the tests confirm the internal angle geometry before and after interaction with a medium discontinuity. As explained in this appendix, the software considers four possible cases, each dependent on the incident ray's direction of travel.

By defining a symmetrical database either in the x and/or y -axes, the resulting ray-tracing field grid can be visually analysed to determine errors. If errors exist in the code, symmetry errors will be observed in the form of different field strengths (shown as different colours) on the left and right, or top and bottom, of the resulting grid. In this study an indoor database exhibiting symmetry in the x -axis was produced. In early versions of the ray-tracing program symmetric results were not obtained, demonstrating errors in the software. A formal process of evaluation and debugging was performed to correct these faults.

After tackling the symmetry faults, a further study was performed to confirm the results were rotationally invariant. The software should produce identical output grid results if the transmitting source and database are simply rotated. Figure C.1 shows the four rotation cases considered in this analysis. The tests are used to debug the ray-tracing and field-reconstruction algorithms, particularly for the case of distant satellite or high altitude platform illumination. Internally, different sub-routines are called depending on the ray's current direction of travel. As described later in this appendix, the problem can be divided into four cases depending on the quadrant in which the ray travels. The four test environments, as shown in figure C.1, are now described in detail.

C.1.1 Case 1: Downward Vertical Ray Test

As shown in figure C.1(a), this case assumes the source (HAP) is located directly above a 6m by 8m indoor environment at position ($x=3\text{m}$, $y=20000\text{m}$). Two virtual transmitters (see section 6.3 in chapter 6) are placed on the rooftop at locations V_{T1}

$(x_1=1, y_1=7)$ and $V_{T2} (x_2=5, y_2=7)$. Rays are launched at angles just less than 270 degrees (quadrant 3) and just more than 270 degrees (quadrant 4). In this test the rays are transmitted and reflected from a horizontal boundary.

C.1.2 Case 2: Upward Vertical Ray Test

As shown in figure C.1(b), this case assumes the source (HAP) is located directly below a 6m by 8m indoor environment at position $(x=3m, y=-19999m)$. The building structure is also rotated 180 degrees to ensure that the same problem is under study. Two virtual transmitters are placed on the rooftop at locations $V_{T1} (x_1=1, y_1=1)$ and $V_{T2} (x_2=5, y_2=1)$. Rays are launched at angles just more than 90 degrees (quadrant 2) and just less than 90 degrees (quadrant 1). In this test the ray are transmitted and reflected from a horizontal boundary.

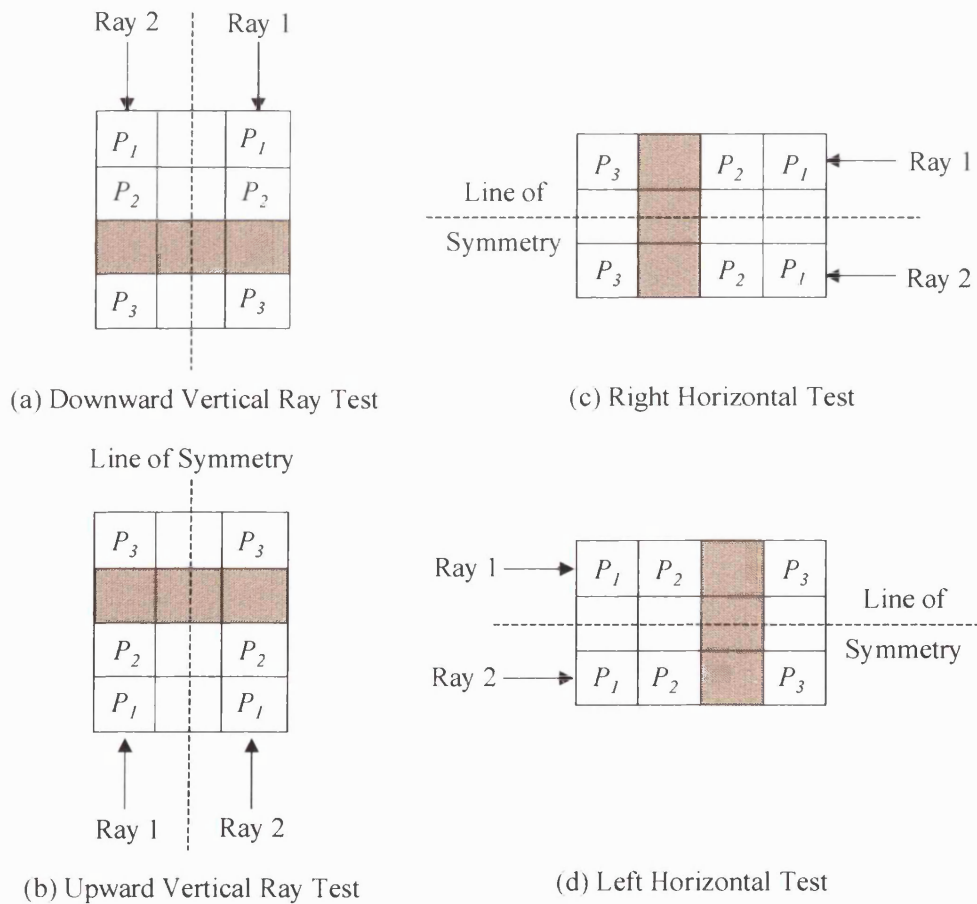


Figure C.1: Ray Tracing Symmetry and Rotational Invariance Tests

C.1.3 Case 3: Right Horizontal Ray Test

As shown in figure C.1(c), this case assumes the source (satellite or hap) is located directly to the right hand side of a 6m by 8m indoor environment at position ($x=20000\text{m}$, $y=3\text{m}$). The building structure is also rotated 90 degrees clockwise (relative to case 1) to ensure that the same problem is under study. Two virtual transmitters are placed on the rooftop at locations V_{T1} ($x_1=7$, $y_1=5$) and V_{T2} ($x_2=7$, $y_2=1$). Rays are launched at angles just less than 180 degrees (quadrant 2) and just more than 180 degrees (quadrant 3). In this test the rays are transmitted and reflected from a vertical boundary.

C.1.4 Case 4: Left Horizontal Ray Test

As shown in figure C.1(d), this case assumes the source (High Altitude Platform) is located directly to the left hand side of a 6m by 8m indoor environment at position ($x=-19999\text{m}$, $y=3\text{m}$). The building structure is also rotated 90 degrees anti-clockwise (relative to case 1) to ensure that the same problem is under study. Two virtual transmitters are placed on the rooftop at locations V_{T1} ($x_1=1$, $y_1=5$) and V_{T2} ($x_2=1$, $y_2=1$). Rays are launched at angles just more than 0 degrees (quadrant 1) and just less than 360 degrees (quadrant 4). In this test the rays are transmitted and reflected from a vertical boundary.

If the software is working correctly, the power levels P_1 , P_2 and P_3 recorded in each of the above cases will be identical.

C.2 Testing and Verification of Satellite Model

Using the methods described in section C.1, a programme of testing and verification was performed to confirm the correct operation of modified satellite model. In the following section, the results from the rotational invariance and symmetry tests are described.

C.2.1 Symmetry Verification

It is vital to check that the output from the ray tracing and field reconstruction software produces a symmetric and rotationally invariant result. Figure C.2 shows an

example of the field strength prediction within a building using the new satellite model (accurate method).

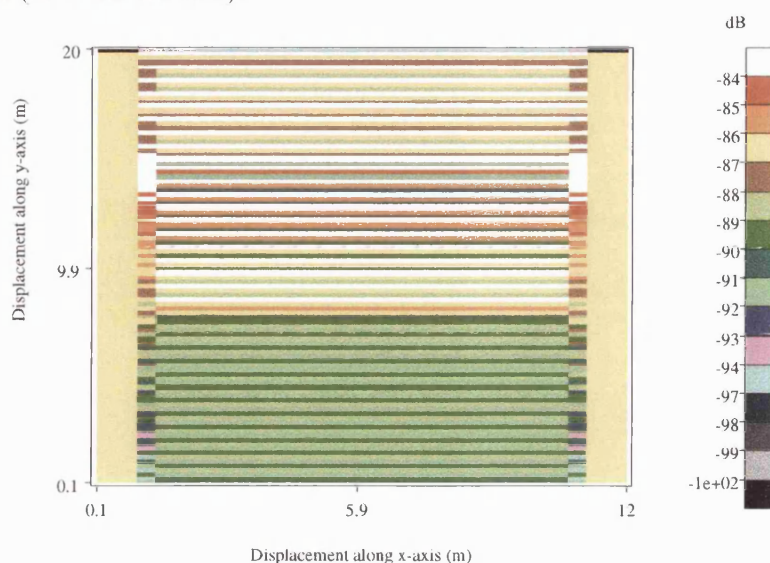


Figure C.2: Symmetric field strength prediction

The prediction demonstrates perfect horizontal symmetry with field predictions on the left-hand side of the map identical to those symmetric positions on the right-hand side of the map. The environment described in figure 6.4 (chapter 6) was used in this study.

Having achieved symmetry for a source transmitter directly above the map, it was now necessary to show that the modified ray tracing results were accurate for any launch angle and HAP location. This was performed using the four rotated environments and launch locations defined in section C.1. The results demonstrate that environment rotations and source launch angles do not affect the prediction output providing the relative angles remain constant. This is a very important result and confirms the correct operation of the internal quadrant mathematics and angle tests.

C.2.1.1 Case 1: Downward Vertical Ray Test

In this section, as shown in figure C.1(a), two virtual transmitters are placed at $x=0.1\text{m}$, $y=0.7\text{m}$ and $x=0.5\text{m}$, $y=0.7\text{m}$. Each transmitter launches a ray into the environment, and this ray then interacts with the surface resulting in reflections and transmission at the medium boundaries. Figures C.3 and C.4 show the resulting field

strengths before and after code modification. Field levels are shown in the air sections above and below the obstruction. Before correction, the prediction field levels at the bottom of figure C.3 failed the symmetry test due to angle errors in the ray launching software. More importantly, after correction the left and right hand results in figure C.4 are symmetric. The corrected field outputs are identical on both sides and this shows that the reflection and transmission mathematics is consistent in quadrants 3 and 4 for a horizontal obstacle.

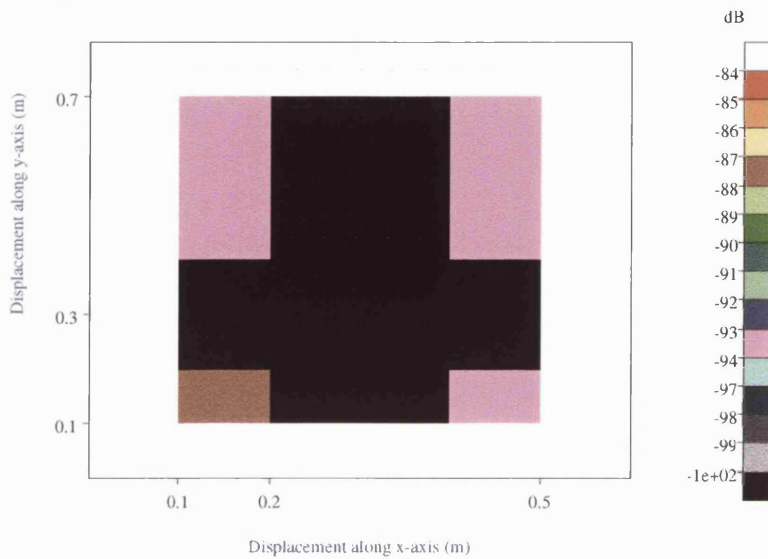


Figure C.3: Predicated Field Strength for rays in quadrant 1 before modification

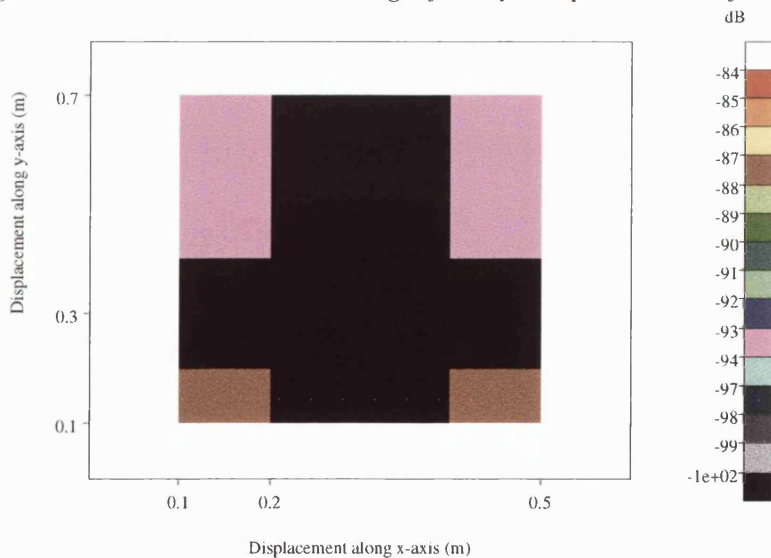


Figure C.4: Predicated Field Strength for rays in quadrant 1 after modification

C.2.1.2 Case 2: Upward Vertical Ray Test

Figure C.1(b) was produced assuming two virtual transmitters placed at $x=1\text{m}$, $y=1\text{m}$ and $x=5\text{m}$, $y=1\text{m}$. Figures C.5 and C.6 show the resulting field strengths before and after modification. Once again, symmetry errors are seen before correction, and these are removed once the modified code is applied. This shows that the reflection and transmission mathematics is consistent in quadrants 1 and 2 for a horizontal obstacle.

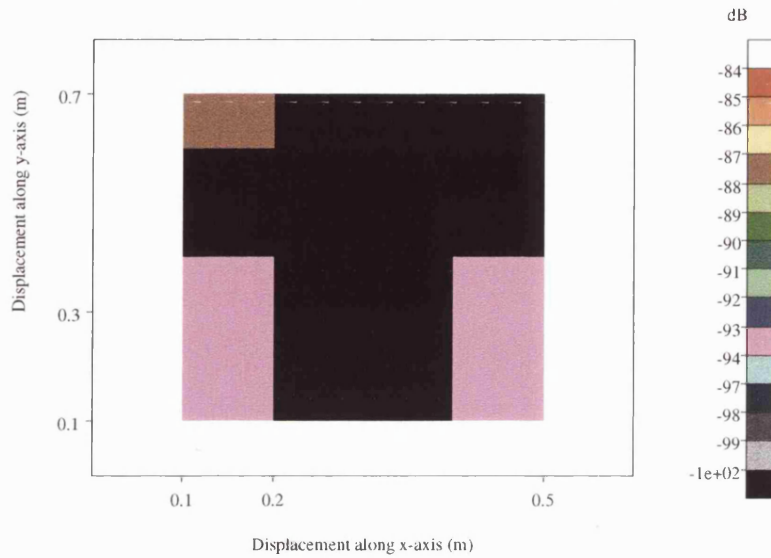


Figure C.5: Predicated Field Strength for rays in quadrant 2 before modification

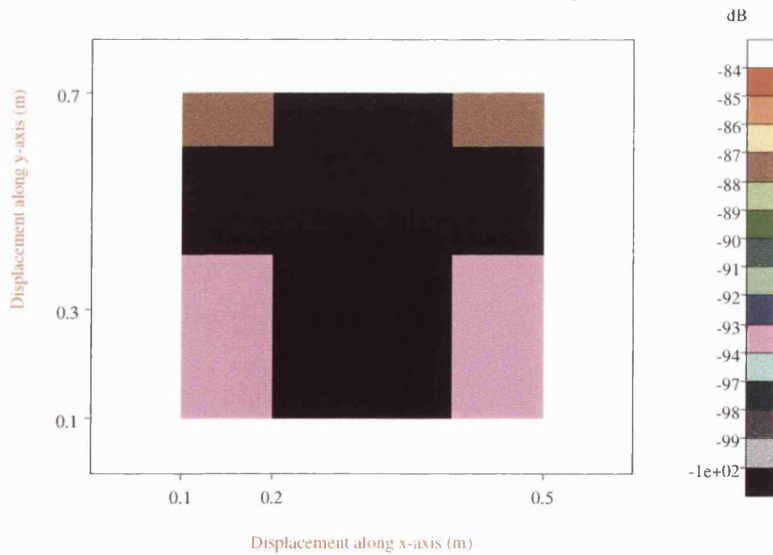


Figure C.6: Predicated Field Strength for rays in quadrant 2 after modification

C.2.1.3 Case 3: Right Horizontal Ray Test

Figure C.1(c) was produced assuming two virtual transmitters placed at $x=7\text{m}$, $y=5\text{m}$ and $x=7\text{m}$, $y=1\text{m}$. Figures C.7 and C.8 show the resulting field strengths before and after modification. Symmetry errors are seen before correction, and these are removed once the modified code is applied. This shows that the reflection and transmission mathematics is consistent in quadrants 2 and 3 for a vertical obstacle.

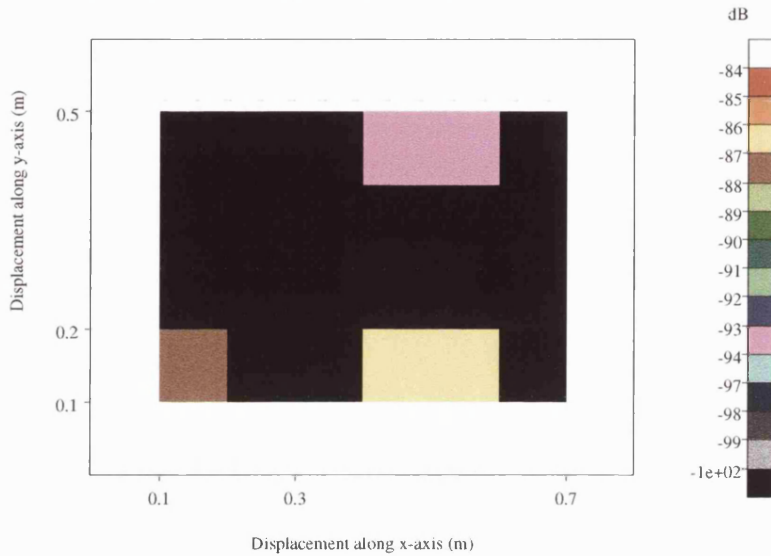


Figure C.7: Predicated Field Strength for rays in quadrant 3 before modification

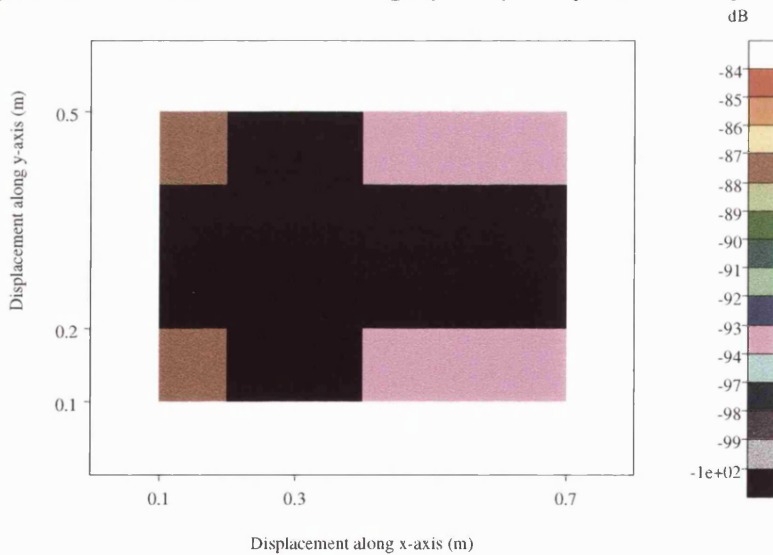


Figure C.8: Predicated Field Strength for rays in quadrant 3 after modification

C.2.1.4 Case 4: Left Horizontal Ray Test

Figure C.1(d) was produced assuming two virtual transmitters placed at $x=1\text{m}$, $y=5\text{m}$ and $x=1\text{m}$, $y=1\text{m}$. Figures C.9 and C.10 show the resulting field strengths before and after modification. Symmetry errors are seen before correction, and these are removed once the modified code is applied. This shows that the reflection and transmission mathematics is consistent in quadrants 1 and 4 for a vertical obstacle.

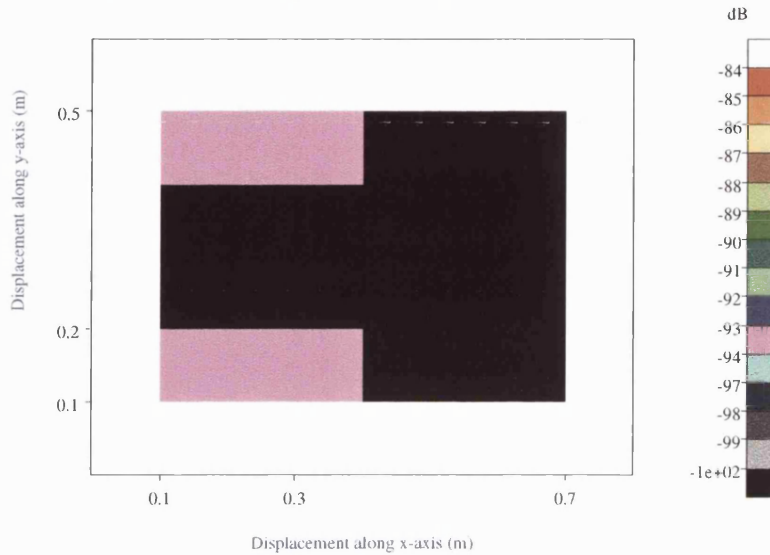


Figure C.9: Predicated Field Strength for rays in quadrant 4 before modification

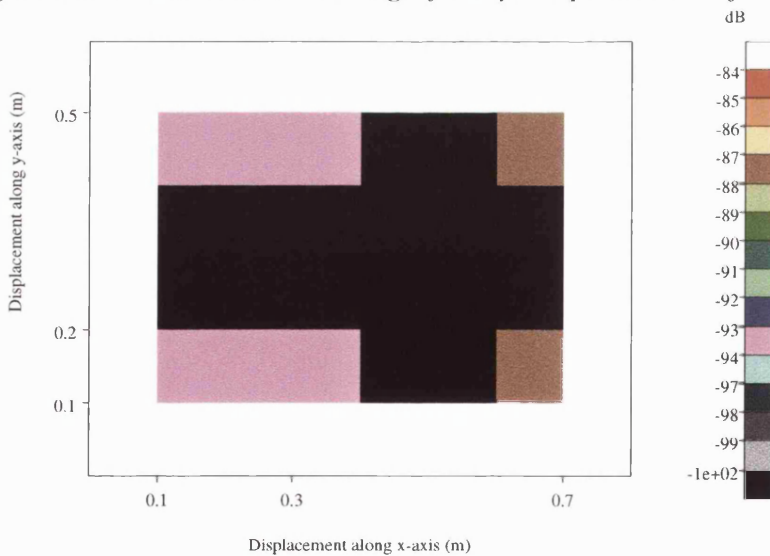


Figure C.10: Predicated Field Strength for rays in quadrant 4 after modification

Appendix D: MIMO Micro versus Macro for Route 2

D.1 Micro Results

This appendix provides the graphical results for the second indoor route shown in figure 7.13 of chapter 7. A description of the various graph types was given in chapter 7 for the first route and also applies to this section.

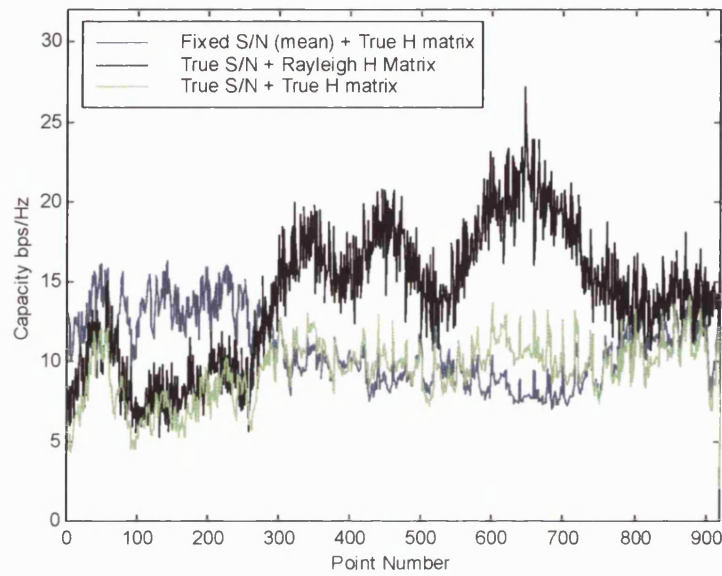


Figure D.1: True and Reference Instantaneous Capacities (micro-MIMO, $\Delta x=0.5\lambda$)

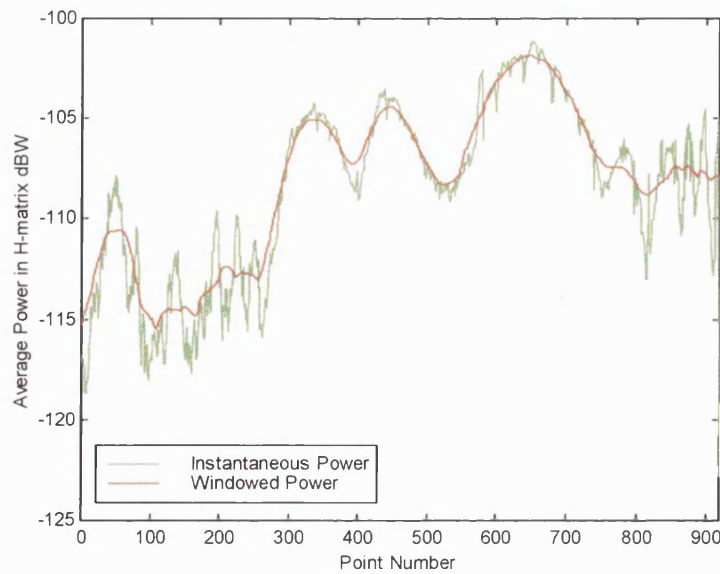


Figure D.2: Instantaneous & Windowed Power for route 2 (micro-MIMO, $\Delta x=0.5\lambda$)

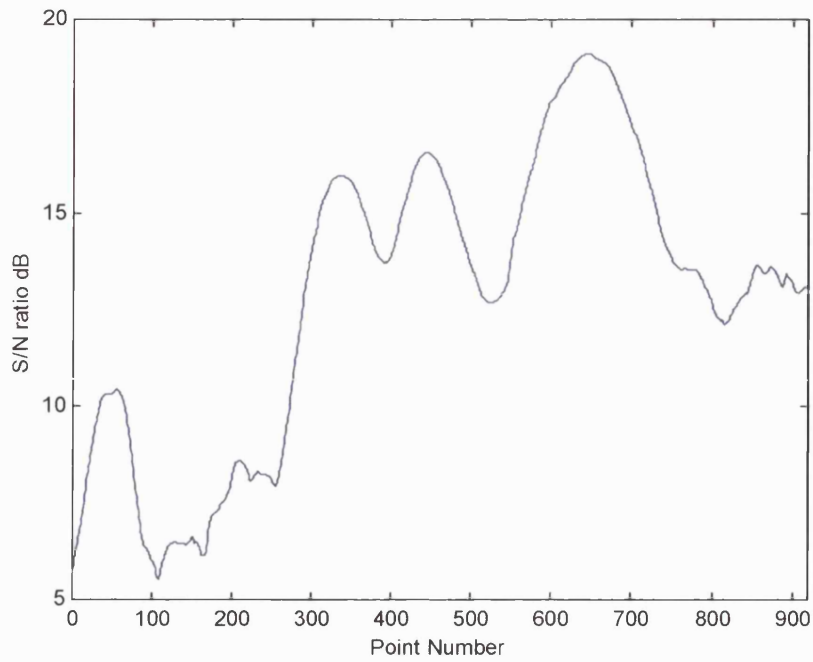


Figure D.3: Windowed SNR for route 2 (micro-MIMO, $\Delta x=0.5\lambda$)

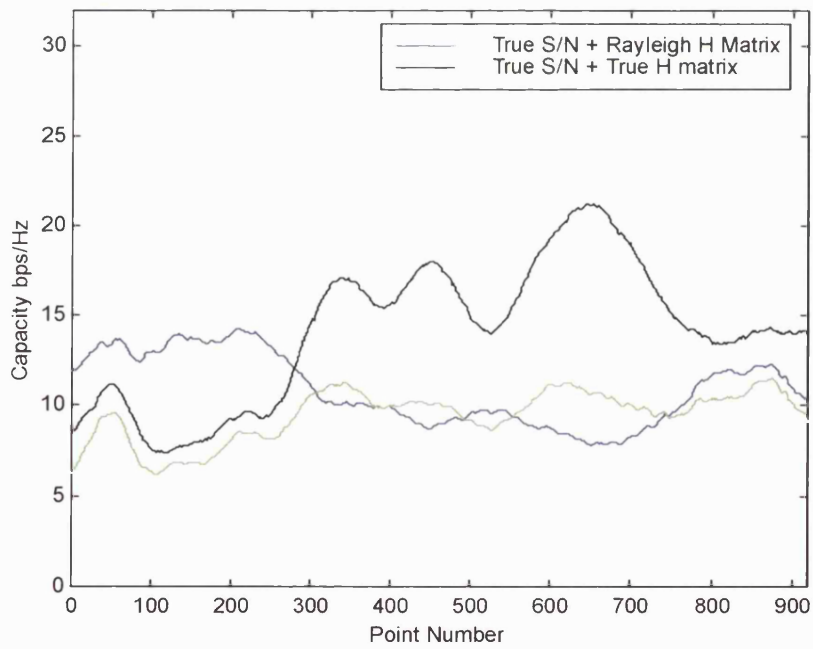


Figure D.4: Windowed Capacities for route 2 (micro-MIMO, $\Delta x=0.5\lambda$)

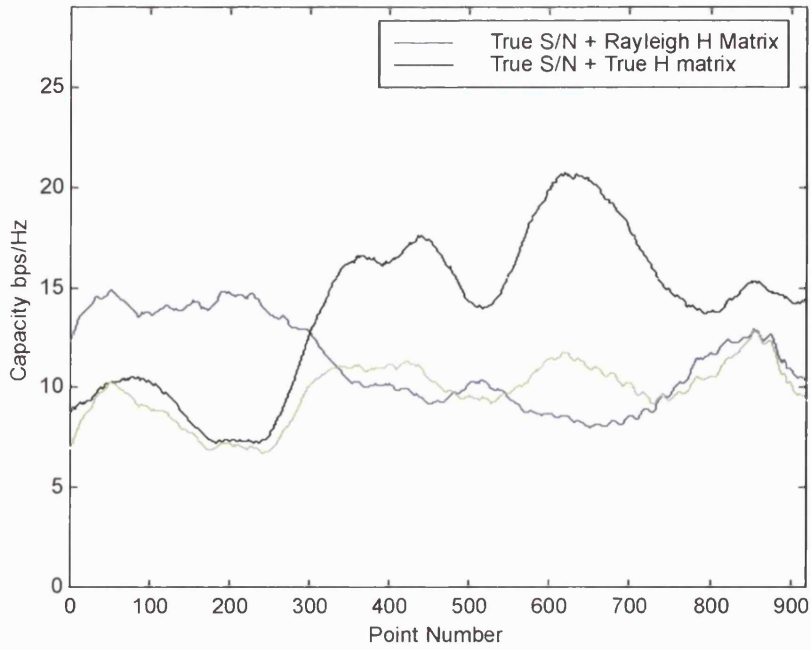


Figure D.5: Windowed Capacities for route 2 (micro-MIMO, $\Delta x=1.0\lambda$)

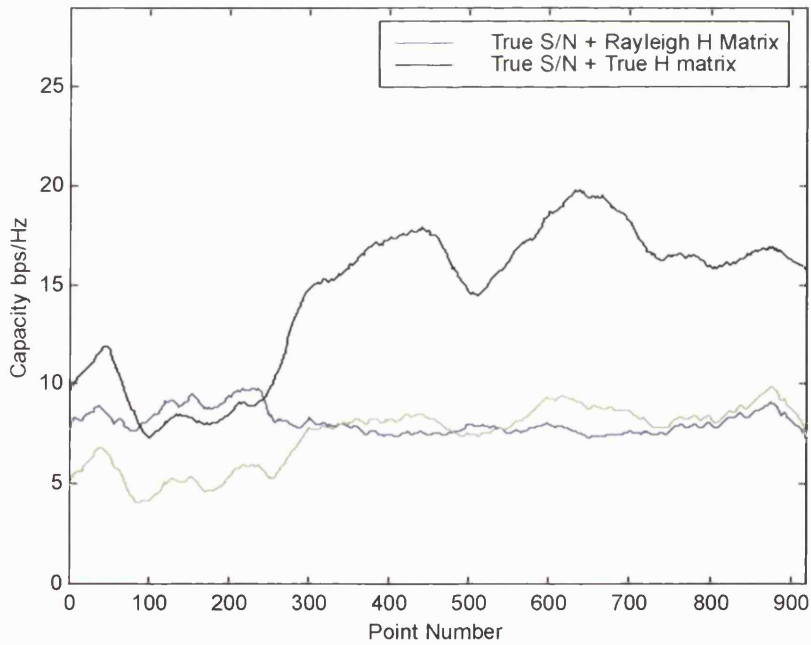


Figure D.6: Windowed Capacities for route 2 (micro-MIMO, $\Delta x=0.1\lambda$)

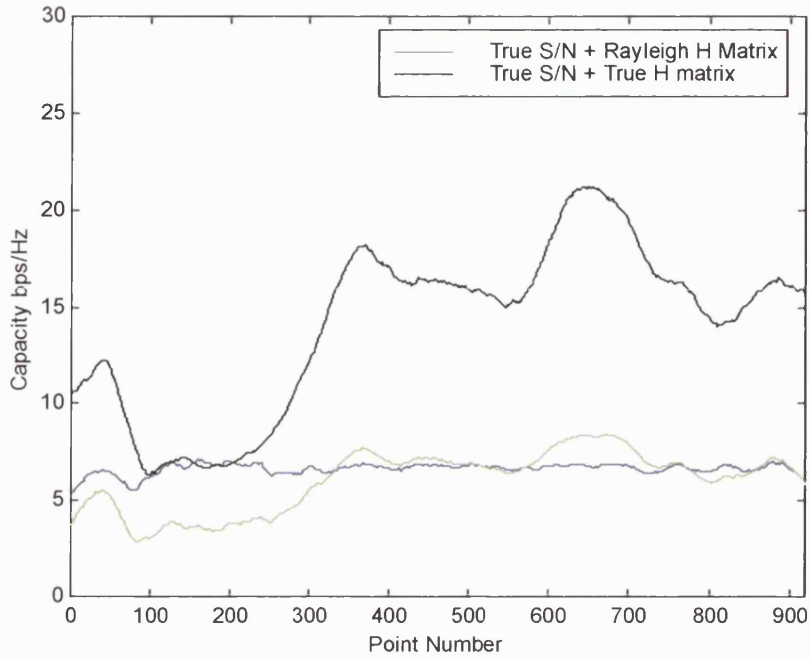


Figure D.7: Windowed Capacities for route 2 (micro-MIMO, $\Delta x=0.01\lambda$)

D.2 Macro Results

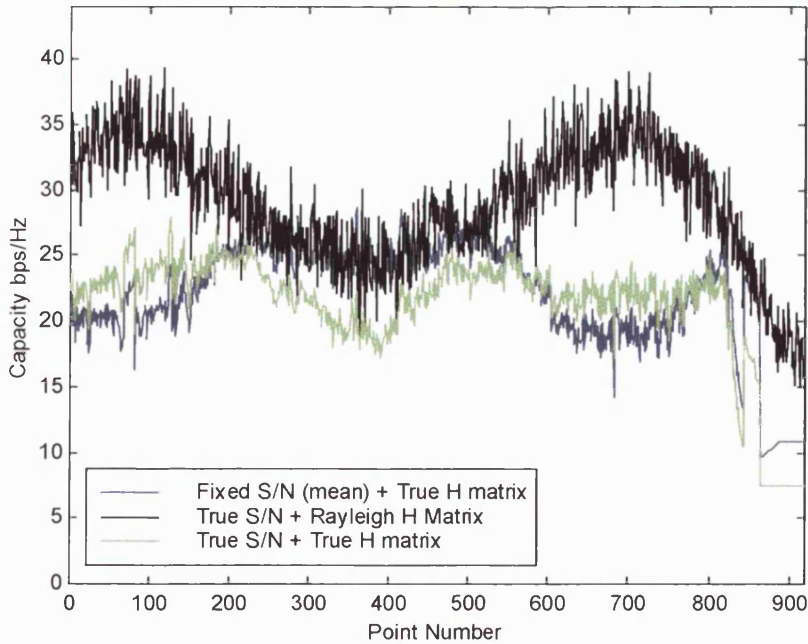


Figure D.8: True and Reference Instantaneous Capacities (macro-MIMO, $\Delta x=0.5\lambda$)

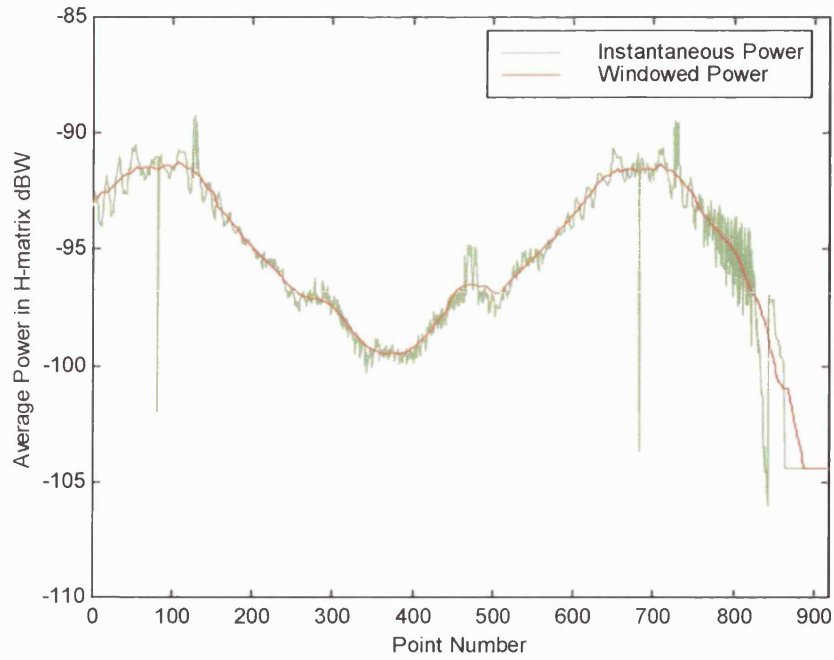


Figure D.9: Instantaneous & Windowed Power for route 2 (macro-MIMO, $\Delta x=0.5\lambda$)

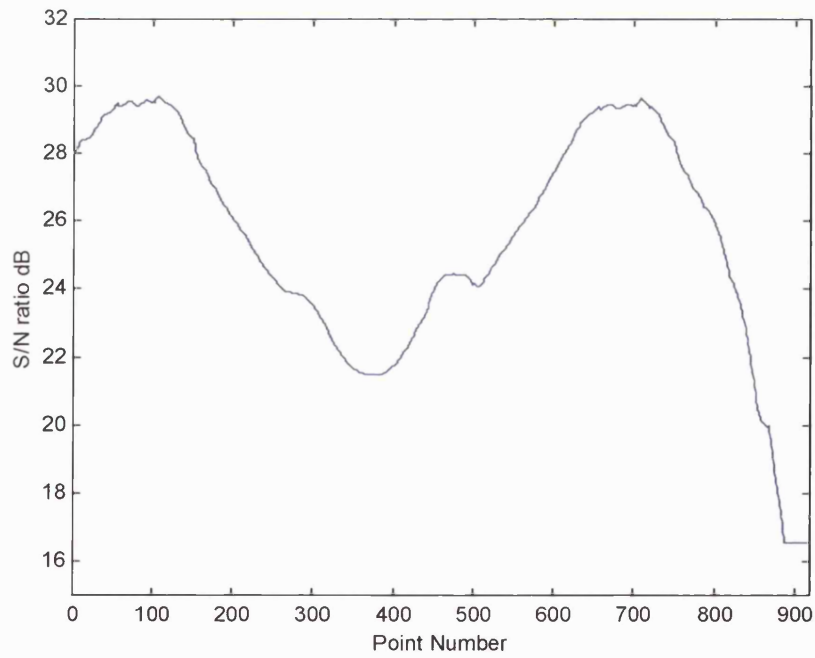


Figure D.10: Windowed SNR for route 2 (macro-MIMO, $\Delta x=0.5\lambda$)

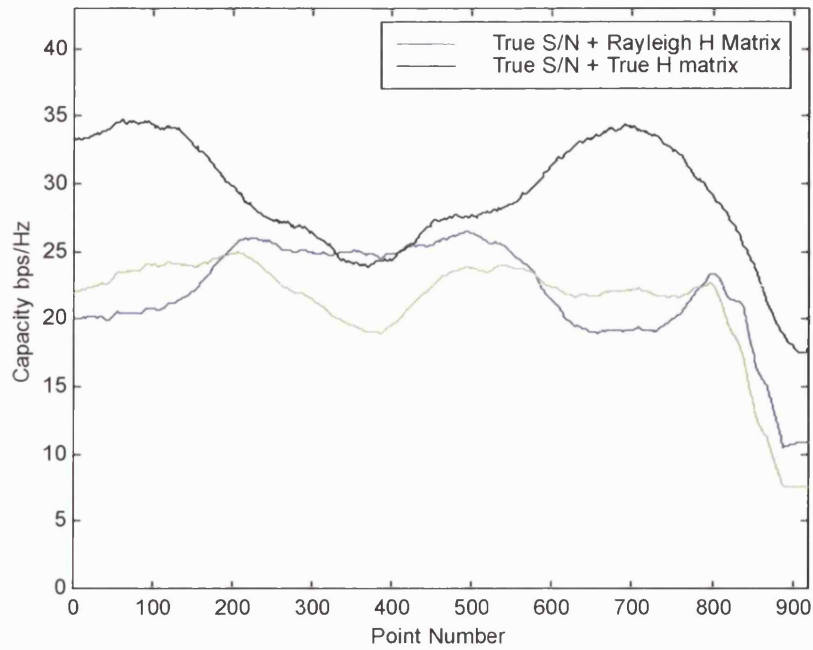


Figure D.11: Windowed SNR for route 2 (macro-MIMO, $\Delta x=0.5\lambda$)

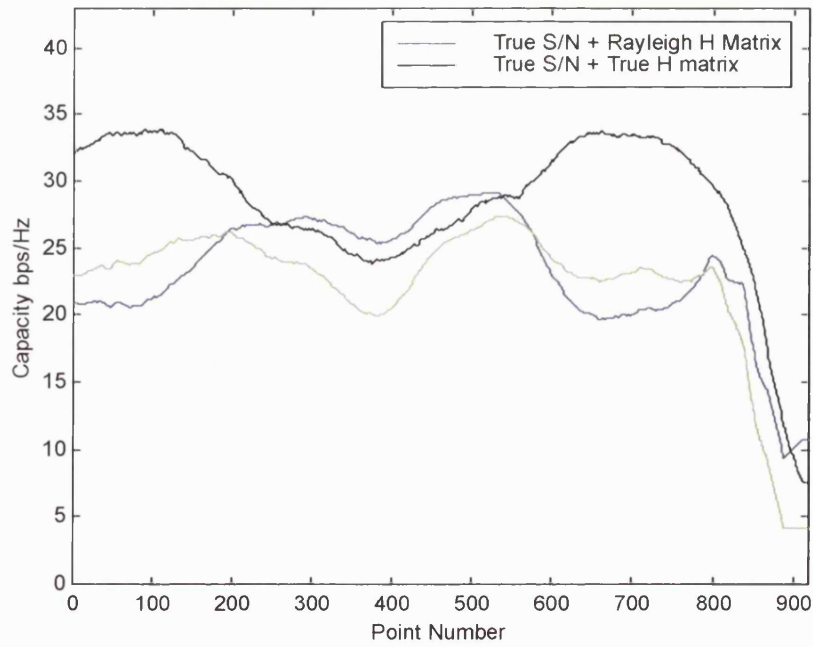


Figure D.12: Windowed Capacities for route 2 (macro-MIMO, $\Delta x=1.0\lambda$)

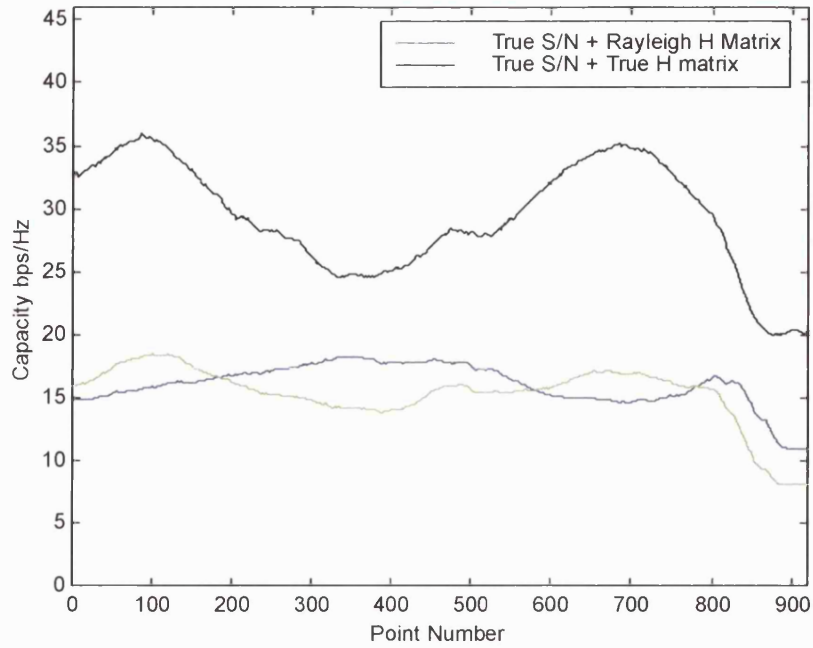


Figure D.13: Windowed Capacities for route 2 (macro-MIMO, $\Delta x=0.1\lambda$)

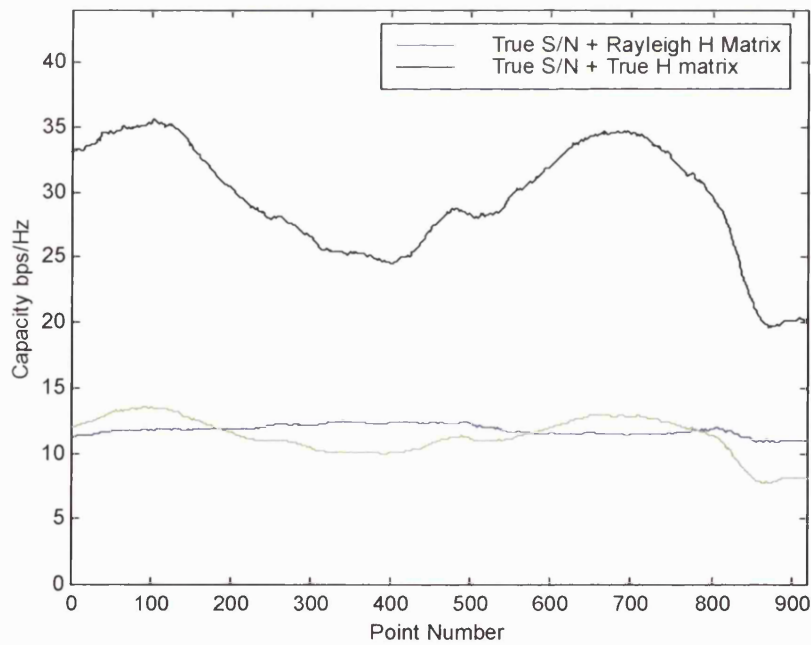


Figure D.14: Windowed Capacities for route 2 (macro-MIMO, $\Delta x=0.01\lambda$)

Appendix E: List of Publications

Evaluation of Indoor Propagation Effects and Diversity Techniques

F. Tila, SR. Pennock and PR. Shepherd

IEE Third Conference on Postgraduate Research in Electronics, Photonics, Communications and Software, Proc. IEE EPSRC PREP

Volume 2, 2001, Page(s): 23-25

Analysis of Indoor-Indoor and Satellite/Hap-Indoor Propagation Effects

F. Tila, P.R. Shepherd and S.R. Pennock

IEE Eleventh International Conference on Antennas and Propagation, (ICAP Conf. Publication No. 480),

Volume 1, Page(s): 203-207, April 2001

Indoor Ray Tracing evaluation of enhanced High Frequency communications using Directional Antennas at the Basestation and Space Diversity at the Terminal

F. Tila, P.R. Shepherd and S.R. Pennock

31st IEEE European Microwave Conference (EuMC),

Volume 3, Page(s): 351-355, Sep. 2001

2GHz Propagation and Diversity Evaluation for In-Building Communications up to 4MHz Using High Altitude Platforms (HAP)

F. Tila, PR. Shepherd and SR. Pennock

54TH IEEE Vehicular Technology Conference, VTC 2001 Fall

Volume 1, Page(s): 121-125, Oct. 2001

Indoor Ray Tracing Evaluation of Directional Antennas and Space Diversity at 17 GHz

F. Tila, SR. Pennock and PR. Shepherd

UK National URSI Symposium, Malvern URSI, Dec. 2001

Theoretical Capacity Evaluation of Indoor Micro and Macro MIMO Systems at 5 GHz, Using Site Specific Ray Modelling

F. Tila, SR. Pennock and PR. Shepherd

IEE Electronic Letter, Volume 39, Number 5, March 2003

MIMO Capacity Evaluation for Rayleigh and Rician Channels with Correlated fading

F. Tila, PR. Shepherd and SR. Pennock

Accepted for publications in IEE 2nd International Symposium Telecommunications (IST), Aug. 2003

Micro and Macro MIMO Configurations and Analysis for Indoor High Capacity Communications

F. Tila, PR. Shepherd and SR. Pennock

In preparation of submitting to IEEE Journal Transactions Magazine 2003

Evaluation of Indoor Propagation Effects and Diversity Techniques

F. Tila, SR. Pennock and PR. Shepherd

RADIO SYSTEMS AND RADIO SCIENCE GROUP, UNIVERSITY OF BATH, UK

Abstract

This paper investigates indoor field strength prediction at 11 and 17 GHz using a newly enhanced two-dimensional ray-tracing model. A range of diversity generation and combining techniques are considered in order to improve the performance of indoor communication systems.

Ray modelling

The results in this paper are based on field strength analysis obtained using an indoor-ray-tracing propagation model [1]. The method uses a system of ray-tube launching and tracing to a predefined field strength threshold. The overall field strength at each receiver point is then calculated as the vector sum of all rays illuminating that point. Factors such as material complex permittivity are highly influential when determining transmission losses. In this study the material parameters are taken from the open literature [1][2].

Diversity Generation and Combining

Wireless communications suffer from fast fading and this can seriously disrupt the quality of the radio link (particularly in non-line-of-sight locations). Indoor links, with the presence of walls, furniture, etc. are particularly susceptible. In this paper space, frequency and polarisation diversity are considered. In the case of space diversity, both transmitter and receiver antenna spacing solutions are considered. Three types of diversity combining are studied: (i) Selection Combining diversity (SC), (ii) Equal Gain Vector Combining (EG-VC) and (iii) Equal Gain Amplitude Combining (EG-AC). Using our ray model, field strength predictions are produced for various transmitter and receiver locations, various centre frequencies and for both vertical and horizontal polarisations. Figure 1 shows the 2D indoor database while Figure 2 shows an example of a typical coverage map, in this case assuming receiver space diversity with EG-AC. Carrier frequencies of 11 GHz and 17 GHz have been simulated. Using these predictions the various diversity methods are analysed and then ranked based on diversity gain in the indoor environment.

Results & Conclusions

Comparison of EG-AC, EG-VC and SC shows that EG-AC generates the strongest field strengths and largest diversity gains. The EG-VC solution

suffers output nulls from the diversity combiner and this results in poor practical performance.

For frequency diversity, carrier separations ranging from 1 MHz to 500 MHz were considered, with diversity gains shown to increase for larger frequency spacings. Figure 3 provides diversity gain versus frequency separation. The first point represents frequency separation of 1MHz which is within the coherence bandwidth; clearly frequency diversity performance for frequency separations between 100 MHz and 500 MHz rather better and is relatively constant.

Predicted field strength grids have been generated for antenna spacings ranging from one quarter of a wavelength up to 3.5 wavelengths. Figure 4 shows space diversity performance has been found to be worst for separations of 0.5λ , 1.5λ , etc and best for separations of $\lambda/4$, $3\lambda/4$, etc. With antenna spacing of an integer number of half wavelengths, through a large proportion of the environment the two signals destructively interfere. Hence the resulting diversity gain is very poor in this case as one channel often has a low signal level.

Polarisation diversity has the major advantage of offering compact solutions (since spaced antennas are not required). While the frequency diversity gain is impressive (assuming spacing beyond the channel coherence bandwidth), the method is not spectrally efficient since at least twice the operating bandwidth is required. Results in Table 1 indicate that polarisation diversity gains in excess of 6.65 dB are possible using EG-AC. While this gain is very high, it should be remembered that the result is highly dependent on the fast fading correlation between simulated vertical and horizontal polarisation. Further work will validate the polarisation predictions of the indoor model.

Diversity combining techniques can be ranked in order of Space, Polarisation and lastly, Frequency. A full set of simulation results and analysis will be included in the final paper.

References

- [1] CH. Ghobadi, PR Shepherd and SR Pennock; "2D Ray Tracing Model for Indoor Radio Propagation at MM Frequencies and the Study of Diversity Techniques," *IEE Proc.-Microw. Antennas Propagation*, Vol.145, No. 4, pp. 349-353, August 1998.
- [2] L.M. Correia, P.O. Frances, 'Estimation of Materials Characteristics from power measurements,' *In Proceedings of PIMRC 94*, pp 510-513.

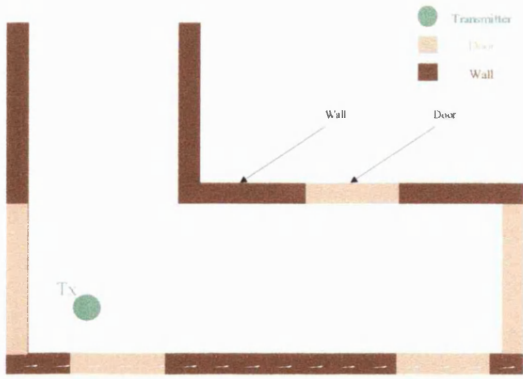


Figure 1: Database for a simple indoor environment [L shape corridor 10m by 5m, with walls (green) and doors (blue)]

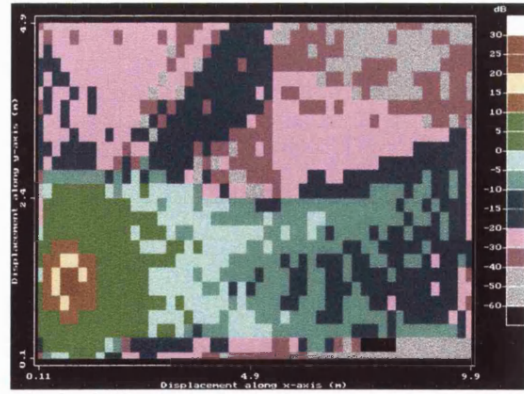


Figure 2: Receiver Space Diversity (EG-AC) Normalised Field Strength Prediction Grid

Diversity Techniques	SC Gain (dB)	EG-VC Gain (dB)	EG-AC Gain (dB)
Space (Rx) – $\lambda/4$	1.85	4.83	6.59
Space (Tx) – $\lambda/4$	2.92	4.78	7.10
Space (Rx) – 3.25λ	4.09	6.29	7.89
Space (Tx) – 3.25λ	2.89	5.41	7.05
Space (Rx) – 3.5λ	4.13	2.65	7.95
Space (Tx) – 3.5λ	2.81	1.19	7.02
Frequency($\Delta f = 1\text{MHz}$)	0.06	4.08	6.01
Frequency($\Delta f = 500\text{MHz}$)	1.87	3.10	6.58
Polarisation	2.92	5.59	6.65

Table 1: Average Diversity Gain Summary (dB)

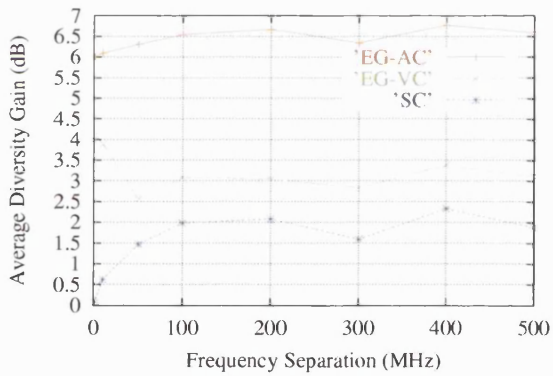


Figure 3: Average Diversity vs Frequency Separation

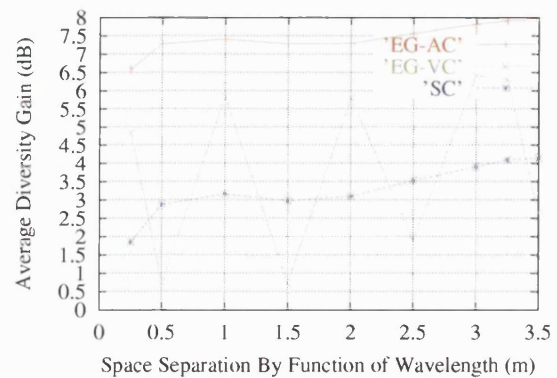


Figure 4: Average Diversity Gain vs Space Receiver Separation

Analysis of Indoor-Indoor and Satellite/HAP-Indoor Propagation Effects

F Tila, PR Shepherd and SR Pennock

Radio Systems and Radio Science Group, University of Bath, UK

eefft@bath.ac.uk, eesprs@bath.ac.uk, eesrp@bath.ac.uk

ABSTRACT

Satellite and High Altitude Platforms (HAPs) are an important concept for next generation fixed and mobile communications.

To predict indoor field strength levels from such distant transmitters, modifications to the standard indoor ray-tracing concept are proposed. These modifications require an array of virtual transmitters to be placed around the building under test.

A range of diversity generation and combining techniques are considered to improve the performance of a 17 GHz indoor to indoor system. Diversity gains are computed and typical generation and combining strategies compared and ranked based on cost, complexity and performance.

Investigation of a HAP to indoor environment shows the weakness of illumination from directly overhead.

I. INTRODUCTION

Over the last 10-15 years a large number of indoor-to-indoor propagation models have been proposed in the literature[1][2][3]. A number of terrestrial to indoor propagation models have also been suggested, however these are generally statistical in nature and do not normally take account of the detailed building geometry involved.

In recent years a radically new type of communication system has been proposed, known as High Altitude Platforms (HAPs) or Unmanned Aerial Vehicles (UAVs) [4]. These HAPs are being developed to operate at an altitude of approximately 20km in the stratosphere. The long radio path through the lower atmosphere normally encountered on a 36,000 km geostationary satellite link causes considerable attenuation. Outdoor to indoor communications from ground-based transmitters overcome the path loss difficulty, however they suffer from shadowing caused by high buildings, mountains and hills. Hence, HAPs offer an interesting alternative for future indoor communications.

In Section II, the properties of an indoor to indoor ray-tracing propagation model are discussed. Section III applies this model to study indoor field strength prediction at 17 GHz and the advantages of diversity generation and combination. In section IV the indoor model is enhanced using a novel array of virtual transmitters to support indoor field strength prediction from distant overhead objects, such as satellites and HAPs. This section also provides preliminary indoor field strength predictions for HAPs operating at 2 GHz. The paper ends with a set of conclusions and areas for future work.

II. RAY MODELLING

The ray modeling work in this paper builds on the developed indoor-only ray-tracing model described in [1]. The method uses a system of ray-tube launching and traces rays through various reflections and refractions at material boundaries to a predefined signal strength. The overall signal strength at a particular receiver point is then calculated by the vector summation of all rays illuminating that point.

Factors such as the thickness, permittivity and conductivity of the building material are considered in the modeling process. In this study, typical material parameters at 2GHz and 17 GHz were taken from the open literature [5][6].

Wireless communications often suffer from severe multipath fading and this can seriously disrupt the quality and range of a radio link (particularly in non-line-of-sight locations). Indoor links, with the presence of walls, floors, furniture, etc. are particularly susceptible to such problems.

To improve communications at this frequency, the impact of space, frequency and polarisation diversity has been studied. Three types of diversity combining method are evaluated:

- (i) Selection combining diversity (SC),
- (ii) Equal gain vector combining (EG-VC)
- (iii) Equal gain amplitude combining (EG-AC).

Normalised field strength predictions (i.e. values relative to the unobstructed field strength at a

distance of one metre from the transmitter) are produced for various transmitter and receiver locations, centre frequencies and for vertically and horizontally polarised antennas.

All studies assume a fixed transmitting basestation and a mobile moving around a pre-determined receiver grid. At each mobile location, a received normalised field strength prediction is calculated.

To enable a diversity study to be performed, field strength grids are produced at different centre frequencies, polarisations and antenna location (transmitter and receiver) offsets. Hence, the effects of Space, Frequency and Polarization diversity can be evaluated.

III. INDOOR-TO-INDOOR ANALYSIS

Figure 1 shows the indoor database for the indoor-to-indoor study, together with the location of the fixed transmitter

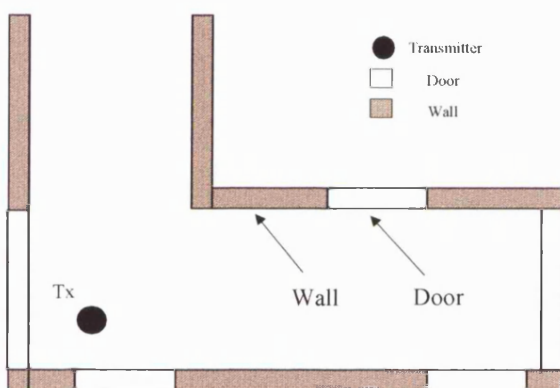


Figure 1: Database for a simple indoor environment [*L* shaped corridor, 10m by 5m, with walls and doors]

Figure 2 shows an example of a reconstructed normalised field strength grid at 17 GHz, assuming 3.5 wavelength spaced receiver diversity and EG-AC combining. In the top right-hand corner of the environment (around 5-10 metres from the transmitter), the normalised received field strength drops to around -60 dB.

Table 1 lists the gains observed as a function of diversity generation technique and combining strategy. Diversity gain is defined as the increase in field strength compared to a single branch (branch 1 in this case). Table 1 shows the average diversity gain over the whole environment. Frequency diversity performance for frequency separations between 100 MHz and 500 MHz is

relatively constant and represents the best case. Space diversity performance has been found to be worst for separations of an integer number of half wavelength, and best for separations of $\lambda/4$, $3\lambda/4$, etc. Based on these optimum diversity gains, it can be concluded that the diversity combining techniques can be ranked in order of Space, Polarization and lastly, Frequency.

Polarisation and space diversity achieve a similar diversity performance, with EG-AC resulting in a diversity gain in the order of 7-9 dB. The choice between these two schemes depends on the fading decorrelation (spatial vs. polarisation) and the choice of reference antenna. Polarisation diversity was found to offer a higher gain in this environment (relative to receiver diversity) when closely spaced antennas ($\lambda/4$) were used. However, for closely spaced transmitter antennas the resulting gain was similar to that of polarisation diversity.

With antenna spacings of an integer number of half wavelengths, through a large proportion of the environment the two signals destructively interfere. Hence the resulting diversity gain is very poor in this case as one channel often has a low signal level.

When larger antenna spacings were used, space diversity slightly outperformed polarisation diversity. Overall, the results show that both techniques could offer a useful improvement in the received field strength.

For space diversity, the results showed that the antenna spacing at either the transmitter or receiver is important when determining the expected diversity gain. Generally speaking, receiver diversity is easier to implement since combining decisions can be made locally using a channel estimate or a Received Signal Strength Indication per branch (RSSI). For transmitter diversity, information from the receiver must be sent back to the transmitter to support the combining process.

Fast fading correlation statistics are important when determining the expected diversity gain using frequency diversity. When the frequency spacing is less than the coherence bandwidth [7], the fast fading is correlated and little diversity gain is seen (e.g., see $\Delta f = 1\text{MHz}$ in Table 1). However, for larger frequency spacings the fading becomes decorrelated and significant diversity gains are observed.

Polarisation and frequency diversity both have the

major advantage of offering a compact solution (since spaced antennas are not required). This advantage may be particularly important for hand-held portable terminals. While the level of frequency diversity gain is impressive (assuming spacings beyond the channel's coherence bandwidth), this method is not spectrally efficient since twice the operating bandwidth is required (assuming two-branch combining). Given the importance of spectral efficiency, frequency diversity is not considered as a viable candidate

applications, the more simple switched solution may prove appropriate (despite its lower performance). Although on average EG-VC was seen to outperform SC in these studies, there were many occasions where destructive combining resulted in inferior performance (worse than either of the input branch signals). In practice, the use of EG-VC would not be recommended since the method is unpredictable and can lower the combined field strength at some locations relative to either input branch.

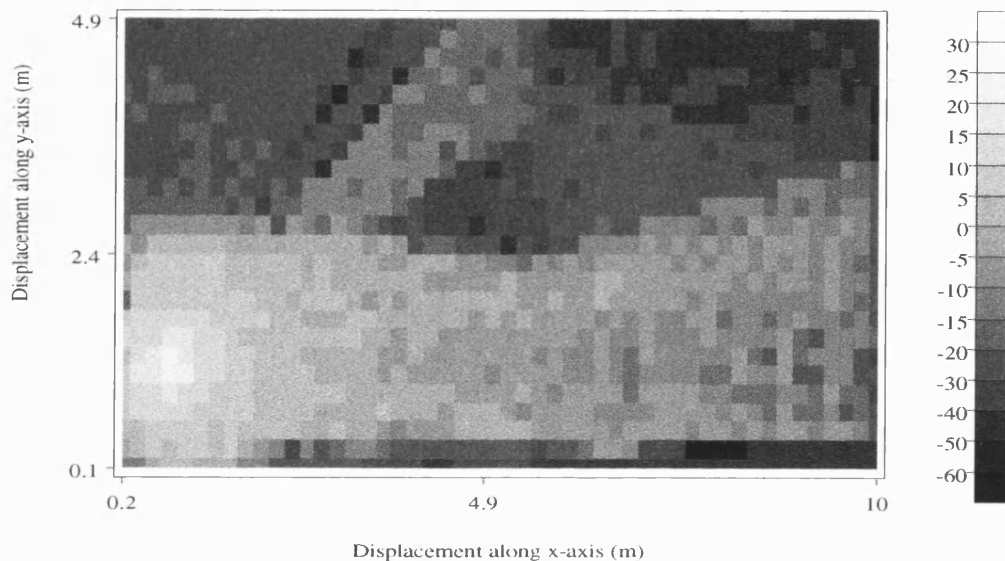


Figure 2: Receiver Space Diversity (EG-AC) Normalised Field Strength Grid

Diversity Technique	SC Gain (dB)	EG-VC Gain (dB)	EG-AC Gain (dB)
Space (Rx) - $\lambda/4$	1.85	4.83	6.59
Space (Tx) - $\lambda/4$	2.92	4.78	7.10
Space (Rx) - 3.25λ	4.09	6.29	7.89
Space (Tx) - 3.25λ	2.89	5.41	7.05
Space (Rx) - 3.5λ	4.13	2.65	7.95
Space (Tx) - 3.5λ	2.81	1.19	7.02
Frequency ($\Delta f = 1$ MHz)	0.08	6.01	6.03
Frequency ($\Delta f = 500$ MHz)	1.88	2.95	6.50
Polarisation	2.92	5.59	6.65

Table 1: Average Diversity Gain Summary (dB)

for the majority of indoor-to-indoor applications.

The three diversity combining strategies are ranked based on the results shown in Table 1 as EG-AC, EG-VC and lastly SC. While EG combining offers the best performance, the method requires additional hardware (relative to SC) when implemented. Hence, for cost sensitive

IV. HAP/SATELLITE MODELLING USING VIRTUAL TRANSMITTERS

In this paper we extend our previous ray-tracing analysis to examine the situation where the transmitter is positioned a large distance from the environment of interest. This is typical of the high altitude outdoor-to-indoor radio link. Given the

large separation distance between the transmitter and an indoor terminal, numeric difficulties present problems to standard ray-tracing methods. This is because the signal strength calculation depends on total path length, but interference effects that cause fading rely critically on absolute path lengths. Given a computer based simulation there is a limited precision to which lengths can be recorded. To overcome this numeric error problem, a novel and accurate prediction method is proposed based on the use of virtual transmitters placed in close proximity to the indoor environment.

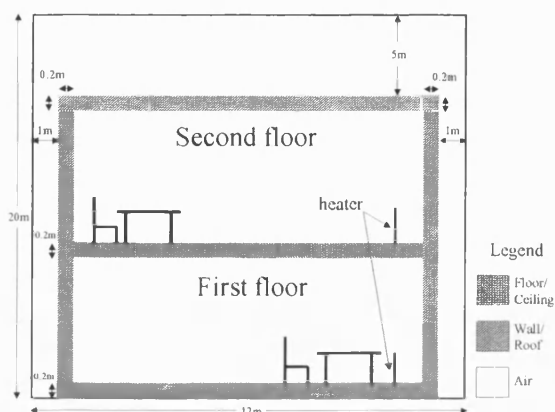


Figure 3: Database for an indoor environment [two floors unfurnished building, 10m by 15m surrounded by air-gaps]

Figure 3 shows the indoor structure used in this HAP/satellite modeling exercise. Figure 4 shows the concept of the virtual transmitters used to simulate propagation from the distant HAP/satellite.

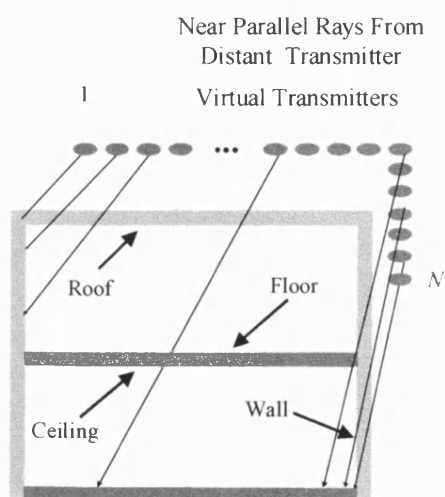


Figure 4: Concept of Virtual Transmitters (N = Number of virtual transmitters) to simulate propagation from a distant HAP

An array of virtual transmitters are located just above the roof and to the side of the building as shown. The exact location of the virtual transmitters depends on the elevation angle of the transmitter. Rays are launched to cover all indoor locations from the top left to the bottom right hand corner of the building. As shown in Figure 4, each virtual transmitter launches a single ray at an angle that corresponds to the equivalent that would have been sent from the transmitter. This method can be used to simulate propagation at any elevation angle from a distant high altitude transmitter.

A frequency of 2 GHz and an altitude of 20 km has been suggested for HAP 3G services, and hence we simulate using this data. However our simulation model does not currently include diffraction effects as it was developed primarily for use at millimetre wave frequencies. At a frequency of 2 GHz these effects would be expected to play a significant role and will be included in the future. This simulation is only being done as an initial investigation to demonstrate the validity of the virtual transmitter approach.

Figure 5 shows the reconstructed field strength for the indoor environment when illuminated from directly overhead without furniture. It demonstrates that the method correctly models the near parallel rays expected from the distant transmitter within the building. The technique confines the ray tracing analysis to a small grid surrounding the indoor environment and thus eases both the memory and run time constraints of the software, as well as overcoming the numeric error problems.

While higher frequency HAPs are planned [4], further simulation work is required to determine their suitability for indoor coverage.

V. DISCUSSIONS AND CONCLUSION

This paper has presented indoor-to-indoor field strength prediction results at 17 GHz for a short range communication system in a typical indoor environment. The improvement of the quality of the propagation link by various diversity techniques has been evaluated, showing the superiority of space diversity and EG-AC. For cost sensitive applications, switched diversity is also worthy of consideration.

The indoor model was extended using the concept of virtual transmitters to enable HAP-to-indoor analysis to be performed. Simulations predicted normalised field strengths in the region of -80 to -100 dB for a two story building structure.

REFERENCES

- [1] C. Ghobadi, P.R. Shepherd and S.R. Pennock, "2D Ray-Tracing Model for Indoor Radio Propagation at Millimeter Frequencies and the Study of Diversity Techniques," *IEE Proc. Microw. Antennas Propagation*, Vol. 145, No. 4, pp. 349-353, Aug. 1998.
- [2] R. Davies, M. Bensebti, J. McGeehan, "Wireless Propagation Measurements in Indoor Mutipath Environments At 1.7 GHz and 60 GHz For Small Cell Systems," *IEEE Trans. Antennas and Propagation*, pp. 589-593, 1991.
- [3] C. Yang, B. Wu and C. Ko, "A Ray-Tracing Method for Modeling Indoor Wave Propagation and Penetration," *IEEE Trans. on Antenna and Propagation*, vol. 46, no. 6, pp. 907-919, Jun. 1998.
- [4] www.estec.esa.nl/halewww/www/hale.htm
- [5] L.M. Correia, P.O. Frances, "Estimation of Materials Characteristics from power measurements," *In Proceedings of PIMRC 94*, pp 510-513.
- [6] D. Bull, C. Canagarajah and A. Nix, "Insights into Mobile Multimedia Communications," *Academic Press*, ISBN 0-12-140310-6, October 1998.
- [7] A.R. Nix, P. Matthews, "Principles of wideband propagation, propagation of radio waves", *The Institute of Electrical Eng.*, Chapter 10 ISBN, 0- 85296-819-1, 1988.

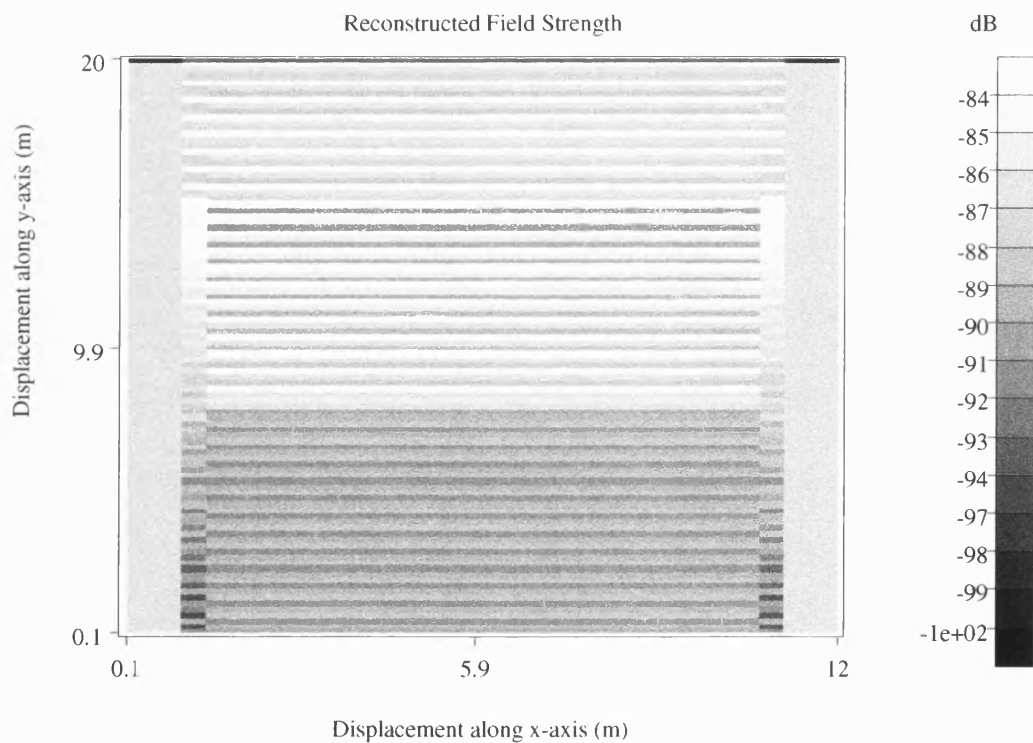


Figure 5: Reconstructed Indoor Field Strength from an overhead HAP

Indoor Ray Tracing Evaluation of Enhanced High Frequency Communications using Directional Antennas at the Basestation and Space Diversity at the Terminal

F. Tila, P. R. Shepherd and S. R. Pennock

Department of Electronic and Electrical Engineering,
University of Bath, Claverton Down, BA7 2AY, United Kingdom

Tel: + 44-(0)1225-826281, Fax: + 44-(0)1225-826305, E-mail: eepft@bath.ac.uk

Abstract

This paper analyses field strength coverage predictions for high frequency indoor communications at 17 GHz using directional antennas at the basestation (BS) and 2 branch spaced antenna diversity at the moveable terminal (MT). Detailed propagation information is generated for a typical two-dimensional indoor environment using a ray-tracing propagation tool developed at the University of Bath. As a performance benchmark, initial field strength predictions are generated for omni-directional BS and MT antennas. Downlink performance is enhanced by the use of 2 branch spaced antenna diversity at the MT. Factors such as antenna spacing and the choice of diversity combining algorithm are considered. At the BS, a novel three branch phased array beam pattern diversity system is compared with an ideal six branch sectorised antenna. For each configuration, detailed propagation studies are performed to determine the relative (compared to omni-directional antennas) coverage improvement over the entire environment with comparison made in terms of the gain for 99% coverage. Results indicate that the use of spaced diversity at the MT can improve the expected coverage for an omni BS antenna by as much as 11.4 dB. Beam pattern and sector switching arrangements at the BS results in a 7.1-10.1 dB improvement. The most impressive gains were observed by combining directional antennas at the BS with equal gain spaced antenna diversity at the MT. Gains of 16.4 dB and 19.9 dB were observed for three (beam pattern) and six (sectorised) branch systems respectively.

I. INTRODUCTION

The need for high capacity indoor communications continues to escalate. Mobile and portable devices demand ever increasing bit rates. The majority of current indoor communications occur in the 2.4 GHz ISM (Industrial, Scientific and Medical) band. Technologies such as Bluetooth and 802.11 enable bit rates in the region 1-2 Mb/s [1]. Future enhancements of 802.11 are planned for use in the 5 GHz band offering bit rates as high as 54 Mb/s [2]. Looking to the future, even larger spectral allocations are available at higher frequencies. Systems such as AWA were proposed in Japan for operation at 19 GHz [3]. ETSI are considering the use of 17 GHz [4] for future versions of their Hiperlan family of radio standards. In the US, spectrum has been made available in the 59-64 GHz band for indoor short-range communications [5].

This paper analyses field strength predictions at 17 GHz for a variety of potential basestation and terminal antenna configurations. The analysis considers omni and directional antennas at the basestation combined with omni and 2 branch spaced antenna diversity at the terminal. The propagation data is generated for a two-dimensional indoor environment using ray-tracing software developed at the University of Bath [6].

Section II describes the ray tracing propagation tool and the indoor environment. Section III discusses the various basestation and terminal antenna structures and the proposed diversity combining and selection algorithms. In section IV a range of field strength coverage predictions are presented and analysed. Initial field strength prediction are generated for omni-directional basestation and terminal antennas. Downlink performance is enhanced by the use of 2 branch spaced antenna diversity at the terminal. Factors such as antenna spacing and the choice of diversity combining algorithm are considered. At the basestation, a novel 3 branch phased array beam pattern diversity antenna is compared with an ideal six branch sectorised antenna. For each configuration, detailed propagation studies are performed to determine the relative (compared to omni-directional antennas) coverage improvement averaged over the entire environment. Section V discusses the results and the paper ends with a set of conclusions and recommendations.

II. RAY MODEL & ENVIRONMENT

The propagation analysis performed in this paper is based on results obtained from a ray-tube launching prediction model [6]. The propagation model can be divided into two distinct modules. Firstly, a process of *ray launching* and tracing is performed from the basestation. Once complete, the resulting data structure is used to perform *field reconstruction* over the entire grid of receiver points. The ray tracing algorithm performs a general analysis of launched ray paths from the transmitter as they reflect and/or transmit at a boundary and onward propagate through the indoor environment. The ray tracing module traces ray tubes from the source transmitter in a predetermined direction, based on azimuth start and stop angles and an angular launch resolution. Object intersections are identified for each ray path (by sensing a material discontinuity) and appropriate reflections and transmissions are calculated. Once the field strength of the ray has fallen below a predefined threshold level (known as the Cut Off Power) then the process stops and a new source ray is initiated at the next launch angle. The ray tracing process is performed based on knowledge of the local environment and the location of the transmitter. The ray launching process is performed once for a given transmitter location to build ray tree that tracks launched rays as they reflect and transmit from planar surfaces. The tracing of rays between the transmitter and receiver is

accomplished using the field reconstruction module via an exhaustive analysis of the ray tree. A ray is said to occur between the transmitter and receiver if an image from the ray tracing tree illuminates the receiver.

Since the ray model is deterministic it requires a database for the environment of interest (including material properties). In practice, any two dimensional environment can be specified. Factors such as material thickness and complex permittivity are highly influential in such models, particularly when determining transmission loss. The building material assumptions used in this study are shown in table 1.

Once the database is generated, the ray model is able to trace the various path reflections and refractions at material boundaries to a predefined signal strength. The received field strength at each grid point is then calculated by the vector summation of field strengths for all rays that illuminate that point. The indoor test environment is shown in figure 1.

The environment consists of a main room surrounded by an L-shaped corridor. The basestation is placed in the main room as shown in figure 1. The environment is divided into a 50 x 25 grid, with receiver points spaced every 0.2m.

III. DIVERSITY GENERATION/COMBINING

Wireless communications are known to suffer from fast fading and this can seriously disrupt the quality of the radio link (particularly in non-line-of-sight locations). Indoor links, with the presence of walls, furniture, etc. are particularly susceptible. In addition to the use of directional transmit and receive antennas, in this paper a number of diversity techniques are analysed to further enhance radio communication in an indoor environment. In particular, switched beam/sector and space diversity schemes are considered at the basestation and terminal respectively. Space diversity represents a common technique for mitigating the effects of fast fading in a radio environment. In this paper the two receiving omni-directional antennas are spaced at a distance of 3.5 wavelengths [7]. For the basestation, a 3 branch beam switching and a 6 branch sectorised arrangement are considered.

The principles of diversity generation and combining have been known for many decades, with the first experiments being reported in 1927. The diversity method requires a number of transmission paths to be available, each carrying the same message, having a similar mean power and suffering independent fading statistics. The probability of experiencing simultaneous deep signal fades on each diversity branch is low providing the fast fading on each branch is uncorrelated. Space diversity is considered to be a strong contender for microwave mobile radio applications [8]. In this paper, diversity signals are generated at the terminal using two spaced antennas.

The spacing of the antennas at the receiver (see figure 2) is chosen to ensure that the individual signals are suitably uncorrelated. Previous work has demonstrated strong decorrelation for an antenna spacing of 3.5 wavelengths[7]. The precise antenna spacing depends on a number of factors, such as the wavelength and the azimuth distribution of the multipaths. Given the use of a 17 GHz carrier frequency, this spacing translates to a distance of around 5 cm. In a high clutter environment, spacings as low as one quarter to one half of a wavelength can still offer good performance [7][8].

Two methods of diversity combining at the terminal are considered. The first technique simply selects the strongest of the two signals at any given time. The second technique, known as Equal Gain Combining (EGC), adds the amplitudes of the two signal branches [9].

Selection Combining: Selection combining operates using two or more uncorrelated diversity branches. The method relies on selecting the best of the available diversity branches. The best branch is usually defined as the strongest branch at any given instant. When implementing selection diversity, it is common to base the branch selection on the Received Signal Strength Indication (RSSI), which is a measure of the signal strength over a short time window [9].

Equal Gain Combining: Having selected a given branch, the energy associated with the unselected branches is effectively lost in the detection process. This obviously results in a sub-optimal solution. In equal gain combining, rather than choosing a single branch for detection, the amplitude from the two received diversity branches are summed to form a single signal for detection [9]. This process is illustrated in figure 3, where m represents the message, and a , θ_1 , b and θ_2 represent the amplitude and phase of the fading on branches 1 and 2.

In practice, amplitude summation is achieved using a process known as cophasing. Cophasing aims to make the phase of branches 1 and 2 identical, thus enabling the signal amplitudes to be summed. The cophasing process requires the phase of each channel to be estimated prior to combining. Given that the channel phase is known, each branch can be multiplied by its unity gain conjugate to remove the channel phase component. EGC is therefore more complex than selection diversity and requires accurate channel estimation, which increases the cost of the combiner. Given that the message adds coherently while the noise components add incoherently, after combining the expected field strength increases by 6 dB, while the noise increases by just 3 dB. This results in a 3 dB increase in average signal to noise ratio.

Beam Pattern Diversity and Sectorised Antennas

At the basestation, two directive antenna strategies are explored. The first technique makes use of a linear phased array to implement beam pattern diversity. The basestation applies one of three sets of phase weights to the phased array to form one of three possible beam patterns. In practice, the number of beam patterns could be increased and depends on the number of individual antenna elements in the array. Figure 4(i) shows the amplitude of one of the three beam patterns considered in this study. Each beam pattern is assumed to have a 4.8 dBi boresight gain. This pattern was generated assuming a 7-element uniform linear array [10]. The second and third beam patterns are identical but rotated clockwise and anti-clockwise by 60 degrees. Using this strategy, all possible terminal locations will fall into the 3dB beamwidth of

one of the three beam patterns. For each terminal location, the best of the three beam patterns must be determined prior to data transmission (i.e. beam pattern selection diversity at the basestation). System performance can be further enhanced by applying space diversity at the terminal *in addition* to beam pattern diversity at the basestation. In this configuration, the beam pattern resulting in the best output from the terminal diversity combiner is chosen. In the case of switched terminal diversity, the algorithm will choose the best combination of basestation sector and terminal antenna element.

A sectorised antenna comprises a number of individual antenna units, each having a single main lobe covering a fraction of the full 360 degrees. In this paper a six sector solution is considered, with each sector having a 60 degree 3-dB beamwidth. To ease the modelling process, idealized individual sector patterns based on a Gaussian beam are assumed [11]. Figure 4(ii) shows the resulting beam pattern for a single sector. The other five sectors are identical, but rotated by 60, 120, 180, 240 and 300 degrees. Each sector has a 7.8 dBi boresight gain.

IV. SYSTEM ANALYSIS

The following 6 system configurations are analysed in this section:

1. Omni basestation antenna to omni terminal antenna
2. Omni basestation antenna to space diversity terminal
3. Phased array basestation with omni terminal antenna
4. Phased array basestation with space diversity terminal
5. Sectorised basestation with omni terminal antenna
6. Sectorised basestation with space diversity terminal

Section III described the diversity methods and antenna patterns used at the basestation and terminal. For each mode, beam pattern and sector, ray tracing field strength prediction grids are generated and the appropriate transmit and/or receive diversity processing applied. Figure 5 shows the field strength prediction grid for omni directional basestation and mobile antenna (mode 1). The received field can be seen to peak in the vicinity of the basestation and remains high in areas of direct line of sight. The field drops dramatically as the signal passes through dividing walls into the corridor. The omni-omni data was used as a reference to compare the coverage performance of the remaining diversity systems.

Figure 6 shows the Cumulative Distribution Function (CDF) of normalized fade depths for an omni basestation with and without space diversity at the terminal. The CDF for each scheme was generated by computing the instantaneous fade depth at each receive point. This fade depth was calculated as the difference between the mean field strength for an omni-omni configuration and the instantaneous field for the mode of interest (calculated from the vector sum of rays). In the case of directional antennas at the BS, a normalized pattern with unity gain on the boresight was used. Hence, the impact of antenna gain needs to be incorporated in the final comparison.

In this paper 1% outage was chosen to ensure 99% coverage, as higher values of coverage are not considered economically viable, while lower values will not provide adequate quality of service. Also this level of coverage highlights the system's ability to remove the problematic deep fading effects.

Figure 6 shows the CDF for branch 1 and branch 2 at the terminal. As expected, the fading statistics for both antennas are near identical, with both requiring a 14.6 dB fade margin. This fade margin is given by $-B$, where B represents the fade level. For the reference omni-omni case, this fade margin is also denoted by the variable $-A$. The first row in Table 2 summarizes the processed data for the omni-omni configuration. Application of switched space diversity can be seen dramatically to improve the resulting CDF. A fade margin of 3.8 dB is now observed ($-B$ on the switched CDF graph). Since this fade margin is computed relative to the mean of a single omni directional antenna, any improvement in mean power is also incorporated in this value. From a field strength coverage point of view, performance is improved by 10.8 dB (i.e. $-(A-B)$). More generally, this system gain can be calculated in dB for 99% coverage as:

$$\text{System Gain (dB)} = D - (A - B)$$

Where D represents the directive gain of the BS antenna (relative to a reference dipole), $-A$ represents the fade margin on a single omni-omni antenna system at a 1% outage level and $-B$ represents the fade margin for the test antenna configuration. The directive gain, D , is required since the propagation grids are computed using normalised patterns (each having a boresight gain of unity), hence the mean improvement using a directive basestation antenna is not directly included in the CDF curves. It is important to note that in the case of EGC, the noise floor would be increased by 3 dB. This is included by subtracting the value from the improved fade margin, B . The final graph in figure 6 shows the CDF for EGC combining at the terminal. The mean power has increased by 6.28 dB relative to the original single antenna configuration. This gain is consistent with EGC, where an approximate 6 dB increase in mean is expected (see section III). For this system, a fade margin of 0.2 dB is shown on the graph. As explained above, this value includes the mean gain of 6.28 dB and needs to be modified to reflect the 3 dB increase in noise floor. In table 2, a modified fade margin of 3.2 dB is quoted.

Figure 7 shows the CDF results for 3 branch beam pattern diversity at the basestation. Assuming a single omni antenna at the terminal, the mean power drops by 0.4 dB and the fade margin improves to 12.3 dB. The beam pattern (see figure 4(i)) has a gain of 4.8 dB relative to the reference dipole, i.e. $10\log(360/BW)$, where BW represents the 3 dB beamwidth of the directional BS antenna. As summarized in row 4 of table 2, this configuration results in an overall gain of 7.1 dB. Switching beam patterns at the basestation does not result in a significant fade margin reduction since the beams do not overlap. This means that the directly illuminating beam pattern is always likely to be chosen, even when the beam suffers a deep fade. This observation is confirmed by figure 8, which shows the most likely beam selection as a function of terminal location. Generally, the beam that points in the direction of the terminal is nearly always chosen, irrespective of fade

depth. The application of diversity at the terminal dramatically improves the fade margin. From figure 7 the fade margin drops to 4.8 dB (from 12.3 dB previously). Taking into account differences in the antenna gain, the overall improvement for this system is 14.6 dB (row 5, table 2). The final graph on figure 7 shows the impact of applying EGC at the terminal. The overall gain now increases to 16.4dB.

The final three rows in table 2 consider the use of a 6 sectored antenna at the basestation. This antenna has a boresight gain of 7.8 dB relative to the reference dipole. Field strength predictions for each of the six sectors are shown in figure 9. The diagram shows the orientation of each sector and confirms that the best coverage for each sector lies within its 3 dB beamwidth. By switching to the sector offering the best coverage at a given point, indoor coverage can be greatly enhanced. Figure 10 shows the resulting CDF statistics for this case. As for the beam pattern scenario, little improvement in fade margin is seen when a single omni antenna is used at the terminal. An overall gain of 10.1 dB is observed (largely due to the 7.8 dB of improved BS antenna gain). The application of switched diversity at the terminal improves performance significantly, with an overall gain of 18.4 dB. The final system considers EGC combining at the terminal with the 6 sector antenna at the basestation. For this system, an overall gain of 19.9 dB was observed.

V. CONCLUSIONS

In this paper a range of diversity systems have been studied at the basestation and terminal. Results indicate that gains of up to 11.4 dB are possible using spaced antenna diversity alone at the terminal. The use of 3 branch pattern diversity at the transmitter can improve performance by 7.1 dB for a single omni antenna at the terminal and by as much as 16.4 dB if EGC space diversity is also applied at the terminal. The final system considered here was a six sectored basestation antenna. This configuration offered in excess of 10.1 dB gain for a single omni terminal antenna and as much as 19.9 dB gain when combined with 2 branch EGC at the terminal. It should be noted that all gains are quoted at a 1% fading outage level. The results indicate that the performance of high frequency indoor systems could be improved by up to 19.9 dB through the careful application of antenna diversity at the MT and BS.

REFERENCES

- [1] S. Souissi and E.F. Mehofer, "Performance evaluation of a Bluetooth network in the presence of adjacent and co-channel interference", *Emerging Technologies Symposium: Broadband, Wireless Internet Access, IEEE*, 2000.
- [2] A.R. Nix et al., "Predicted HIPERLAN coverage and outage performance at 5.2 GHz and 17 GHz using indoor 3D-ray-tracing techniques", *Wireless Personal Communication Journal HIPERLAN special edition*, Kluwer, New York, 1996.
- [3] M. Umehira et al., "An ATM Wireless Access System for Tetherless Multimedia Services", *ICUPC*, 1995.
- [4] Radio Equipment and Services (RES), High Performance Radio Local Area Networks (HIPERLANs), Requirements and Architectures for Wireless ATM Access and Interconnection, ESTI, TR101 031, V1.1.1, 1997-04.
- [5] Rules of Permit use of Radio Frequencies above 40 GHz for New Radio applications. FCC ET Docket No. 94-124, first report and order/second notice of proposed rulemaking December 1995.
- [6] F. Tila, P.R. Shepherd and S.R. Pennock, "Analysis of Indoor-Indoor and Satellite/Hap-Indoor Propagation Effects", *11th International Antennas and propagation Professional Network ICAP*, pp. 203-7, Manchester, April 2001.
- [7] F. Tila, S.R. Pennock and P.R. Shepherd, "Evaluation of Indoor Propagation Effects and Diversity Techniques", *Proc. IEE PREP*, pp. 23-25, 2001.
- [8] Ch. Ghobadi, S.R. Pennock and P.R. Shepherd, "Evaluation of Diversity Techniques in Complex Indoor Environments", *28th European Microwave Conference Amsterdam*, pp. 345-350, 1998.
- [9] W.C. Jakes, "Microwave Mobile Communication", *John Wiley Inc.*, First Edition, ISBN 0-471-43720-4, 1974.
- [10] C.A. Balanis, "Antenna theory analysis and design", *New York: Harper & Row*, Second Edition, ISBN 0-06-040458-2, 1982.
- [11] M.R. Williamson and A.R. Nix, "Investigating the effects of Antenna Directivity on Wireless Indoor Communications at 60 GHz", *8th IEEE Personal and Indoor Mobile Radio Conference, Helsinki, Finland*, pp. 635-639, Sept. 1997.

TABLE 1
MATERIAL PROPERTIES

Material Type	Relative permittivity	Conductivity	dB/cm	Thickness (cm)
Exterior Wall	2.7	0.05	0.5	20
Door	5.0	0.05	0.4	10
Desk	4.0	0.055	0.5	20
Partition Wall	2.7	0.05	0.5	20

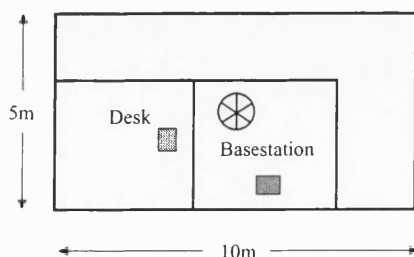


Figure 1: Example Environment

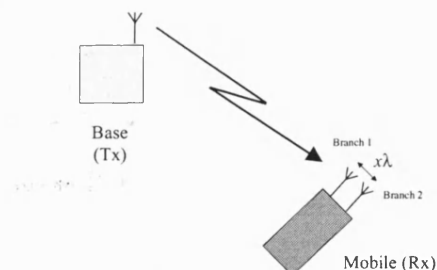


Figure 2: Receiver Space Diversity

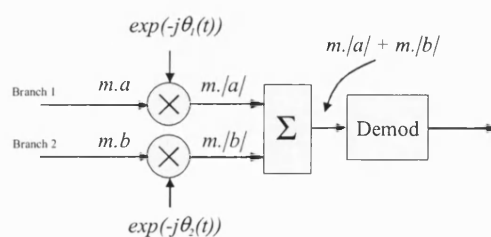


Figure 3: Equal Gain Combining: Amplitude Summation

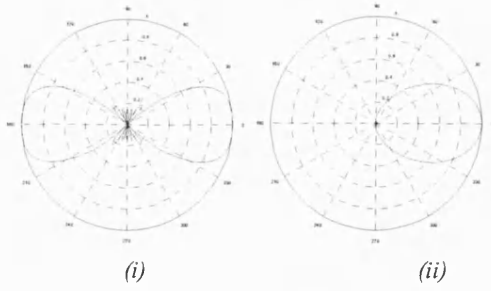


Figure 4: (i) 2 x 60 degree Phased Array Beam Pattern, (ii) 60 degree Sector Approximation

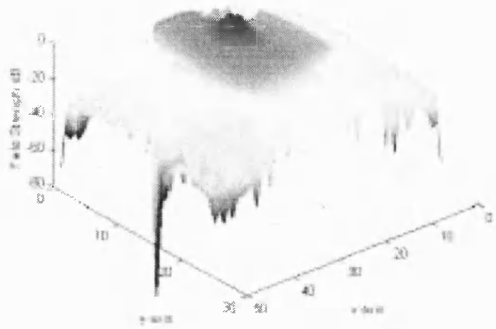


Figure 5: 3-D field strength grid plot

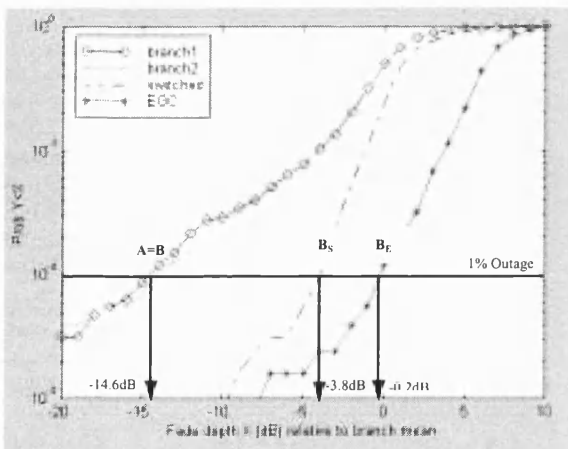


Figure 6: Fading CDF for omni basestation (relative to single antenna mean)

TABLE 2
SYSTEM GAIN VS BS/MT ANTENNA STRATEGY (* 3 DB ADDED TO COMPENSATE FOR INCREASED EGC NOISE FLOOR)

System Type	1% Fade Margin, -B dB	BS Relative Directive Gain, D dB	System Gain, D-(A-B) dB
Omni BS – Omni	14.6	0.0	0.0
Omni BS – SW MT	3.8	0.0	10.8
Omni BS – EGC MT	3.2*	0.0	11.4
3 Branch BS – Omni	12.3	4.8	7.1
3 Branch BS – SW	4.8	4.8	14.6
3 Branch BS – EGC	3.0*	4.8	16.4
6 Branch – Omni MT	12.3	7.8	10.1
6 Branch – SW MT	4.0	7.8	18.4
6 Branch SW EGC	2.5*	7.8	19.9

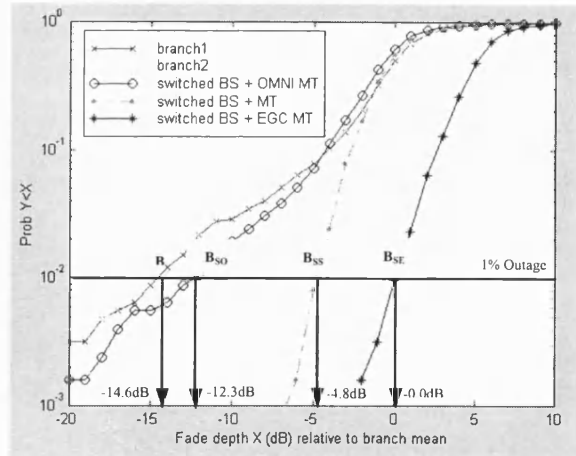


Figure 7: Fading CDF for 3 branch beam pattern basestation (relative to single antenna mean)

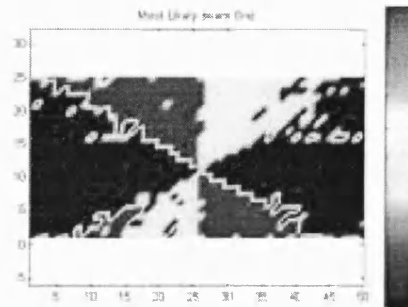


Figure 8: Most Likely Beam Pattern (1: 0 degrees, 2: +60 degrees, 3: -60 degrees – see figure 4(ii))

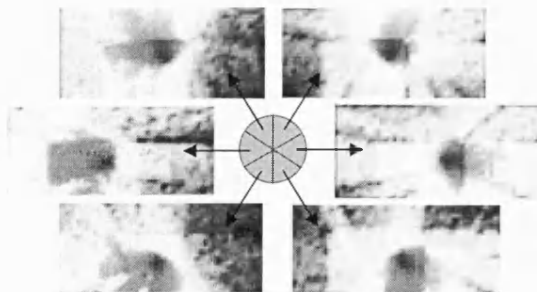


Figure 9: Individual Sector Plot (omni MT antenna)

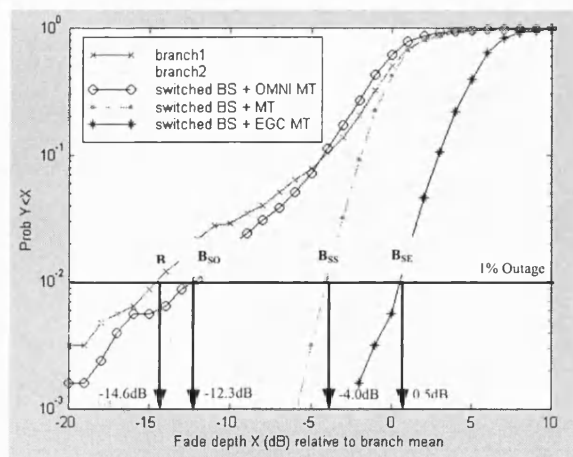


Figure 10: Fading CDF for 6 branch sector basestation (relative to single antenna mean)

2GHz Propagation and Diversity Evaluation for In-Building Communications up to 4MHz using High Altitude Platforms (HAP)

F. Tila, P. R. Shepherd and S. R. Pennock

Department of Electronic and Electrical Engineering,
University of Bath, Claverton Down, BA7 2AY, United Kingdom

Tel: + 44-(0)1225-826281, Fax: + 44-(0)1225-826305, E-mail:eeptf@bath.ac.uk

Abstract – This paper investigates in-building radio coverage at 2GHz from a High Altitude Platform (HAP). The HAP is located at a height of 20km above the earth. The propagation analysis is based on a novel two-dimensional ray-model. The model makes use of an array of virtual transmitters placed around the building. To improve radio reception, two branch switched and equal gain diversity combining are applied at the terminal. Propagation coverage grids are generated over a pair of multi-floor building structures. Results include the calculation of in-building penetration loss and the derivation of link margins for 90% and 99% indoor area coverage. Using this data, the required HAP transmit power is calculated as a function of diversity technique, area coverage and operating bandwidth. Assuming a 1km radius spot beam, a 3G compatible operating bandwidth of 4MHz and 90% in-building area coverage, the results indicate that space diversity at the terminal reduces the HAP transmit power from 2.15 Watts to 0.84 Watts.

I. INTRODUCTION

Over the last 10-15 years a large number of indoor to indoor propagation models have been proposed in the literature. Outdoor to indoor propagation models have also been developed, mainly to determine indoor penetration loss from terrestrial basestations. Recently, the use of High Altitude Platforms (HAP) has been proposed as a means of offering broadband third and fourth generation services [1]. HAP basestations are located at a height of approximately 20km, thus avoiding the high path losses observed with satellite communications. The use of overhead platforms also reduces the path loss observed in dense urban terrestrial radio systems.

Traditionally, given the large separation distance between the HAP and the mobile terminal, ray-launching methods have been difficult to apply. In this paper, novel modifications to a previous indoor-only ray-tracing model [3] are described that enable HAP analysis to be performed. These enhancements involve the placing of an array of virtual transmitters around the building of interest. This array enables indoor prediction from the HAP for any elevation angle and height.

Wireless communications are known to suffer from fast fading and this can seriously disrupt the quality of the radio link (particularly in non-line-of-sight locations). Indoor links, with the presence of walls, furniture, etc. are particularly susceptible to fading. The need to improve the link budget is vital in the case of broadband HAP communications.

In this paper switched and equal gain diversity techniques are analysed to enhance the radio link for HAP to indoor communication. The analysis concentrates on the use of space diversity with antennas

separated at half a wavelength (7.5 cm at 2 GHz). A range of antenna spacing have been analysed, the figure of half a wavelength provides a good compromise between high diversity gain and relatively small physical size.

This paper is structured as follows. Section II covers the mathematical calculation of path loss in the HAP environment. Section III describes the ray model and the novel use of an array of virtual transmitters to simulate transmission from a distant HAP. The building structure used in this analysis is described together with the assumptions made for the various building materials. Section IV presents the predicted coverage grids and the impact of antenna diversity at the terminal. Results include a calculation of in-building penetration loss and the derivation of link margins for 90% and 99% indoor area coverage. Section V considers a typical link budget and determines the required HAP transmit power as a function of diversity technique, area coverage and operating bandwidth. The paper ends with a number of conclusions and recommendations.

II. HAP PATH LOSS CALCULATION

Figure 1 shows the concept of HAP communication. Rather than using a terrestrially mounted basestation, the equipment is mounted, for example, in an unmanned airship (*H*) located approximately 20km above the surface of the earth [4]. Using highly directive spot beams from the HAP, communication occurs with mobile terminals on the ground. HAP systems do not suffer from the high path loss associated with satellite communications. They also avoid the high losses observed in dense urban environments when low mounted terrestrial basestations are used.

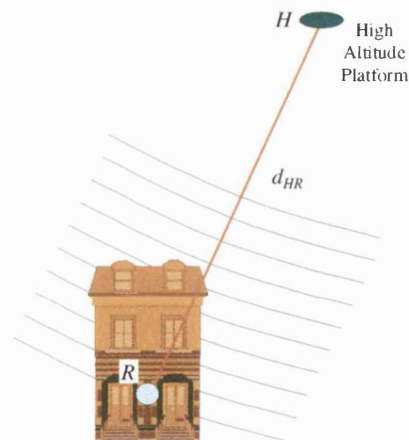


Figure 1: HAP Indoor Coverage

We first assume that the signal arrives at a point R on the ground after travelling a distance d_{HR} metres. The received power (assuming a line of sight path) can be calculated using the following equation:

$$P_R = P_T G_T G_R \frac{\lambda^2}{(4\pi d_{HR})^2} = \frac{P_T G_T G_R}{L_S} \quad (1)$$

where:

$$L_S = \text{Spreading Loss} = \frac{(4\pi d_{HR})^2}{\lambda^2} \quad (2)$$

It is common to calculate only the loss associated with the radio channel, since this removes the impact of transmit power and antenna gain. These factors can be added at a later date. Assuming $P_T G_T G_R = 1$, we get:

$$P_R = \frac{\lambda^2}{(4\pi d_{HR})^2} = \frac{1}{L_S} \quad (3)$$

It is also common to normalise $P_T G_T G_R / L_S = 1$ at a distance of one metre [5]. Given that $P_T G_T G_R = 1$, we can denote the normalised spreading loss using the variable, L'_S . Under these conditions we can write:

$$L'_S = 1, d = 1 \text{ hence } L'_S = L_S \frac{\lambda^2}{(4\pi)^2} \text{ or } L_S = L'_S \frac{(4\pi)^2}{\lambda^2} \quad (4)$$

Hence, to calculate the true spreading loss from a normalised value, we must multiply the normalised loss by a factor $(4\pi)^2 / \lambda^2$.

For the HAP scenario shown in figure 1, the received signal suffers from three losses:

- Spreading Loss (as discussed above), L_S
- Building Penetration and Shadowing Loss, L_P
- Fast Fading Loss, L_F

In practice it is difficult to separate these mechanisms. The first loss term was discussed earlier in this section. The second loss occurs due to attenuation as the waves pass through structures such as the roof, ceiling, walls and floors. A shadow loss margin is required to protect against these losses. The third loss occurs since we do not receive just a single path from the HAP, but a number of scattered, reflected and transmitted paths from within the building structure. The actual signal is formed from the vector sum of these multipaths and a fade margin is required to protect the quality of the system. We can write the following equation for the received power, P_{RM} , in a HAP environment:

$$P_{RM} = \frac{P_T G_T G_R}{L_S L_P L_F} \quad (5)$$

Again, assuming $P_T G_T G_R = 1$, we get:

$$P_{RM} = \frac{1}{L_S L_P L_F} = \frac{1}{L'_S L_P L_F} \frac{\lambda^2}{(4\pi)^2} \quad (6)$$

For the simple LoS example the spreading loss, L_S , at 2 GHz for a separation distance of 20,000 metres is 124.48 dB. The normalised spreading loss, L'_S , is 86.02 dB (a reduction of 38.46 dB due to the normalisation process). To model the building penetration, shadowing and fast fading losses, a deterministic ray tracing model is used. Given the large distance between the HAP and the mobile terminal, the real scenario cannot be directly modelled since it would require the creation of a huge environment grid. Hence, some form of ray tracing modification is required to enable the HAP scenario to be modelled.

III. HAP RAY MODELLING

In this section a number of modifications to the ray-tracing software described in [2][3] are discussed to enable accurate propagation prediction from a HAP. The method required modifications to both the ray tracing and field reconstruction modules [3]. The proposed technique is accurate and does not make use of approximations.

A. Explanation of the Virtual Transmitter method

It is known that real waves traced from the HAP to the building will have virtually parallel wave fronts. The method used to enhance the ray model places an array of virtual transmitters around the building under test (as shown in figure 2). Each virtual transmitter is now used to launch a single ray. Using knowledge of the location of the HAP and the virtual transmitters, a precise ray launch angle for each virtual transmitter can be calculated. This angle is used to launch a single ray that emulates the path that would have been traced from the HAP. By using an array of virtual transmitters, the software can simulate a number of uniformly launched rays from the HAP. To overcome the path length problem (i.e. the shorter distance from the virtual transmitter), modifications are made in both the ray tracing and field reconstruction modules to add the extra path length from the HAP paths. Using this technique, a number of rays can be launched from the array of virtual transmitters to mimic the set of rays that would have been launched from the HAP. An accurate simulation can be achieved for any point in the test environment by:

- Restricting each virtual transmitter to a single ray launch,
- Calculating the launch angle using knowledge of the HAP position,
- Modifying the path length to reflect the distance to the HAP.

This concept is shown in figure 2. A simple indoor structure is shown comprising two floors. An array of N (450 in this case) virtual transmitters is shown at a distance of 5 metres above the roof and to the side of the building. The HAP can be located at any height and elevation above the building.

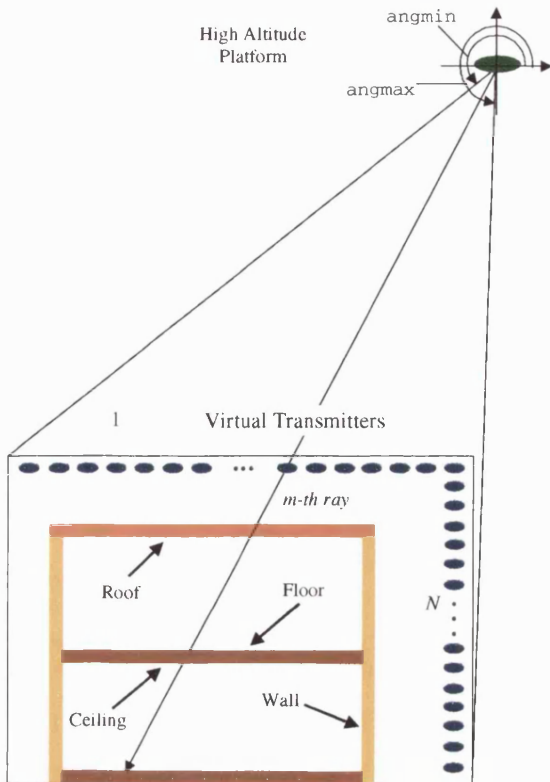


Figure 2: Concept of Virtual Transmitters (N = Number of virtual transmitters placed around the building to simulate propagation from a distant HAP)

The algorithm now calculates the angle to the first and last virtual transmitter, these are then denoted by the variables $angmin$ and $angmax$. The ray-tracing algorithm proceeds to trace rays uniformly between these two angles. The step size used in the launch algorithm is determined by the spacing of the virtual transmitters, which in turn is controlled by the width of the building and the size of the grid. The spacing between the virtual transmitters must be smaller than the environmental grid spacing to ensure that the launched rays do not miss illuminating points in the grid.

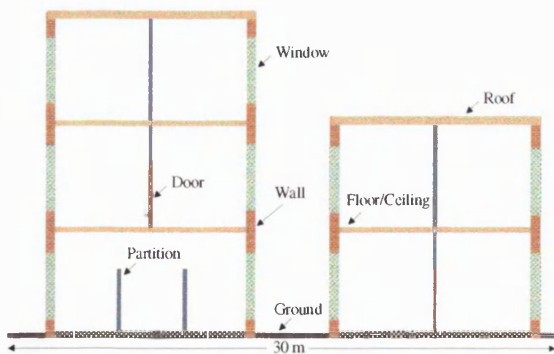


Figure 3: Description of Test Environment

B. Test Environment

The test environment used in this paper is shown in figure 3. Two multistory buildings placed side by side

are assumed. The buildings comprise outer load bearing walls, windows, doors, partitions, ceilings, floors and a roof. The HAP is located at an elevation angle of around 60 degrees to the right of the buildings.

Table I: Assumed Material Parameters

Material Type (Env.)	Attenuation (dB/cm)	Thickness (cm)
Wall	0.6	20
Roof	0.5	20
Floor/Ceiling	0.3	20
Door	0.75	4
Partition	0.4	10
Window	2	1
Ground	0.3	20

Table I provides a list of the material types, thickness and transmission losses [6-8] assumed in the ray model. Each material in the database has a value of permittivity and conductivity. Using this information, angle dependent transmission and reflection coefficients are calculated in the modelling process.

IV. PROPAGATION RESULTS

Figure 4 shows the predicted normalised path loss (see section II) for the entire grid area. Above each building, a path loss of approximately 87.3 dB is observed (86 dB due to the normalised spreading loss and 1.3 dB due to the use of a vertical dipole pattern in the receiver). In practice, fading is seen above the buildings due to the roof-top reflected path. As the rays enter each building, significant penetration is observed for all cases other than windows, where just 2 dB of attenuation is observed. Diffraction is not included in the analysis, although it is known that diffraction can be a significant effect at this frequency. It is planned to include diffraction modeling in future work.

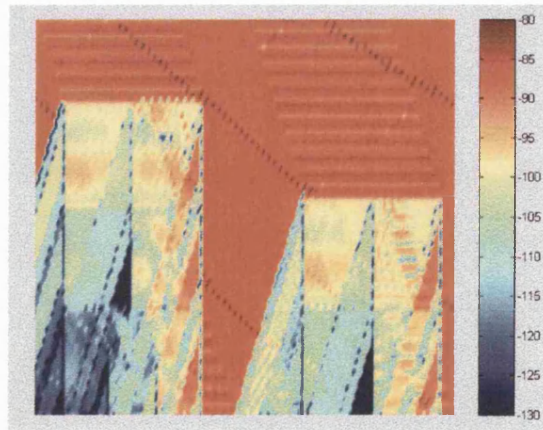


Figure 4: Instantaneous Normalised Path Loss (dB)

From figure 4 it can be seen that the left-hand side of the ground floor suffers the highest levels of attenuation. To analyse mathematically the in-building instantaneous normalised path loss statistics, the Cumulative Distribution Function (CDF) is shown in figure 5 for the case of a single antenna and two branch switched and EGC space diversity.

Figure 5 shows that the normalised instantaneous path loss for a single antenna varies from 80 dB to less than 160 dB.

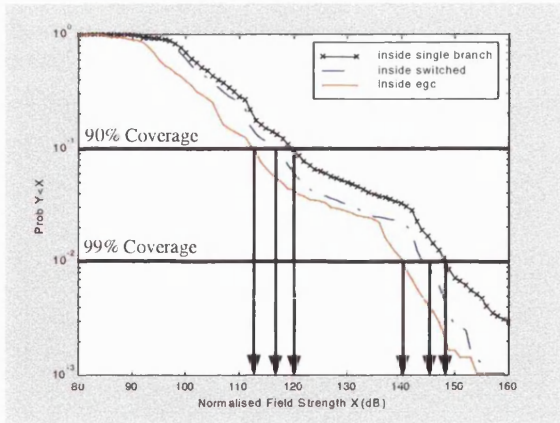


Figure 5: Normalised Path Loss CDF

Figure 5 can be used to determine the path loss margin required to achieve a given area coverage. Table II lists the normalised path loss values and margins assuming indoor area coverage requirements of 90% and 99%. The 90% and 99% values were obtained from the 0.1 and 0.01 probability thresholds in figure 5. Results are given for single antenna, switched diversity and EGC diversity solutions. Table III shows the additional path loss (or fade margin) that can be tolerated (relative to the average indoor loss of 97.82 dB). For 90% in-building coverage, for a single antenna an additional loss of 22.0 dB must be tolerated. For 99% coverage, this additional margin increases to 50.3 dB. The far larger 99% margin shows the difficulty of achieving high percentage coverage inside the building.

Table II: Normalised Path Loss vs Percentage Area Coverage

System	90% Coverage Margin (dB)	99% Coverage Margin (dB)
Single Branch	119.8	148.1
Switched	116.2	145.5
EGC	112.7	140.1

Table III: Path Loss Margin vs Percentage Area Coverage (* includes an addition 3dB due to increase in noise floor for EGC)

System	90% Coverage Margin (dB)	99% Coverage Margin (dB)
Single Branch	22.0	50.3
Switched	18.4	47.7
EGC	17.9*	45.3*

In the case of ideal equal gain combining, while the mean signal strength increases statistically by 6 dB, the noise floor will increase by 3 dB [9]. To compensate for this factor, the fade margin for EGC has been increased by 3 dB.

V. HAP SYSTEM PERFORMANCE

In this section the required HAP transmit power is calculated as a function of coverage quality, spot beam dimensions, system bandwidth (10kHz to 4MHz) and diversity technique. The shadow and fade margins given in tables II and III are used in the analysis. Table IV shows the link budget for a system operating with 4MHz of bandwidth (similar to that required in 3G) using equal gain combining. From section III, an in-building normalised path loss of 97.82 dB is assumed. The additional loss at 1 metre (38.46dB) is also added to the link budget. From table III, the path loss margins for 90% and 99% area coverage are 22.0 dB and 50.3 dB respectively for a single antenna. For EGC, these margins reduce to 17.9 dB and 45.3 dB respectively.

For a bandwidth of 4MHz, the background noise power is given by kTB , where k represents Boltzmann's constant, T the temperature in degrees Kelvin and B the operating bandwidth in Hertz. A temperature of 290 degrees Kelvin is assumed in these calculations. Using these numbers, a noise floor of -137.95 dBW is obtained. After adding a 5 dB noise figure (a value compatible with 3G terminals), the expected noise power rises to -132.95 dBW.

Table IV: Link Budget Example with EGC and 4 MHz BW

	90% Spatial	99% Spatial
Normalised Mean Indoor Loss (dB)	97.82	97.82
Denormalise Loss at 1m (dB)	38.46	38.46
EGC Path Loss Margin (dB)	17.9	45.3
Average Indoor Received Power (dBW)	-105.05	-77.65
Noise Power (5 dB noise figure) (dBW)	-132.95	-132.95
S/N Ratio	10	10
Indoor Power after margins (dBW)	-122.95	-122.95
PtGt (dBW)	31.23	58.63

Assuming (conservatively) that a 10 dB signal to noise ratio is required for acceptable modem performance [9], this implies the received power after adjusting for margins must be -122.95 dBW. The Effective Isotropic Radiated Power (PtGt) for the HAP can now be computed. For 90% and 99% area coverage, an EIRP of 31.23 dBW and 58.63 dBW respectively is required to balance the link.

The HAP antenna gain can be approximated using equation 7, where G_{HAP} , r_{HAP} and r_{SPOT} represent the HAP antenna gain in dBi, the distance to the HAP in meters and the radius of the spot beam in meters.

$$G_{HAP} \approx 10 \log_{10} \frac{4r_{HAP}^2}{r_{SPOT_BEAM}^2} \quad (7)$$

Assuming the HAP is located 20km above the earth and illuminates the city with a 1km radius spot beam, a HAP antenna gain of 32 dBi is obtained. Under these assumptions, HAP transmit powers of -0.77 dBW (0.84 Watts) and 26.63 dBW (460.3 Watts) are required for 90% and 99% indoor coverage. This analysis was

repeated for operating bandwidths between 10 kHz and 4 MHz with and without diversity at the mobile terminal. Figures 6 and 7 show the required EIRP at the HAP for 90% and 99% area coverage (and 99% fade coverage). These graphs can be used to compute the HAP transmit power for any given HAP antenna gain.

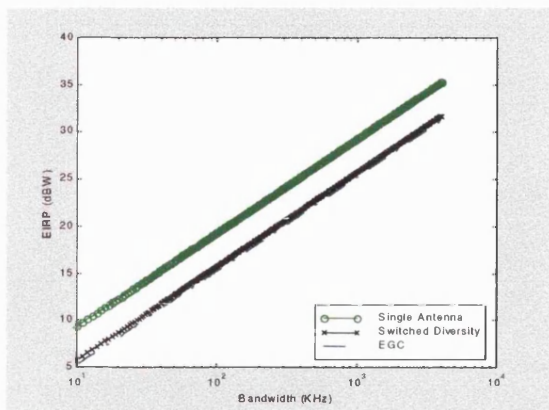


Figure 6: Require EIRP at HAP for 90% Area Coverage (10 dB S/N)

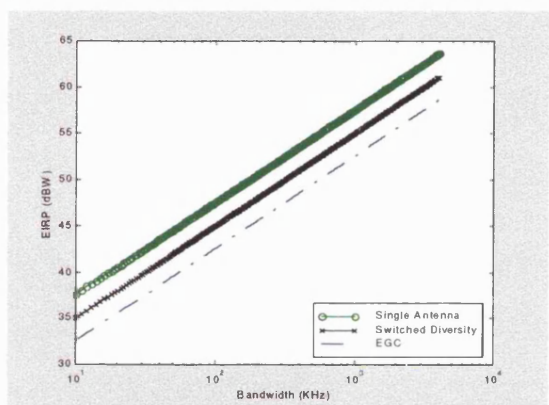


Figure 7: Require EIRP at HAP for 99% Area Coverage (10 dB S/N)

Tables V and VI state the HAP transmit power required for a 32dBi antenna gain as a function of system bandwidth, antenna configuration and area coverage.

Table V: HAP Transmit Power (dBW) for 32 dBi HAP gain and 90% Indoor Area Coverage

	Single Antenna	EGC Combining
10 kHz	-22.69	-26.79
100 kHz	-12.69	-16.79
500 kHz	-5.71	-9.81
4 MHz	3.33	-0.77

Table VI: HAP Transmit Power (dBW) for 32 dBi HAP Gain and 99% Indoor Area Coverage

	Single Antenna	EGC Combining
10 kHz	5.61	0.61
100 kHz	15.61	10.61
500 kHz	22.59	17.59
4 MHz	31.63	26.63

Using equal gain combining, for 90% area coverage, the HAP transmit power varies from 2.1 mW (10 kHz) to

0.84 W (4MHz). For 90% coverage the performance on the ground floor would be poor. To achieve 99% indoor area coverage, the HAP transmit power would need to vary between 1.15 W (10 kHz) and 460.3 W (4MHz).

Without the use of diversity, for 90% area coverage, the HAP transmit power would need to vary between 5.4 mW (10 kHz) and 2.15 W (4MHz).

99% area coverage using a single antenna requires HAP transmit powers between 3.64 W (10kHz) and 1.45 kW (4MHz). Such high values may be impractical.

VI. CONCLUSIONS

This paper has analysed in-building propagation at 2GHz from a HAP. Assuming a 1km radius spot beam, a 3G compatible operating bandwidth of 4MHz and 90% in-building area coverage, the results indicate that space diversity at the terminal reduces the HAP transmit power from 2.15 Watts to 0.84 Watts. An area coverage of 99% was shown to require unreasonably high transmit powers at larger bandwidths (due to the large margin required) even with diversity at the terminal.

REFERENCES

- [1] J. Thornton, D. Grace, C. Spillard, T. Konefal, T.C. Tozer, "Broadband communications from a high-altitude platform: the European helinet programme", *Electronics & Communication Engineering Journal*, Vol. 13, Issue 3, pp. 138-144, June 2001.
- [2] F. Tila, P.R. Shepherd and S.R. Pennock, "Analysis of Indoor-Indoor and Satellite/Hap-Indoor Propagation Effects", *11th International Conference on Antennas and Propagation*, pp. 203-207, April 2001.
- [3] F. Tila, P.R. Shepherd and S.R. Pennock, "Indoor Ray Tracing evaluation of enhanced High Frequency communications using Directional Antennas at the Basestation and Space Diversity at the Terminal", to be published at the 31st European Microwave Conference (EuMC), 2001.
- [4] <http://www.york.ac.uk/admin/presspr/haps.htm>.
- [5] Ch. Ghobadi, P.R. Shepherd and S.R. Pennock, "2D Ray-Tracing Model for Indoor Radio Propagation at Millimeter Frequencies and the Study of Diversity Techniques," *IEE Proc.-Microw. Antennas Propagation*, vol. 145, no. 4, pp. 349-353, Aug. 1998.
- [6] L.M. Correia and P.O. Frances, "Estimation of Materials Characteristics from power Measurements at 60GHz", *IEEE PIMRC*, pp. 510-513, 1995.
- [7] T. Harrold et al, "The indoor-outdoor radio environment," *Electronics & Communication Engineering Journal*, Vol. 12, Issue 6, pp. 249-261, Dec. 2000.
- [8] G.E Athanasiadou and A.R Nix, "A novel 3-D indoor ray-tracing propagation model: the path generator and evaluation of narrow-band and wide-band predictions," *IEEE Transactions on Vehicular Technology*, vol. 49, issue 4, pp. 1152-1168, July 2000.
- [9] J. Proakis, "Digital Communications," Third Edition, 2000.

Indoor Ray Tracing Evaluation of Directional Antennas and Space Diversity at 17 GHz

F. Tila, S.R. Pennock & P.R. Shepherd

Department of Electronic and Electrical Engineering,
University of Bath, UK

Tel: + 44-(0)1225-826281, Email: eepft@bath.ac.uk

Abstract

This paper presents an evaluation of enhanced high frequency indoor communications using directional antennas at the basestation. Frequencies at 17GHz are assumed [1]. Additional schemes such as spaced antenna diversity at the terminal and antenna sectorisation at the basestation are also explored. Detailed propagation information is supplied using a site specific two-dimensional ray-tracing propagation model developed previously at the University of Bath. Based on this analysis, the most appropriate antenna configurations will be identified for future high frequency indoor communications.

Propagation Modelling & Diversity

The propagation analysis uses a system of ray-tube launching from each of the basestation antennas. First an example indoor database is generated (including material properties) and then ray tracing is applied to track the various path reflections and refractions at material boundaries to a predefined signal strength [2][3]. The indoor test environment is shown in figure 1. Wireless communications are known to suffer from fast fading and this can seriously disrupt the quality of the radio link (particularly in non-line-of-sight locations). In this paper a number of diversity techniques are analysed to further enhance radio communication in an indoor environment.

System Analysis

In presentation the techniques described in the previous section will be analysed in detail. More specifically, it will focus on the following operating modes:

- i) Sectorised directional antenna to omni terminal antenna
- ii) Sectorised directional antenna to space diversity terminal

For each mode, ray tracing prediction grids will be generated and the appropriate transmit and/or receive diversity processing applied. Normalised field strength grids will be produced throughout the indoor environment to determine the relative service quality for each method. Figure 2 shows the result for sectorised directional basestation antenna communicating with a mobile terminal employing spaced antenna diversity. These results will then be compared to determine the relative strengths and weaknesses of each mode. Additional factors such as the cost and power consumption of each scheme will be used in the final comparison and ranking.

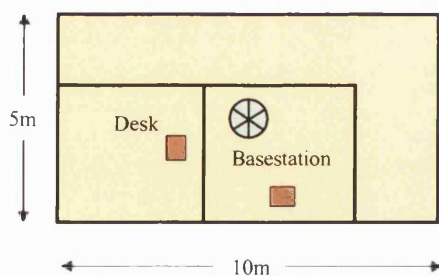


Figure 1: Example Environment

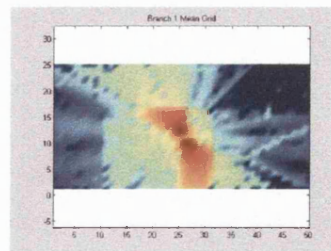


Figure 2: Normalised field strength Grid (sector no. 4, phased array basestation to space diversity terminal in test environment)

References

- [1] F. Tila, P.R. Shepherd and S.R. Pennock, "Analysis of Indoor-Indoor and Satellite-Indoor Propagation Effects", *ICAP*, April 2001.
- [2] Ch. Ghobadi, P.R. Shepherd and S.R. Pennock, "2D Ray-Tracing Model for Indoor Radio Propagation at Millimetre Frequencies and the Study of Diversity Techniques," *IEE Proc.-Microw. Antennas Propagation*, vol. 145, no. 4, pp. 349-353, Aug. 1998.
- [3] F. Tila, SR. Pennock and PR. Shepherd, "Evaluation of Indoor Propagation Effects and Diversity Techniques", *Proc. IEE PREP*, pp. 23-25, 2001.

Theoretic Capacity Evaluation of Indoor Micro- and Macro-MIMO systems at 5GHz using Site Specific Ray Tracing

F. Tila, PR. Shepherd and SR. Pennock

Department of Electronic & Electrical Engineering, University of Bath

Email: eept@bath.ac.uk

Indexing terms: MIMO Capacity, Ray Tracing, Micro MIMO, Macro MIMO

Abstract: This paper provides simulation results for the capacity distribution of an indoor Multiple Input Multiple Output (MIMO) communications system. Results are based on ray-traced propagation data for micro- and macro-MIMO array configurations. Capacity levels are compared with well known mathematical results for uncorrelated Rayleigh fading. Significant capacity gains are seen using a macro MIMO configuration.

Introduction: This letter explores the impact of realistic multipath statistics and practical Access Point (AP) and Mobile Terminal (MT) array configurations on the theoretic MIMO capacity bound. In particular, the use of widely spaced configurations at the AP (termed macro-MIMO) is explored. Instead of assuming identical and independently distributed (i.i.d) Rayleigh fading statistics across the transmit and receive arrays, here capacity is obtained from a detailed Ray Tracing (RT) analysis [1] of the various antenna element to element links in a site specific indoor environment. The work is performed in the 5.2 GHz band and is considered applicable to future high bit rate extensions of IEEE 802.11a.

Micro and Macro MIMO: The use of RT enables the impact of array configurations and practical multipath fading statistics to be considered in the MIMO analysis. In this contribution the number of transmit and receive elements, N_t and N_r , are both fixed at 4. The MT is modelled as a Uniform Linear Array (ULA) of vertical dipoles with half wavelength inter-element spacing. Two types of AP array are explored. The first approach, *micro*-MIMO, assumes a half wavelength ULA of vertical dipoles mounted in the corner of the room. The second configuration, *macro*-MIMO, comprises individual AP dipoles placed in each corner of the room. The operating environment (which includes a table, desk and several doors), the array locations and the measurement routes are shown in Fig. 1. For the RT analysis, the transmit power per element was fixed at -10dBm and the noise floor was assumed to lie at -91 dBm.

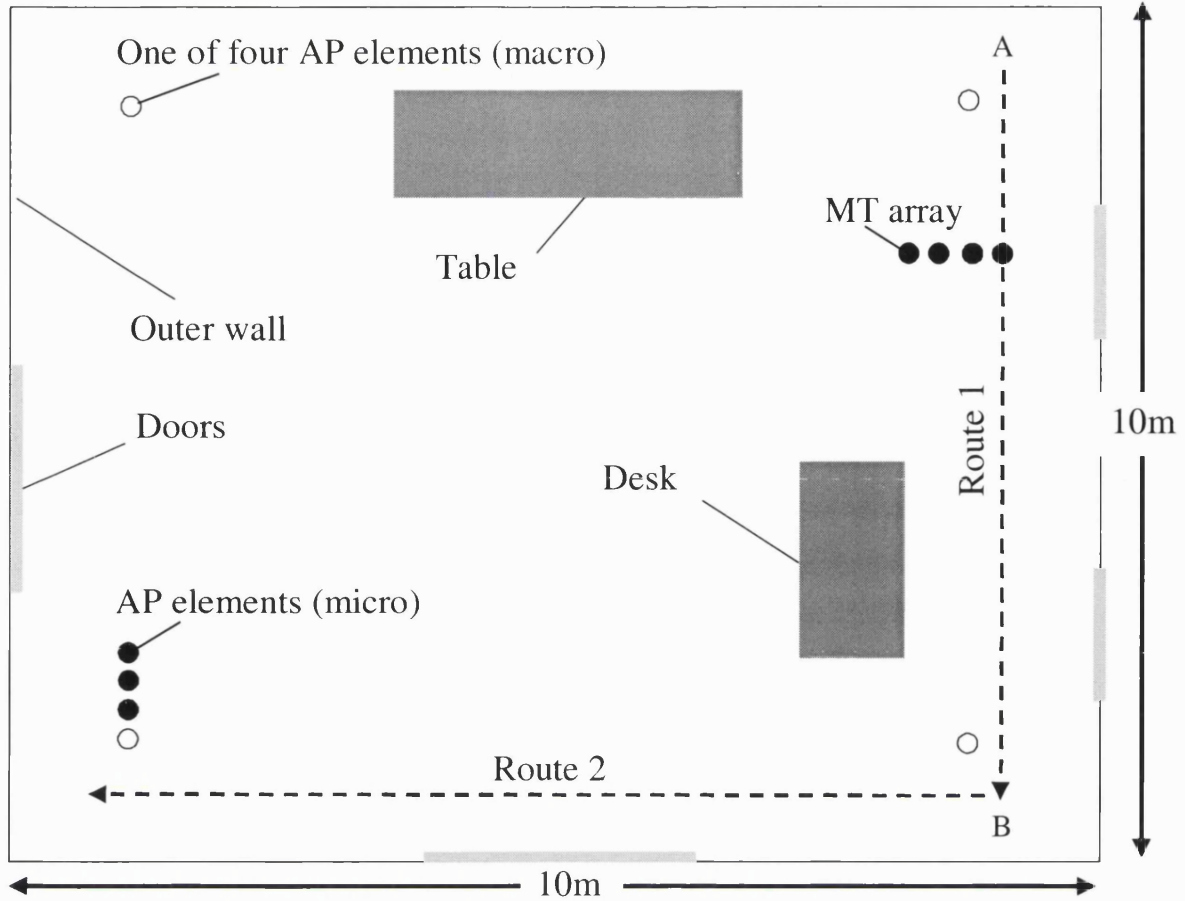


Fig.1: Indoor test environment, array configuration and routes. Walls are concrete (relative permittivity 5.0, conductivity 0.137) and doors and furniture is made of wood (relative permittivity 2.0, conductivity 0.0006).

MIMO RT Capacity Bound: The average MIMO capacity can be calculated at each point along the route using eqn (1), where $E\{\}$ represents the expectation function, C the average channel capacity, d the distance along the measurement route, $\bar{\gamma}$ the measured signal to noise ratio and \mathbf{H}_n the normalised MIMO link matrix [2].

$$C(d) = E\left\{\log_2 \left| \det \left(I + \bar{\gamma}(d) \mathbf{H}_n(d) \mathbf{H}_n^*(d) \right) \right| \right\} \quad (1)$$

The elements of \mathbf{H} and the value for $\bar{\gamma}$ at each point along a given route are extracted from a detailed RT analysis that incorporates details of the array geometries and element patterns involved. MIMO capacity depends on both the SNR and the scattering observed in the \mathbf{H} matrix. Using a RT propagation model [1], the resulting fading is not constrained to follow either a Rayleigh distribution or to remain perfectly decorrelated over the arrays.

MIMO Rayleigh Capacity Bound: In [2] the elements of \mathbf{H} are randomly generated using i.i.d complex Gaussian samples. Sufficient samples are taken to provide a good approximation to the expectation function. This analysis is non-environment specific and provides the well known Rayleigh fading MIMO capacity bound.

In order to evaluate the capacity loss due to correlation and/or a lack of scatter in the measured \mathbf{H} matrix, the capacity assuming i.i.d Rayleigh fading is also computed. The resulting average capacity bound is given by eqn (2), where \mathbf{H}_{Ray} denotes a normalised and uncorrelated Rayleigh fading matrix and all other parameters are as defined in eqn (1).

$$C_{Ray}(d) = E\left\{\log_2\left|\det\left(I + \bar{\gamma}(d)\mathbf{H}_{ray}(d)\mathbf{H}_{ray}^*(d)\right)\right|\right\} \quad (2)$$

Results: In this section the average SNR, the \mathbf{H} -matrix and the MIMO capacity bounds are calculated for the two routes illustrated in Fig. 1. The routes are each 9.2m in length and samples are taken every centimetre. RT is used to predict the SNR and \mathbf{H} -matrix entries for each point in the route. This data is then processed to compute the RT MIMO capacity bound and the i.i.d Rayleigh fading capacity bound (using the RT predicted SNR). This analysis is repeated for the micro and macro configurations.

Fig. 2 shows the predicted SNR $\bar{\gamma}(d)$ for the micro and macro MIMO configuration. The analysis is based on the radio parameters and noise floor assumptions listed earlier. We assume a constant transmitter power and do not consider the use of active power control [3]. Under these assumptions it is clear that the macro-MIMO configuration results in a significantly higher average SNR along the route. From table 1, gains of more than 12 dB and 6 dB are seen for routes 1 and 2 respectively.

System	Capacity, Ray Traced (b/s/Hz)	Capacity, Rayleigh (b/s/Hz)	Average S/N (dB)
Micro (Route 1)	9.45	14.11	14.28 (see fig. 2)
Micro (Route 2)	12.34	16.25	17.02
Macro (Route 1)	21.26	29.13	26.58 (see fig. 2)
Macro (Route 2)	23.73	25.93	23.18

Table 1: Summary of Average SNR and Capacity over Routes 1 and 2

capacity using RT was found to be around 71% of the ideal Rayleigh bound. Application of macro-MIMO resulted in an approximate doubling of the theoretic capacity.

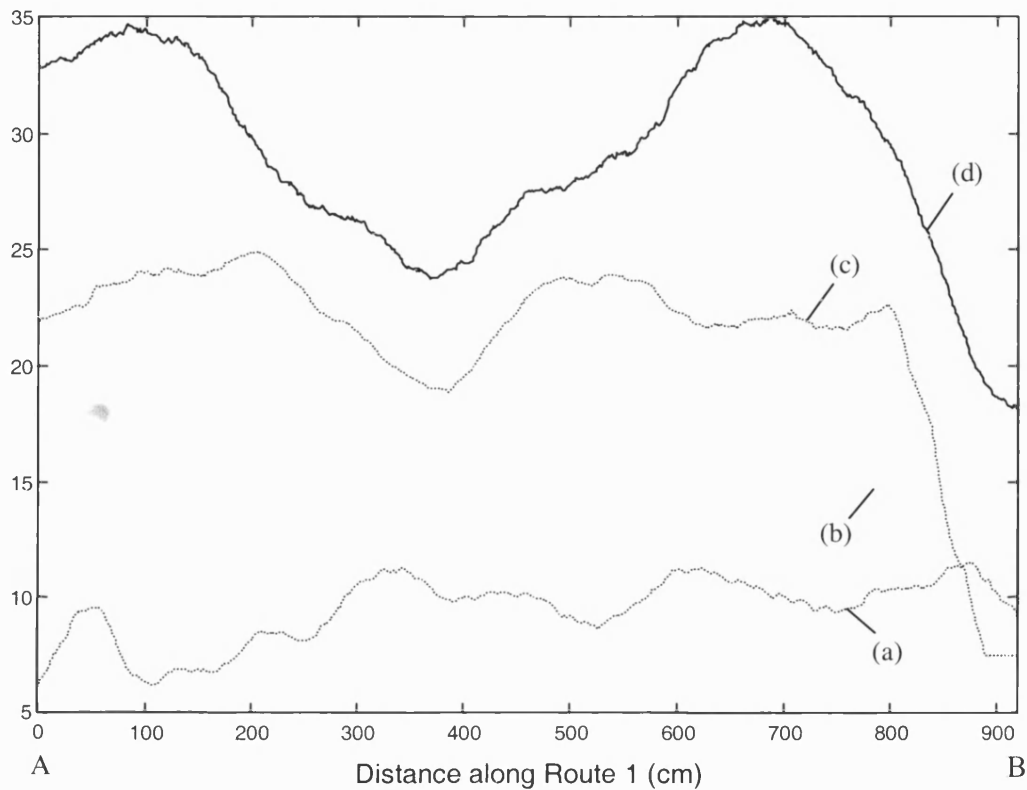


Figure 3: Comparison of MIMO capacity along Route 1. (a) Micro (RT generated SNR and \mathbf{H} -matrix), (b) Micro (RT generated SNR and i.i.d Rayleigh \mathbf{H} -matrix) (c) Macro (RT generated SNR and \mathbf{H} -matrix) (d) Macro (RT generated SNR and i.i.d Rayleigh \mathbf{H} -matrix)

References

- [1] F. Tila, PR. Shepherd and SR. Pennock, "Analysis of Indoor-Indoor and Satellite/Hap-Indoor Propagation Effects", *11th International Antennas and Propagation Professional Network ICAP*, pp. 203-7, Manchester, April 2001.
- [2] Gerald J. Foschini, "Layered Space-Time Architecture for Wireless Communication in a Fading Environment When Using Multi-Element antennas", *Bell Labs Technical Journal*, Autumn 1996.
- [3] P. F. Driessen & G. J. Foschini. 'On the Capacity Formula for Multiple Input-Multiple Output Wireless Channels: A Geometric Interpretation', *IEEE Trans. On Communications*, Vol. 47, No. 2, pp. 173-6, February 1999.